MEASUREMENT OF THE $t\bar{t}$ PRODUCTION CROSS SECTION IN $p\bar{p}$ COLLISIONS AT $\sqrt{s} = 1.96$ TeV USING LEPTON+JETS EVENTS IN THE CDF DETECTOR AT FERMILAB

MEDIDA DE LA SECCIÓN EFICAZ DE PRODUCCIÓN $t\bar{t}$ EN COLISIONES $p\bar{p}$ CON $\sqrt{s} = 1.96$ TeV UTILIZANDO SUCESOS DE LEPTON+JETS EN EL DETECTOR CDF DE FERMILAB

Instituto de Física de Cantabria
(CSIC-Universidad de Cantabria)
y
Departamento de Física Moderna
(Universidad de Cantabria)

Memoria presentada por:
Enrique Palencia Cortezón
para optar al grado de Doctor
en Ciencias Físicas

Da. Teresa Rodrigo Anoro, Catedrática de Universidad del área de Física Atómica, Molecular y Nuclear de la Facultad de Ciencias de la Universidad de Cantabria, y **D. Gervasio Gómez Gramuglio**, investigador Ramón y Cajal del CSIC adscrito al Instituto de Física de Cantabria (CSIC-Universidad de Cantabria),

Certifican:

Que la presente memoria: **"Medida de la Sección Eficaz de Producción de Pares top-antitop en Colisiones $p\bar{p}$ con $\sqrt{s} = 1.96$ TeV Utilizando Sucesos de Lepton+Jets en el Detector CDF de Fermilab"**, ha sido realizada bajo nuestra dirección en el Departamento de Física Moderna de la Facultad de Ciencias de la Universidad de Cantabria por *Enrique Palencia Cortezón*, para optar al grado de Doctor en Ciencias Físicas.

Y para que así conste, en cumplimiento de la legislación vigente, presentamos ante la Universidad de Cantabria esta memoria, firmando el presente certificado:

Santander, a 7 de Diciembre de 2006

To my family and friends.

Contents

List of Figures

List of Tables

Chapter 1

Introduction

The top quark is the most massive fundamental particle observed so far, and the study of its properties is interesting for several reasons ranging from its possible special role in electroweak symmetry breaking to its sensitivity to physics beyond the standard model (SM). In particular, the measurement of the top quark pair production cross section $\sigma_{t\bar{t}}$ is of interest as a test of QCD predictions. Recent QCD calculations done with perturbation theory to next-to-leading order predict $\sigma_{t\bar{t}}$ with an uncertainty of less than 15% [1, 2], which motivate measurements of comparable precision.

Top quark pairs in the SM are produced via either quark-antiquark annihilation or gluon-gluon fusion in hadron colliders. At the Fermilab Tevatron collider, with a center-of-mass energy of 1.96 TeV in $p\bar{p}$ collisions, about 85% of the total top pair production comes from quark-antiquark annihilation. At this center-of-mass energy, the calculated cross section, for the combined Tevatron Run I top mass of 178 GeV/c^2 [3], is $6.1^{+0.6}_{-0.8}$ pb [1] and decreases by approximately 0.2 pb for each increase of 1 GeV/c^2 in the value of the top mass over the range 170 GeV/c^2 $< m_t <$ 190 GeV/c^2. The standard model top quark decays to a W boson and a b quark almost 100% of the time, resulting in a final state from $t\bar{t}$ production of two W bosons and two b jets from b quark fragmentation. When one W decays leptonically and the other W decays to quarks, the $t\bar{t}$ event typically contains a high momentum charged lepton, an undetected neutrino and four high transverse momentum jets, two of which originate from b quarks. The undetected neutrino results in an imbalance of the transverse energy of the event, labeled as "missing E_T" ($\not\!\!E_T$). This decay mode is called "lepton+jets".

In this thesis, we report a measurement of the cross section for pair production of top quarks in the lepton+jets channel in 318 pb^{-1} of $p\bar{p}$ collision data at $\sqrt{s} = 1.96$ TeV. The data were recorded between March 2002 and September 2004, during Run II of the Tevatron, by the CDF II detector, a general purpose detector which combines charged particle trackers, sampling calorimeters, and muon detectors. Processes in which a W boson is produced in association with several jets with large transverse momentum can be misidentified as $t\bar{t}$, since they have the same signature. In order to separate the $t\bar{t}$ events from this background, we develop a method to tag b-jets based on tracking information from the silicon detector. The main event selection requires at least one tight (more restrictive) b tag in the event. As a cross check, we also measure the cross section using events with a loose (less restrictive)

b tag and events which have at least two tight or at least two loose b tags. Background contributions from heavy flavor production processes, such as $Wb\bar{b}$, $Wc\bar{c}$ or Wc, misidentified W bosons, electroweak processes, single top production, and mistagged jets are estimated using a combination of Monte Carlo calculations and independent measurements in control data samples. An excess over background in the number of events that contain a lepton, missing energy and three or more jets with at least one b-tag is assumed to be a signal of $t\bar{t}$ production and is used to measure the production cross section $\sigma_{t\bar{t}}$.

Previous measurements [4] at $\sqrt{s} = 1.8$ TeV gave a production cross section consistent with the standard model prediction. Recent CDF measurements at $\sqrt{s} = 1.96$ TeV are reported in Refs. [5–9] and use different techniques and top decay channels. The measurement described here analyzes more data than the above, and uses a jet probability b-tagging algorithm. A feature of this algorithm is that b-tagging is based on a continuous probability function rather than on a discrete object such as a secondary vertex. Potentially, this tagger can also be used to statistically separate b and c heavy flavor contributions.

The organization of this paper is as follows. Chapter 3 reviews the detector systems relevant to this analysis. In Chapter 4, we describe the data sample and event reconstruction. The b-tagging algorithm and its efficiency and misidentification ("fake") rate are discussed in Chapter 5. Chapter 6 describes the event selection. The estimate of the different backgrounds is presented in Chapter 7. The $t\bar{t}$ event acceptance and tagging efficiency are derived in Chapter 8. The $t\bar{t}$ production cross section measurements in single and double tagged events are reported in Chapters 9, and 10, respectively. Finally, the conclusions are presented in Chapter 11.

Chapter 2

Theoretical Overview

This analysis studies the production cross section for $t\bar{t}$ events at $\sqrt{s} = 1.96$ TeV. This chapter examines the theoretical overview of phenomenology associated with the top quark's properties, production and decay.

At present, top quarks can only be directly produced at the Tevatron. The top quark is, by far, the heaviest of the six fundamental quarks in the Standard Model (SM) of particle physics. Its large mass made the search for the top quark a long process, since accelerators with high centre-of-mass energies are needed. In 1977 the discovery of the bottom quark indicated the existence of a third quark generation, and shortly thereafter the quest for the top quark began. Searches were conducted in electron-positron (e^+e^-) and proton-antiproton ($p\bar{p}$) collisions during the 1980s and early 1990s. Finally, in 1995 the top quark was discovered at the Fermilab Tevatron $p\bar{p}$ collider. Subsequently, its mass was precisely measured to be $M_{\rm top} = (178.0 \pm 4.3)\,{\rm GeV}/c^2$ [10] [†]. The relative precision of this measurement (2.4%) is better than our knowledge of any other quark mass. As is shown in Fig. 2.1, the top quark is about 40 times heavier than the second-heaviest quark, the bottom quark. Its huge mass makes the top quark an ideal probe for new physics beyond the SM. It remains an open question to particle physics research whether the observed mass hierarchy is a result of unknown fundamental particle dynamics. It has been argued that the top quark could be the key to understand how particle masses are generated by the mechanism of electroweak symmetry breaking, since its mass is close to the energy scale at which the breakdown occurs (vacuum expectation value of the Higgs field = 246 GeV) [12]. The most favoured framework to describe electroweak symmetry breaking is the Higgs mechanism. The masses of the Higgs boson, the W boson and the top quark are closely related through higher order corrections to various physics processes. A precise knowledge of the top quark mass together with other electroweak precision measurements can therefore be used to predict the Higgs boson mass.

The outline of this chapter is as follows: In Section 2.1 we give a brief introduction to the SM of particle physics and stress the importance of the top quark for higher order corrections to electroweak perturbation theory. In particular, we discuss electroweak precision

[†] Recently, the top mass was measured with a higher accuracy, $M_{\rm top} = (172.5 \pm 2.3)\,{\rm GeV}/c^2$ [11] (relative precision of 1.3%). In the work presented here, a SM top quark with a mass of $178\,{\rm GeV}/c^2$ is assumed because this was the top mass world average when the analysis was started.

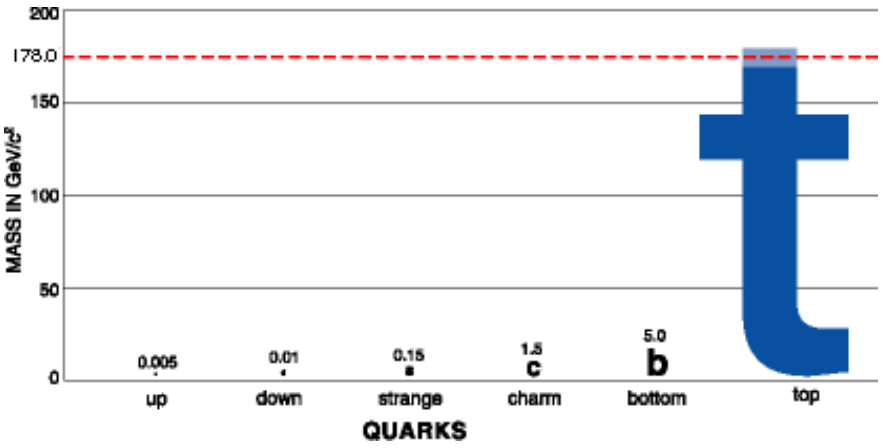

Figure 2.1: Comparison of masses of SM quarks.

measurements used to predict the top quark and Higgs boson mass within the SM. But there are some features that SM cannot explain, we will cover them in Section 2.2. Section 2.3 describes top quark physiscs including the theoretical description of SM top quark production at hadron colliders (2.3.1), the top quark decay (2.3.2), the top quark signature in $t\bar{t}$ events (2.3.3) and some top related physics processes beyond the SM (2.3.4). In Section 2.4 we recall the early searches for the top quark in the 1980s and the discovery at the Tevatron in 1994/95. Finally, in Section 2.5 we present the motivation of the analysis and the technique used to measure the top-antitop pair production cross section.

2.1 The Standard Model

The Standard Model (SM) of particle physics is a theory of fundamental particles which postulates that all matter is composed of a few basic, point-like and structureless constituents: elementary particles. One distinguishes two groups: quarks and leptons. Both of them are fermions and carry spin 1/2. The quarks come in six different flavours: up, down, charm, strange, top and bottom; formally described by assigning flavour quantum numbers. The SM incorporates six leptons: the electron (e^-) and the electron-neutrino (ν_e), the muon (μ^-) and the muon-neutrino (ν_μ), the tau (τ^-) and the tau-neutrino (ν_τ). They carry electron, muon and tau quantum numbers. Quarks and leptons can be grouped into three generations (or families) as shown in Table 2.1 which also contains the charges and masses of the particles.

The three generations exhibit a striking mass hierarchy, the top quark having by far the highest mass. Understanding the deeper reason behind the hierarchy and generation structure is one of the open questions of particle physics. Each quark and each lepton has an associated antiparticle with the same mass but opposite charge. The antiquarks are denoted $\bar{u}$, $\bar{d}$, etc. The antiparticle of the electron is the positron (e^+).

The forces of nature acting between quarks and leptons are described by quantized fields. The interactions between elementary particles are due to the exchange of field quanta which

Table 2.1: Charges and masses of the three generations of quarks and leptons [13].

Generation	First		Second		Third	
Quarks (spin = 1/2)						
Symbol	u	d	c	s	t	b
Charge	+2/3	-1/3	+2/3	-1/3	+2/3	-1/3
Mass (MeV/c^2)	1.5-4	4-8	(1.15-1.35)·10^3	80-130	(178.0±4.3)·10^3	(4.1-4.4)·10^3
Interaction	EM, Weak, Strong					
Leptons (spin = 1/2)						
Symbol	ν_e	e^-	ν_μ	μ^-	ν_τ	τ^-
Charge	0	-1	0	-1	0	-1
Mass (MeV/c^2)	$< 3 \cdot 10^{-6}$	0.51	<0.19	106	<18.2	1777
Interaction	Weak	EM, Weak	Weak	EM, Weak	Weak	EM, Weak

are said to mediate the forces. The SM incorporates the electromagnetic force, responsible for the emission of light from excited atoms, the weak force, which for instance causes nuclear beta decay, and the strong force which keeps nuclei stable. Gravitation is not included in the framework of the SM but rather described by the theory of general relativity. All particles with mass or energy feel the gravitational force. However, due to the weakness of gravitation with respect to the other forces acting in elementary particle reactions it is not further considered in this thesis.

The electromagnetic, weak and strong forces are described by so called quantum gauge field theories (see explanation below). The quanta of these fields carry spin 1 and are therefore called gauge bosons. Table 2.2 shows the charges and masses of the gauge bosons. The electromagnetic force is mediated by the massless photon (γ), the weak force by the massive $W^\pm$, $M_W = (80.425 \pm 0.038)$ GeV/c^2 [13], and the Z^0, $M_Z = (91.1876 \pm 0.0021)$ GeV/c^2 [13], and the strong force by eight massless gluons (g).

Table 2.2: Charges and masses of the gauge bosons.

Gauge Bosons (spin = 1)				
Symbol	Force	Coupling	Charge	Mass (GeV/c^2)
γ	EM	10^{-2}	0	0
W	Weak	10^{-13}	± 1	80.4
Z	Weak	10^{-13}	0	91.2
g	Strong	1	0	0

Quarks participate in electromagnetic, weak and strong interactions. All leptons experience the weak force, the charged ones also feel the electromagnetic force. But leptons do not take part in strong interactions. A thorough introduction to the SM can be found in various text books of particle physics [14–17].

2.1.1 Electroweak Interactions

In quantum field theory quarks and leptons are represented by spinor fields Ψ which are functions of the continuous space-time coordinates x_μ. To take into account that the weak interaction only couples to the left-handed particles, left- and right-handed fields $\Psi_{\mathbf{L}} = \frac{1}{2}(1-\gamma_5)\,\Psi$ and $\Psi_{\mathbf{R}} = \frac{1}{2}(1+\gamma_5)\,\Psi$ are introduced. The left-handed states of one generation are grouped into weak-isospin doublets, the right-handed states form singlets:

$$\begin{pmatrix} u \\ d \end{pmatrix}_L \quad \begin{pmatrix} c \\ s \end{pmatrix}_L \quad \begin{pmatrix} t \\ b \end{pmatrix}_L \qquad \begin{pmatrix} \nu_e \\ e \end{pmatrix}_L \quad \begin{pmatrix} \nu_\mu \\ \mu \end{pmatrix}_L \quad \begin{pmatrix} \nu_\tau \\ \tau \end{pmatrix}_L$$

$$\begin{array}{lll} u_R & c_R & t_R \\ d_R & s_R & b_R \end{array} \qquad e_R \qquad \mu_R \qquad \tau_R$$

The weak-isospin assignment for the doublet is: up-type quarks (u,c,t) and neutrinos carry $T_3 = +\frac{1}{2}$; down-type quarks (d,s,b), electron, muon and tau lepton have $T_3 = -\frac{1}{2}$. In the original SM the right-handed neutrino states are omitted, since neutrinos are assumed to be massless. Recent experimental evidence [18–20], however, strongly indicates that neutrinos have mass and the SM needs to be extended in this respect.

The dynamics of the electromagnetic and weak forces follow from the free particle Lagrangian density

$$\mathcal{L}_0 = i\,\overline{\Psi}\,\gamma^\mu \partial_\mu\,\Psi \tag{2.1}$$

by demanding the invariance of $\mathcal{L}_0$ under local phase transformations:

$$\Psi_{\mathbf{L}} \longrightarrow e^{ig\alpha(x)\cdot\mathbf{T}+ig'\beta(x)Y}\,\Psi_{\mathbf{L}} \qquad \text{and} \qquad \Psi_{\mathbf{R}} \longrightarrow e^{ig'\beta(x)Y}\,\Psi_{\mathbf{R}}\,. \tag{2.2}$$

For historical reasons these transformations are also referred to as gauge transformations. In Eq. 2.2 the parameter $\alpha(x)$ is an arbitrary three-component vector and $\mathbf{T} = (T_1,\, T_2,\, T_3)^t$ is the weak-isospin operator whose components T_i are the generators of $SU(2)_L$ symmetry transformations. The index L indicates that the phase transformations act only on left-handed states. The matrix representations are given by $T_i = \frac{1}{2}\,\tau_i$ where the τ_i are the Pauli matrices. The T_i do not commute: $[T_i, T_j] = i\,\epsilon_{ijk}\,T_k$. That is why the $SU(2)_L$ gauge group is said to be non-Abelian. $\beta(x)$ is a one-dimensional function of x. Y is the weak hypercharge which satisfies the relation $Q = T_3 + Y/2$, where Q is the electromagnetic charge. Y is the generator of the symmetry group $U(1)_Y$. Demanding the Lagrangian $\mathcal{L}_0$ to be invariant under the combined gauge transformations of $SU(2)_L \times U(1)_Y$, see Eq. 2.2, requires the addition of terms to the free Lagrangian which involve four additional vector (spin 1) fields: the isotriplet $\mathbf{W}_\mu = (W_{1\,\mu}\,, W_{2\,\mu}\,, W_{3\,\mu})^t$ for $SU(2)_L$ and the singlet B_μ for $U(1)_Y$. This is technically done by replacing the derivative ∂_μ in $\mathcal{L}_0$ by the covariant derivative

$$D_\mu = \partial_\mu + i\,g\,\mathbf{W}_\mu \cdot \mathbf{T} + i\,g'\frac{1}{2}B_\mu Y \tag{2.3}$$

and adding the kinetic energy terms of the gauge fields: $-\frac{1}{4}\mathbf{W}_{\mu\nu}\cdot\mathbf{W}^{\mu\nu} - \frac{1}{4}B_{\mu\nu}\cdot B^{\mu\nu}$. The field tensors $\mathbf{W}_{\mu\nu}$ and $B_{\mu\nu}$ are given by $\mathbf{W}_{\mu\nu} = \partial_\mu \mathbf{W}_\nu - \partial_\nu \mathbf{W}_\mu - g\cdot\mathbf{W}_\mu \times \mathbf{W}_\nu$ and $B_{\mu\nu} =$

$\partial_\mu B_\nu - \partial_\nu B_\mu$. Since the vector fields $\mathbf{W}_\mu$ and B_μ are introduced via gauge transformations they are called gauge fields and the quanta of these fields are named gauge bosons. For an electron-neutrino pair, for example, the resulting Lagrangian is:

$$\begin{aligned}\mathcal{L}_1 &= i\,\overline{\begin{pmatrix}\nu_e\\ e\end{pmatrix}}_L \gamma^\mu \left[\partial_\mu + i\,g\,\mathbf{W}_\mu\cdot\mathbf{T} + i\,g'\,Y_L\,\frac{1}{2}\,B_\mu\right]\begin{pmatrix}\nu_e\\ e\end{pmatrix}_L + \\ &\quad i\,\bar{e}_R\,\gamma^\mu\left[\partial_\mu - g'\,Y_R\,\frac{1}{2}\,B_\mu\right]e_R - \frac{1}{4}\,\mathbf{W}_{\mu\nu}\cdot\mathbf{W}^{\mu\nu} - \frac{1}{4}B_{\mu\nu}\cdot B^{\mu\nu} \qquad (2.4)\end{aligned}$$

This model developed by Glashow [21], Weinberg and Salam [22, 23] in the 1960s allows to describe electromagnetic and weak interactions in one framework. One therefore refers to it as unified electroweak theory.

2.1.2 The Higgs Mechanism

One has to note, however, that $\mathcal{L}_1$ describes only massless gauge bosons and massless fermions. Mass-terms such as $\frac{1}{2}M^2B_\mu B^\mu$ or $-m\overline{\Psi}\Psi$ are not gauge invariant and therefore cannot be added. To include massive particles into the model in a gauge invariant way the Higgs mechanism is used. Four scalar fields are added to the theory in form of the isospin doublet $\mathbf{\Phi} = (\phi^+,\,\phi^0)^t$ where ϕ^+ and ϕ^0 are complex fields. This is the minimal choice. The term $\mathcal{L}_H = |D_\mu\Phi|^2 - V(\Phi^\dagger\Phi)$ is added to $\mathcal{L}_1$. The scalar potential takes the form $V(\Phi^\dagger\Phi) = \mu^2\,\mathbf{\Phi}^\dagger\mathbf{\Phi} + \lambda\,(\Phi^\dagger\Phi)^2$.

In most cases particle reactions cannot be calculated from first principles. One rather has to use perturbation theory and expand a solution starting from the ground state of the system which is in particle physics called the vacuum expectation value. The parameters μ and λ can be chosen such that the vacuum expectation value of the Higgs potential V is different from zero: $|\Phi_{\text{vac}}| = \sqrt{-\frac{1}{2}\,\mu^2/\lambda}$ and thus does not share the symmetry of V. The scalar Higgs fields inside Φ are redefined such that the new fields, $\xi(x) = (\xi_1(x), \xi_2(x), \xi_3(x))^t$ and $H(x)$, have zero vacuum expectation value. When the new parameterization of $\mathbf{\Phi}$ is inserted into the Lagrangian, the symmetry of the Lagrangian is broken, that is, the Lagrangian is not an even function of the Higgs fields anymore. This mechanism where the ground states do not share the symmetry of the Lagrangian is called spontaneous symmetry breaking. As a result, one of the Higgs fields, the $H(x)$ field, has acquired mass, while the other three fields, ξ, remain massless [24, 25].

Applying spontaneous symmetry breaking as described above to the combined Lagrangian $\mathcal{L}_2 = \mathcal{L}_1 + \mathcal{L}_H$ and enforcing local gauge invariance of $\mathcal{L}_2$, makes the three electroweak gauge bosons acquire mass. After all, this is the aim of the whole procedure. The massive bosons are, however, not the original fields $\mathbf{W}_\mu$ and B_μ but rather mixtures of those: the $W_\mu^\pm = (W_\mu^1 \mp i\,W_\mu^2)/\sqrt{2}$, the Z^0 and the photon field A_μ:

$$\begin{pmatrix}A_\mu\\ Z_\mu\end{pmatrix} = \begin{pmatrix}\cos\theta_W & \sin\theta_W\\ -\sin\theta_W & \cos\theta_W\end{pmatrix}\begin{pmatrix}B_\mu\\ W_\mu^3\end{pmatrix} \qquad (2.5)$$

The mixing angle θ_W is the Weinberg angle defined by the coupling constants $g'/g = \tan\theta_W$.

Spontaneous symmetry breaking also generates lepton masses if Yukawa interaction terms of the lepton and Higgs fields are added to the Lagrangian:

$$\mathcal{L}_{\text{Yukawa}}^{\text{lepton}} = -G_e \left[\bar{e}_R \left(\mathbf{\Phi}^\dagger \begin{pmatrix} \nu_e \\ e \end{pmatrix}_L \right) + \left(\overline{(\nu_e, e)}_L^t \mathbf{\Phi} \right) \; e_R \right] \tag{2.6}$$

Here the Yukawa terms for the electron-neutrino doublet are given as an example. G_e is a further coupling constant describing the coupling of the electron and electron-neutrino to the Higgs field. In this formalism neutrinos are assumed to be massless.

Quark masses are also generated by adding Yukawa terms to the Lagrangian. However, for the quarks, both the upper and the lower member of the weak-isospin doublet need to acquire mass. For this to happen an additional conjugate Higgs multiplet has to be constructed: $\Phi_c = i\tau_2\Phi^* = (\phi^{0^*}, -\phi^-)^t$. The Yukawa terms for the quarks are given by:

$$\mathcal{L}_{\text{Yukawa}}^{\text{quark}} = \sum_{i=1}^{3}\sum_{j=1}^{3} \tilde{G}_{ij} \; \bar{u}_{iR}\tilde{\Phi}^\dagger \begin{pmatrix} u_j \\ d_j \end{pmatrix}_L + G_{ij} \; \bar{d}_{iR} \; \Phi^\dagger \begin{pmatrix} u_j \\ d_j \end{pmatrix}_L + \text{ h.c.} \tag{2.7}$$

The u_j and d_j are the weak eigenstates of the up-type (u, c, t) and the down-type (d, s, b) quarks, respectively. Couplings between quarks of different generations are allowed by this ansatz. After spontaneous symmetry breaking the Yukawa terms produce mass terms for the quarks which can be described by mass matrices in generation space: $\overline{(u_1, u_2, u_3)}_R \; \mathcal{M}^u \; (u_1, u_2, u_3)_L^t$ and $\overline{(d_1, d_2, d_3)}_R \; \mathcal{M}^d \; (d_1, d_2, d_3)_L^t$ with $\mathcal{M}_{ij}^u = |\Phi_{\text{vac}}| \cdot \tilde{G}_{ij}$ and $\mathcal{M}_{ij}^d = |\Phi_{\text{vac}}| \cdot G_{ij}$. The mass matrices are non-diagonal but can be diagonalized by unitary transformations, which essentially means to change basis from weak eigenstates to mass eigenstates, which are identical to the flavour eigenstates u, c, t and d, s, b. In charged-current interactions ($W^\pm$ exchange) this leads to transitions between mass eigenstates of different generations referred to as generation mixing. It is possible to set weak and mass eigenstates equal for the up-type quarks and ascribe the mixing entirely to the down-type quarks:

$$\begin{pmatrix} d' \\ s' \\ b' \end{pmatrix}_L = \mathbf{V} \begin{pmatrix} d \\ s \\ b \end{pmatrix}_L = \begin{pmatrix} V_{ud} & V_{us} & V_{ub} \\ V_{cd} & V_{cs} & V_{cb} \\ V_{td} & V_{ts} & V_{tb} \end{pmatrix} \begin{pmatrix} d \\ s \\ b \end{pmatrix}_L \tag{2.8}$$

where d', s' and b' are the weak eigenstates. The mixing matrix $\mathbf{V}$ is called the Cabbibo-Kobayashi-Maskawa (CKM) matrix [26].

2.1.3 Strong Interactions

The theory of strong interactions is called quantum chromodynamics (QCD) since it attributes a colour charge to the quarks. There are three different types of strong charges (colours): "red", "green" and "blue". Strong interactions conserve the flavour of quarks. Leptons do not carry colour at all, they are inert with respect to strong interactions. QCD is a quantum field theory based on the non-Abelian gauge group $SU(3)_C$ of phase transformations

on the quark colour fields. Invoking local gauge invariance of the Lagrangian yields eight massless gauge bosons: the gluons. The gauge symmetry is exact and not broken as in the case of weak interactions. Each gluon carries one unit of colour and one unit of anticolour. The strong force binds quarks together to form bound-states called hadrons. There are two groups of hadrons: mesons consisting of a quark and an antiquark and baryons built of either three quarks or three antiquarks. All hadrons are colour-singlet states. Quarks cannot exist as free particles. This experimental fact is summarised in the notion of quark confinement: quarks are confined to exist in hadrons.

2.2 Physics Beyond the Standard Model

In spite of all its success, the SM is not complete, many mysteries remain. The already mentioned non null mass of the neutrinos calls for an extension of the SM. Another caveat of the SM that needs to be solved: the Higgs mass is subject to divergent quadratic radiative corrections that need to be somehow controlled in order for the Higgs mass to remain at the electroweak scale. If the SM is to remain valid up to the Planck scale without extension, such a cancellation requires some fine-tuned cancellation: this is referred to as the hierarchy problem. Several ways of solving the hierarchy problem have been proposed. For example, new strong dynamics could appear around 1 TeV (technicolor theories).

Another possibility is that the radiative corrections are canceled by a new spectrum of particles at the electroweak scale: supersymmetric (SUSY) theories propose that to every SM particle corresponds a supersymmetric partner with different spin, so that radiative correction contributions to the Higgs mass from a particle is cancelled by the contribution from its supersymmetric partner. To SM fermions (bosons) correspond bosonic (fermionic) superpartners. For example, the superpartner of the top quark is called stop, the superpartner of the gluon is the gluino $\tilde{g}$, and the superpartner of the gauge bosons W and Z are the gauginos $\tilde{\chi}^0$, $\tilde{\chi}^{\pm}$. SUSY requires additional Higgs fields in order to provide mass to both up and down families. In the minimal supersymmetric extension of the SM (MSSM), there are five Higgs bosons: h, H, A, and $H^{\pm}$.

Furthermore, the SM is unable to describe gravity, and cannot explain the existence of dark matter and dark energy without some extension.

2.3 Top Quark Physics

2.3.1 Production

In this Section we present the phenomenology of top quark production at hadron colliders. We limit the discussion to SM processes. Anomalous top quark production and non-SM decays will be covered in Section 2.3.4. Specific theoretical cross section predictions refer to the Fermilab Tevatron, running at $\sqrt{s} = 1.8$ TeV (Run I) or $\sqrt{s} = 1.96$ TeV (Run II), or to the future Large Hadron Collider (LHC) at CERN ($\sqrt{s} = 14$ TeV). In the intermediate

future the Tevatron and the LHC are the only two colliders where SM top quark production can be observed.

The two basic production modes of top quarks at hadron colliders are the production of $t\bar{t}$ pairs, which is dominated by the strong interaction, and the production of single top quarks due to electroweak interactions.

$t\bar{t}$ Production

We discuss only top quark pair production via the strong interaction. $t\bar{t}$ pairs can also be produced by electroweak interactions if a Z^0 or a photon are exchanged between the in- and outgoing quarks. However, at a hadron collider the cross sections for theses processes are completely negligible compared to the QCD cross section. The cross section for the pair production of heavy quarks has been calculated in perturbative QCD, i.e. as a perturbation series in the QCD running coupling constant $\alpha_s(\mu^2)$.

Figure 2.2 shows the corresponding tree level Feynman diagrams for the $t\bar{t}$ production processes. The production process shown on the left is called $q\bar{q}$ annihilation and the others are called gg fusion. Calculation at the next-to-leading order predicts that the relative contributions to the $t\bar{t}$ production from these two processes at Tevatron Run II are 85% and 15% respectively. The total cross section for the $t\bar{t}$ pair production is theoretically calculated to be $6.7^{+0.7}_{-0.9}$ pb for a top quark mass of 175 GeV/c^2 [27, 28].

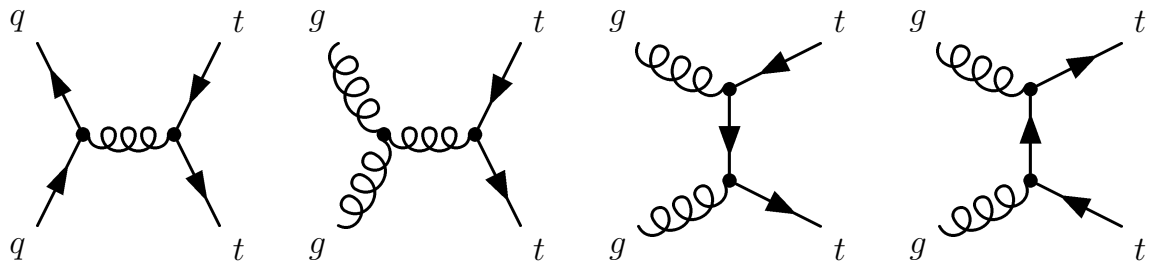

Figure 2.2: Feynman diagrams of the leading order processes for $t\bar{t}$ production: quark-antiquark annihilation ($q\bar{q} \to t\bar{t}$) and gluon fusion ($gg \to t\bar{t}$).

Figure 2.3 summarizes the total cross section measured at the CDF experiment in Run I and Run II compared to the prediction of the SM.

Single Top Quark Production

Top quarks can be produced singly via electroweak interactions involving the Wtb vertex. There are three production modes which are distinguished by the virtuality Q^2 of the W boson ($Q^2 = -q^2$, where q is the four-momentum of the W):

1. the **t-channel** ($q^2 = \hat{t}$): A virtual W strikes a b quark (a sea quark) inside the proton. The W boson is spacelike ($q^2 < 0$). This mode is also known as *W-gluon fusion*, since the b quark originates from a gluon splitting into a $b\bar{b}$ pair. Feynman diagrams representing this process are shown in Fig. 2.4a and Fig. 2.4b . W-gluon fusion is the dominant production mode, both at the Tevatron and at the LHC.

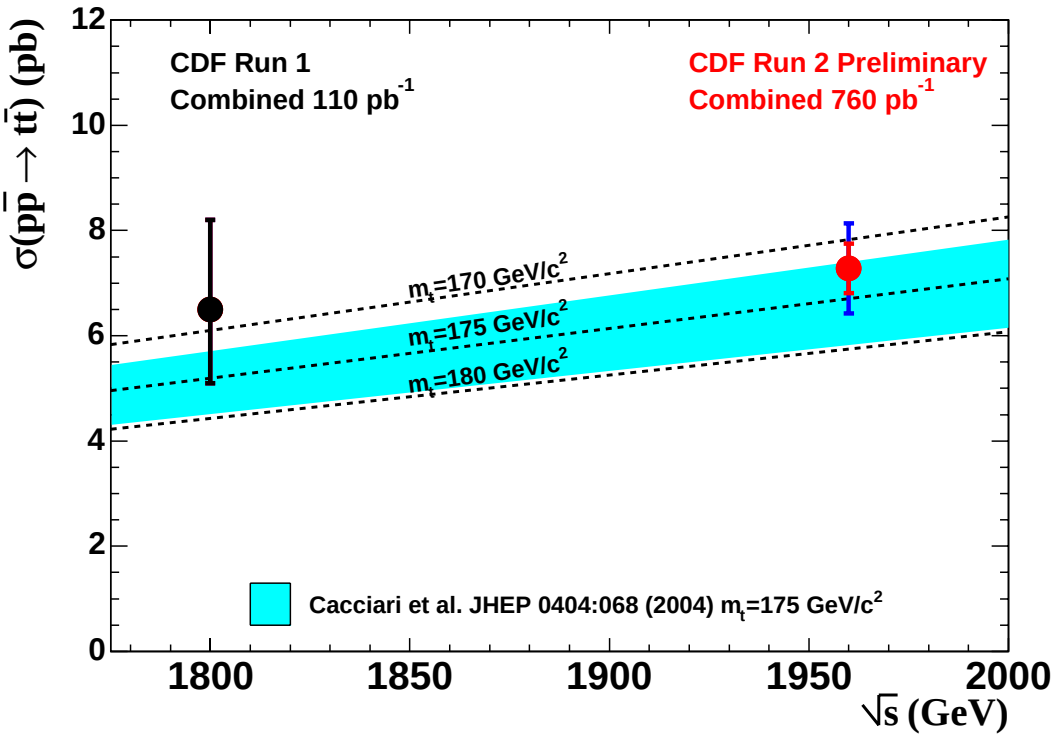

Figure 2.3: $t\bar{t}$ production cross section measured at CDF in Run I ($\sqrt{s} = 1.8\,\text{TeV}$) and Run II ($\sqrt{s} = 1.96\,\text{TeV}$). The band shows the theoretical prediction of the SM.

2. the **s-channel** ($q^2 = \hat{s}$): This production mode is of Drell-Yan type. A timelike W boson with $q^2 \geq (M_{\text{top}} + m_b)^2$ is produced by the fusion of two quarks belonging to an SU(2) isospin doublet. See Fig. 2.4c for the Feynman diagram.

3. **associated production**: The top quark is produced in association with a real (or close to real) W boson ($q^2 = M_W^2$). The initial b quark is a sea quark inside the proton. Figure 2.4d shows the Feynman diagram. The cross section is negligible at the Tevatron, but of considerable size at LHC energies where associated production even supercedes the s-channel.

In $p\bar{p}$ and pp collisions the cross section is dominated by contributions from up and down quarks coupling to the W boson on one side of the Feynman diagrams. That is why the (u, d) quark doublet is shown in the graphs of Fig. 2.4. There is of course also a small contribution from the second weak isospin quark doublet, (c, s); an effect of about 2% for s- and 6% for t-channel production [29]. Furthermore, we only consider single top quark production via a Wtb vertex. The production channels involving a Wtd or a Wts vertex are strongly suppressed due to small CKM matrix elements: $0.0048 < |V_{td}| < 0.014$ and $0.037 < |V_{ts}| < 0.043$ [13]. Thus, their contribution to the total cross section is quite small: $\sim 0.1\%$ and $\sim 1\%$, respectively [30].

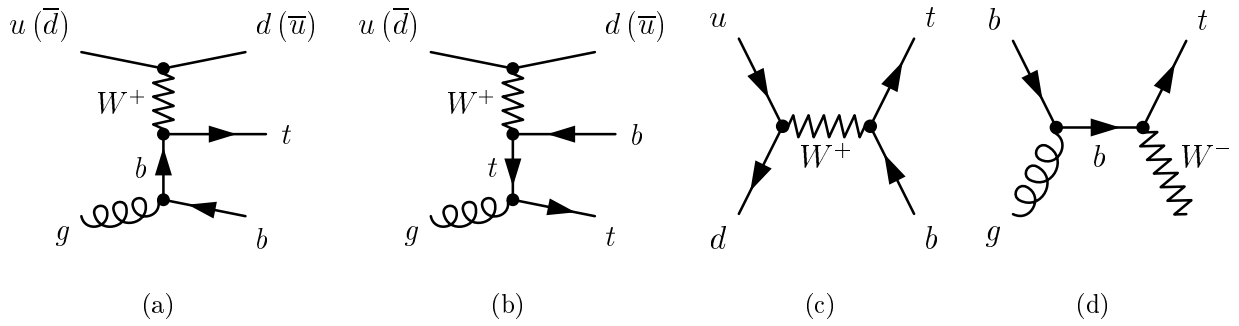

Figure 2.4: Representative Feynman diagrams for the three single top production modes. a) and b) show W-gluon fusion graphs, c) the s-channel process and d) associated production. We chose to draw the graphs in a), b) and c) with the (u, d) weak-isospin doublet coupling to the W. This is by far the dominating contribution. In general, also the (c, s) doublet contributes. The graphs show single top quark production, the diagrams for single antitop quark production can be obtained by interchanging quarks and antiquarks.

2.3.2 Decay

In the SM top quarks decay predominantly into a b quark and a W boson. The decays $t \to d + W^+$ and $t \to s + W^+$ are CKM suppressed relative to $t \to b + W^+$ by factors of $|V_{td}|^2$ and $|V_{ts}|^2$. If we assume the CKM matrix to be unitary the values of these matrix elements can be inferred from other measured matrix elements: $0.0048 < |V_{td}| < 0.014$ and $0.037 < |V_{ts}| < 0.043$ [13]. In the discussion of the following paragraphs we will therefore only consider the decay $t \to b + W^+$. Potential non-SM decays which would signal new physics will be discussed in Section 2.3.4.

At Born level the amplitude of the decay $t \to b + W^+$ is given by

$$\mathcal{M}(t \to b + W) = \frac{i\, g}{\sqrt{2}}\, \bar{b}\, \not{\epsilon}^W\, \frac{1 - \gamma_5}{2}\, t\ . \tag{2.9}$$

The decay amplitude is dominated by the contribution from longitudinal W bosons because the decay rate of the longitudinal component scales with M_{top}^3. In contrast, the top quark decay rate into transverse W bosons increases only linearly with M_{top}. In both cases the W^+ couples solely to b quarks of left-handed chirality (a general feature of the SM). Since the b quark is effectively massless compared to the mass scale set by M_{top}, left-handed chirality translates into left-handed helicity for the b quark. If the b quark is emitted anti-parallel to the top quark spin axis, the W^+ must be longitudinally polarized, $h^W = 0$, to conserve angular momentum. If the b quark is emitted parallel to the top quark spin axis, the W^+ boson has helicity $h^W = -1$ and is transversely polarized. Thus, elementary angular momentum conservation forbids the production of W bosons with positive helicity, $h^W = +1$, in top quark decays. The ratios of decay rates into the three W helicity states are given

by [31]:

$$\mathcal{A}(h^W = -1) : \mathcal{A}(h^W = 0) : \mathcal{A}(h^W = +1) = 1 : \frac{M_{\rm top}^2}{2\,M_W^2} : 0. \tag{2.10}$$

For the decay of antitop quarks negative helicity is forbidden. In the SM the top quark decay rate, including first order QCD corrections, is given by

$$\Gamma_t = \frac{G_F\ M_{\rm top}^3}{8\,\pi\,\sqrt{2}}\ \ |V_{tb}|^2\ \left(1 - \frac{M_W^2}{M_{\rm top}^2}\right)^2\ \left(1 + 2\,\frac{M_W^2}{M_{\rm top}^2}\right)\ \left[1 - \frac{2\,\alpha_s}{3\,\pi}\cdot f\,(y)\right] \tag{2.11}$$

with $y = (M_W/M_{\rm top})^2$ and $f(y) = 2\,\pi^2/3 - 2.5 - 3y + 4.5y^2 - 3y^2 \ln y$ [31–33]. Using $y = (80.45/174.3)^2$ we find $f(y) = 3.85$. The QCD corrections of order α_s lower the Born decay rate by -10%. A useful approximation of (2.11) is given by $\Gamma_{\rm top} \simeq 175$ MeV$/c^2 \cdot (M_{\rm top}/M_W)^3$ [31, 43]. The decay width increases from 1.07 GeV$/c^2$ at $M_{\rm top} = 160$ GeV$/c^2$ to 1.53 GeV$/c^2$ at $M_{\rm top} = 180$ GeV$/c^2$. Expression (2.11) neglects higher order terms proportional to $m_b^2/M_{\rm top}^2$ and α_s^2. Corrections of order α_s^2 were lately calculated, they lower $\Gamma_{\rm top}$ by about -2% [34, 35]. Because the top quark width is small compared to its mass, interference between QCD corrections to production and decay amplitudes has a small effect of order $\mathcal{O}(\alpha_s\Gamma_{\rm top}/M_{\rm top})$ [36]. The decay width for events with hard gluon radiation ($E_g >$ 20 GeV) in the final state has been estimated to be 5 – 10% of $\Gamma_{\rm top}$, depending on the gluon jet definition (cone size $\Delta R = 0.5$ to 1.0) [37]. Electroweak corrections to $\Gamma_{\rm top}$ have also been calculated and increase the decay width by $\delta_{\rm EW} = +1.7\%$ [38, 39]. Taking the finite width of the W boson into account leads to a negative correction $\delta_\Gamma = -1.5\%$ such that $\delta_{\rm EW}$ and δ_Γ almost cancel each other [40].

The large top decay rate implies a very short lifetime of $\tau_{\rm top} = 1/\Gamma_{\rm top} \approx 4 \cdot 10^{-25}$ s which is smaller than the characteristic formation time of hadrons $\tau_{\rm form} \approx 1/\Lambda_{\rm QCD} \approx 2 \cdot 10^{-24}$ s. In other words top quarks decay before they can couple hadronically to light quarks and form hadrons. The lifetime of $t\bar{t}$ bound states, toponium, is too small, $\Gamma_{t\bar{t}} \sim 2\,\Gamma_{\rm top}$, to allow for a proper definition of a bound state with sharp binding energy. This feature of a heavy top quark was already pointed out in the early and mid 1980s [41–43].

Even though top hadrons cannot be formed, there are other long-distance QCD effects associated with hadronization which have to be considered. The colour structure of the hard interaction process influences the subsequent fragmentation and hadronization process. In the process $e^+e^- \to t\bar{t}$ the top and antitop quark are produced in a colour-singlet state. In hadronic collisions, on the contrary, the production cross section is dominated by configurations where the t or $\bar{t}$ forms a colour-singlet with the proton or antiproton remnant, respectively. The colour field – or in the picture of string fragmentation the string – carries the more energy the further the top quark and the remnant are apart. If the distance in the top-remnant centre-of-mass system reaches about 1 fm before the top quark decays, the colour string carries enough energy to form light hadrons. Whether or not a significant fraction of top events exhibit the described "early" fragmentation process, depends strongly on the centre-of-mass energy of the hadron collider. While at Tevatron energies early top quark fragmentation effects are negligible [44], they may well play a role at the LHC, where top quarks are produced with a large Lorentz boost. If there is no early fragmentation,

long-range QCD effects connect the top quark decay products, the b quarks or the quarks from hadronic W decays. Even if early fragmentation happens, the fragmentation of heavy quarks is hard, as seen in c and b quark decays, i.e. the fractional energy loss of top quarks as they hadronize is small. Therefore, it will be quite challenging to observe top quark fragmentation experimentally, even at the LHC.

Within the constraints discussed above we can assume that top quarks are produced and decay like free quarks. The angular distribution of their decay products follow spin $\frac{1}{2}$ predictions. The angular distribution of W bosons from top decays is propagated to its decay products. In case of leptonic W decays the polarization is preserved and can be measured [45]. The angular distribution of charged leptons from W decays originating from top quarks is given by

$$\frac{1}{\Gamma}\frac{d\Gamma}{d\cos\theta_\ell} = \frac{3}{4}\frac{M_{\rm top}^2 \sin^2\theta_\ell + M_W^2(1-\cos\theta_\ell)^2}{M_{\rm top}^2 + 2\,M_W^2} \tag{2.12}$$

where $\pi - \theta_\ell$ is the angle between the b quark direction and the charged lepton in the W boson rest frame [46].

2.3.3 Top Quark Signature in $t\bar{t}$ Events

In this Section we discuss the experimental signature of top quark events. We constrain the discussion to the decay mode which dominates in the SM: $t \to W + b$ with a branching ratio close to 100%. We further concentrate on the signatures of $t\bar{t}$ events, since pair production is the main source of top quarks at the Tevatron and at the LHC.

Once both top quarks have decayed, a $t\bar{t}$ event contains two W bosons and two b quarks: $W^+W^-b\bar{b}$. Figure 2.5 shows the Feynman diagram for $t\bar{t}$ production by $q\bar{q}$ annihilation and the subsequent top quark decay. Experimentally, $t\bar{t}$ events are classified according to the decay modes of the W bosons. There are three leptonic modes ($e\nu_e$, $\mu\nu_\mu$, $\tau\nu_\tau$) and six decay modes into quarks of different flavour ($u\bar{d}$, $u\bar{s}$, $u\bar{b}$, $c\bar{d}$, $c\bar{s}$, $c\bar{b}$). We distinguish four $t\bar{t}$ event categories:

1. Both W bosons decay into light leptons (either $e\nu_e$ or $\mu\nu_\mu$) which can be directly seen in the detector. This category is called *dilepton* channel.

2. One W boson decays into $e\nu_e$ or $\mu\nu_\mu$. The second W decays into quarks. This channel is called *lepton-plus-jets*.

3. Both W bosons decay into quarks. We refer to this mode as the *all hadronic* channel.

4. At least one W boson decays into a tau lepton ($\tau\nu_\tau$) which itself can decay either leptonically (into $e\nu_e$ or $\mu\nu_\mu$) or hadronically into quarks.

In good approximation we can neglect all lepton masses with respect to the W mass and write:

$$\Gamma_W^0 \equiv \Gamma(W \to e\nu_e) = \Gamma(W \to \mu\nu_\mu) = \Gamma(W \to \tau\nu_\tau)$$

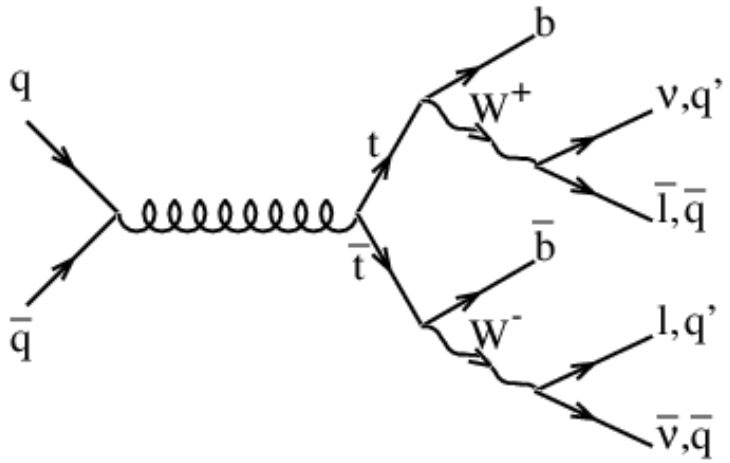

Figure 2.5: The tree level Feynman diagram for $t\bar{t}$ production by $q\bar{q}$ annihilation and its standard model decay chain.

At lowest order in perturbation theory the decay rate into a quark-antiquark pair, $q_1\bar{q}_2$, is given by the rate into leptons Γ^0_W multiplied by the square of the CKM matrix element $|V_{q_1q_2}|^2$ and enhanced by a colour factor of 3, which takes into account that quarks come in three different colours:

$$\Gamma(W \to q_1\bar{q}_2) = 3\,|V_{q_1q_2}|^2\;\Gamma^0_W\;.$$

The hadronic decay width $\Gamma_{\rm had}$ of the W is summed over all six quark-antiquark modes. Since only V_{ud} and V_{cs} are of order one, the sum is dominated by these terms. In the approximation $V_{ud} \approx V_{cs} \approx 1$, neglecting the other terms, one obtains $\Gamma_{\rm had} = 6\,\Gamma^0_W$. Therefore, each leptonic channel has a branching ratio of 1/9, while the hadronic decay channel into two quarks has a branching ratio of 6/9. For the $t\bar{t}$ decay categories we get thus the probabilities as listed in Table 2.3. (i) Dilepton mode: 4/81, (ii) lepton-plus-jets: 24/81, (iii) all-hadronic channel: 36/81, (iv) tau modes: 17/81. These four different types of $t\bar{t}$ events can be isolated by their distinct event topologies.

Table 2.3: Categories of $t\bar{t}$ events and their branching fractions.

W decays	$e/\mu\nu$	$\tau\nu$	$q\bar{q}$
$e/\mu\nu$	4/81	4/81	24/81
$\tau\nu$	—	1/81	12/81
$q\bar{q}$	—	—	36/81

Dilepton Channel This final state includes (1) two high p_T leptons, electron or muon, (2) a large imbalance in the total transverse momentum (missing transverse energy, $\not\!\!E_{\rm T}$) due to two neutrinos, and (3) two b quark jets. The dilepton event category has low backgrounds,

especially in the $e\mu$ channel, since Z^0 mediated events do not contribute. However, the drawback of the dilepton channel is its low branching ratio of about 5%. There is a small contribution from tau events to the dilepton channel, if the tau decays into e or μ. This cross feed has to be taken into account when calculating acceptances for dilepton analyses. Since dilepton events contain two neutrinos which contribute to the $\not\!\!E_{\mathrm{T}}$, the top quarks cannot be fully reconstructed. This is a drawback if one wants to measure the top quark mass. However, this disadvantage is partially compensated by the precisely measured lepton momenta, in contrast to the only fair measurement of jet energies in the lepton-plus-jets channel.

Lepton-Plus-Jets Channel The lepton-plus-jets channel is characterised by (1) exactly one high-p_T electron or muon, which is also called the primary lepton, (2) missing transverse energy, (3) two b quark jets from the top decays, and (4) two additional jets from one W decay. An event display of a lepton-plus-jets candidate event measured at CDF II is shown in Fig. 2.6. The big advantage of the lepton-plus-jets channel is its high branching fraction of about 30%. The backgrounds are considerably higher than in the dilepton channel, but still manageable. Again, as in the dilepton channel, there is some cross feed from tau modes which has to be taken into account for acceptances. In lepton-plus-jets events the momentum of the leptonically decaying W boson can be reconstructed up to a twofold ambiguity. The transverse momentum of the neutrino is assumed to be given by $\not\!\!E_{\mathrm{T}}$. Two solutions for the z component of the neutrino are obtained from the requirement that the reconstructed invariant mass of the lepton and the neutrino be equal to the well known W mass: $M_{\ell\nu} = M_W$. To fully reconstruct the momenta of the top and antitop quark in the event, one has to assign the measured hadronic jets to the quarks. Without identification of b quark jets there are 24 possible combinations, including the ambiguity of the neutrino reconstruction. If one jet is identified as likely to originate from a b quark 12 combinations remain. If there are two identified b-jets the ambiguity is down to 4 options. This illustrates the importance of b quark jet identification for top quark physics. On top of this, requiring b-tagging increase significantly the signal over background ratio.

All Hadronic Channel The all hadronic channel has the largest branching ratio out of all $t\bar{t}$ event categories, about 44%. However, backgrounds are quite considerable. While there is the advantage that all final state partons are measured, one has to deal with numerous combinations when reconstructing the top quark momenta. Even if two jets are identified as b quark jets, 12 possible combinations remain. Another drawback is that jet energies as measured in the calorimeter have large uncertainties. The combination of these disadvantages leads to the conclusion that the all hadronic channel, even though a clear $t\bar{t}$ signal has been established here, proves to be very challenging to further investigate top quark properties.

Tau Modes Top quark events containing the decay $W \to \tau\nu_\tau$ are difficult to identify and analysis are underway.

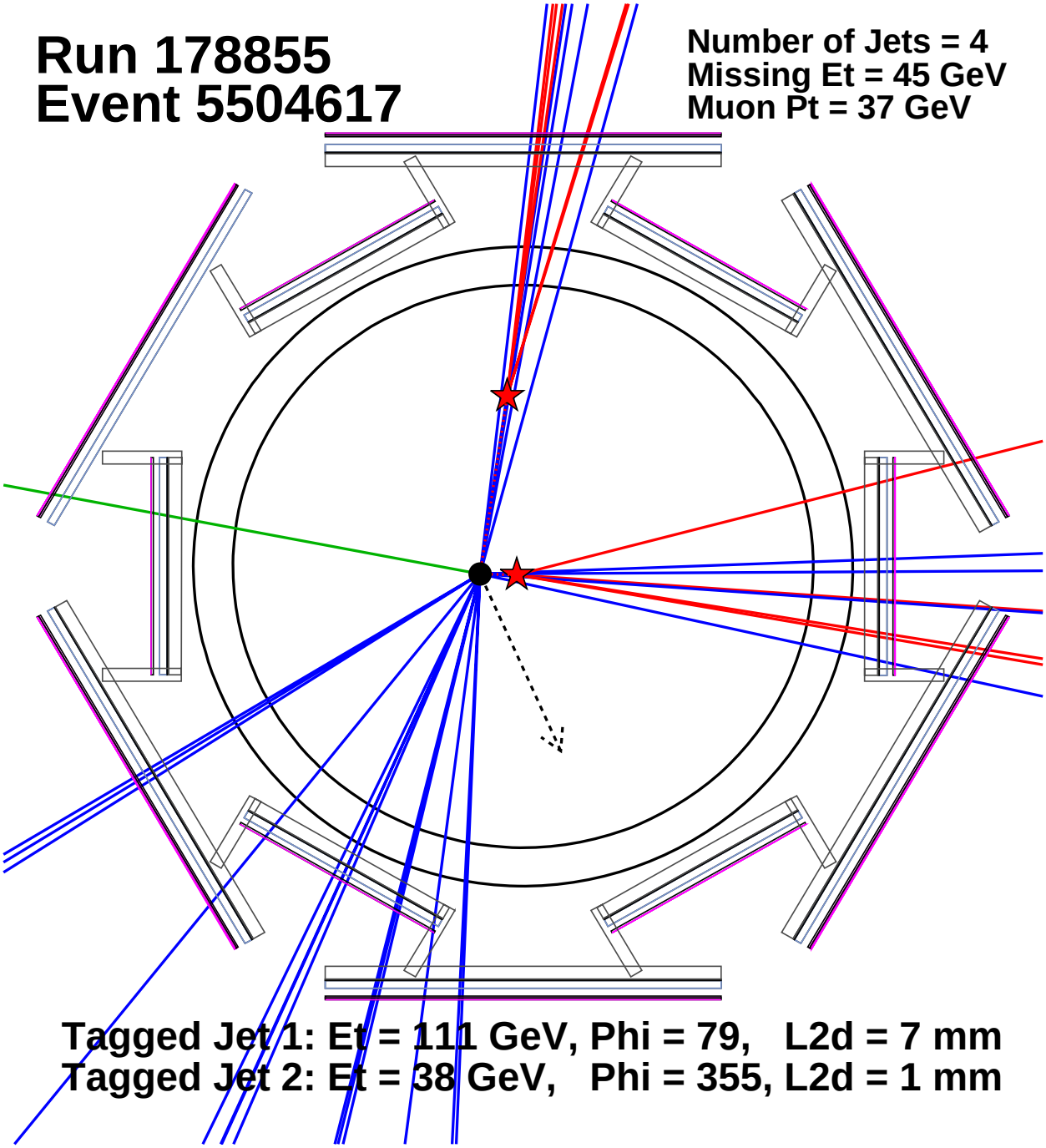

Figure 2.6: Event display of a CDF II muon-plus-jets event. The isolated line on the left hand side shows the muon trajectory. The arrow on the lower right indicates the direction of the $\not\!\!E_{\mathrm{T}}$. The event features four hadronic jets, two of which containing a displaced vertex consistent with a b-jet.

2.3.4 The Top Quark Beyond the Standard Model

Mainly because of its large mass the top quark has fostered speculations that it offers a unique window to search for physics beyond the SM. One possibility to test this hypothesis is to measure top quark properties and check whether the observations are in agreement with the SM predictions. This approach is based on the measurements involving top properties such as the $t\bar{t}$ cross section, the top mass, or the W helicity in top quark decays. A second approach is to search directly for new particles coupling to the top quark or for non-SM decays. In this Section we present those topics which have led to specific analyses at the Tevatron.

Decays to a Charged Higgs Boson

In the SM a single complex Higgs doublet scalar field is responsible for breaking the electroweak symmetry and generating the masses of gauge bosons and fermions. Many extensions of the SM include a Higgs sector with two Higgs doublets and are therefore called Two Higgs Doublet Models (THDM). In a THDM, electroweak symmetry breaking leads to five physical Higgs bosons: two neutral CP-even scalars h^0 and H^0, one neutral CP-odd pseudoscalar A^0, and a pair of charged scalars $H^{\pm}$. The extended Higgs sector is described by two parameters: the mass of the charged Higgs, M_{H^+}, and $\tan\beta = v_1/v_2$, the ratio of the vacuum expectation values v_1 and v_2 of the two Higgs doublets. One distinguishes two types of THDMs. In a type I THDM, only one of the Higgs doublets couples to fermions; in a type II THDM, the first Higgs doublet couples to the up-type quarks (u, c, t) and neutrinos, while the second doublet couples to down-type quarks (d, s, b) and charged leptons. The analyses we discuss in this Section are concerned with type II models. A particular example for a type II THDM is the minimal supersymmetric model (MSSM).

If the charged Higgs boson is lighter than the difference of top quark and b quark mass, $M_{H^{\pm}} < M_{\rm top} - M_b$, the decay mode $t \to H^+ b$ is possible and competes with the SM decay $t \to W^+ b$. The branching fraction depends on $\tan\beta$ and M_{H^+}. The MSSM predicts that the channel $t \to H^+ b$ dominates the top quark decay for $\tan\beta \leq 1$ and $\tan\beta \geq 70$. In most analyses it is assumed that $\mathrm{BF}(t \to W^+ b) + \mathrm{BF}(t \to H^+ b) = 1$. At tree level the $H^{\pm}$ does not couple to vector bosons. Therefore, the $H^{\pm}$ decays only to fermions. In the parameter region $\tan\beta < 1$ the dominant decay mode is $H^+ \to c\bar{s}$, while for $\tan\beta > 1$ the decay channel $H^+ \to \tau^+\nu_\tau$ is the most important one. For $\tan\beta > 5$ the branching fraction to $\tau^+\nu_\tau$ is nearly 100%. Thus, in this region of parameter space type II THDM models predict an excess of $t\bar{t}$ events with tau leptons over the SM expectation.

Search for $X^0 \to t\bar{t}$ Decays

Several extensions of the SM predict the existence of narrow resonances that decay to $t\bar{t}$ pairs. One such model is, for example, a Z' predicted by top-colour-assisted technicolour [47]. This model speculates that the spontaneous breaking of electroweak symmetry is related to the observed fermion masses, in particular the large top quark mass, and can be accomplished by dynamical effects [48].

FCNC Decays

In the SM, flavour changes at leading order (tree level) are induced by charged currents, the exchange of W bosons. Flavour changing neutral currents (FCNC) are only possible at higher orders in perturbation theory (loop level). FCNC decays of the top quark are strongly suppressed in the SM due to the Glashow-Iliopoulos-Maiani (GIM) mechanism [49]. Compared to the top quark mass, the masses of down-type quarks (d, s, b) occurring in loop diagrams are small and degenerate. Therefore, the sum over the respective amplitudes nearly cancels. Fig. 2.7 shows one of the Feynman diagrams that describe the decay $t \to cZ^0$. This type of diagram is also called penguin diagram. The SM predicts the branching fractions for $t \to cZ^0$ and $t \to c\gamma$ to be of the order of 10^{-12}, while $\mathrm{BF}(t \to cg) \simeq 10^{-10}$ and $\mathrm{BF}(t \to cH^0) \simeq 10^{-7}$ [50].

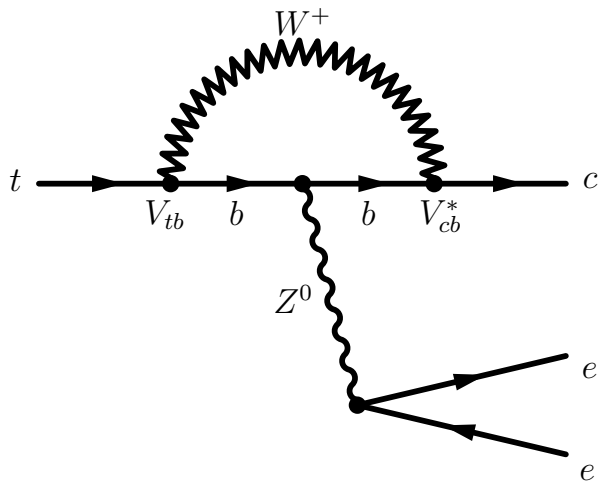

Figure 2.7: Feynman diagram for the FCNC decay $t \to cZ^0$ with $Z \to e^+e^-$. Other diagrams involve the d and the s quark within the loop instead of the b quark. All diagrams together nearly cancel and cause the branching ratio of this decay to be very small, $\mathcal{O}(10^{-12})$, in the SM.

In extensions of the SM, FCNC top quark decays can be considerably enhanced by several orders of magnitude if FCNC couplings at tree level are allowed [51–53]. In Two Higgs Doublet Models where the neutral scalar h^0 posses flavor changing couplings the decay $t \to ch^0$ can be considerably enhanced [54]. A similar enhancement can be reached in supersymmetric models were R-parity is violated [55]. In top colour-assisted technicolour theories the branching ratio for $t \to cW^+W^-$ can reach values up to 10^{-3} [56]. Since the SM predictions for FCNC interactions have much smaller rates, they are useful probes for new physics beyond the SM.

Anomalous Single Top Production

At the Tevatron the search for anomalously enhanced FCNC in top quark decays is statistically restricted by the number of $t\bar{t}$ pairs produced. More stringent limits on anomalous

$tq\gamma$ or tqZ couplings at tree level are set by searching for the production of single top quarks via FCNC at LEP and HERA.

At the Tevatron there are no searches for anomalous single top quark production yet. Possible FCNC processes at tree level could be $q_1\bar{q}_1 \to t\bar{q}_2$, $q_1\bar{q}_2 \to t\bar{q}_2$, $qg \to tg$, and $gg \to t\overline{q}$. Example Feynman diagrams for these processes are shown in Fig. 2.8. Another option for FCNC top quark production is the $2 \to 1$ quark-gluon fusion process $g + u/c \to t$.

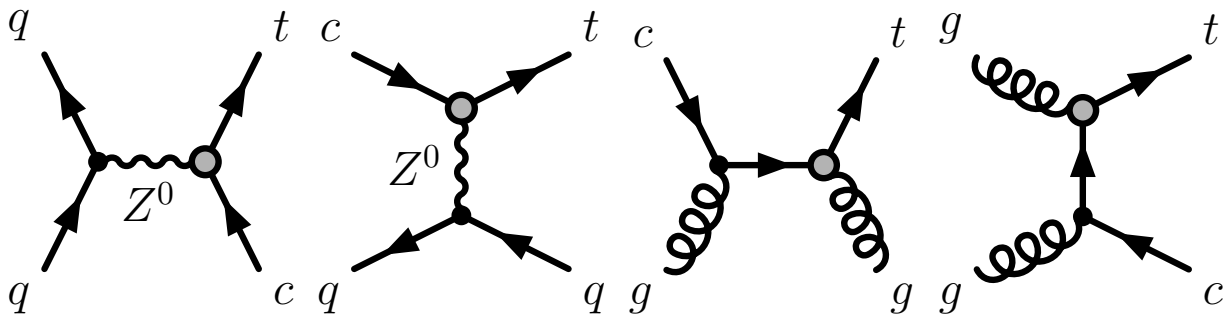

Figure 2.8: Feynman diagrams for single top production via $2 \to 2$ FCNC processes in hadron collisions.

2.4 Top Quark Discovery

Immediately after the discovery of the b quark in 1977 the existence of a weak isospin doublet partner, the top quark, was hypothesised. The mass of the sixth quark was unknown and a wealth of predictions appeared based on many different speculative ideas, see for example references [57–59]. Typical expectations were in the mass range of about 20 GeV/c^2, which became accessible two years later with measurements at the PETRA e^+e^- collider.

The CDF experiment at the Tevatron joined the race for discovery of the top quark in 1988. Due to the higher centre-of-mass energy at the Tevatron of $\sqrt{s} = 1.8$ TeV, top quarks are predominantly produced as $t\bar{t}$ pairs. The first CDF top quark search uses a data sample with an integrated luminosity of 4.4 pb^{-1} accumulated in Run 0 which lasted from 1988 to 1989 [60, 61].

In 1992, with the start of Tevatron Run I, the DØ experiment joined the hunt for the top quark. In April of 1994, DØ published its first top quark analysis setting the last lower limit on the top quark mass before its discovery [62]. The data sample was recorded in 1992/93 and corresponds to an integrated luminosity of 15 pb^{-1}.

In 1993 and 1994, CDF saw mounting evidence for a top quark signal. The detector upgrade for Run I, mainly the addition of a silicon vertex detector, was the keystone for the discovery of the top quark at CDF. The new silicon detector allowed for the reconstruction of secondary vertices of b hadrons and a measurement of the transverse decay length L_{xy} with a typical precision of 130 μm. Secondary vertex b tagging proved to be a very powerful tool to discriminate the top quark signal against the W+jets background and increase the sensitivity of the lepton-plus-jets $t\bar{t}$ analysis. In July 1994, CDF published a paper announcing first

evidence for $t\bar{t}$ production at the Tevatron based on events in the dilepton and the lepton-plus-jets channel [63, 64]. The analysis uses a data sample with an integrated luminosity of (19.3 ± 0.7) pb^{-1}. The resulting top mass distribution, shown in Fig. 2.9 (left), is fitted to a sum of the expected distributions from W+jets and $t\bar{t}$ production for different top quark masses. The fit yields a value of $M_{\rm top} = (174 \pm 10^{+13}_{-12})$ GeV/c^2. The corresponding log likelihood distribution is depicted in the inset in Fig. 2.9 (left).

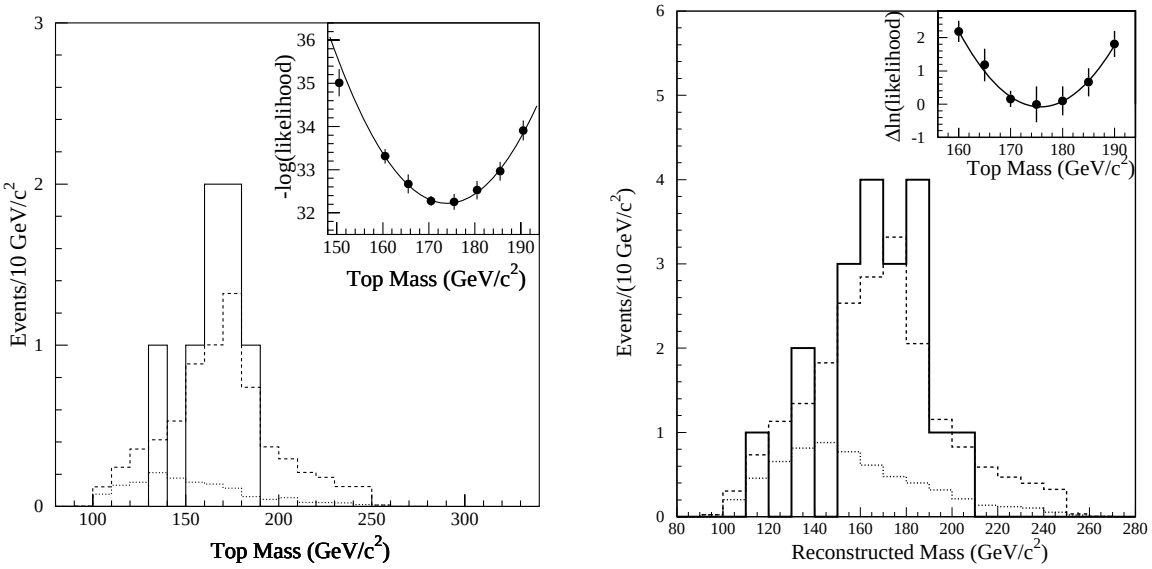

Figure 2.9: Reconstructed top mass distributions as published (left) in the CDF evidence paper of 1994 [63] and (right) in the CDF discovery paper [65]. The solid histogram shows CDF data. The dotted line shows the shape of the expected background, the dashed line the sum of background plus $t\bar{t}$ Monte Carlo events for $M_{\rm top} = 175$ GeV/c^2. In both plots, the inset shows the likelihood curve used to determine the top quark mass.

In November 1994 the DØ collaboration confirmed the evidence seen at CDF. An update of the previous DØ analysis, now with an integrated luminosity of (13.5 ± 1.6) pb^{-1}, added soft muon b tagging [66, 67]. In total, DØ observed nine events over a background of 3.8 ± 0.9.

As Run I continued more data were accumulated and finally, in April 1995, CDF and DØ were able to claim discovery of the top quark [65, 68]. CDF used a data sample corresponding to 67 pb^{-1} and significantly improved its secondary vertex b tagging techniques. The efficiency to identify at least one b quark jet in a $t\bar{t}$ event with more than three measured jets was found to be $(42 \pm 5)\%$, almost double the previous value of the 1994 analysis. In the new analysis the background estimate is also considerably improved. There are 27 jets with a secondary vertex b tag in 21 $W+ \geq 3$ jets events. The estimated background is 6.7 ± 2.1 b tags. The probability for this observation to be a background fluctuation is $2 \cdot 10^{-5}$.

The 1995 dilepton and soft lepton b tag lepton-plus-jets analyses are only slightly changed compared to those of 1994. Six dilepton events are observed over a background of 1.3 ± 0.3. There are 23 soft lepton tags observed in 22 events, with 15.4 ± 2.0 b tags expected from background sources. Six events contain both a jet with a secondary vertex and a soft lepton

tag. The probability for all CDF data events to be due to a background fluctuation alone is $1 \cdot 10^{-6}$, which is equivalent to a 4.8 σ deviation in a Gaussian distribution. Again the top quark mass is kinematically reconstructed for $W+ \geq 4$ jets events as described above. The mass distribution is shown in Fig. 2.9 (right). The best fit is obtained for $M_{\rm top} = (176 \pm 8 \pm 10)$ GeV/c^2.

Simultaneously to CDF, the DØ collaboration updated its top quark analyses based on data with an integrated luminosity of 50 pb^{-1} [68]. The updated analysis is very similar to the previous searches, involving the dilepton channel, soft muon b tagging and the topological analysis. From all channels, DØ observes 17 events with an expected background of 3.8 ± 0.6 events. The probability for this measurement to be an upward fluctuation of the background is $2 \cdot 10^{-6}$, which corresponds to 4.6 standard deviations for a Gaussian probability distribution. To measure the top quark mass, lepton+4 jets events are subjected to a constrained kinematic fit. A likelihood fit to the observed mass distribution yields a central value for the top quark mass of $M_{top} = 199^{+19}_{-21}$ (stat.) $\pm$ 22 (syst.) GeV/c^2.

In September 1995 CDF completed the series of publications establishing the top quark discovery with a complementary kinematic analysis without b tagging, that used the $E_{\rm T}$ of the second and third highest $E_{\rm T}$ jets to calculate a relative likelihood for each event to be top-quark-like or background-like [69, 70]. The probability for the observed data to be due to a background fluctuation was found to be 0.26%.

Finally, 17 years after the discovery of the b quark, its weak isospin partner, the top quark, was firmly established. In Fig. 2.10 we summarise the long lasting quest for the top quark. The figure shows the lower experimental limits on the top quark mass (histogram) [60,62,71–77], theoretical predictions mainly based on flavour symmetries within the quark mass matrix (dots) [59, 78–83] and predictions based on electroweak precision measurements at LEP and SLC (squares) [84–89]. The direct measurements by CDF [63, 65, 90, 91] and DØ [68, 92–94] are also included (triangles). The good agreement between the measured top quark mass and the prediction obtained from electroweak precision measurements constituted a major success of the Standard Model.

2.5 Motivation and Analysis Overview

2.5.1 Motivation

Within the SM the $t\bar{t}$ cross section is calculated with a precision of about 15% [27, 28]. The SM further predicts that the top quark decays to a W boson and a b quark with a branching ratio close to 100%. Measuring the cross section in all possible channels tests both production and decay mechanisms of the top quark. A significant deviation from the SM prediction would indicate either the presence of a new production mechanism, e.g. a heavy resonance decaying into $t\bar{t}$ pairs, or a novel decay mechanism, e.g. into supersymmetric particles. The $t\bar{t}$ cross section depends sensitively on the top quark mass. In the mass interval of $170 \leq M_{\rm top} \leq 190\,{\rm GeV}/c^2$ the cross section drops by roughly 0.2 pb for an increase of 1 GeV/c^2 in $M_{\rm top}$. This theoretically predicted dependence can be exploited to turn a cross section measurement into an indirect determination of the top quark mass. A 15%

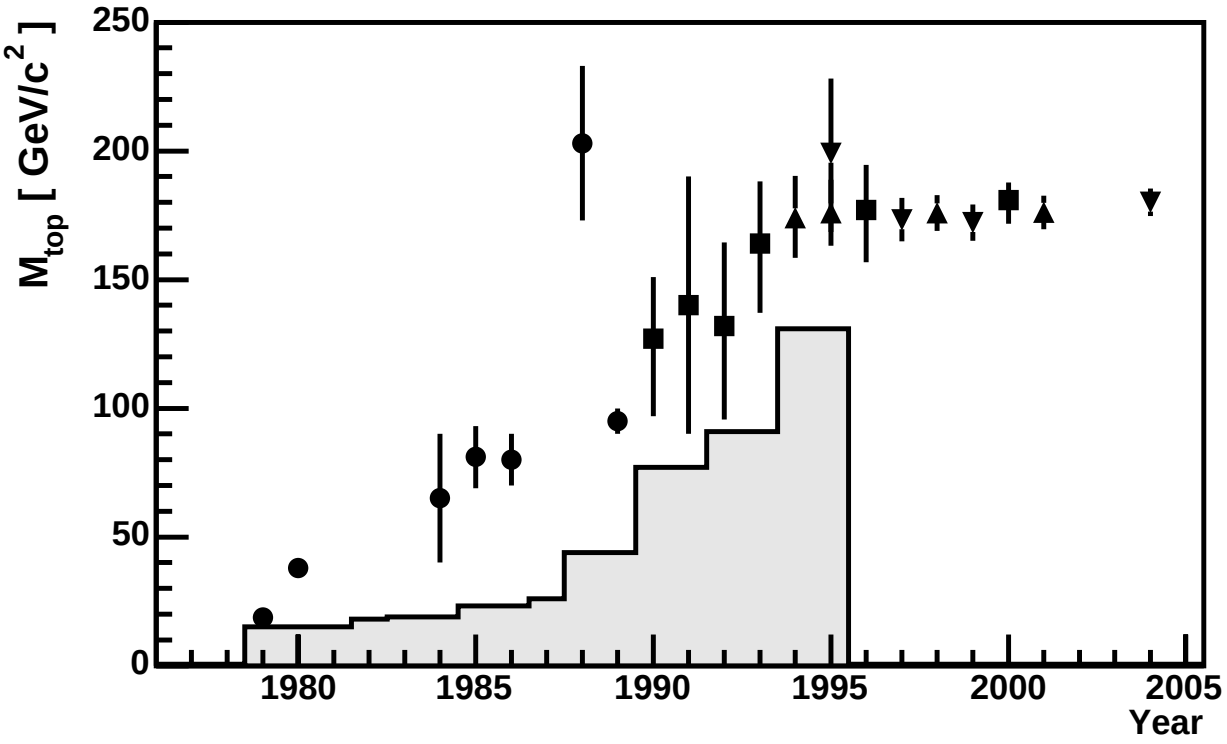

Figure 2.10: History of the quest for the top quark. The shaded histogram shows experimental lower limits on the top quark mass. Theoretical predictions based on flavour symmetries are shown (dots) as well as predictions based on electroweak precision measurements (squares). Direct measurements of M_{top} by CDF and DØ are represented by the triangle (triangles pointing up: CDF; triangles pointing down: DØ).

measurement of the cross section is approximately equivalent to a 3% measurement of M_{top}. One can also turn the argument around and use the measurements of the cross section and the top quark mass and test their compatibility with the theoretically predicted cross section and its mass dependence.

The $t\bar{t}$ cross section measurements are very fundamental to top quark physics at the Tevatron, since these analyses isolate data samples that are enriched in $t\bar{t}$ events and lay thereby the foundations for further investigations of top quark properties.

2.5.2 Method

This analysis measures the $t\bar{t}$ production cross section in the lepton-plus-jets channel assuming an SM top quark (in particular, SM branching ratios) with a mass of 178 GeV/c^2 [10]. Because this measurement is sensitive to the top mass itself, the result will be given as a function of the top mass. In this Section the basic steps of the analysis are presented. More detailed explanations are given in the rest of the dissertation.

The signature of the $t\bar{t}$ lepton-plus-jets channel comprises a high-p_{T} electron or muon, missing transverse energy and four jets, see Section 2.3.3. The branching fraction of this

channel is about 30% which is one of the advantages over the dilepton channel. However, W + multijet backgrounds are large and call for dedicated strategies to improve the signal to background ratio. In this Section we discuss four important methods to reduce backgrounds in the lepton-plus-jets channel and obtain a measurement of the $t\bar{t}$ cross section.

While each $t\bar{t}$ event features two b quark jets, only about 2% of the W + jets background contain a b quark. Therefore, the $t\bar{t}$ signal can be significantly enhanced by identifying b quark jets. Three different b jet identification methods are used in CDF. In the analysis presented in this thesis, the Jet Probability tagging method has been used. This method relies on the long lifetime of b hadrons, but the explicit reconstruction of a secondary vertex is not required. The algorithm rather asks for tracks with high impact parameter significance. In the analysis presented here a jet is b tagged if its probability to be consistent with a zero lifetime hypothesis is below 0.01 or 0.05. The Jet Probability tagging algorithm is described in more detail in Chapter 5.

The analysis uses a data sample triggered by high momentum electrons or muons corresponding to an integrated luminosity of 318 pb^{-1}. The electron selection requires an isolated cluster in the central calorimeter with $E_{\mathrm{T}} > 20\,\mathrm{GeV}$ matched to a track with $p_{\mathrm{T}} > 10\,\mathrm{GeV}/c$. Muon candidates have a track in the drift chamber with $p_{\mathrm{T}} > 20\,\mathrm{GeV}/c$ that is matched to a track segment in the muon chambers. Events consistent with being photon conversions (electrons) or cosmic rays (muons) are rejected. The missing transverse energy is required to be $\not\!\!E_{\mathrm{T}} > 20\,\mathrm{GeV}$. By requiring one and only one well identified lepton, $t\bar{t}$ dilepton events and $Z \to e^+e^-/\mu^+\mu^-$ events are suppressed. To improve the removal efficiency for Z bosons, events are also removed if a second, less stringently identified lepton is found that forms an invariant mass $M_{\ell\ell}$ with the primary lepton within the window of $76 < M_{\ell\ell} < 106\,\mathrm{GeV}/c^2$. Jets are defined as clusters in the calorimeter with $E_{\mathrm{T}} > 15\,\mathrm{GeV}$ and $|\eta| < 2.0$ and large hadronic energy fraction. At least three jets are required for an event to fall into the signal region. One of these jets has to be identified as containing a b quark using the Jet Probability tag algorithm. The final cut is on the total transverse energy and demands $H_{\mathrm{T}} > 200\,\mathrm{GeV}$. A more detailed description of the event selection is given in Chapter 6.

The backgrounds to the Jet Probability tagged sample are (i) W plus heavy flavour jets, (ii) W plus light quark jets events where one jet is falsely identified as heavy flavour (mistags), (iii) direct QCD production of heavy flavour quarks without an associated W boson (non-W QCD), (iv) diboson production, single top quark, and $Z \to \tau^+\tau^-$ production.

The estimate of these backgrounds is partially derived from CDF data and partially from Monte Carlo simulation. In particular, the number of b tagged W + jets background events is calibrated with the number of observed W + jets events before b tagging. Therefore, the first step in the background calculation is to estimate the number of background events that do not contain a W boson in the pretag sample and subtract that background from the observed number of events.

(i) W + heavy flavour: The production of a W boson in association with heavy flavour quarks is the main background to the $t\bar{t}$ signal with a Jet Probability tag. Heavy quarks occur in the process $q_1\bar{q}_2 \to W + g$ where the gluon splits into a $b\bar{b}$ or a $c\bar{c}$ pair, and in the process $gq \to Wc$. As mentioned in Section 4.6, the ALPGEN Monte Carlo program [95] is used to generate several samples of exclusive $W + n$ jets final states. This includes $W + b\bar{b}/c\bar{c} + n$

jets, and Wc + jets.

The number of W+ heavy flavour background events for the $t\bar{t}$ analysis is computed by multiplying the derived heavy quark fractions by the number of pretag events, after subtracting the non-W background.

(ii) Mistags: The mistag rate of the secondary vertex algorithm is measured using inclusive jet samples. Mistags are caused mostly by a random combination of tracks which are displaced from the primary vertex due to finite tracking resolution. The main idea is to use the rate of events with negative two-dimensional decay length as an estimate of the mistag rate. Corrections due to material interactions, long-lived light flavour particles (e.g. K_s^0 and Λ), and negatively tagged heavy flavour jets are determined using fits to the effective lifetime spectra of tagged vertices. The mistag rate is parameterized as a function of four jet variables: E_{T}, the number of Jet Probability good tracks in the jet N_{trk}, η and ϕ of the jet as well as two event variables, i.e. the scalar sum of the E_{T} of all jets with $E_{\mathrm{T}} > 8\,\mathrm{GeV}$ and the z vertex position, Z_{vtx}, of the event. To estimate the mistag background in the W + jets sample each jet in the pretag sample is weighted with its mistag rate. The sum of weights over all jets in the sample is then scaled down by the fraction of non-W events in the pretag sample. Since the mistag rate per jet is sufficiently low, this prediction of mistagged jets is a good estimate on the number of events with a mistagged jet.

(iii) Non-W QCD background: The non-W background is mainly due to events where a jet is misidentified as an electron and the $\not\!\!E_{\mathrm{T}}$ is mismeasured, or due to muons from semileptonic b decays which pass the isolation criterion. Since the background sources in the electron and muon sample are different, one has to treat these two samples separately. The non-W background estimate uses the $\not\!\!E_{\mathrm{T}}$ variable and the isolation variable R_{iso}, that is defined as the ratio of calorimeter energy E_{iso} contained in an isolation annulus of $\Delta R = 0.4$ around the lepton (excluding the energy associated to the lepton) divided by the lepton energy E_ℓ. The R_{iso} versus $\not\!\!E_{\mathrm{T}}$ plane is divided into a signal region ($R_{\mathrm{iso}} < 0.1$ and $\not\!\!E_{\mathrm{T}} > 20\,\mathrm{GeV}$) and three sideband regions. One assumes that the two variables are uncorrelated for non-W background events and calculates the number of background events in the signal region as a simple proportion of events in the sideband regions. The contribution of true W and $t\bar{t}$ events in the sideband regions is subtracted using Monte Carlo predictions normalized to the observed number of events in the signal region.

(iv) Diboson, single top and $Z \to \tau^+\tau^-$: There is a number of smaller backgrounds which can be reliably predicted by combining the event detection efficiency for these processes as determined from Monte Carlo events with the theoretically predicted cross section. This method is feasible, since the cross section predictions for diboson production processes, i.e. WW, WZ and ZZ, and single top quark production have relatively small uncertainties. Diboson events can mimic a $t\bar{t}$ signal if one boson decays leptonically and the other one decays into jets, where at least one jet is due to a b or c quark. In addition, Z+jet production can mimic $t\bar{t}$ events if the Z boson decays into $\tau^+\tau^-$ and one τ decays leptonically producing an isolated electron or muon, while the second τ decays hadronically.

The $t\bar{t}$ cross section is calculated according to the formula

$$\sigma(t\bar{t}\,) = \frac{N_{\mathrm{obs}} - N_{\mathrm{bkg}}}{\epsilon_{\mathrm{evt}} \cdot \mathcal{L}_{\mathrm{int}}}\ , \tag{2.13}$$

where N_{obs} is the number of observed events, N_{bkg} is the number of expected background events, and ϵ_{evt} is the event detection efficiency which includes the kinematic acceptance, lepton id, b-tagging, trigger and reconstruction efficiencies, and the branching ratio into lepton+jets events. Therefore, to compute the $t\bar{t}$ cross section according to Eq. 2.13, the event detection efficiency ϵ_{evt} for $t\bar{t}$ events is needed. It is obtained from a sample of `PYTHIA` $t\bar{t}$ Monte Carlo events. More details are given in Chapter 8. The trigger efficiency as well as several correction factors that account for differences between data and Monte Carlo events are measured with control data samples. Particularly important is the correction factor for the b tagging efficiency. A sample of inclusive electrons with $p_{\mathrm{T}} > 8\,\mathrm{GeV}$ is used for this purpose. Many electrons in this momentum regime originate from semileptonic b decays. Therefore, the sample is enriched in heavy flavour.

Chapter 3

Experimental Apparatus

The analysis presented in this thesis uses data collected between February 2002 and September 2004 from proton-antiproton collisions produced by the Tevatron at a center-of-mass energy of 1.96 TeV and observed by the Collider Detector at Fermilab (CDF). This chapter describes the collider apparatus and the detector.

Between 1997 and 2001, both the accelerator complex and the collider detectors underwent major upgrades, mainly aimed at increasing the luminosity of the accelerator, and gathering data samples of 2 fb^{-1} or more. The upgraded machine accelerates 36 bunches of protons and antiprotons, whereas the previous version of the accelerator operated with only 6. Consequently, the time between bunch crossings has been decreased from 3.5 μs for the previous version to 396 ns for the current collider. The center of mass energy was also increased from 1.8 to 1.96 TeV.

The new configuration required detector upgrades at CDF II to ensure a maximum response time shorter than the time between beam crossings.

In the subsequent sections, we describe how the proton and antiproton beams are produced, accelerated to their final center of mass energy of 1.96 TeV, and collided. We then describe the components used to identify and measure properties of the particles produced in the collision.

3.1 The Tevatron Collider and the Fermilab Accelerator Complex

The Fermilab's Tevatron Collider represents the high energy frontier in particle physics. It is a proton-antiproton storage ring system located at Fermilab (Fermi National Laboratory) in Batavia, Illinois (USA). With a center-of-mass energy of $\sqrt{s} = 1.96$ TeV it is currently the source of the highest energy proton-antiproton ($p\bar{p}$) collisions and the only apparatus capable of producing top quarks. The collisions occur at two points on an underground ring, which has a radius of about 1 km. At these collision points there are two detectors: the Collider Detector at Fermilab (CDF II) and DØ. The 2 km diameter storage ring is the last step of a complex chain of accelerators that produce and accelerate the proton and antiproton

beams (see Fig. 3.1).

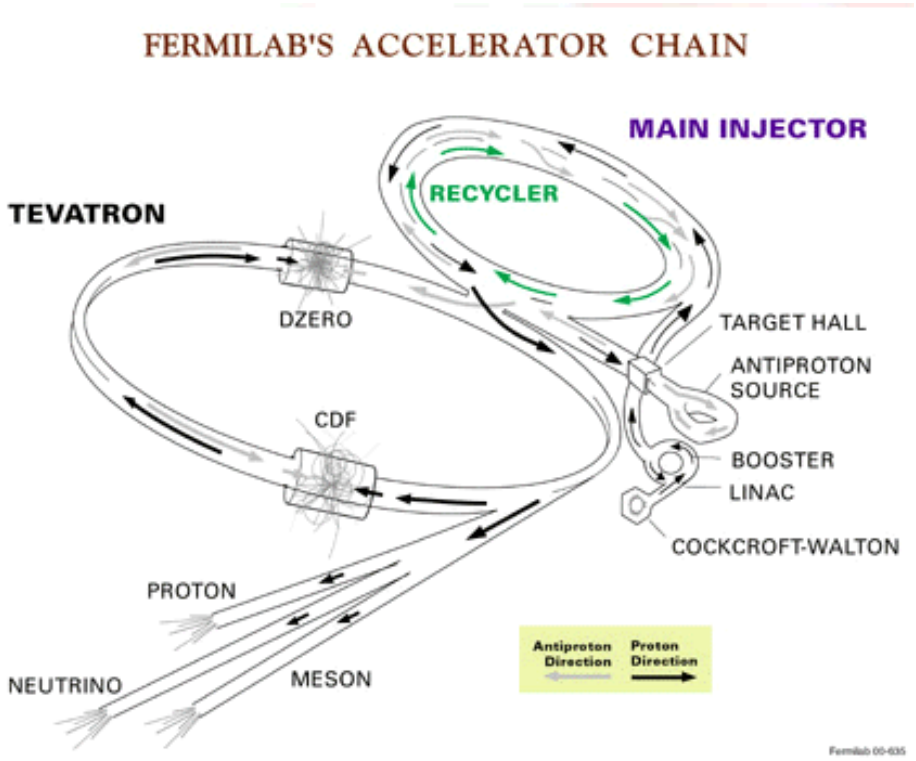

Figure 3.1: Layout of the Fermilab accelerator complex.

Production and acceleration of protons and antiprotons at Fermilab require a chain of accelerators, each one boosting particles to higher energies. Each step will be described in the following pages.

3.1.1 Proton Production and Boosting

The Cockcroft-Walton [96] pre-accelerator provides the first stage of acceleration. Inside this device, hydrogen gas is ionized to create H^- ions, which are accelerated to 750 keV of kinetic energy. The pre-accelerator produces 750 keV hydrogen ions every 66 ms.

Next, the H^- ions enter a linear accelerator (Linac) [97], approximately 150 m long, where they are accelerated to 400 MeV. This acceleration is also done every 66 ms (with an offset to catch the ions from the preacc). The Linac itself was upgraded in 1993, increasing its energy from 200 to 400 MeV; this made it possible, during Run IIb, to double the number of protons per bunch and to increase by about 50% the production rate of antiprotons. The acceleration in the Linac is done by a series of "kicks" from Radio Frequency (RF) cavities. The oscillating electric field of the RF cavities groups the ions into bunches.

The 400 MeV H^- ions are then injected into the Booster [97], a circular synchrotron (circular accelerator) 74.5 m in diameter. A carbon foil strips the electrons from the H^- ions

at injection, leaving bare protons. The intensity of the proton beam is increased by injecting new protons into the same orbit as the circulating ones. The protons are accelerated from 400 MeV to 8 GeV by a series of "kicks" applied by RF cavities. Each turn around the Booster, the protons accumulate about 500 keV of kinetic energy. The Booster is the first synchroton in the Tevatron complex. It is composed of a series of 75 magnets arranged around a 74.5 m radius circle, with 18 RF cavities inside. This stage of production is also operated at 66 ms, with sufficient phase offset to catch the ions from the Linac.

Together, Linac and Booster are able to provide pulses of $5 \cdot 10^{12}$ protons for antiproton production every 1.5 s, or $6 \cdot 10^{10}$ protons per bunch in series of 5 to 7 bunches, repeated 36 times every 4 s.

At this point, protons are transfered to the Main Injector, a newly built circular accelerator that replaced the older Main Ring.

3.1.2 Main Injector

The Main Ring was originally built to provide 400 GeV protons to Fermilab's fixed target experiment; later on, it was converted to act as an injector to the Tevatron. The new operational requirements for the Main Ring did not match its original design. Therefore, during Run I, the Main Ring was a performance bottleneck, and the situation would be even worse in Run II.

The Main Injector was designed to solve this problem while providing further benefits, being capable of containing larger proton currents than its predecessor, which results in a higher rate of antiproton production. It is a 3 km long? circular accelerator. It is composed of 18 accelerating RF cavities and can accelerate protons from a kinetic energy of 8 GeV to a total energy of up to 150 GeV every 2.2 s. The Main Injector can be used in other different operation modes:

- Antiproton production: it produces 120 GeV protons which are then used to strike the antiproton source and create antiprotons. This process is called "stacking pbars"
- Proton and antiproton boosting, before injection into the Tevatron in collider mode
- Antiproton deceleration, in order to recover antiprotons after a Tevatron collision run
- Proton and antiproton acceleration for fixed target experiment, either directly or as a booster for the Tevatron

3.1.3 Antiproton Production

In order to produce antiprotons, a pulse of $5 \cdot 10^{12}$ protons at 120 GeV is extracted from the Main Injector and focused into a nickel target. In the collisions, about 20 antiprotons are produced for each million protons, with a mean kinetic energy of 8 GeV. The antiprotons produced by the collision are collected by a lithium lens and separated from other particle species by a pulsed magnet.

Before the antiprotons can be used in the narrow beams needed in the collider, the differences in kinetic energy between the different particles need to be reduced. Since this process reduces the spread of the kinetic energy spectrum of the beam, it is referred to as "cooling" the beam. New batches of antiprotons are initially cooled in the Debuncher Ring (rounded triangular synchrotron with a mean radius of 90 m), collected and further cooled using stochastic cooling [98] in the 8 GeV Accumulator (also a rounded triangular synchrotron). The principle of stochastic cooling is to sample a particles motion with a pickup sensor and correct its trajectory later with a kicker magnet. In reality, the pickup sensor samples the average motion of particles in the beam and corrects for the average. Integrated over a long period of time, this manifests itself as a damping force applied onto individual particles which evens out their kinetic energies. It takes between 10 and 20 hours to build up a "stack" of antiprotons which is then used in collisions in the Tevatron. Antiproton availability is the most limiting factor for attaining high luminosities, assuming there are no technical problems with the accelerator (assuming, for example, perfect transfer efficiencies between accelerator subsystems) [97, 99].

Roughly once a day, the stacked antiprotons (36 bunches of about 3×10^{10} antiprotons per bunch) are injected back into the Main Injector. They are accelerated to 150 GeV together with 36 bunches of roughly 3×10^{11} protons. Both the protons and antiprotons are transferred to the Tevatron.

3.1.4 Recycler Ring

Not all antiprotons in a given store are used up by the collisions. Recycling the unused antiprotons and reusing them in the next store significantly reduces the stacking time. The task of the Recycler is to receive antiprotons from a Tevatron store, cool them and re-integrate them into the stack, so that they can be used in the next store.

Antiproton production is one of the limiting factors in the efficiency in the Tevatron; by recycling 2/3 of these antiprotons, the average luminosity can be increased by a factor of two.

The Recycler Ring lies in the same enclosure as the Main Injector and, contrarily to the other rings at Fermilab, it is built with permanent magnets. During Run I the antiproton accumulation ring was found to suffer some kind of failure approximately once a week; this led to the loss of the entire store. Permanent magnets, not being prone to the most common causes of failure (such as power loss and lightning) provide a very stable repository for up to $3 \cdot 10^{12}$ antiprotons at a time.

In principle, the Recycler Ring can accept antiprotons from the Tevatron after a store is ended, however this functionality has not been proved possible. The Recycler also maintains the antiprotons momenta at 8 GeV. It can transfer these antiprotons back into the Tevatron for shots. Right now, while the Recycler is not capable of accepting recycled protons from the Tevatron, it is being used to pull antiprotons off the Accumulator, "stacking" the ones which can then be injected into the Tevatron.

3.1.5 Tevatron

The Tevatron is the last stage of Fermilab's accelerator chain. It is a circular synchroton with a 1 km radius. It is composed of eight accelerating cavities, quadrupole and dipole focusing magnets. The Tevatron is also cryogenically cooled to 4 K, and the accelerating cavities are made of superconducting materials. It is desirable to use superconducting magnets because the very large fields necessary to maintain TeV-scale energies would require currents so large that it is more cost effective to use superconducting magnets than ordinary resistive magnets.

The Tevatron is not a perfect circle. There are six sectors (A-F) and each one has five service buildings (0-4). The "0" sections have large straight sections. A0 is where the Tevatron tunnel connects to the injection point. It also contains one of two beam aborts. B0 contains CDF (which will be described below), and the D0 detector is aptly named for it's place along the ring. At B0 and D0, the colliding beams are focused into very narrow beamlines of order 32 μm, and the beams then collide. C0 is the location of the other beam abort (protons only). E0 used to be the site of the old Main Ring transfer to the Tevatron, but now it is unused. F0 houses the RF stations which "kick" the beam back into position if it has wandered off its axis. It is also where the transfer lines from the Main Injector connect with the Tevatron. It also houses the transfer line to the antiproton source.

The Tevatron receives 150 GeV protons and antiprotons from the Main Injector or the Recycler (for antiprotons) and accelerates them to 980 GeV in 85 s. Since the antiprotons and protons are oppositely charged, they circle in opposite directions in the magnetic field, and are housed in the same ring. The beams are brought to collision at two "collision points", B0 and D0. The two collider detectors, the Collider Detector at Fermilab (CDF II) and DØ, are built around the respective collision points. The Tevatron can then sustain both beams for hours at a time (called a "store").

The Tevatron can also be used in fixed-target mode: it can accelerate up to $3 \cdot 10^{13}$ protons at a time to an energy of 800 GeV and deliver single bunches to be used in proton, meson and neutrino experiments.

3.1.6 Luminosity

The number of collisions per second is described by the "luminosity", $\mathcal{L}$. Making use of the upgrades in the rest of the accelerator chain, the Tevatron can provide an initial luminosity of 10^{32} cm^{-2}s^{-1}. During a collider store, instant luminosity slowly decreases. In the early stage of the store, the most important cause for this decrease is intrabeam scattering; some hours later, the depletion of antiprotons during collisions becomes more relevant. Luminosity is expected to decrease to 50% in about seven hours, and to $1/e$ in twelve hours. After a tipical store duration of eight hours, 75% of the antiprotons are still available; they are decelerated in the Tevatron and in the Main Injector, and then stored in the Recycler Ring.

The luminosity of collisions can be expressed as:

$$\mathcal{L} = \frac{f N_B N_p N_{\bar{p}}}{2\pi(\sigma_p^2 + \sigma_{\bar{p}}^2)} F\left(\frac{\sigma_l}{\beta^*}\right), \tag{3.1}$$

where f is the revolution frequency in Hz, N_B is the number of bunches, $N_{p(\bar{p})}$ is the number of protons (antiprotons) per bunch, and $\sigma_{p(\bar{p})}$ is the protons (antiprotons) RMS beam size at the interaction point. This is multiplied by a form factor, F, that depends on the ratio of the bunch longitudinal RMS size, σ_l, and the beta function at the interaction point, β^*, which is a measure of the transverse beam width and it is proportional to the beam's x and y extent in phase space. Table 3.1 shows a comparison of Run I and design Run II [99] accelerator parameters. Figure Fig. 3.2 shows the total luminosity collected by CDF as of December 2006.

Table 3.1: Accelerator parameters for Run I and Run II configurations.

Parameter	Run Ib	Run II
Number of bunches (N_B)	6	36
Protons/bunch (N_p)	2.3×10^{11}	2.7×10^{11}
Antiprotons/bunch ($N_{\bar{p}}$)	5.5×10^{10}	3.0×10^{10}
Total antiprotons	3.3×10^{11}	1.1×10^{12}
β^* [cm]	35	35
Bunch length [m]	0.6	0.37
Bunch spacing [ns]	3500	396
Interactions/crossing	2.5	2.3
Energy [GeV/particle]	900	980
Integrated luminosity [pb^{-1}]	112	1800
Peak luminosity [cm^{-2}s^{-1}]	2×10^{31}	$\sim 2 \times 10^{32}$

However, the luminosity is not determined from this formula, but from the measured rate of some reference physical processes. The measurement of the luminosity delivered by the Tevatron to the CDF experiment is described in Sec. 3.9.

3.1.7 Beam Monitors

Operation of colliders at the Tevatron requires a constant monitoring of the beam position and luminosity. From a conceptual point of view, this is done in Run II as it was done in Run I.

The luminosity monitor consists of two arrays of scintillators, placed on both sides of the interaction region. A coincidence of particles moving away from the interaction point, both in the p and $\bar{p}$ direction, is interpreted as a contribution to luminosity. Bunches of particles moving in a single direction, without a coincident bunch in the opposite direction, are flagged as beam losses.

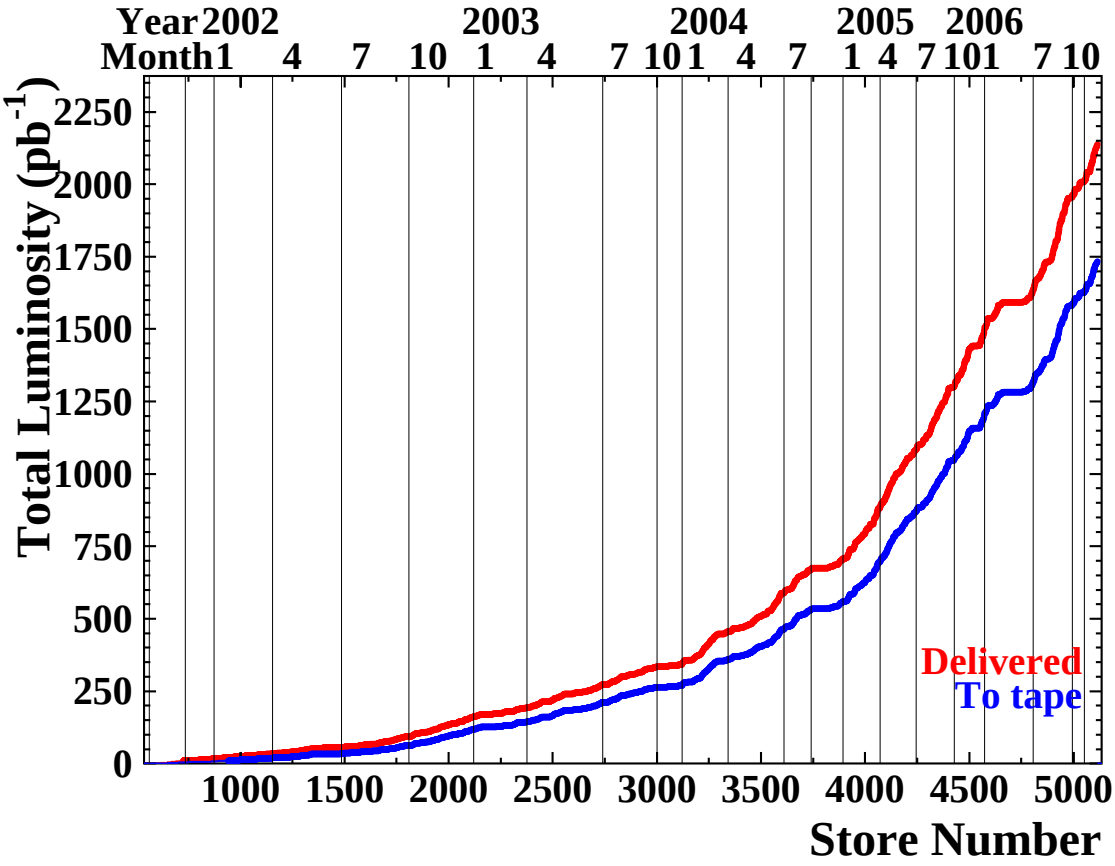

Figure 3.2: Total luminosity gathered by the CDF detector as of December 2006. The red curve is luminosity delivered and the blue curve is luminosity written to tape by CDF.

The beam position, on the other hand, is measured by the collider detectors themselves. During Run I, the detector was able to locate the beam within 5 μm in about five minutes; other beam parameters, such as slope and transverse profile, were calculated over longer time intervals (about two hours). In Run II, the same operations are performed but more quickly.

3.2 The CDF II Detector

The CDF II Detector [100, 101] is a substantial upgrade of the original CDF Detector [102]. It is located at the B0 collision point of the Tevatron Collider. The detector is designed to detect and measure properties of particles emanating from $p\bar{p}$ collisions. The design is not geared toward one particular physics measurement, but rather optimized toward extracting a number of different properties about all particle species created in the $p\bar{p}$ collision. Such particle detectors are often called multi-purpose detectors.

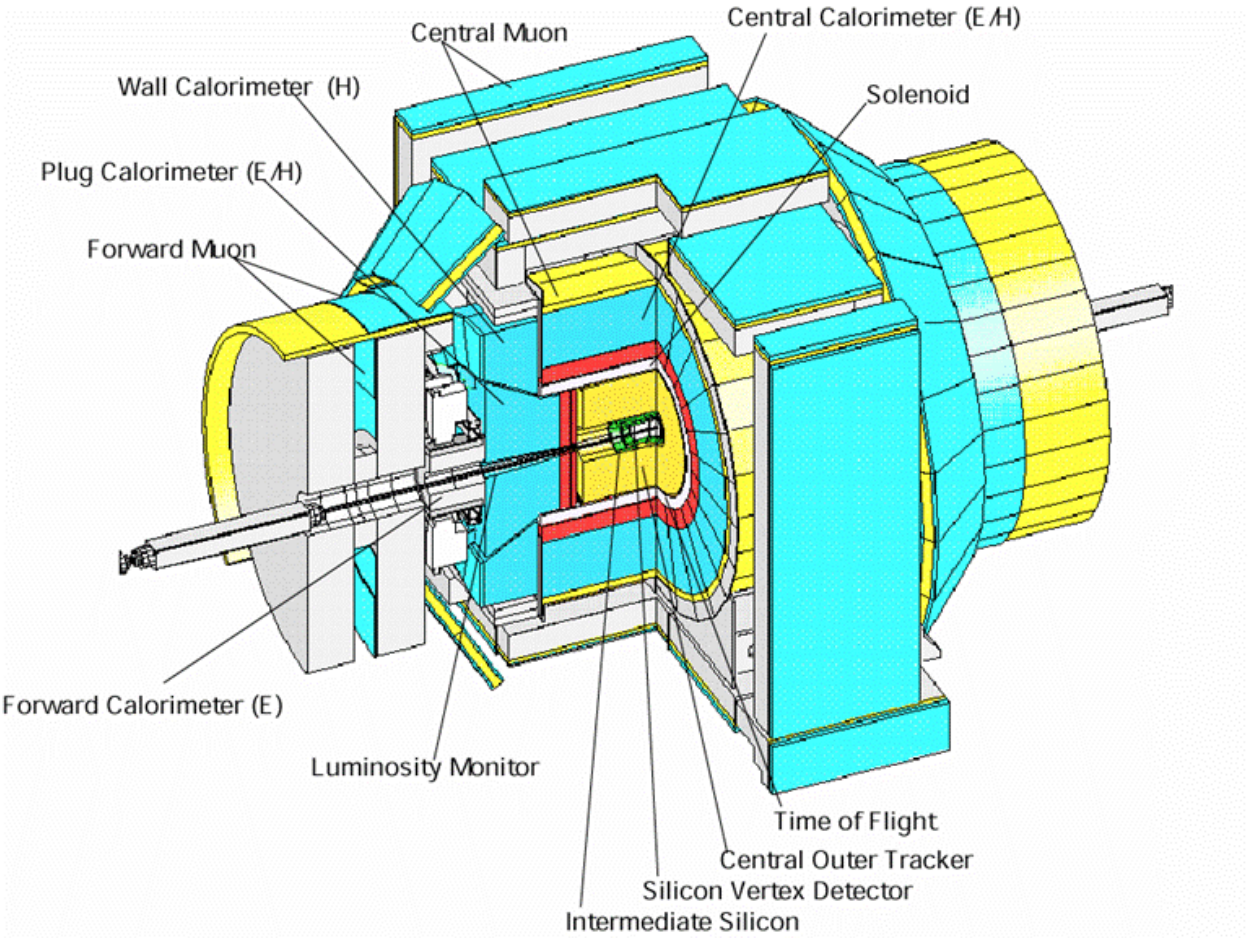

Figure 3.3: The CDF II Detector with quadrant cut to expose the different subdetectors.

A diagram of the CDF II Detector is shown in Fig. 3.3. A quadrant of the detector is cut out to expose the different subdetectors. The detector consists of 3 primary subsiystems: the tracking, the calorimetry and the muon systems. All these systems surround the "beam pipe", a vacuum tube of diameter 2.2 cm located at the innermost part of the detector and where the proton and antiproton beams travel and collide. The beam pipe is made of beryllium because this metal has the best mechanical qualities, yet lowest nuclear interaction cross section of all materials.

The detector subsystems can be grouped as follows. The innermost system is the integrated tracking system. The tracking system is barrel-shaped and consists of cylindrical subsystems which are concentric with the beam. It is designed to detect charged particles, measure their momenta and displacements from the point of collision (primary interaction vertex). The tracking system is surrounded by the Time of Flight system, designed to provide particle identification for low-momentum charged particles. Both the tracking and Time of Flight systems are placed inside a superconducting coil, which generates a 1.4 T solenoidal

magnetic field. The coil is surrounded by calorimetry systems, which measure the energy of particles that shower when interacting with matter. The calorimetry systems are surrounded by muon detector systems. When interacting with matter, muons act as "minimally ionizing particles" - they only deposit small amounts of ionization energy in the material. Therefore, they are able to penetrate both the tracking and calorimeter systems. The integrated material of the tracking system, TOF, solenoid and calorimetry systems serves as a particle filter. Particles which penetrate through all that material are mostly muons, and they are detected by leaving tracks in the muon detection system, located outside of the calorimeter. The Cherenkov Luminosity Counter (CLC) measures the rate of interactions near the beam used for luminosity measurements.

The rest of this chapter will provide a short description of each detector subsystem, with an emphasis on the upgrades since Run I. More detailed information on each system can be found in the Technical Design Report of the CDF II Detector [100].

3.3 Standard Definitions in CDF

Figure 3.4 shows an elevation view of the detector. Protons enter the detector from the west side and antiprotons enter from the east side.

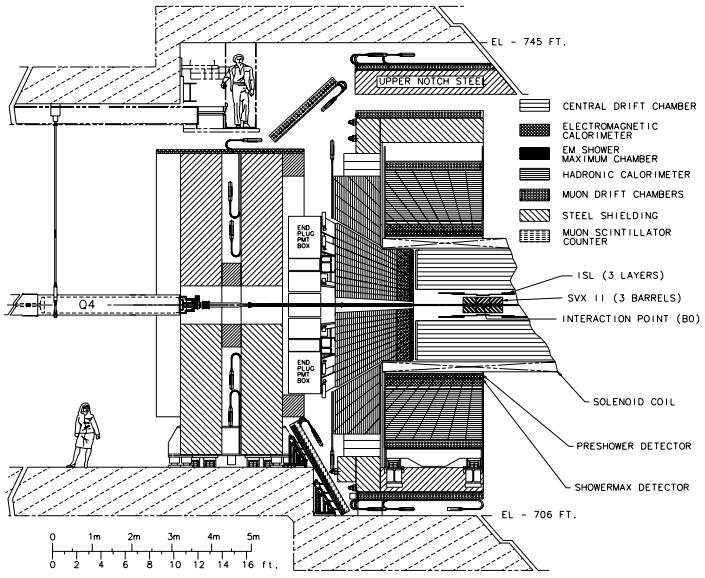

Figure 3.4: Elevation view of the Collider Detector at Fermilab (CDF). West (East) corresponds to the right (lef) side of the picture.

Because of its barrel-like detector shape, the CDF II Detector uses a cylindrical coordinate system (r, ϕ, z) with the origin at the center of the detector and the z-axis along the nominal direction of the proton beam (toward east). The y-axis points upwards. Since the coordinate

system is right-handed, this also defines the direction of the x-axis; it is horizontal pointing north (outward with respect to the center of the Tevatron).

Spherical coordinates are also commonly used: the polar angle θ is defined with respect to the proton beam and the azimuthal angle ϕ is defined with respect to the x-axis. However, θ is not a good variable to use in this case because it is not a Lorentz invariant. Due to the fact that the proton (and antiproton) is an extended object, the actual constituent partons will not be travelling at 980 GeV. Thus, the number of particles per unit angle ($dN/d\theta$) will not be the same for particles with different velocity.

Instead, we use the concept of the *rapidity*, defined as

$$Y \equiv \frac{1}{2} \ln \frac{E + p_z}{E - p_z} \tag{3.2}$$

where E is the energy and p_z is the z component of the momentum of the particle. For the high energy particles, $p \gg m$ so $E \sim p$ and the rapidity is approximated by the *pseudo-rapidity*, defined as

$$\eta \equiv -\ln \tan \left(\frac{\theta}{2} \right) . \tag{3.3}$$

In this case, the number of particles per unit rapidity ($dN/d\eta$) is invariant under boosts in the z direction.

Particles moving through a homogeneous solenoidal magnetic field follow helical trajectories. Reconstructed charged particle trajectories are referred to as "tracks". The plane perpendicular to the beam is referred to as the "transverse plane", and the transverse momentum of the track is referred to as p_T. As opposed to e^+e^- collisions, in $p\bar{p}$ collisions not all of the center of mass energy of the $p\bar{p}$ system is absorbed in the collision. The colliding partons inside the proton carry only a fraction of the kinetic energy of the proton. As a result, the center of mass system of the parton collisions is boosted along the beam direction (the "longitudinal" direction) by an unknown amount, but quantities defined in the transverse plane are conserved in the collisions. For instance, the sum of all transverse momenta of particles in a collision is zero, $\sum \vec{p_T} = 0$.

To uniquely parameterize a helix in three dimensions, five parameters are needed. The CDF II coordinate system chooses three of these parameters to describe a position, and two more to describe the momentum vector at that position. The three parameters which describe a position describe the point of closest approach of the helix to the beam line. These parameters are d_0, ϕ_0, and z_0, which are the ρ, ϕ and z cylindrical coordinates of the point of closest approach of the helix to the beam. The momentum vector is described by the track curvature (c) and the angle of the momentum in the $r-z$ plane ($\cot\theta$). From the track curvature we can calculate the transverse momentum. The curvature is signed so that the charge of the particle matches the charge of the curvature. From $\cot\theta$, we can calculate $p_z = p_T \cdot \cot\theta$. At any given point of the helix, the track momentum is a tangent to the helix. This basically means that the angle ϕ_0 implicitly defines the direction of the transverse momentum vector at the point of closest approach, $\vec{p_T}$.

The impact parameter (d_0) of a track is another signed variable; its absolute value corresponds to the distance of closest approach of the track to the beamline. The sign of d_0 is taken to be that of $\hat{p} \times \hat{d} \cdot \hat{z}$, where $\hat{p}$, $\hat{d}$ and $\hat{z}$ are unit vectors in the directions of $\vec{p}$, $\vec{d_0}$ and $\vec{z}$, respectively.

For decaying particles, we often define the displacement L_{xy},

$$L_{xy} = \vec{d} \cdot \hat{p_T} \,, \tag{3.4}$$

where $\vec{d}$ is the displacement of the decay vertex in the transverse plane, and $\hat{p_T}$ is the unit vector in the direction of $\vec{p_T}$.

3.4 Tracking Systems

The detector has a cylindrical tracking system immersed in a 1.4 T solenoidal magnetic field for the measurement of charged-particle momenta. We will describe this system starting from the devices closest to the beam and moving outwards. The innermost tracking device is a silicon strip vertex detector, which consists of three subdetectors: Layer 00 (L00), the Silicon Vertex Detector (SVX-II) and the Intermediate Silicon Layers (ISL). Fig. 3.5 shows a view in the $r - \phi$ plane of the three subsystems.

Surrounding the silicon detector is the Central Outer Tracker (COT), a 3.1 m-long cylindrical open-cell drift chamber covering radii from 43.4 to 132.3 cm. Figure 3.6 shows the coverage of the whole tracking system.

The silicon detectors provide excellent impact parameter, azimuthal angle and z resolution. They are also instrumental in vertexing. The COT provides excellent resolution of the curvature, ϕ and η. Together they provide very accurate measurements of the helical paths of charged particles.

3.4.1 Silicon Tracking Detectors

Silicon tracking detectors are used to obtain precise position measurements of the path of a charged particle. A silicon tracking detector is fundamentally a reverse-biased p-n junction. When a charged particle passes through the detector material, it causes ionization. In the case of a semiconductor material, this means that electron-hole pairs will be produced. Electrons drift towards the anode, and holes drift toward the cathode, where the charge is gathered. The amount of charge is, to first order, proportional to the path length traversed in the detector material by the charged particle.

By segmenting the p or n side of the junction into "strips" and reading out the charge deposition separately on every strip, we obtain sensitivity to the position of the charged particle. All the CDF II silicon tracking detectors are implemented as microstrip detectors. The typical distance between two strips is about 60 μm. Charge deposition from a single particle passing through the silicon sensor will be read out on one or more strips. This charge deposition is called a "cluster". There are two types of microstrip detectors: single and double-sided. In single-sided detectors only one (p) side of the junction is segmented

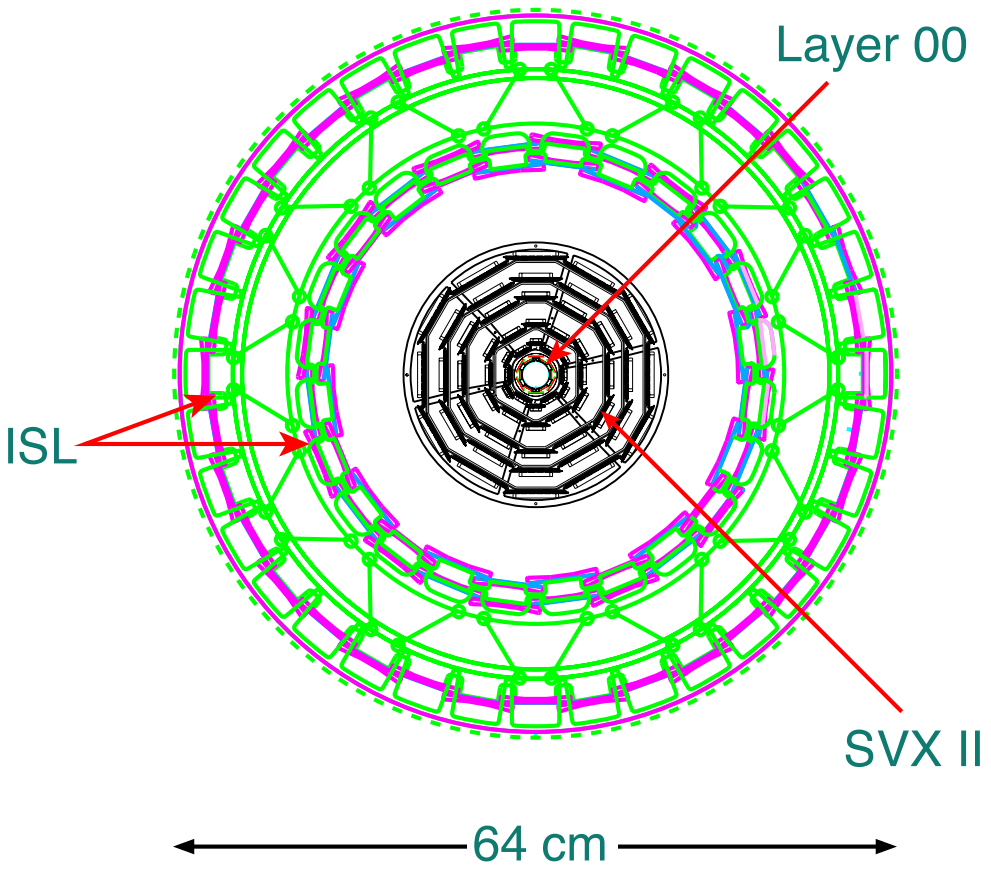

Figure 3.5: Transversal view of the Silicon Vertex Detector at CDF showing the different layers and parts of the detector.

into strips. Double-sided detectors have both sides of the junction segmented into strips. The benefit of double-sided detectors is that while one (p) side has strips parallel to the z direction, providing $r-\phi$ position measurements, the other (n) side can have strips at an angle (stereo angle) with respect to the z direction, which will give z position information.

The innermost layer, L00 [103], is a radiation-hard, single-sided silicon detector installed directly onto the beryllium vacuum beam pipe. L00 is the most recent addition to the CDF II tracker. The geometry of L00 is such that there are two overlaping hexagonal structures at radii between 1.35 and 1.62 cm from the beam. Figure 3.7 shows a detailed view of the L00. It only provides $r-\phi$ measurements. Being so close to the interaction point, L00 improves noticeably the spacial resolution up to $\approx$15 μm per hit.

The layer of silicon on the beam pipe is followed by the SVX-II [104]. It consists of five concentric layers of double-sided silicon sensors. One side of each sensor provides measurements in the transverse plane (axial strips); the other side's strips deliver 3D information. SVX-II extends radially from 2.5 to 11 cm, and along z up to 45 cm on either side of the interaction point. The spacial resolution of the SVX-II is $\approx$20 μm.

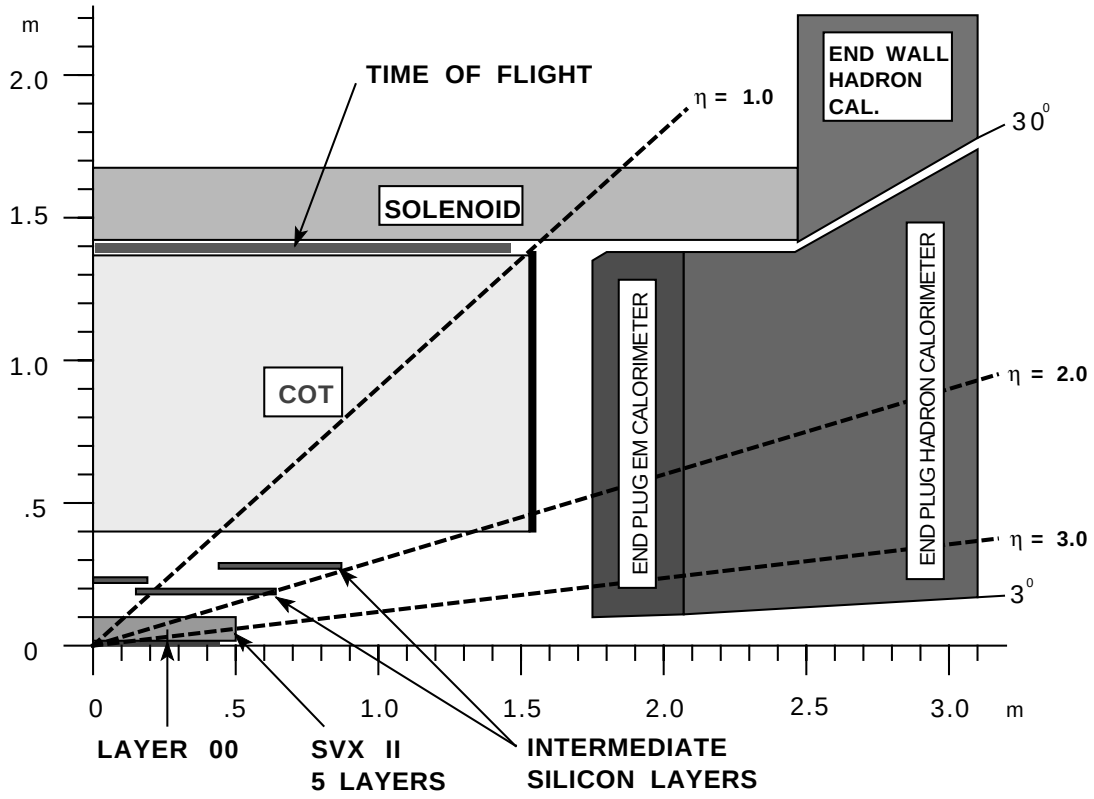

Figure 3.6: The CDF II tracker layout showing the different subdetector systems.

The Intermediate Silicon Layers (ISL) [105] are the outermost silicon subdetector systems, consisting of one double-sided silicon, similar to those on SVX-II, placed at a radius of 22 cm in the central region ($|\eta| < 1$), and two forward layers ($1 < |\eta| < 2$) at radii 20 and 28 cm from the beam line. Together with SVX-II, the ISL makes it possible to reconstruct tracks in the forward regions, which lie beyond the acceptance region of the outer tracker.

The SVX-II and ISL are made of double-sided silicon sensors. As shown in Table 3.2, the SVX-II layers have different stereo angles. Two layers have a 1.2° stereo angle and three have a 90° stereo angle. The ISL detector provides small angle (1.2°) stereo information.

Four silicon sensors are stacked length-wise into a "ladder" structure which is 29 cm long. The readout electronics are mounted onto the ends of the ladders. The ladders are organized in an approximately cylindrical configuration, creating "barrels". A SVX-II barrel is segmented into 12 wedges, each covering approximately 30° in ϕ with a small overlap at the edges, allowing for several silicon hits per track. There are three SVX-II barrels, adjacent to each other along the z-axis, covering the nominal interaction point in the center of the CDF II Detector. The coverage of the silicon detector subsystems is shown in Fig. 3.8. The

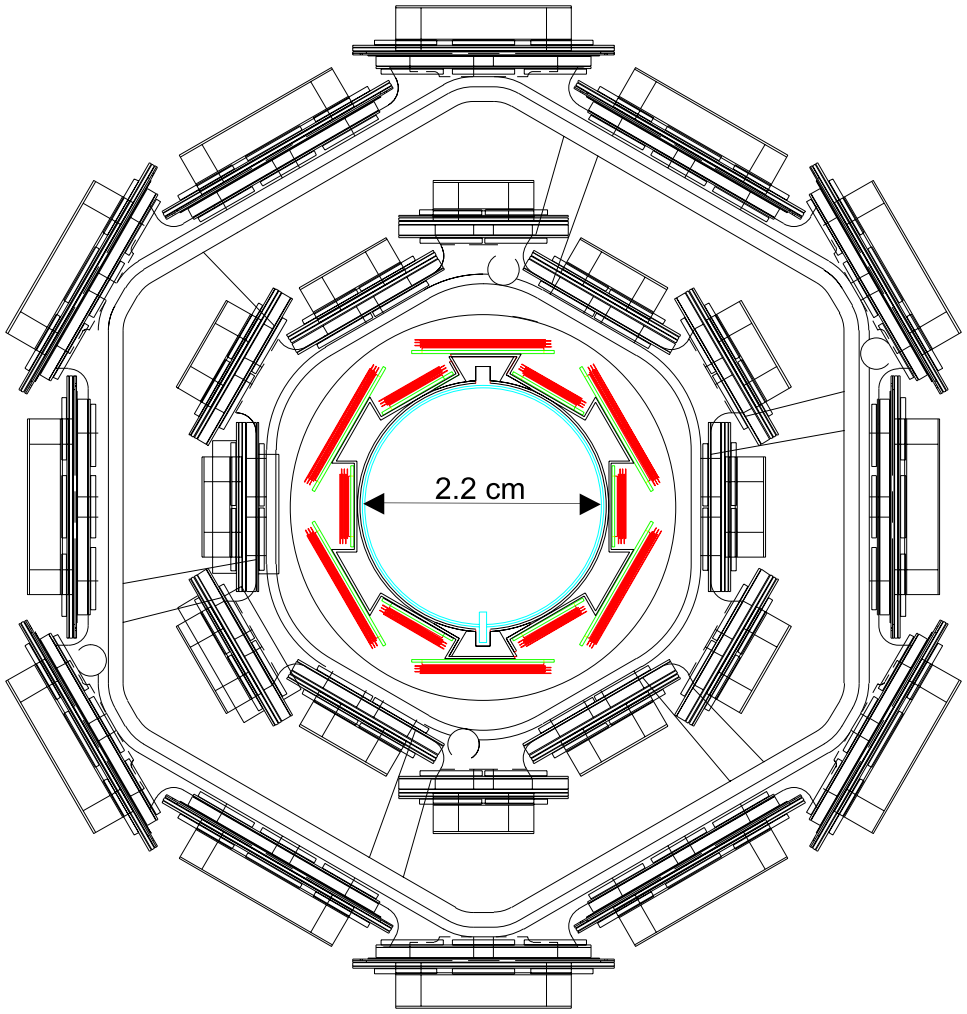

Figure 3.7: Detailed view of the Silicon L00 along with the two innermost layers of the SVX.

silicon tracking system is used in stand-alone mode to provide an extension of tracking down to 2.8 in pseudorapidity.

Compared to the shorter, 4-layer, single-sided vertex detector of Run I, the new silicon tracker provides a much wider acceptance, better resolution, three-dimensional reconstruction and, as stated above, can be used in stand-alone mode without input from the Central Outer Tracker (described hereafter).

3.4.2 Central Outer Tracker

The Central Outer Tracker (COT) [106] is a multiwire drift chamber built to replace the one used in Run I (CTC). The active volume of the COT begins at a radius of 43.4 cm from

Table 3.2: Relevant parameters for the layout of the sensors of the SVX-II layers.

Property	Layer 0	Layer 1	Layer 2	Layer 3	Layer 4
Number of ϕ strips	256	384	640	768	869
Number of z strips	512	576	640	512	869
Stereo angle	90°	90°	-1.2°	90°	+1.2°
ϕ strip pitch [μm]	60	62	60	60	65
z strip pitch [μm]	141	125.5	60	141	65
Active width [mm]	15.30	23.75	38.34	46.02	58.18
Active length [mm]	72.43	72.43	72.38	72.43	72.43

the nominal beamline and extends out to a radius of 132.3 cm. The chamber is 310 cm long. The COT contains 96 sense wire layers, which are radially grouped into eight "superlayers", as inferred from the end plate section shown in Fig. 3.9(a). Four superlayers (axial superlayers) provide $r-\phi$ measurements and are alternated with the remaining four that provide 2° stereo measurements (stereo superlayers). Each superlayer is divided in ϕ into "supercells", and each supercell has 12 sense wires and a maximum drift distance that is approximately the same for all superlayers. Therefore, the number of supercells in a given superlayer scales approximately with the radius of the superlayer. The entire COT contains 30,240 sense wires. Approximately half the wires run along the z direction ("axial"). The other half are strung at a small angle (2°) with respect to the z direction ("stereo"). Particles originating from the interaction point, which have $|\eta| < 1$, pass through all 8 superlayers of the COT. Particles which have $|\eta| < 1.3$ pass through 4 or more superlayers.

The COT drift chamber provides accurate information in the $r-\phi$ plane for the measurement of transverse momentum, p_T, and substantially less accurate information in the $r-z$ plane for the measurement of the z component of the momentum, p_z.

The supercell layout, shown in Fig. 3.9(b) for superlayer 2, consists of a wire plane containing sense, potential and shaper (for field shaping) wires and a field (or cathode) sheet on either side. Both the sense and potential wires are 40 μm diameter gold plated Tungsten. The field sheet is 6.35 μm thick Mylar with vapor-deposited gold on both sides. Each field sheet is shared with the neighboring supercell.

The COT is filled with an Argon-Ethane gas mixture and Isopropyl alcohol (49.5:49.5:1). The mixture is chosen to have a constant drift velocity across the cell width. This allows a maximun drift time of 177 ns with a drift velocity of 100 μm/ns. This prevents pileup of events in the drift chamber from the previous event.

When a charged particle passes through, the gas is ionized. Electrons drift towards the sense wires. The electric field in a cylindrical system grows exponentially with decreasing radius. As a result, the electric field very close to the sense wire is large, resulting in an avalanche discharge when the charge drifts close to the wire surface. This effect provides a gain of $\sim 10^4$. Due to the magnetic field that the COT is immersed in, electrons drift at a Lorentz angle of $\sim 35°$. The supercell is tilted by 35° with respect to the radial direction to

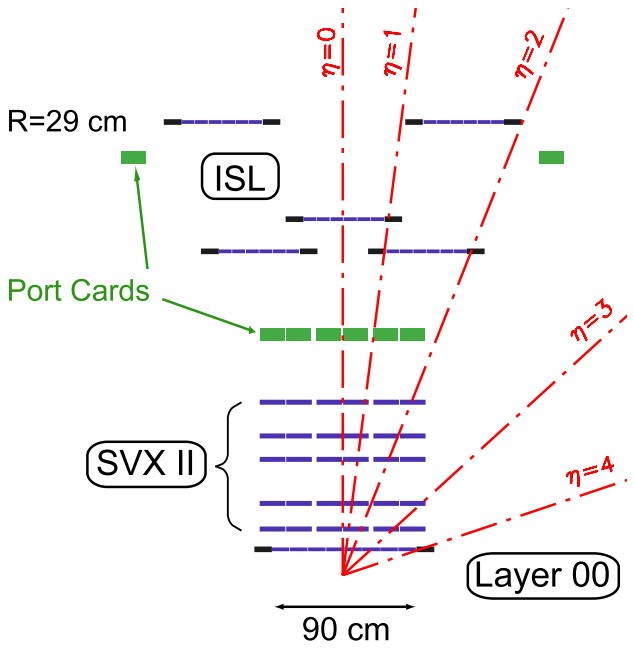

Figure 3.8: Coverage of the different silicon subdetectors projected into the $r-z$ plane. The r and z axes have different scales.

compensate for this effect.

Signals on the sense wires are processed by the ASDQ (Amplifier, Shaper, Discriminator with charge encoding) chip, which provides input protection, amplification, pulse shaping, baseline restoration, discrimination and charge measurement [107]. The charge measurement is encoded in the width of the discriminator output pulse, and is used for particle identification by measuring the ionization along the trail of the charged particle (dE/dx). The pulse is sent through $\sim$ 11 m of micro-coaxial cable, via repeater cards to Time to Digital Converter (TDC) boards in the collision hall. Hit times are later processed by pattern recognition (tracking) software to form helical tracks. The hit resolution of the COT is about 140 μm. The transverse momentum resolution has been measured using cosmic ray events to be

$$\frac{\sigma_{p_T}}{p_T^2} = 0.17\% \ [\mathrm{GeV/c}]^{-1}. \tag{3.5}$$

3.4.3 Pattern Recognition Algorithms

As explained in the previous sections, charged particles leave small charge depositions as they pass through the tracking system. By following, or "tracking", these depositions, pattern recognition algorithms can reconstruct the charged particle track.

There are several pattern recognition algorithms used to reconstruct tracks in the CDF II tracking system. Most of the tracks are reconstructed using "Outside-In" algorithms which we will describe here. The name of this group of algorithms suggests that the track is followed

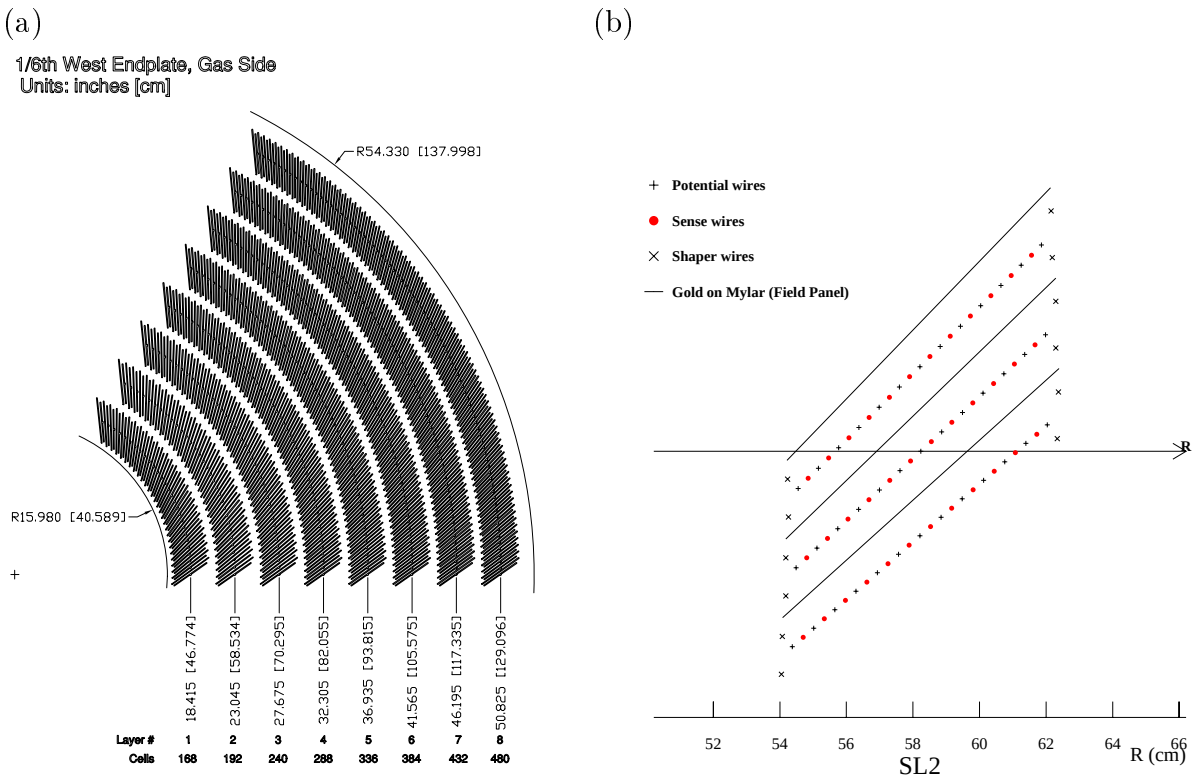

Figure 3.9: (a) Layout of wire planes on a COT endplate. (b) Layout of wires in a COT supercell.

from the outside of the tracking system inwards.

The track is first reconstructed using only COT information. The COT electronics report hit time and integrated charge for every wire in an event. The hit time corresponds to the time that an avalanche occurred at a sense wire. The hit time can be interpreted as the drift time of the charge in the gas, but first it has to be corrected for time of flight. The hit timing resolution is of the order of a few ns; this roughly corresponds to the average spread in collision times. It is assumed that the collision times always happen at the same time in a cycle during a store. An average of collision times is done for many previous events and this is used as the event collision time. Hit times corrected for the collision time are interpreted as drift times and used in pattern recognition. To perform the final track fit, an additional time of flight correction is performed assuming massless particles.

The helical track, when projected into the two dimensional $r-\phi$ plane, is a circle. This simplifies pattern recognition, so the first step of pattern recognition in the COT looks for circular paths in radial superlayers of the COT. Supercells in the radial superlayers are searched for sets of 4 or more hits that can be fit to a straight line. These sets are called "segments". The straight-line fit for a segment gives sufficient information to extrapolate rough measurements of curvature and ϕ_0. Once segments are found, there are two approaches to track finding. One approach is to link together segments for which the measurements of

curvature and ϕ_0 are consistent. The other approach is to improve the curvature and ϕ_0 measurement of a segment reconstructed in superlayer 8 by constraining its circular fit to the beamline, and then adding hits which are consistent with this path. Once a circular path is found in the $r-\phi$ plane, segments and hits in the stereo superlayers are added by their proximity to the circular fit. This results in a three-dimensional track fit. Typically, if one algorithm fails to reconstruct a track, the other algorithm will not. This results in a high track reconstruction efficiency ($\sim 95\%$) in the COT for tracks which pass through all 8 superlayers ($p_T \geq 400$ MeV/c). The track reconstruction efficiency mostly depends on how many tracks there are to be reconstructed in the event. If there are many tracks present close to each other, hits from one track can shadow hits from the other track, resulting in efficiency loss.

Once a track is reconstructed in the COT, it is extrapolated into the SVX-II. Based on the estimated errors on the track parameters, a three-dimensional "road" is formed around the extrapolated track. Starting from the outermost layer, and working inwards, silicon clusters found inside the road are added to the track. As a cluster gets added, the road gets narrowed according to the knowledge of the updated track parameters. Reducing the width of the road reduces the chance of adding a wrong hit to the track, and also reduces computation time. In the first pass of this algorithm, $r-\phi$ clusters are added. In the second pass, clusters with stereo information are added to the track.

3.5 Time of Flight

Outside the tracking system, still inside the superconducting magnetic coil, CDF II has a Time of Flight (TOF) [108] system. The TOF system is designed to distinguish low momentum pions, kaons and protons by measuring the time it takes these particles to travel from the primary vertex of the $p\bar{p}$ collision to the TOF system. The system consists of 216 bars of scintillating material, roughly 300 cm in length and with a cross section of 4×4 cm^2. The bars are arranged into a barrel around the COT cylinder, at a radius of $\sim$140 cm. They are surrounded by the superconducting solenoid on the outside. The scintillating material is Bicron 408, which has a short rise time and a long (380 cm) attenuation length.

Particles passing through the scintillating material of the bars deposit energy causing small flashes of visible light. This light is detected by photomultiplier (PMT) tubes which are attached at both ends of each bar and provide time and pulse height measurements. The signal from the photomultiplier tube is processed by a pre-amplifier circuit mounted directly onto the tube. The readout electronics perform both time and amplitude digitization of the signal. The TDC information is a digitization of the time when the signal pulse reaches a fixed discriminator threshold. This time depends on the amplitude of the pulse, since a large pulse crosses the threshold earlier (time walk). The digitization of the pulse amplitude is needed to correct for this effect. After correcting for time walk effects, the timing resolution of the TOF system is about 110 ps for particles crossing the bar exactly in front of one of the photomultiplier tubes. The timing resolution varies with displacement from the photomultiplier tube. Large pulses give better timing resolution, as light attenuates

while travelling through the scintillator material. Therefore, particles passing through the bar near the photomultiplier tube have better timing resolution than those which are farther away. A more detailed description can be found in [109].

3.6 The Solenoid

The tracking and the TOF systems are enclosed in a superconducting solenoid which provides a nearly uniform magnetic field of up to 1.4 T along the detector axis, over a cylindrical fiducial volume 3.5 m long and 2.8 m in diameter.

The coil itself is 4.8 m long and ≈25 cm thick, with an inner radius of 1.4 m. It is built of an aluminium-stabilized Nb Ti superconductor, able to withstand currents up to 5000 A, and operating at liquid helium temperature. During most of Run I, the magnet operated at 4650 A, corresponding to a current density of 1115 A/m and a central field of 1.4 T.

Although the design lifetime of the solenoid was only ten years, it is possible to reuse the magnet during Run II. The cool-down procedures that were used during Run I limited mechanical stress to the coil, avoiding fatigue damage.

3.7 Calorimeters

The main effort of the Run II upgrade of the CDF II calorimeter system dealt with upgrading the electronics to handle the faster bunch crossings. The active detector parts were taken over from Run I without modification. We will describe shortly this system in the next subsections. A more detailed description can be found in the CDF II Technical Design Report [100].

3.7.1 Overview

The basic structure of the CDF calorimeters is based on scintillating sampling. That is, the detector after the absorbing material is a acintillating sheet, guided into a fiber, where the light produced from the incoming particles is passed through a wavelength shifting fiber to a photomultiplier tube, and then on to an amplifier. The calorimeter is divided into separate electromagnetic (large number of radiation lenghts X_0 and small number of interaction lenghts λ for photon and electron identification and energy measurement) and hadronic (large number of interaction lenghts for hadron energy measurement) sections.

The entire calorimeter is segmented into "projective towers", whose geometry is summarized in Table 3.3. This means that it is segmented in η and ϕ "towers" that point to the interaction region. The coverage of the calorimetry system is 2π in ϕ and $|\eta| < 3.6$ in pseudorapidity.

The calorimeter system is divided into three regions: central, plug and forward. Corresponding to these regions, the subsystems will have one of the letters C, P and F in their acronym. Each calorimeter tower consists of an electromagnetic shower counter followed by a hadron calorimeter. This allows for comparison of the electromagnetic and hadronic

Table 3.3: Calorimeter segmentation.

η range	$\Delta\phi$	$\Delta\eta$
0 - 1.1 (1.2 had)	15°	0.1
1.1 (1.2 had) - 1.8	7.5°	0.1
1.8 - 2.1	7.5°	0.16
2.1 - 3.6	15°	0.2 - 0.6

energies deposited in each tower, and therefore separation of electrons and photons from hadrons.

There are three subdetectors for the electromagnetic calorimeter: CEM, PEM and FEM. These correspond to the central, plug and forward regions of $|\eta|$, respectively. The hadron calorimeters in the central region are the central (CHA) and the endwall (WHA). The plug and forward regions are covered by the PHA and FHA calorimeters, respectively.

The central region of the detector is covered by the Central Electromagnetic (CEM) [110] and Centarl Hadronic (CHA) [111] calorimeters, in the pseudorapidity ranges $|\eta|$ <1.1 and $|\eta|$ <0.9, respectively. In the forward region, the plug electroamgnetic (PEM) [112] and hadronic (PHA) calorimeters cover the regions 1.1< $|\eta|$ <3.6 and 1.3< $|\eta|$ <3.6 respectively. The Wall Hadronic Calorimeter (WHA) [111] fills the gap between the CHA and the PHA in the pseudorapidity range 0.7< $|\eta|$ <1.3.

The pseudorapidity coverage, resolutions, thickness and absorber material for the different electromagnetic and hadron calorimeters are given in Table 3.4. The details of each calorimeter are based on the specific physics needs and are discussed below.

Table 3.4: Pseudorapidity coverage, energy resolution and thickness for the different calorimeter subdetectors of the CDF II Detector. The $\oplus$ symbol means that the constant term is added in quadrature to the resolution. λ_0 signifies interaction lengths and X_0 radiation lengths.

System	η coverage	Energy Resolution (%)	Thickness	Absorber
CEM	$\lvert\eta\rvert < 1.1$	$13.5/\sqrt{E_T} \oplus 2$	$18X_0$	3.18 mm lead
PEM	$1.1 < \lvert\eta\rvert < 3.6$	$16/\sqrt{E_T} \oplus 1$	$21X_0$	4.5 mm lead
CHA	$\lvert\eta\rvert < 0.9$	$50/\sqrt{E_T} \oplus 3$	$4.5\lambda_0$	2.5 cm steel
WHA	$0.7 < \lvert\eta\rvert < 1.3$	$75/\sqrt{E_T} \oplus 4$	$4.5\lambda_0$	5 cm steel
PHA	$1.3 < \lvert\eta\rvert < 3.6$	$80/\sqrt{E_T} \oplus 5$	$7.0\lambda_0$	5.08 cm steel

3.7.2 Central Calorimeter

Apart from the electronics, the central calorimeter in the CDF II detector is the same used during Run I.

The CEM is a sampling device made of 31.5 mm thick layers of polystyrene scintillator, alternated with 3.18 mm thick layers of aluminum-clad lead. In order to mantain a constant number of radiation lengths as a function of θ, some lead layers are replaced by acrylic (Plexiglas), so that the actual number of absorber layers varies from 30 near the center to 20 at $\eta \approx 1.1$. The CEM is divided into four arches (Noert-West, South-West, North-East and South-East) made of identical 15° modules, each of them being segmented into 10 projective towers. Thus each tower covers a solid angle of 0.1 by 15° in $\eta \times \phi$ space. The blue light emitted by the scintillators is collected on each side of the two towers by acrylic wavelength shifters that convert it to green light and guide the light toward two photomultipliers (Hamamatsu R580) outside the CHA (see Fig. 3.10). The two most forward towers of one of the CEM and CHA modules are not instrumented (the so called "chimney"), in order to provide acess for cryogenics to the solenoid. Based on test beam data, the CEM energy resolution for an electron going through the center of a tower is found to be $\frac{13.7\%}{\sqrt{E}} \oplus 2\%$.

The Central EM Max Detector (CES) [110] is a strip chamber designed to provide a measurement of charged tracks very close to the calorimeter, with very little material in between. This is done to distinguish electrons from photons, which otherwise look very similar in the detector. They are located between the 8^{th} lead layer and the 9^{th} scintillator layer (counting outward), which is the expected position of shower maximum ($\approx 6X_0$, including tracking and solenoid material). In each CEM module, a CES module is a multi-wire proportional chamber with 64 anode wires parallel to the beam axis, spaced 0.73 cm apart and split at $|z| = 121$ cm. The spatial resolution achieved is ≈ 2 mm.

The CEM is also equipped with a pre-shower detector (CPR), useful in discriminating between hadrons and photons/electrons. The CPR is a set of multi-wire proportional chambers with wires parallel to the beam providing transverse measurements and strip cathodes providing z information, with a resolution of the order of a few milimeters.

The CHA is a sampling hadronic calorimeter surrounding the CEM, following the same segmentation (0.1 by 15° in $\eta \times \phi$). The WHA extends the CHA coverage and uses the same technology as the CHA. Altogether, a wedge contains 12 towers, 6 of which are fully in the CHA, 3 in the WHA and 3 are shared between the two. The number of interaction lengths is constant through the entire range of pseudorapidity and is equal to 4.5. The CHA is made of 32 layers of 2.5 cm thick steel absorber and 1.0 cm thick scintillator. The WHA is made of 15 layers of 5.0 cm thick steel absorber and 1.0 cm thick scintillator. Two PMT's per tower are linked to the scintillators by a wavelength shifter and a light guide. The CHA and WHA single pion energy resolutions are $\frac{50\%}{\sqrt{E}} \oplus 3\%$ and $\frac{75\%}{\sqrt{E}} \oplus 4\%$, respectively.

3.7.3 Plug Calorimeter

The Plug Calorimeter, shown in Fig. 3.11, covers the η region between 1.1 and 3.64, corresponding to polar angles between 37° and 3°. It was designed and built to replace the

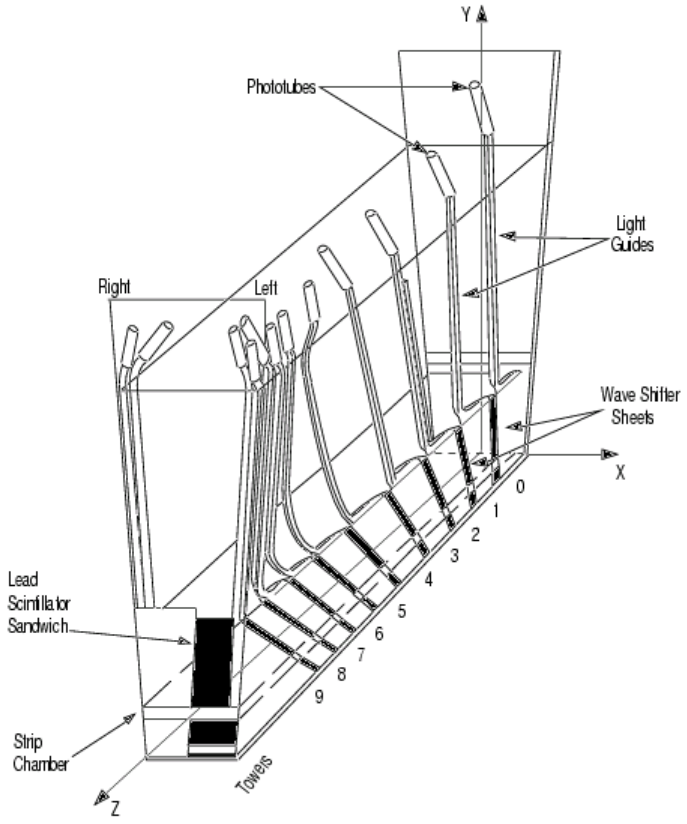

Figure 3.10: Wedge of the Central Electromagnetic Calorimeter.

CDF I forward calorimeters, and to cope with the Run II requirements (higher luminosity and 132 ns bunch spacing).

The Plug Calorimeter consists of an electromagnetic (PEM) and hadronic (PHA) calorimeter with the same projection segmentation. Figure 3.12 shows the segmentation patern of a 15° module: towers cover an azimuthal angle of 7.5° down to $\eta = 2.22$ and 15° further; similarly, the segmentation in η becomes coarser as one moves closer to the beam. Figure 3.12 also shows how towers are combined for the purpose of being used by the trigger system.

The PEM is made of 22 layers of 4.5 mm lead and 4 mm thick scintillator tiles. Each scintillator tile is read by a single PMT. In front of the 22 sampling layers is a 1 cm thick scintillator tile read out by a multi-anode photomultiplier (MAPMT) which is used as a pre-shower detector. The PEM energy resolution is $\frac{16\%}{\sqrt{E}} \oplus 1\%$.

As in the Central Calorimeter, a shower maximum detector (PES) is also embedded in the PEM. It is made of two sets of scintillating strips that provide precise 2D shower position measurement (resolution $\approx$1 mm).

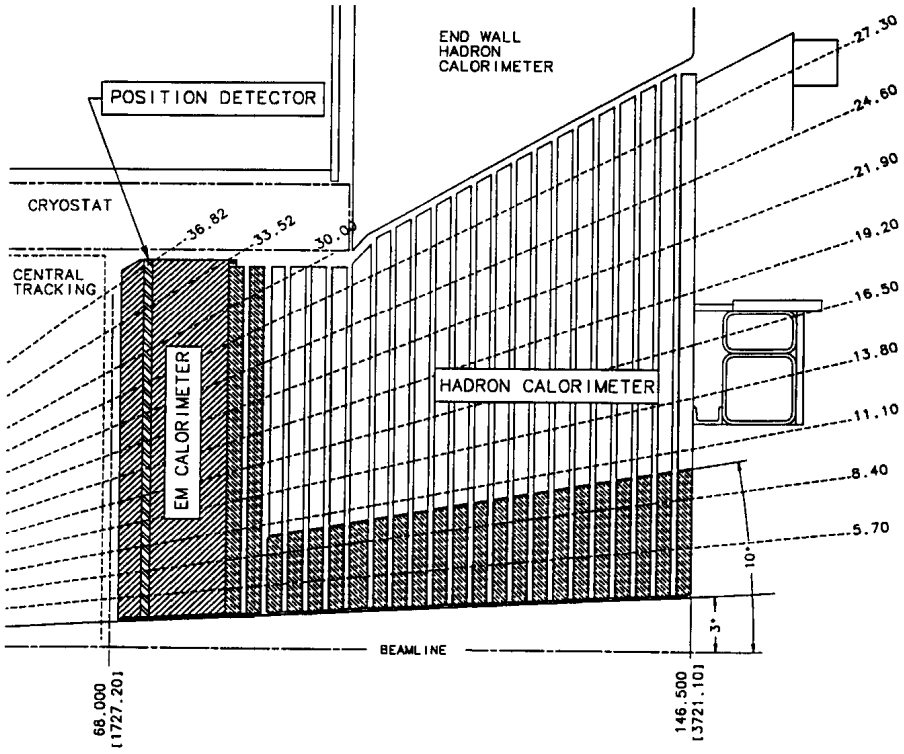

Figure 3.11: View of the Plug Calorimeter (PEM and PHA).

The PHA is made of 23 layers of 5.08 cm thick steel absorber and 6 mm thick scintillator. Its resolution is $\frac{80\%}{\sqrt{E}} \oplus 5\%$.

3.8 Muon Systems

Muons are particles which interact with matter only by ionization. For energies relevant to this experiment, they do not cause showers in the electromagnetic or hadronic calorimeters. As a result, if a muon is created in the collision and has enough momentum, it will pass through the calorimeter with minimal interaction with the material inside. Therefore, the calorimeter can be considered as a filter which retains particles that shower when interacting with matter and muons, which do not. Muon detection systems are therefore placed radially outside the calorimeters, being the outermost component of CDF.

The muon detectors at CDF make use of single wire drift chambers as well as scintillator counters for fast timing. The various subsystems are the Central Muon Detector (CMU), the Central Muon uPgrade Detector (CMP), the Central Scintillator uPgrade (CSP), the Central Muon eXtension Detector (CMX), the Central Scintillator eXtension (CSX), the Toroid Scintillator Upgrade (TSU), the Barrel Muon Upgrade (BMU) and the Barrel Scintillator

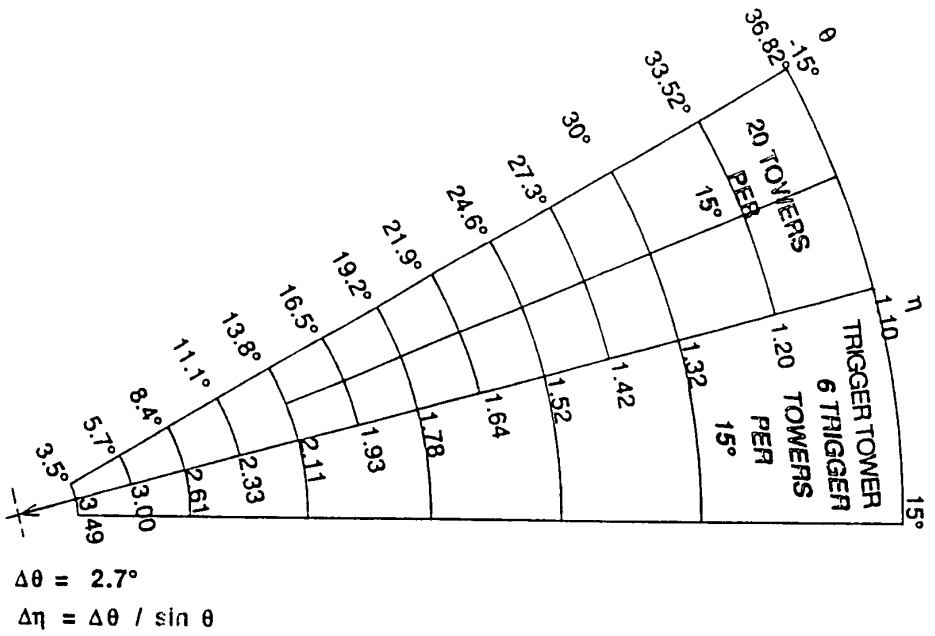

Figure 3.12: Segmentation of the Plug Calorimeter (PEM and PHA).

Upgrade (BSU). The CMU, CMP and CSP cover $|\eta| < 0.6$, the CMX and CSX cover $0.6 < |\eta| < 1.0$ and the TSU, BMU and BSU cover $1.0 < |\eta| < 2.0$. Three muon detectors are used for the analysis described in this thesis: the CMU, the CMP and the CMX. The data from the TSU, BMU and BSU systems was not available for triggering. Figure 3.13 shows the coverage of each subdetector in the $\eta \times \phi$ coordinates.

Table 3.5 summarizes the information on the muon subsystem.

The first muon system built at CDF, the CMU [113], is placed just outside the CHA. It provides roughly 5.5 interaction lengts for pions, absorbing more than 99% of the outgoing charged hadrons. The p_T threshold of the CMU is 1.4 GeV/c. It is cylindrical in geometry with a radius of 350 cm, arranged into 12.6° wedges. Each wedge contains three modules (stacks) with four layers of four rectangular drift cells. The cells have 50 μm sense wires at the center of the cell, parallel to the z direction. The system is filled with an Argon-Ethane gas mixture and alcohol (49.5:49.5:1) as the COT.

A second set of chambers, the CMP, is situated outside an additional layer 60 cm thick of steel to act as an absorber, which is 3.5 additional interaction lenghts (for a total of $9.0\lambda_0$). The p_T threshold of the CMP is 2.2 GeV/c. It is rectangular in geometry, consisting in four layers of single-wiredrift cells, staggered by one half cell per layer.

On the other surface of the CMP lies the CSP [114], a single layer of rectangular scintillator tiles, with a waveguide to move the scintillated light into a PMT. This provides a fast detection mechanism used in triggering muons.

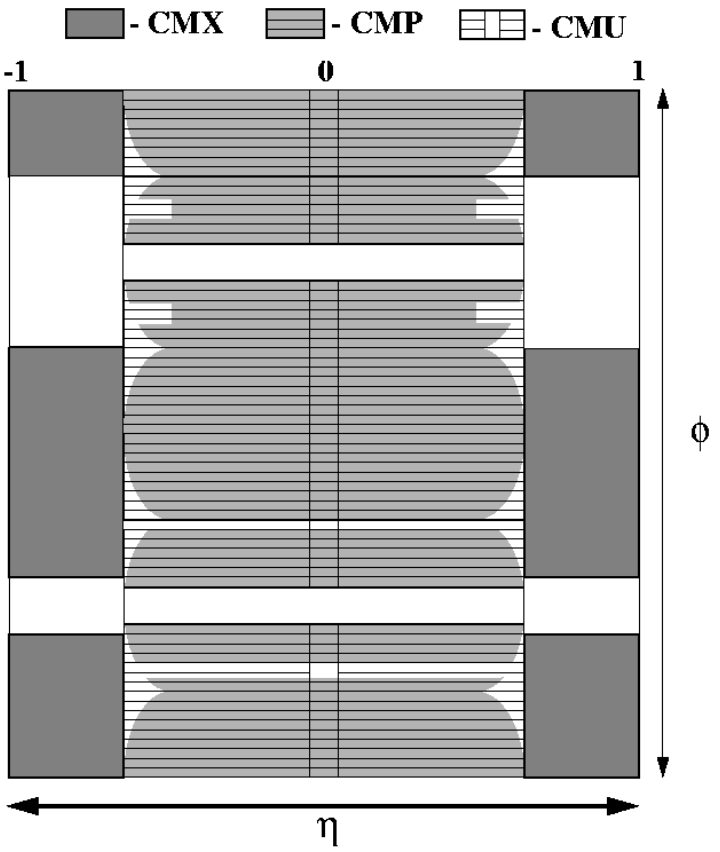

Figure 3.13: Coverage (in the $\eta \times \phi$ plane) of the upgraded CDF muon system.

The CMX is located on either side of the detector straddling the beamline. It is a conical geometry of drift tubes with drift chambers, similar to the CMP, and scintillators on both sides. The CSX is another scintillator array similar to the CSP. The CMX cover 360° in ϕ. The segmentation is in 15° wedges in azimuthal angle. Each wedge consists of eight layers of rectangular tubes in the radial direction, also offset to provide better resolution.

Using the timing information from the drift cells of the muon systems, short tracks (called "stubs") are reconstructed. Tracks reconstructed in the COT are extrapolated to the muon systems. Based on the projected track trajectory in the muon system, the estimated errors on the tracking parameters and the position of the muon stub, a χ^2 value of the track-stub match is computed. To ensure good quality of muons, an upper limit is placed on the value of χ^2_ϕ, the χ^2 of the track-stub match in the ϕ coordinate.

Table 3.5: Parameters of the Muon Detectors at CDF.

	CMU	CMP/CSP	CMX/CSX
η coverage	0 - 0.6	0 - 0.6	0.6 - 1.0
Min p_T [GeV/c]	1.4	2.2	1.4
Drift Tubes			
Thickness [cm]	2.68	2.5	2.5
Width [cm]	6.35	15	15
Length [cm]	226	640	180
Max drift time [μs]	0.8	1.4	1.4
Scintillators			
Thickness [cm]	N/A	2.5	1.5
Width [cm]	N/A	30	30 - 40
Length [cm]	N/A	320	180

3.9 The Cherenkov Luminosity Counter

The Cherenkov Luminosity Counter (CLC) [115, 116] was designed for the Tevatron Run II in order to achieve a precision measurement of the instantaneous luminosity up to $\approx 2{\cdot}10^{32}$ cm^{-2}s^{-1} and to cope with the 132 ns bunch-spacing that was originally envisioned. Since luminosity measurement is critical to the cross section measurement presented in this document, it is explained here in some detail.

The detector, located in the 3° gap between the plug calorimeter and the beam pipe as shown in Fig. 3.14, is made of two identical CLC modules installed at small angles, inside the Plug Calorimeter, on each side of the interaction point. Figure 3.15 shows two views of such a module. Each module is composed of 48 thin, long, conical, gaseous Cherenkov counters pointing toward the interaction point and covering the pseudorapity range $3.7 < |\eta| < 4.7$. The counters are arranged around the beam pipe in three concentric layers, with 16 counters each. The cones in the two outer layers are about 180 cm long and the inner layer counters (closer to the beam pipe) have a length of 110 cm; their diameter varies from 2 to 6 cm. At the widest end of each one (the furthest away from the interaction point), a conical mirror collects the Cherenkov light into 2.5 cm diameter photomultiplier tubes (Hamamatsu R5800Q). The tubes have a concave-convex, 1 mm thick, quartz window for efficient collection of the ultraviolet part of Cherenkov spectra and operate at a gain of $2 \cdot 10^6$. The modules are filled with isobutane at atmospheric pressure; it is however possible to increase the pressure up to 2 atm, in order to increase the yield of Cherenkov light. Isobutane was chosen because of its large refractive index at atmospheric pressure and its good transparency to ultraviolet light. The Cherenkov angle is 3.1° and the momentum threshold for light emission is 9.3 MeV/c for electrons and 2.6 GeV/c for pions.

Because of the narrow shape and the orientation of the cones, particles produced by $p\bar{p}$ interactions close to the center of the detector are likely to go through a large portion of the

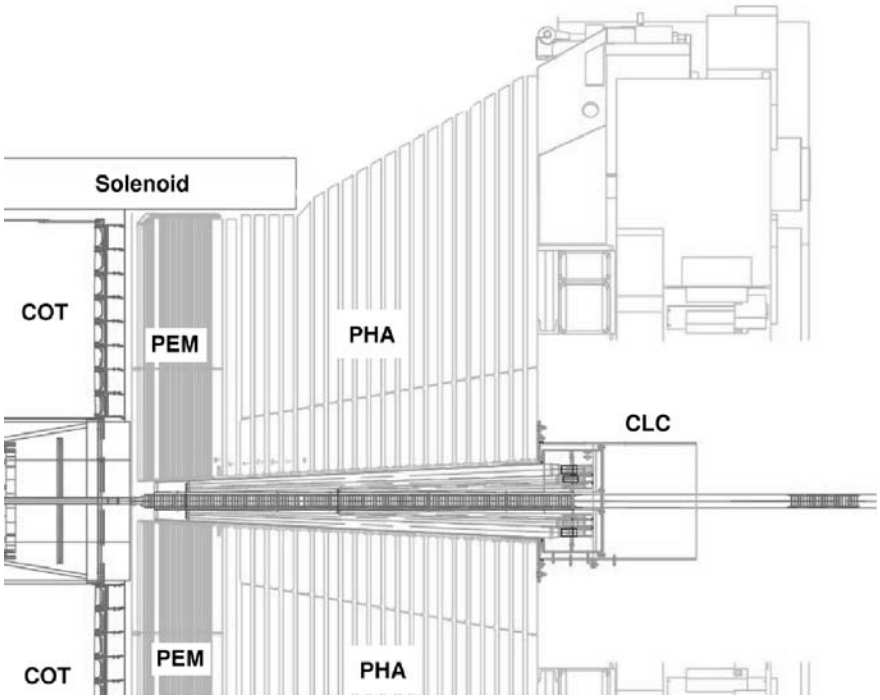

Figure 3.14: Location of the CDF Cherenkov Luminosity Counter in the 3° gap between the plug calorimeter and the ebam pipe.

CLC, producing an important light yield (several hundred photo-elelectrons), while particles from the beam halo or from secondary interactions traverse the detector at large angle, and have lower energy, hence producing a much smaller light signal. Thus the background is easily rejected by requiring a certain minimal light yield threshold in each channel; the number of particles is measured from the total yield in the module. Thanks to the CLC's excellent time resolution (less than 100 ps), it is also possible to select hits from prompt particles by requiring time coincidence between hits in the two different modules.

At hadron collider experiments the beam luminosity can be expressed as a function of the number of hits per bunch-crossing as follows:

$$L = \frac{f_{bc}}{\sigma_{in} \cdot \epsilon} \cdot \mu \,, \tag{3.6}$$

where L is the instantaneous luminosity, f_{bc} is the rate of bunch-crossings in the Tevatron, σ_{in} is the inelastic scattering cross section, ϵ is the acceptance times efficiency of the CLC for inelastic scattering events and μ is the (measured) average number of interactions per bunch-crossing.

In Eq. 3.6, f_{bc} and ϵ are known and the total inelastic cross section was measured in several experiments. CDF Run I and E811 measurements were combined, giving $\sigma_{in} = 60.4 \pm 2.3$ mb at 1.8 TeV, which can be extrapolated to 61.7 ± 2.4 mb at 1.96 TeV. Therefore, we just need to know the number of hits per bunch-crossing in order to calculate the luminosity. And this

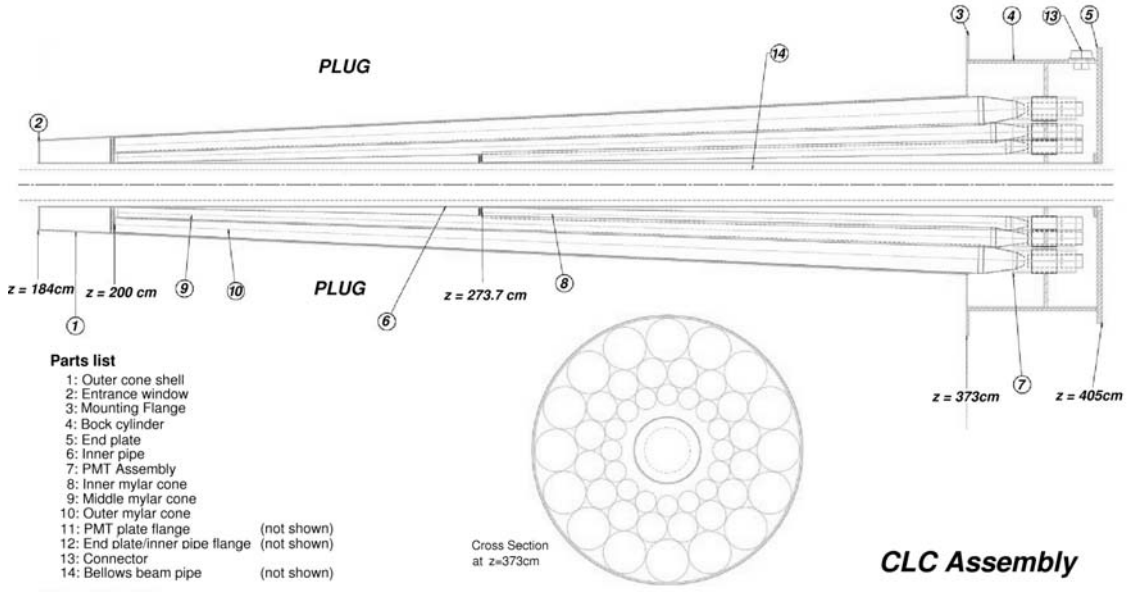

Figure 3.15: The CLC assemnly diagram. The cross section view at z=373 cm is also shown.

is what the CLC was designed for by measuring the number of particles and their arrival time in each bunch-crossing. A precision of 5.9% [117] on the luminosity is achieved with the CLC; 4.4% comes from the CLC acceptance and operation of the luminosity monitor and 4% from the calculation of the inelastic cross section. The luminosity measured by the CLC is used to monitor the Tevatron's performance.

3.10 Trigger

Triggering systems are necessary because it is not physically possible to store information about every single $p\bar{p}$ collision. Collisions happen roughly at a rate of 2.5 MHz, and the readout of the full detector produces an event roughly the size of 250 kB. There is no medium available which is capable of recording data this quickly, nor would it be practical to analyze all these data later on. The trigger system is a pre-filter, which reduces data rates and volumes to manageable levels, according to all possible or foreseen physics prescriptions.

The CDF II triggering system is designed based on three conditions. The first condition is that the trigger has to be deadtimeless. This means that the trigger system has to be quick enough to make a decision for every single event, before the next event occurs. The second condition is imposed by the Tevatron upgrade for Run II, and it is the time between collisions, 132 ns. The last condition is that the data logging system can write about 30-50 events per second to tape, because of limited resources. In short, the trigger has to be fast enough to analyze every collision, and it has to figure out which 50 of 2.5 million events it

should save in a given second. This is achieved by staging trigger decisions in three levels, as shown in Fig. 3.16. This new architecture is fully capable of withstanding a 132 ns bunch separation, while keeping dead time as short as possible.

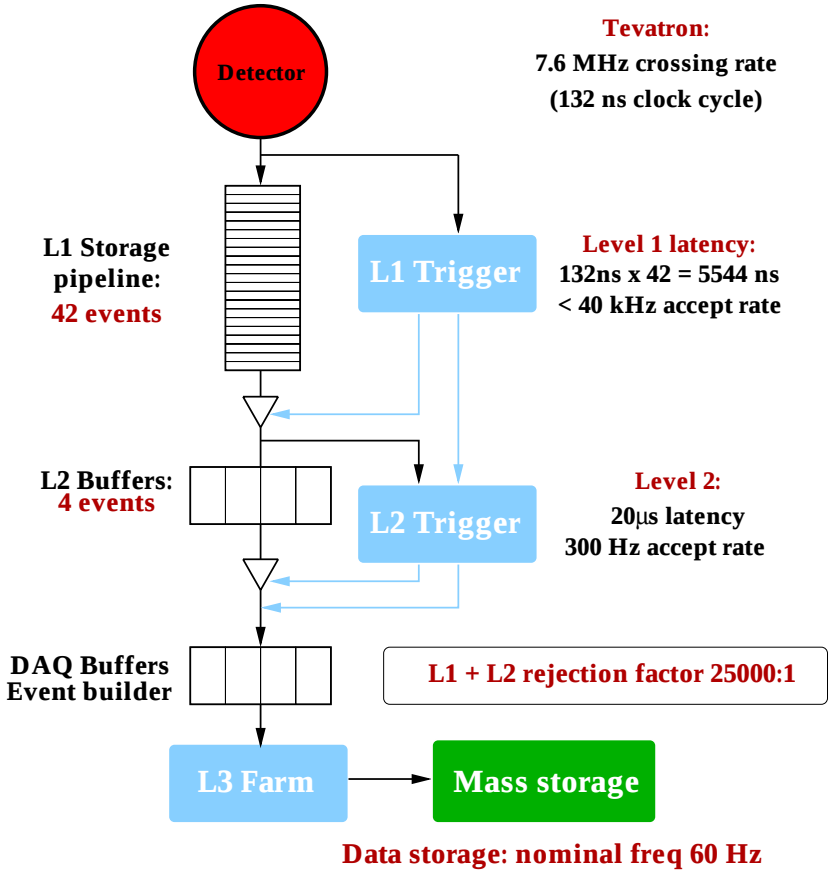

Figure 3.16: Diagram of the CDF II Detector trigger system.

Each level of the trigger is given a certain amount of time to reach a decision about accepting or rejecting an event. By increasing the time allowed for triggering at different levels of the trigger, the complexity of reconstruction tasks can be increased at every level. At the first level of the trigger, only very rough and quick pattern recognition and filtering algorithms are used. In order to do this in time, the Level 1 and Level 2 triggering mechanisms are implemented with custom electronics. The third level of the trigger is implemented with a PC farm with about 300 CPUs.

The delay necessary to make a trigger decision is achieved by storing detector readout information in a storage pipeline.

A set of requirements that an event has to fulfill at Level 1, Level 2 and Level 3 constitutes a trigger path. Requiring that an event be accepted through a well defined trigger path eliminates volunteer events. A volunteer event is an event which passed a higher level (L2, L3) trigger requirement but did not pass the preceding lower level (L1, L1/L2) trigger

requirement. The CDF II trigger system implements about 100 trigger paths. An event will be accepted if it passes the requirements of any one of these paths.

3.10.1 Level 1 Trigger

At Level 1, for every Tevatron clock cycle, the event is moved up one slot in the pipeline. By the time it reaches the end of the pipeline, the trigger will have reached a decision whether to accept or reject this event. If the event is accepted, its information will be sent to the higher level of the trigger. Otherwise, the event is simply ignored.

The front-end electronics of all detectors is fitted with a synchronous pipeline, 42 events deep, where the entire data regarding each event is stored for 5544 ns. Meanwhile, part of the data is examined in a first layer of dedicated, synchronous, highly parallel hardware processors:

- XFT [118], the eXtremely Fast Tracker, which reconstructs tracks on the transverse plane of the COT to propagate them to the calorimeters and muon chambers;
- the Calorimeter Trigger, which detects electron and photon candidates, jets, total transverse energy, and missing transverse energy;
- the Muon Trigger, which matches XTRP (eXTRaPolation module) tracks [119] to stubs in the muon chambers.

Since the Level 1 buffer has 42 slots, the time allocated for making a trigger decision is about 5 μs. The rejection factor after Level 1 is about 150, so the Level 1 accept rate is below 40 kHz.

3.10.2 Level 2 Trigger

Events matching the requirements of the Level 1 are downloaded into one of four asynchronous event buffers, and further analized by a second set of hardware processors. This allows for 20 μs for the trigger decision. The Level 2 rejection factor is again around 150, and the accept rate is around 300 Hz.

The Level 2 is able to reconstruct calorimeter clusters, and to use the maximum shower detector information. A novelty in hadronic physics, it is also able to use the Silicon Vertex Detector: the Silicon Vertex Trigger (SVT) [120] uses XFT tracks as an input and tries to reconstruct tracks based on silicon hits in the neighborhood of an XFT track. This technique significantly reduces the number of candidate hits, hence allows very fast reconstruction, while achieving a resolution comparable with the full tracking reconstruction. The SVT is able to identify tracks that are significantly displaced from the beam location, hence selecting heavy flavor enriched events. Figure 3.17 shows what information is available to Level 1 and Level 2.

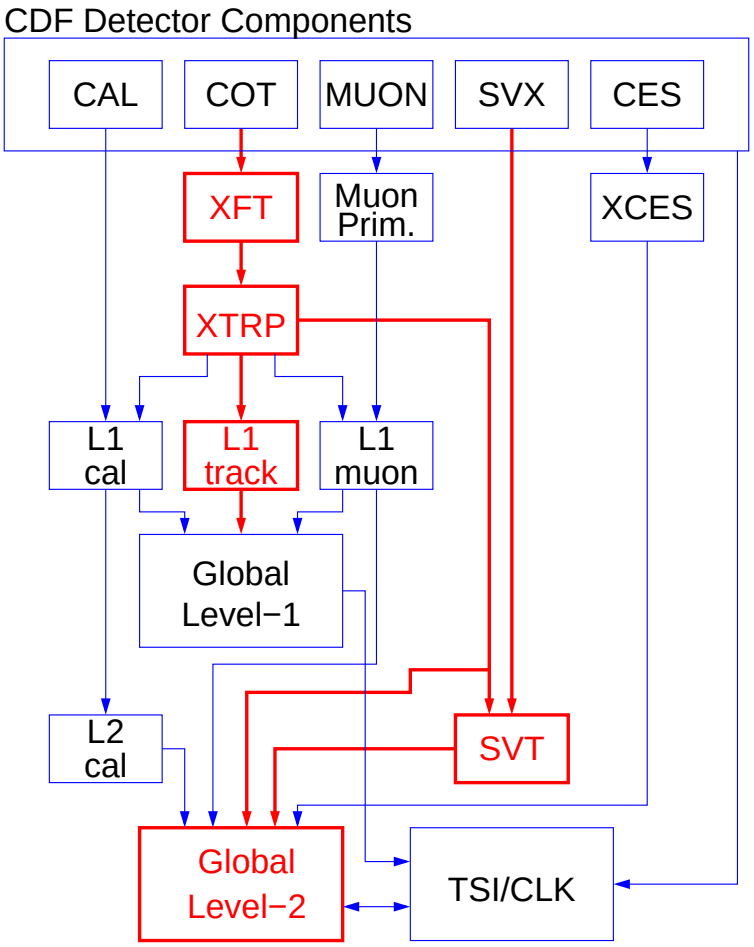

Figure 3.17: Block diagram of the Level 1 and Level 2 trigger paths.

3.10.3 Level 3 Trigger

Finally, after being accepted by the Level 2, the entire event data is read out and loaded into a Linux PC farm, where the event is fully reconstructed in software. The Level 3 reconstruction program is almost fully written in C++, using object-oriented techniques. After an event is reconstructed, it is sent to an event counter, where its characteristics are histogrammed; if the event passes the Level 3 cuts, it is also permanently stored to tape.

Every CPU in the farm provides a processing slot for one event. With roughly 300 CPUs, and an input rate of $\sim$ 300 Hz, this allocates approximately 1 second to do event reconstruction and reach a trigger decision. As a result, nearly offline quality event reconstruction is available at the third level of triggering. The Level 3 rejection rate is about 10, resulting in 30 events/sec being accepted by the Level 3 trigger and written to tape.

Fig. 3.18 shows the implementation of the Level 3 farm. The detector readout from the Level 2 buffers is received via an Asynchronous Transfer Mode (ATM) switch and distributed to 16 "converter" node PCs , shown in Fig. 3.18 in light blue. The main task of these nodes

is to assemble all the pieces of the same event as they are delivered from different subdetector systems through the ATM switch. The event is then passed via an Ethernet connection to a "processor" node, of which there are about 150 in the farm and are shown in Fig. 3.18. Each processor node is a separate dual-processor PC. Each of the two CPUs on the node process a single event at a time. The Level 3 decision is based on near-final quality reconstruction performed by a "filter" executable. If the executable decides to accept an event, it is then passed to the "output" nodes of the farm. These nodes send the event onward to the Consumer Server / Data Logger (CSL) system for storage first on disk, and later on tape.

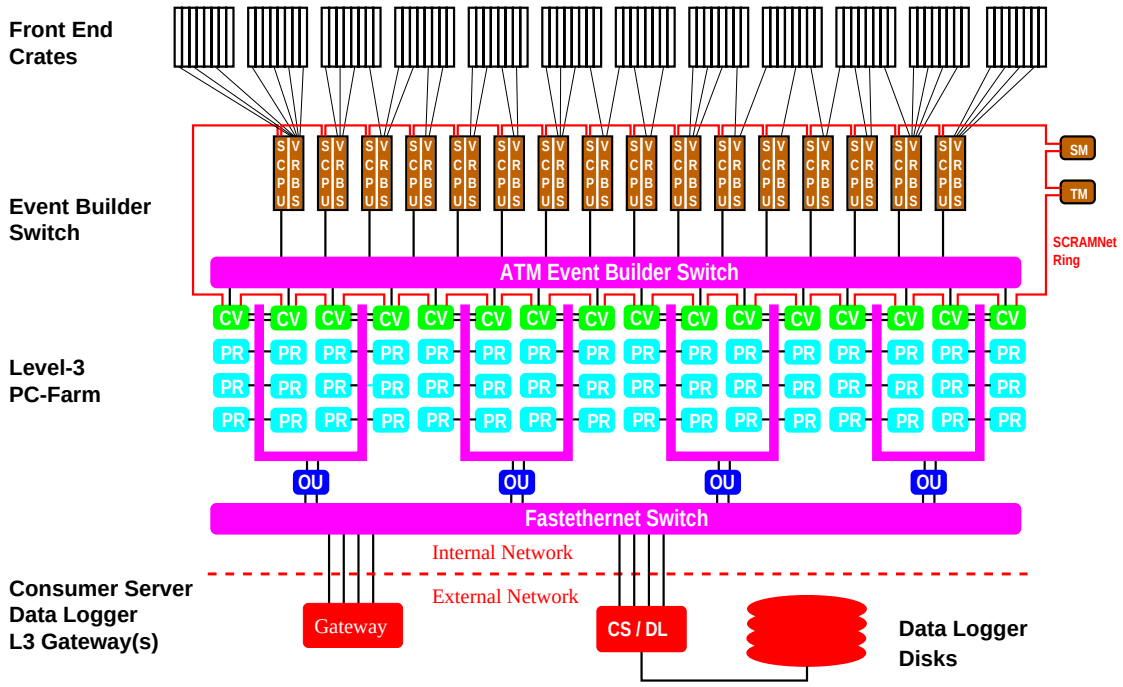

Figure 3.18: Principle of Event Building and Level 3 Filtering. Data from the front end crates is prepared by Scanner CPUs (SCPU) and fed into the ATM switch. On the other side of the switch, converter nodes (CV) assemble events and pass them to processor nodes (PR). Accepted events are passed to output nodes (OU) which send them to the Consumer Server and Data Logging systems (CS/DL).

3.10.4 Online Monitoring

The CDF detector consists of many detector subsystems and runs a high rate large bandwidth data transfer environment. To take data with high efficiency and high quality, it is necessary to quickly spot problems with one of these subdetectors in real time. Multiple event monitor programs are attached to the DAQ system [121, 122]. The online monitoring programs are called Consumers, where a Consumer is defined as a process which receives events from Consumer Server Logger (CSL) in real time. CSL sends the data to the com-

puter center where they are written to tape and forwards copies of a subset of the data to the online monitoring programs. Figure 3.19 shows a schematic view of the CDF online monitoring system (Consumer Framework). The task of the Consumers is to analize and monitor the event data and to make histograms and tables. These results could be viewed by the display browser via a server in real time. Results of the monitor are also stored as data files periodically during a run, and also archived systematically. The display browser provides a GUI to view the online monitored results, while also providing some basic utilities to do comparisons with previously stored results. By separating the two tasks of monitoring and displaying, we remove CPU bound associated with displaying graphics from the machine which runs the consumers. During the data taking, multiple consumer processes run in parallel, receiving event data with the desired trigger types from the CSL. Communication between consumers and run control, which controls the overall CDF DAQ system, is handled by the error Receiver. Severe errors detected by a consumer monitor program are forwarded to run control to take necessary actions. The state manager watches the state of consumers.

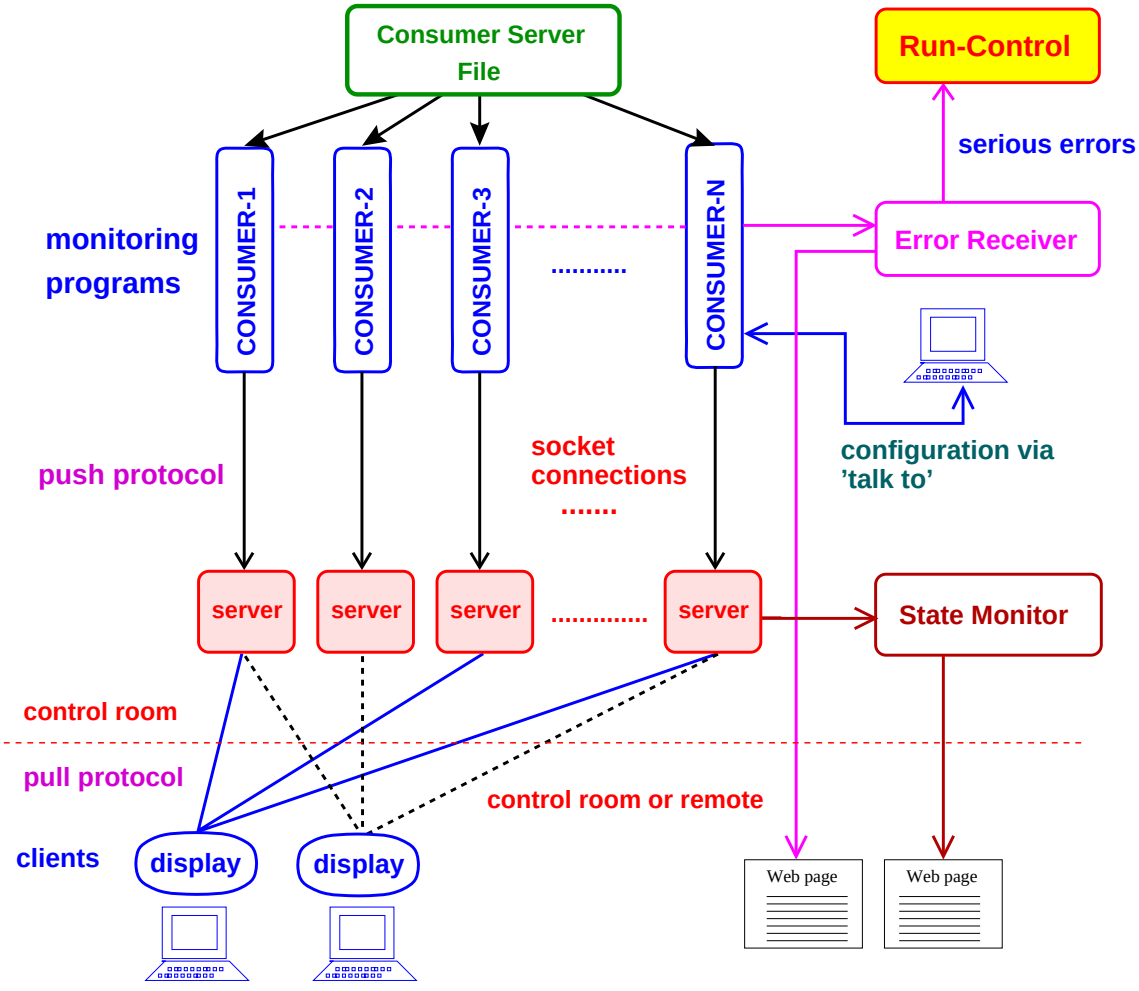

Figure 3.19: Design of the CDF online consumer framework.

Chapter 4

Data Sample and Event Reconstruction

The data used in this analysis are from $p\bar{p}$ collisions at a center-of-mass energy of $\sqrt{s} = 1.96$ TeV recorded by the CDF II detector between March 2002 and September 2004. The data sample has been collected by triggers based on the selection of a high transverse momentum lepton (electron or muon). The total integrated luminosity is 318 pb^{-1} for CEM electron and CMUP muon candidates, and 305 pb^{-1} for CMX muon candidates. Briefly, we discuss the trigger and lepton identification requirements, the reconstruction of jets, and the missing transverse energy, $\not\!\!E_T$.

CDF has a three-level trigger system to filter events from a 2.5 MHz beam crossing rate down to 60 Hz for permanent storage. The first two levels of triggers are special purpose hardware and the third consists of a farm of computers.

The first trigger level (L1) reconstructs charged particle tracks in the COT r-ϕ projection using a hardware track processor called the Extremely Fast Tracker (XFT) [123]. The L1 electron trigger requires a XFT track with $p_T > 8$ GeV/c matched to an EM calorimeter tower with $E_T > 8$ GeV and with a ratio of hadronic-to-electromagnetic energy less than 0.125. The L1 muon trigger requires an XFT track with $p_T > 4$ GeV/c matched to a muon track segment with $p_T > 6$ GeV/c from the CMU and CMP chambers or a track with $p_T > 8$ GeV/c matched to a muon track segment with $p_T > 6$ GeV/c in the CMX chambers.

The second level (L2) electron trigger requires the XFT track found at L1 to be matched to a cluster of energy in the central EM calorimeter with $E_T > 16$ GeV. The cluster adds the energy of the neighboring trigger towers with $E_T > 7.5$ GeV to the original L1 trigger tower. A trigger tower consists of two calorimeter towers. The L2 muon trigger accepts events passing L1.

The third trigger level (L3) is a farm of Linux computers which perform on-line event reconstruction, including 3D charged particle reconstruction. The L3 electron trigger requires a track with $p_T > 9$ GeV/c matched to an energy cluster of three adjacent towers in pseudo-rapidity in the central EM calorimeter with $E_T > 18$ GeV, consistent with the shower profile expected from test beam electrons. The L3 muon trigger requires a track with $p_T > 18$ GeV/c matched to a track segment in the muon chambers within 10 cm in the $r - \phi$ view

and, for CMU and CMX muons only, within 20 cm in the z view. The efficiency of these triggers is measured using $W^{\pm} \to e^{\pm}\nu$ and $Z \to \mu^{+}\mu^{-}$ data (the method is described in Ref. [124]) and is found to be (96.2 ± 0.6)% for CEM electrons, and (90.8 ± 0.5)% and (96.5 ± 0.4)% for CMUP and CMX muons respectively, for electrons and muons passing through the fiducial volume of these detectors.

4.1 Track and Primary Vertex Reconstruction

The trajectories of charged particles are found (in a first approximation) as a series of segments in the axial superlayers of the COT. Two complementary algorithms associate the segments lying on a common circle to define an axial track. Segments in the stereo layers are associated with the axial tracks to reconstruct 3D tracks. For muons and electrons used in this analysis, COT tracks are required to have at least 3 axial and 2 stereo segments with at least 5 hits per superlayer. The efficiency for finding isolated high momentum COT tracks in the COT fiducial volume with $p_T > 10$ GeV/c is measured using electrons from $W^{\pm} \to e^{\pm}\nu$ events and is found to be (98.3 ± 0.1)%. Silicon hit information is added to reconstructed COT tracks using an "outside-in" tracking algorithm. The COT tracks are extrapolated to the silicon detector and the track is refit using the information from the silicon measurements. The initial track parameters provide a width for a search region in a given layer. For each candidate hit in that layer, the track is refit and used to define the search region into the next layer. The search uses the two best candidate hits in each layer to generate a small tree of final track candidates, and the one with the best fit χ^2 is selected. The efficiency to associate at least three silicon hits with an isolated COT track is found to be (91 ± 1)%.

The primary vertex location for a given event is found by fitting well-measured tracks to a common point of origin. At high luminosities, more than one collision can occur on a given bunch crossing. For a luminosity of $\sim 10^{32}$ cm^{-2}s^{-1}, there are ∼2.3 interactions per bunch crossing. The luminous region is long, with $\sigma_z = 29$ cm; therefore the primary vertices of each collision are typically separate in z. The first estimate of the primary vertices (x_V, y_V, z_V) is binned in the z coordinate, and the z position of each vertex is then calculated from the weighted average of the z coordinate of all tracks within 1 cm of the first iteration vertex, with a typical resolution of 100 μm. The primary vertex is determined event by event by an iterative algorithm which uses tracks around a seed vertex, defined as above, to form a new vertex. The χ^2 for all tracks relative to the new vertex is calculated, tracks with bad χ^2 are removed, and the cycle is repeated until all tracks have a good χ^2. The locus of all primary vertices defines the beamline, the position of the luminous region of the beam-beam collisions through the detector. A linear fit to (x_V, y_V) vs. z_V yields the beamline for each stable running period. The beamline is used as a constraint to refine the knowledge of the primary vertex in a given event. The transverse beam cross section is circular, with a rms width of ≈ 30 μm at $z = 0$, rising to ≈ 50 - 60 μm at $|z| = 40$ cm. The beam is not necessarily parallel nor centered in the detector.

4.2 Electron Identification

Electron reconstruction begins with a track with $p_T > 9$ GeV/c that extrapolates to a cluster of three CEM towers adjacent in pseudo-rapidity with a total $E_T > 20$ GeV. Several cuts are successively applied in order to improve the purity of the electron selection, as summarized in Table 4.1. Electron candidates passing these requirements are called tight electrons.

Table 4.1: Selection requirements for tight electrons.

Electron Variable	Cut
p_T	≥ 10 GeV/c
E_T	≥ 20 GeV
COT Axial Segments	≥ 3
COT Stereo Segments	≥ 2
Hits for Each COT Segment	≥ 5
E_{HAD}/E_{EM}	$\leq 0.055 + 0.00045 \times E$
E/p	≤ 2.0 unless $p_T \geq 50$ GeV/c
Isolation	≤ 0.1
L_{shr}	≤ 0.2
CES $\lvert\Delta z\rvert$	≤ 3.0 cm
CES $Q \times \lvert\Delta x\rvert$	$-3.0 \leq Q \times \lvert\Delta x\rvert \leq 1.5$ cm
CES χ^2_{strip}	≤ 10
Photon Conversions	Veto if $D \leq 0.2$ cm and $\Delta\cot(\theta) < 0.04$

The ratios between the hadronic and the electromagnetic cluster energies E_{HAD}/E_{EM} and between the cluster energy and the track momentum E/p are required to be consistent with an electron's energy deposition in the calorimeters. The cluster is further required to be isolated, the isolation I being defined as the ratio of the additional transverse energy in a cone of radius $R = \sqrt{(\Delta\phi)^2 + (\Delta\eta)^2} = 0.4$ around the cluster to the transverse energy of the cluster itself.

The position of the electromagnetic shower measured by the CES detector is used to define matching requirements between the extrapolated track and the cluster in the CES x and z local coordinates. In particular, a charge dependent cut in the x position is applied to take into account the different flow of energy deposited by bremsstrahlung photons emitted by an electron or a positron. In addition, the CES provides electron identification through the observed shower shape. The CES shower shape is fitted in the z view to the distribution expected for an electron, and the chisquare probability for the fit, χ^2_{strip}, is used as a cut on the shower profile. Finally, the sharing of energy between adjacent calorimeter towers is quantified by the lateral shower profile L_{shr}, which measures how close the energy distribution in the CEM towers adjacent to the cluster seed is to the electron hypothesis.

Distributions of some of these variables for high p_T lepton data and $t\bar{t}$ Monte Carlo are

shown in Figs. 4.1 and 4.2. Note that some data distributions (electron p_T and E_T and L_{shr} for instance) show a big jump just where we apply our selection cut. This is because these requirements are applied already at a trigger level. Since we do not require the simulation to pass the trigger, Monte Carlo distributions do not show this behaviour. Also note that, as shown, the distributions do not totally agree. This is something expected because they are different processes: one, the Monte Carlo, is $t\bar{t}$ signal while the second, high p_T lepton data, is dominated by W backgrounds (mainly if there is no jet requirement) and there is no top.

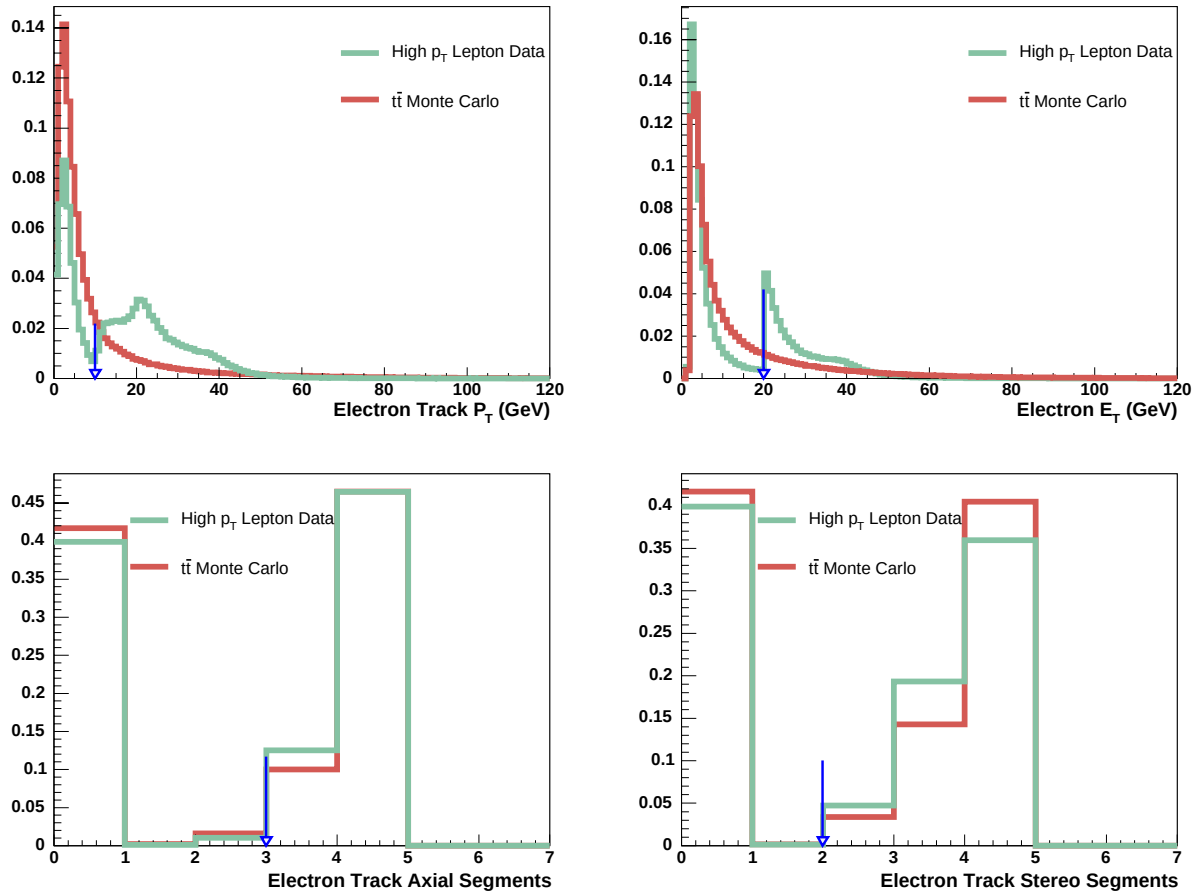

Figure 4.1: Distributions, for high p_T lepton data and $t\bar{t}$ Monte Carlo, of some of the variables used in the electron identification. From the top-left corner: transverse momentum, transverse energy, number of axial segments in the COT and number of stereo segments in the COT. The blue arrow indicates the place where the cut is applied.

Electrons from photon conversions throughout the detector material are vetoed by rejecting electron candidates if an oppositely charged track with a small distance of closest approach (D) is found. This analysis is sensitive to any loss in efficiency from the misidentification of an electron from the W boson decay as a photon conversion. Therefore, in order to

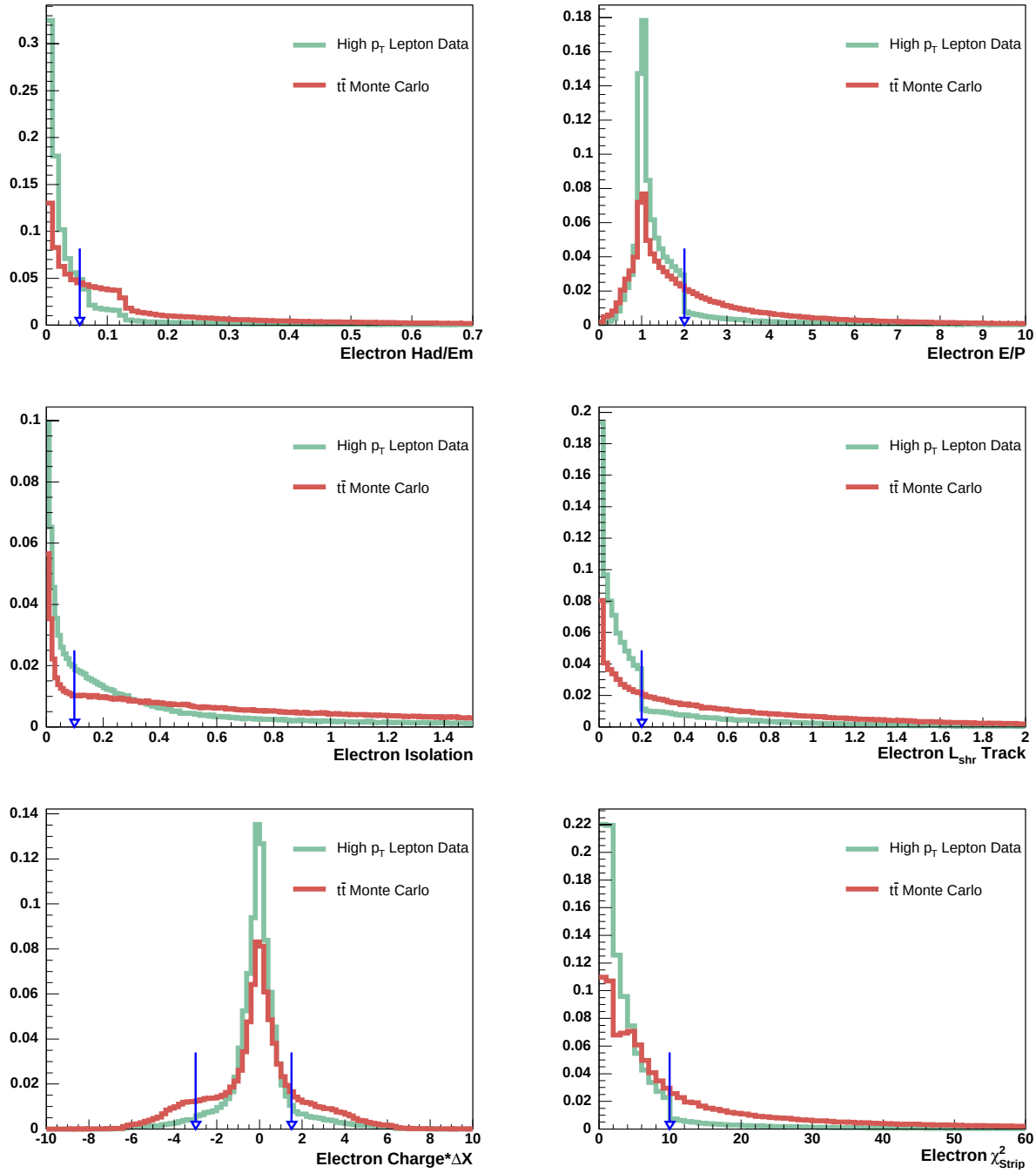

Figure 4.2: Distributions, for high p_T lepton data and $t\bar{t}$ Monte Carlo, of some of the variables used in the electron identification. From the top-left corner: fraction of hadronic versus electromagnetic energy deposited in the calorimeter and fraction of energy versus momentum, isolation, lateral shower profile, charge of the electron times ΔX and chi square probability of the fit. The blue arrow indicates the place where the cut is applied.

avoid loss of efficiency, the veto is not applied to events consistent with electrons radiating a photon that subsequently converts. The performance of this algorithm to identify electrons from photon conversions is estimated to be $(72.6 \pm 0.1)\%$ [9], where the uncertainty covers both statistical and systematic.

The efficiency of the electron selection on $t\bar{t}$ events is determined by means of Monte Carlo simulation. Studies of $Z \to e^+e^-$ processes show that a data to Monte Carlo simulation scale factor of $(99.6\ ^{+0.4}_{-0.5})\%$ is needed to correct the simulation predictions for the efficiency for CEM electron identification.

Other electron categories are defined. Candidate electrons passing all the above requirements except for the isolation cut are called loose electrons. Tracks matched to an energy deposit in the plug calorimeter ($1.2 < |\eta| < 2.0$) are called plug electrons.

4.3 Muon Identification

Muon identification starts by requiring an isolated, high momentum COT track that extrapolates to a track segment in the muon chambers. Several additional requirements are imposed in order to minimize contamination from hadrons punching through the calorimeter, decays in flight of charged hadrons and cosmic rays. Table 4.2 lists the selection requirements for candidate muons. Muon candidates passing these cuts are called tight muons.

Table 4.2: Selection requirements for tight muons.

Muon Variable	Cut
p_T	≥ 20 GeV/c
COT Axial Segments	≥ 3
COT Stereo Segments	≥ 2
Hits for Each COT Segment	≥ 5
$\lvert d_0 \rvert$	≤ 0.2 cm if no silicon hits
$\lvert d_0 \rvert$	≤ 0.02 cm if silicon hits
E_{HAD}	$\leq \max(6, 6 + 0.0280(p - 100))$ GeV
E_{EM}	$\leq \max(2, 2 + 0.0115(p - 100))$ GeV
CMU $\lvert \Delta x \rvert$	≤ 3.0 cm
CMP $\lvert \Delta x \rvert$	≤ 5.0 cm
CMX $\lvert \Delta x \rvert$	≤ 6.0 cm
Isolation	≤ 0.1
Cosmic Rays	Veto

The COT track must have $p_T \geq 20$ GeV/c, and at least 3 axial and 2 stereo segments with a minimum of 5 hits per segment. The distance of closest approach of the track to the beamline in the transverse plane, d_0, must be small in order to select prompt muons (coming from the interaction primary vertex) and reject cosmics and in-flight decays. The energy

deposition in the EM and HAD calorimeters, $E_{\rm EM}$ and $E_{\rm HAD}$, must be small as expected for the passage of a minimum ionizing particle. The distance between the extrapolated COT track and the track segment in the muon chambers, Δx, must be small in order to ensure a good match. If a track is matched to a CMU segment, a matching CMP segment is also required, and vice versa. Isolation is defined as the ratio between any additional transverse energy in a cone of radius $R = 0.4$ around the track direction and the muon p_T, and it is required to be smaller than 0.1. Cosmic rays are efficiently identified and rejected through their asynchronous track timing relative to the beam crossing time and their incoming and outgoing back-to-back track topology.

Distributions of these variables for high p_T lepton data and $t\bar{t}$ Monte Carlo simulation are shown in Figs. 4.3 and 4.4. As noted and explained in the previous Section, some distributions (muon p_T for instance) show a big jump just where we apply our selection cut and there is not a good agrement between data and simulation.

Studies of $Z \rightarrow \mu^+\mu^-$ processes show that a data to Monte Carlo simulation scale factor of $(87.4 \pm 0.9)\%$ ($(98.9 \pm 0.6)\%$) is needed to correct the simulation predictions for the CMUP (CMX) muon identification efficiency.

As for the electrons, candidate muons passing all the cuts except the isolation cut are called loose muons. A track matched to a CMU or a CMP segment only, which passes all the other cuts including isolation, is also accepted as a loose muon.

4.4 Jet Reconstruction and Corrections

The jets used in this analysis are reconstructed from calorimeter towers using a cone algorithm [125] with a radius $R \leq 0.4$, for which the E_T of each tower is calculated with respect to the z coordinate of the event. The calorimeter towers belonging to any electron candidate are not used by the jet clustering algorithm. The energy of the jets is corrected [126] for the pseudo-rapidity dependence of the calorimeter response, the calorimeter time dependence, and extra E_T from any multiple interactions.

By definition, tight jets have corrected $E_T \geq 15$ GeV and detector $|\eta| < 2.0$, whereas loose jets have corrected $E_T \geq 8$ GeV and detector $|\eta| < 2.0$. Detector η is the pseudo-rapidity of the jet calculated with respect to the center of the detector.

4.5 Missing Transverse Energy Reconstruction

The presence of neutrinos in an event is inferred by an imbalance of transverse energy in the detector. The missing transverse energy, $\not\!\!E_T$, is defined as the magnitude of $-\sum_i [E_{T,i} cos(\phi_i), E_{T,i} sin(\phi_i)]$, where $E_{T,i}$ is the transverse energy of the calorimeter tower i calculated with respect to the z coordinate of the event, ϕ_i is its azimuthal angle, and the sum is over all calorimeter towers. The $\not\!\!E_T$ is corrected by subtracting the transverse momentum of the muon track and adding back the transverse energy in the calorimeter towers traversed by the muon. Because the $\not\!\!E_T$ calculation uses all calorimeter towers, the

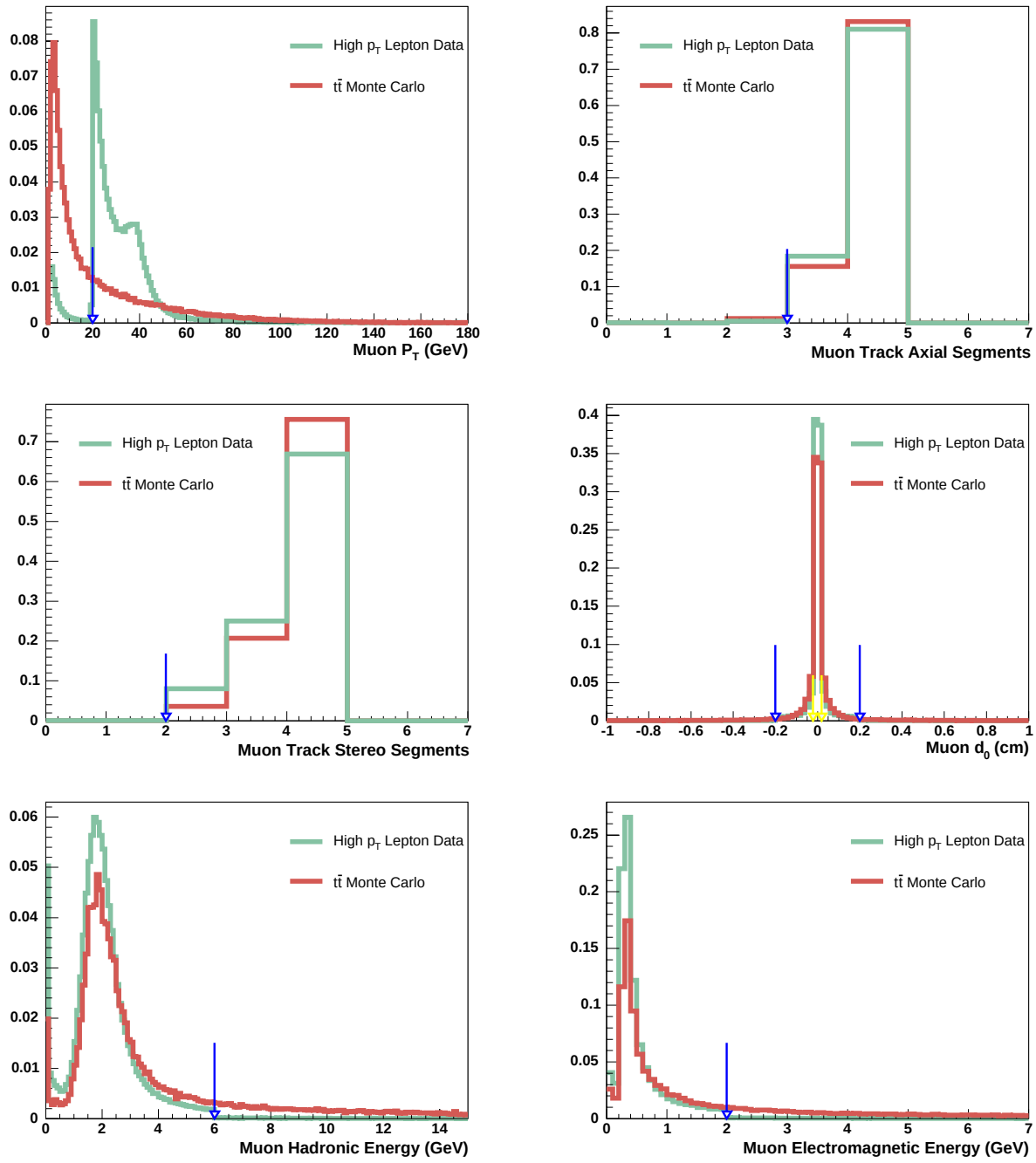

Figure 4.3: Distributions, for high p_T lepton data and $t\bar{t}$ Monte Carlo, of some of the variables used in the muon identification. From the top-left corner: transverse momentum, number of axial segments in the COT, number of stereo segments in the COT, impact parameter and energy deposited in the hadronic and electromagnetic calorimeter. The blue arrow indicates the place where the cut is applied.

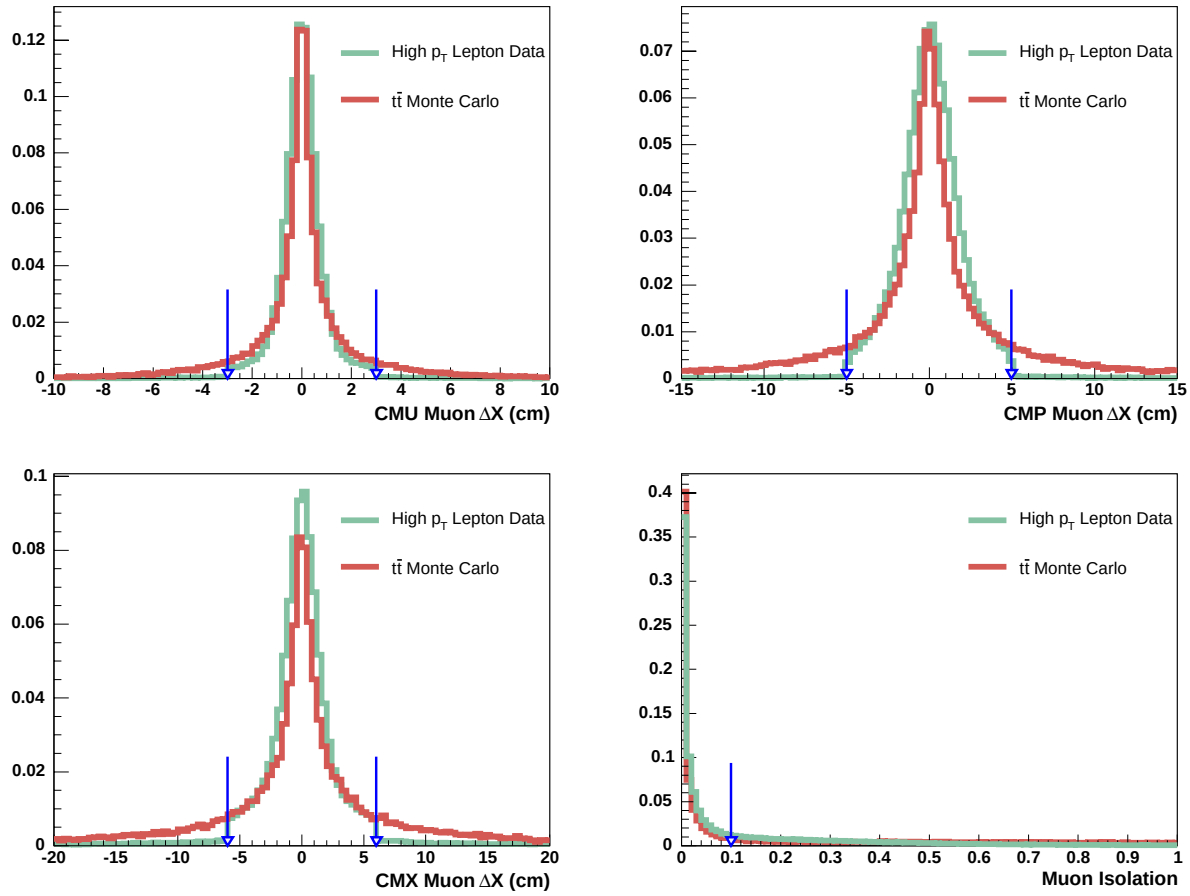

Figure 4.4: Distributions, for high p_T lepton data and $t\bar{t}$ Monte Carlo, of some of the variables used in the muon identification. From the top-left corner: Δx for CMU, CMP and CMX muons and isolation.

$\not\!\!E_T$ vector is adjusted for the effect of the jet corrections for all jets with $E_T \geq 8$ GeV and $|\eta| < 2.5$.

4.6 Monte Carlo Samples and Detector Simulation

The understanding of acceptances, efficiencies and backgrounds relies on detailed simulation of physics processes and detector response.

The detector acceptance for $t\bar{t}$ events is modeled using `PYTHIA v6.2` [127] and `HERWIG v6.4` [128]. This analysis uses the former for the final cross section estimate and the latter to estimate the systematics due to differences in the modeling of $t\bar{t}$ production and decay. These generators employ leading order matrix elements for the hard parton scattering, followed by parton showering to simulate gluon radiation and fragmentation effects. The generators are used with the `CTEQ5L` parton distribution functions [129]. Decays of b and c hadrons

are modeled using QQ v9.1 [130]. Estimates of backgrounds from W bosons produced in association with jets are derived using the ALPGEN generator [95] with parton showering provided by HERWIG. The background from electroweak processes and single top production is studied using PYTHIA.

The CDF II detector simulation reproduces the response of the detector and uses the same detector geometry database as the event reconstruction. Particle interactions through matter are performed with GEANT3 [131]. Charge deposition in the silicon detectors is calculated using a simple geometrical model based on the path length of the ionizing particle and an unrestricted Landau distribution. The drift model for the COT uses a parametrization of a GARFIELD [132] simulation with parameters tuned to match COT collider data [106]. The calorimeter simulation uses the GFLASH [133] parametrization package interfaced with GEANT3. The GFLASH parameters are tuned to test beam data for electrons and high-p_T pions and they are checked by comparing the calorimeter energy of isolated tracks in collision data to their momentum as measured in the COT. More details on the CDF II simulation can be found in Ref. [134].

Chapter 5

Jet Probability *b*-Tagging Algorithm

The jet probability b-tagging algorithm [135] is used to determine whether a jet has been produced from the hadronization process of a light parton or a heavy parton. The latter result in long-lived hadrons whose decay gives rise to tracks displaced from the primary interaction vertex. This algorithm uses tracks associated with a jet to determine the probability for these to come from the primary vertex of the interaction. The calculation of the probability is based on the impact parameters (d_0) of the tracks in the jet and their uncertainties. The impact parameter is assigned a positive or negative sign depending on the position of the track's point of closest approach to the primary vertex with respect to the jet direction, as shown in Fig. 5.1. By construction, the probability for tracks originating from the primary vertex is uniformly distributed from 0 to 1. For a jet coming from heavy flavor hadronization, the distribution peaks at 0, due to tracks from long lived particles that have a large impact parameter with respect to the primary vertex.

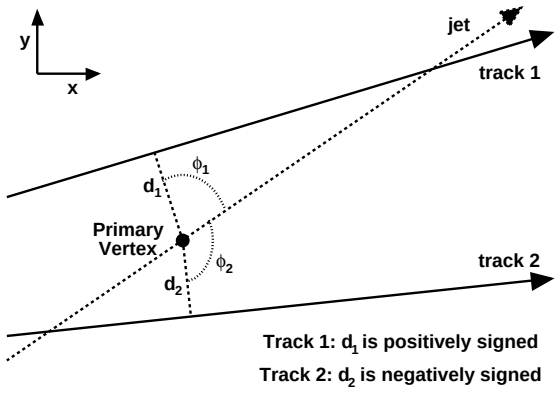

Figure 5.1: The sign of the impact parameter of a track. The impact parameter is positive (negative) if the angle ϕ between the jet axis and the line connecting the primary vertex and the track's point of closest approach to the primary vertex itself is smaller (bigger) than $\pi/2$.

The particles in a jet coming from a light parton originate at the primary vertex, but these tracks are reconstructed with a non-zero impact parameter due to the finite tracking resolution. They have an equal probability of being positively or negatively signed. Jets which originate from a heavy parton contain long lived hadrons giving rise to tracks displaced in the jet direction, which preferentially populate the positive side of the signed impact parameter distribution. The width of the negative impact parameter distribution is solely due to the tracking detector resolution, beam spot size, and multiple scattering.

The tracking resolution can be extracted from the data by fitting the negative side of the signed impact parameter distribution of tracks from prompt jets, which are the dominant component of inclusive jet data. Tracks are divided into 72 different categories according to the number and quality of SVX hits, detector η and p_T. To minimize the contribution from badly measured tracks with a large reconstructed impact parameter, the signed impact parameter significance, S_{d_0} (ratio of the impact parameter to its uncertainty), is parameterized for each track category. Tracks are fitted to a helix, and the impact parameter is corrected for beam offsets in order to take into account any displacement of the primary vertex from the nominal position. The uncertainty in the impact parameter is given by the error propagation of the uncertainties in the fit and in the beam offset correction. We parameterize the impact parameter significance for tracks satisfying the quality criteria listed in Table 5.1 that are associated with jets with $E_T > 7$ GeV and $|\eta| < 2.5$. These tracks must have $p_T > 0.5$ GeV/c, impact parameter less than 0.1 cm (in order to reject long lived K's and Λ's), three to five hits on different axial layers of the SVX, at least 20 (17) hits in the COT axial (stereo) layers, and the z position of the track must be within 5 cm of the event primary vertex. Tracks passing this selection are called jet probability tracks. The $|d_0|$ is measured with respect to the primary vertex. The event is required to have a primary vertex, and the vertex with highest sum of transverse momentum of all tracks is chosen in events which have more than one vertex.

Table 5.1: Selection criteria for tracks used by the jet probability algorithm.

Variable	Cut
p_T	$> 0.5\,\mathrm{GeV/c}$
$\|d_0\|$	< 0.1 cm
$N_{\mathrm{SVX\ axial}}$	≥ 3 and ≤ 5
$N_{\mathrm{COT\ axial}}$	≥ 20
$N_{\mathrm{COT\ stereo}}$	≥ 17
$\|z_{trk} - z_{pv}\|$	< 5 cm

Figure 5.2 shows the distribution of the impact parameter significance of tracks in an inclusive jet sample for one of the track categories, namely tracks with at least 5 good SVX hits, $p_T > 5$ GeV/c and $|\eta| < 0.6$. The negative side of this distribution is fitted with a function $R(S)$ called the resolution function, which is used to determine the probability, $P_{tr}(S_{d_0})$, that the impact parameter significance of a given track is due to the detector

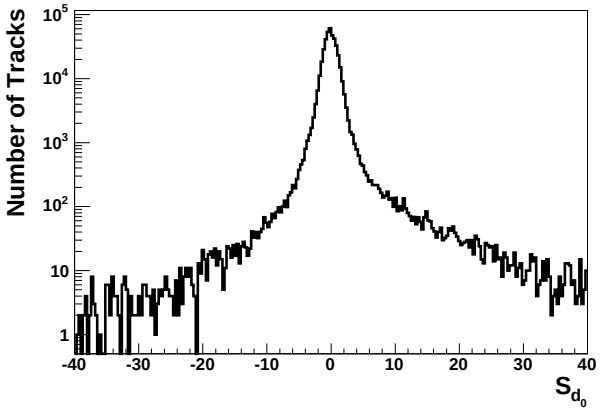

Figure 5.2: Distribution of the impact parameter significance for tracks in an inclusive jet sample with at least 5 good SVX hits, $p_T > 5$ GeV/c, and $|\eta| < 0.6$.

resolution, defined as:

$$P_{tr}(S_{d_0}) = \frac{\int_{-\infty}^{-|S_{d_0}|} R(S)dS}{\int_{-\infty}^{0} R(S)dS}. \tag{5.1}$$

The S_{d_0} distribution peaks at zero and falls quickly with increasing absolute value of $|S_{d_0}|$, but the tails are rather long. In order to improve the statistics and obtain a better fit in the tail, we use non-linear bins by transforming it to $X = \ln(|S^-_{d_0}|)$, where the minus sign indicates that only the negative part of S_{d_0} is used. Figure 5.3 shows the result of such a fit, together with the fit residues defined as (data-fit)/uncertainty, where the uncertainty is taken as the statistical uncertainty on each data point. A resolution function parameterized as the convolution of four Gaussians with means at zero is found to fit well all distributions for all 72 track categories:

$$R(S) = \sum_{i=1}^{4} \frac{p_i}{\sqrt{2\pi}\sigma_i} e^{-S^2/2\sigma_i^2}. \tag{5.2}$$

After the transformation to a logarithmic axis, the resolution function becomes

$$R(X) = \sum_{i=1}^{4} \frac{p_i}{\sqrt{2\pi}\sigma_i} e^{(X - \frac{e^{2X}}{2\sigma_i^2})} \tag{5.3}$$

and $R(X)$ is used to fit the transformed $X = \ln(|S^-_{d_0}|)$ distribution.

The jet probability P_J that a jet is consistent with a zero lifetime hypothesis is defined as

$$P_J = \prod \times \sum_{k=0}^{N_{trk}-1} \frac{(-ln \prod)^k}{k!}, \tag{5.4}$$

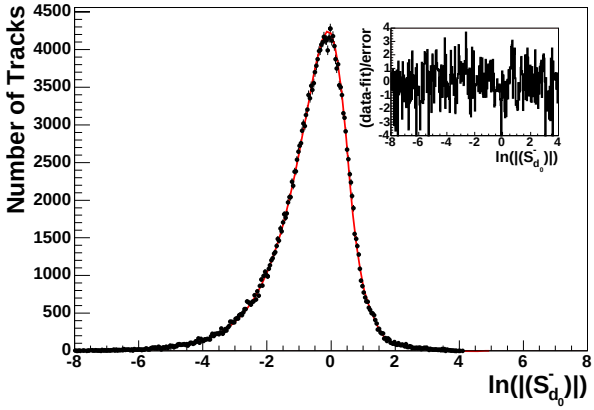

Figure 5.3: Fit to the transformed impact parameter significance, $\ln(|S^-_{d_0}|)$, where only the negative side of the S_{d_0} distribution is used. The resolution function is chosen as the convolution of four Gaussians. The inset shows the residues of the fit, (data-fit)/uncertainty.

where

$$\prod = \prod_{l=1}^{N_{trk}} P_{tr} \tag{5.5}$$

and N_{trk} is the number of jet probability tracks with positive impact parameter. Jets are required to have at least two jet probability tracks with positive impact parameter to be taggable. Both of these distributions should be uniformly distributed in the interval [0-1] for jets having only prompt tracks. Tracks with negative impact parameter are used to define a negative P_J, which is used to check the algorithm and to estimate the misidentification rate. We define positive (negative) tagged jets as those jets whose positive (negative) P_J is less than a cutoff, where we use 1% (main result) and 5% (cross check). Positive tagged jets are expected to be enriched in heavy flavor. The 1% cut was used in previous publications [135] and has similar performance to the secondary vertex tagger [7], while the loose (less restrictive) 5% cut was chosen near the point where the P_J distribution becomes flat (see Fig. 6.1). Further gain in $t\bar{t}$ selection efficiency resulting from a looser P_J cut is accompanied by an increase in background from light jets misidentified as heavy flavor (mistags). For comparison, both the 1% and 5% numbers and figures are presented together throughout the paper.

A feature of this algorithm is that the b-tagging is performed using a continuous variable instead of a discrete object like a reconstructed secondary vertex. It therefore provides a variable that allows one to move continuously along the efficiency curve and to select the optimal signal to background point for a specific analysis. Furthermore, the ability to adjust the P_J cut is a valuable tool to understand the heavy flavor content of the sample. Potentially [135], this method can be used to statistically separate b and c heavy flavor contributions. This feature is illustrated in the left plot in Fig. 5.4, where the jet probability distributions for b, c and light jets are shown. Monte Carlo simulated $2 \to 2$ parton events are used as described in Section 5.1. In the right plot, we show the jet probability distributions

observed in two different data sets of jets. The first sample is enriched in heavy flavor content by requiring the jets to contain a soft momentum electron; here, events are triggered on low p_T inclusive electrons (see Section 5.1). The second set consists of generic QCD jets selected by requiring events with at least one jet with $E_T > 50$ GeV (the Jet50 sample).

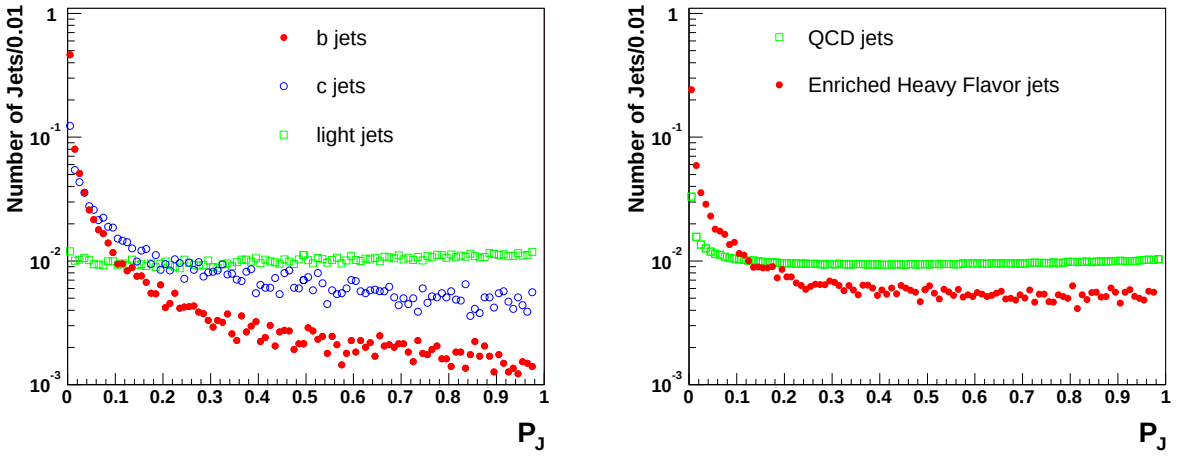

Figure 5.4: Left: jet probability distributions for jets matched to b (full circles), c (empty circles) and light (empty squares) quarks in Monte Carlo simulated events. Right: jet probability distributions for electron jets in inclusive electron data (full circles) and for generic QCD jets in Jet50 data (empty squares).

In this section we discuss the b-tagging algorithm itself, independently of the other details of this analysis.

5.1 Measurement of the Tagging Efficiency for Heavy Quark Jets

The method used to measure the jet probability tagging efficiency for heavy flavor jets is described in detail in Ref. [7]. The ideal events to study this efficiency are $b\bar{b}$ dijet events. We use a calibration data sample of jets whose heavy flavor fraction can be measured: a sample triggered on low p_T inclusive electrons which is enriched in semileptonic decays of bottom and charm hadrons. The tagging efficiency is also measured for simulated jets by using a Monte Carlo sample similar to the calibration sample. We use `HERWIG` to generate 2→2 parton events, which are passed through a filter requiring an electron with $p_T > 7$ GeV/c and $|\eta| < 1.3$. Events passing this filter are processed using the detector simulation described in Section 4.6. Electrons are identified using a selection similar to that described in Section 4.2, except that they are required to be non-isolated and have a lower energy threshold ($E_T > 9$ GeV and track $p_T > 8$ GeV/c). The heavy flavor content of the sample is

further enhanced by requiring two jets in the event, an "electron jet", presumed to contain the decay products of a heavy flavor hadron, and an "away jet". The electron jet must have $E_T > 15$ GeV and be within 0.4 of the electron direction in η-ϕ space. The away jet is required to have $E_T > 15$ GeV and $|\eta| < 1.5$, and it must be approximately back-to-back with the electron jet ($\Delta\phi_{e-j} > 2$ rad). If the fraction of electron jets containing heavy flavor for which the away jet is tagged (F^a_{HF}) is known, and if there were no prompt jets misidentified as b-jets, the efficiency to tag a heavy flavor jet containing an electron would be given by

$$\epsilon = \frac{N^{e+}_{a+}}{N_{a+}} \cdot \frac{1}{F^a_{HF}}, \tag{5.6}$$

where N^{e+}_{a+} is the number of events for which both the electron jet and the away jet are positively tagged, and N_{a+} is the total number of events for which the away jet is positively tagged. Since light jets can be tagged as well, we correct for this effect by subtracting the number of negative tags. We define the positive tag excess for events with a positive or negative tag in the away jet as

$$\Delta_{a+} = N^{e+}_{a+} - N^{e-}_{a+} \tag{5.7}$$
$$\Delta_{a-} = N^{e+}_{a-} - N^{e-}_{a-} \tag{5.8}$$

where, for example, N^{e-}_{a+} is the number of events where the electron jet is negatively tagged and the away jet is positively tagged. The tagging efficiency for heavy flavor jets containing an electron is then given by

$$\epsilon = \frac{\Delta_{a+} - \Delta_{a-}}{(N_{a+} - N_{a-})} \cdot \frac{1}{F^a_{HF}}. \tag{5.9}$$

Since events with an electron jet and a tagged away jet are mostly due to heavy flavor pair production, one expects F^a_{HF} to be close to unity. This number is less than 1.0 due to events in which the away jet is mistagged or contains heavy flavor due to gluon splitting or flavor excitation, and the electron is either a jet misidentified as electron or part of a photon conversion pair. If P denotes the probability to positively tag the away jet in an event where the electron jet is a light jet, then F^a_{HF} is given by

$$F^a_{HF} = 1 - P(1 - F_{HF}), \tag{5.10}$$

where $F_{HF} = F_b + F_c = F_b \cdot (1 + F_{c/b})$ denotes the total heavy flavor fraction of electron jets. Here F_b and F_c are the total b and c fractions of electron jets, respectively, and $F_{c/b}$ is the c to b fraction ratio. We estimate P using identified conversions as

$$P = \frac{\frac{N^{a+}_c - N^{a-}_c}{N_{a+} - N_{a-}} - \epsilon'_c}{\frac{N_c}{N} - \epsilon'_c}, \tag{5.11}$$

where N is the number of events passing the selection, $\epsilon'_c = \frac{N^{e+}_c - N^{e-}_c}{N_{e+} - N_{e-}}$, and the c subscript refers to events where the electron was identified as a conversion. A full derivation of this

expression can be found in Ref. [7]. Two methods are used to measure the b-fraction, F_b, of the electron jets. The first method is to reconstruct $D^0 \to K^-\pi^+$ decays within the electron jet and use the invariant mass sidebands to subtract background. The second method involves searching for secondary muons within the electron jet resulting from cascade $b \to c \to l\nu q$ decays using the same-sign rate to estimate the background. The contribution from charm, $F_{c/b}$, is determined from Monte Carlo simulation to be $F_{c/b} = 0.61 \pm 0.10$. For inclusive electron data we measure $F_{HF} = 0.259 \pm 0.064$ and $F^a_{HF} = 0.71 \pm 0.05$.

The efficiencies to tag a taggable heavy flavor jet with $E_T > 15$ GeV in data are summarized in Table 5.2 for $P_J < 1\%$ and 5%. The ratio of data efficiency to Monte Carlo simulation efficiency is called the tagging scale factor (SF). The uncertainties shown are statistical and systematic, which are described below.

Table 5.2: Efficiency to tag a taggable heavy flavor electron jet in data and the tagging scale factor (SF) for jet probability cuts of 1% and 5%.

	$P_J < 1\%$	$P_J < 5\%$
ϵ (Data)	0.258 ± 0.011	0.334 ± 0.016
SF	0.817 ± 0.07	0.852 ± 0.072

It is crucial to understand the tagging efficiency and scale factor dependences on the jet E_T in order to characterize the jet probability algorithm performance. The E_T dependence observed in the inclusive electron sample is shown in Fig. 5.5 and 5.6 for the tagging efficiency and scale factor respectively. Due to the lack of statistics at high jet E_T, we repeat the study using two samples of high energy jets selected by requiring events with at least one jet with $E_T > 20$ GeV (the Jet20 sample) or with $E_T > 50$ GeV (the Jet50 sample).

The absolute value of the SF can not be extracted because of the unknown content of heavy flavor in these samples. However, since the variations of heavy flavor fraction are relatively small over a large range of E_T, we can still estimate the E_T dependence of the scale factor from the E_T dependence of the ratio of positive tag excess between data and Monte Carlo simulation. Table 5.3 shows the results of a linear fit of the tagging scale factor to the jet E_T in the inclusive electron, Jet20 and Jet50 samples. The combined estimate of

Table 5.3: Summary of the scale factor *vs.* E_T slope measurements in various samples.

Sample	$P_J < 1\%$	$P_J < 5\%$
Inclusive Electron	-0.0082 $\pm$ 0.0037	-0.0081 $\pm$ 0.0044
Jet 20	-0.0008 $\pm$ 0.0019	-0.0028 $\pm$ 0.0024
Jet 50	0.0005 $\pm$ 0.0008	0.0005 $\pm$ 0.0009
Weighted Average	-0.00002 $\pm$ 0.00070	-0.00020 $\pm$ 0.00072

the slopes is found to be consistent with a flat E_T dependence of the scale factor both when

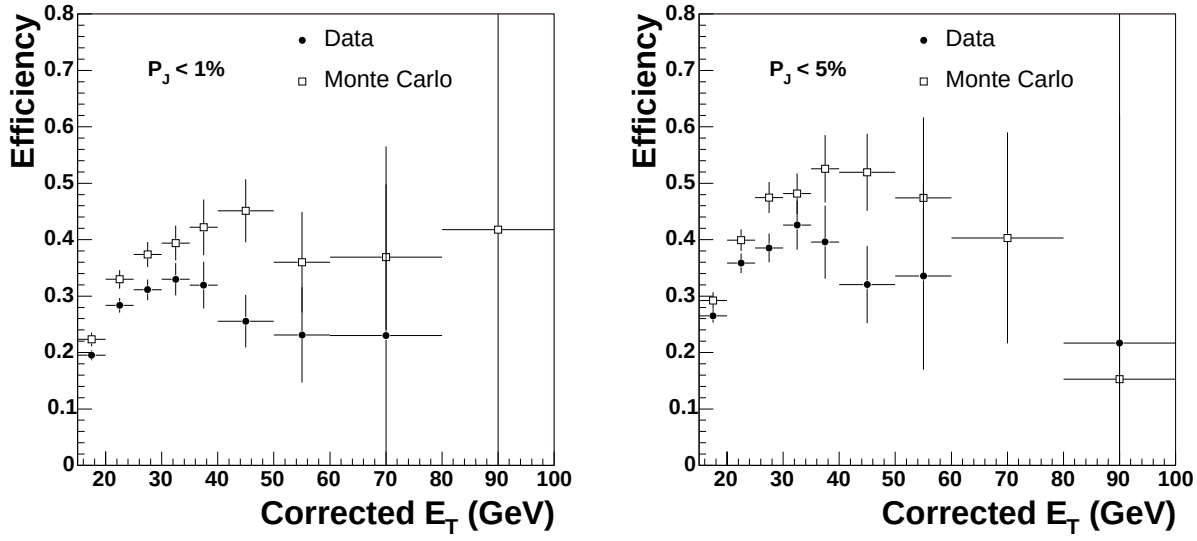

Figure 5.5: Efficiency to tag a heavy flavor jet as a function of corrected jet E_T in data and Monte Carlo simulation for 1% (left) and 5% (right) jet probability cut values.

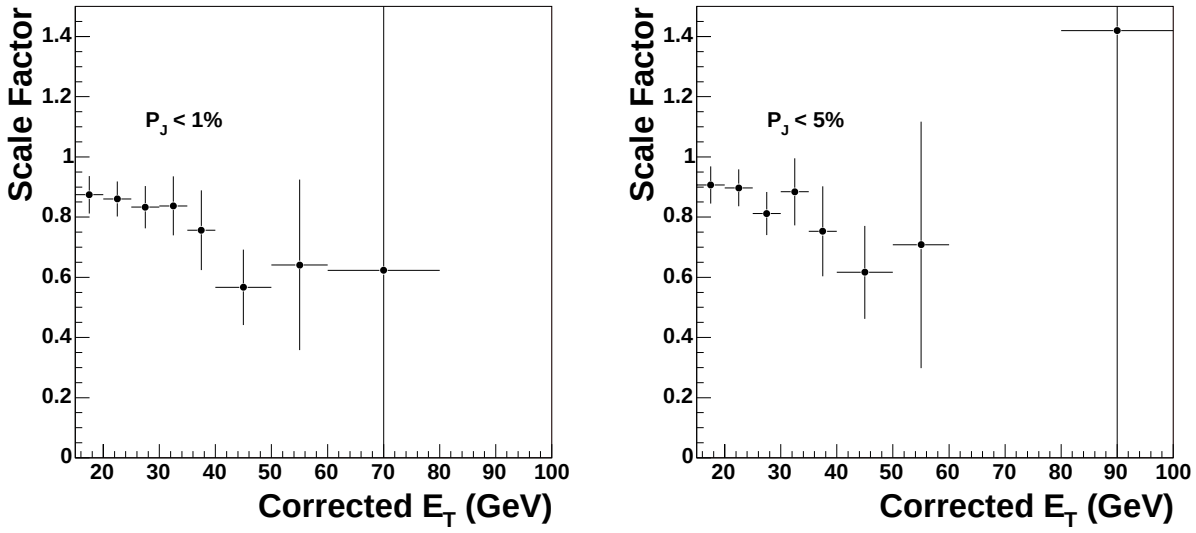

Figure 5.6: The scale factor (SF) as a function of corrected jet E_T for 1% (left) and 5% (right) jet probability cut values.

a P_J cut of 1% and 5% is applied. Based on these results, we conclude that the scale factor measured in the inclusive electron sample is valid at any E_T.

Different sources of systematic uncertainty in the determination of SF have been considered. An uncertainty on the value of F_b, determined from the rate of $D^0 \to K\pi$ decays,

comes from the branching ratio $BR(B \to l\nu D^0 X)$. A factor 1.131 ± 0.070 is used to normalize the Monte Carlo simulation prediction to the PDG [136] value. The uncertainty includes both the PDG branching ratio uncertainty and the Monte Carlo simulation statistical error. Another uncertainty on F_b comes from the difference in D^0 reconstruction efficiency, ϵ_{D^0}, between data and Monte Carlo simulation. This uncertainty is derived by studying the efficiency of reconstruction for simulated $D^0 \to K\pi$ decays embedded into data events, and is found to be 10%. There is an additional uncertainty due to the assumption of symmetry between negative tags and positive mistags implicit in the derivation of Equation 5.9. The effect of a mistag asymmetry is estimated by scaling the subtracted negative tags by different factors ranging from 0 to 2 (0.4 to 1.4) for 1% (5%) jet probability cuts, and an uncertainty of 7% is conservatively derived on the tagging scale factor due to this effect. Final estimates for jet probability tagging efficiencies and scale factors are summarized in Table 5.2.

We do not measure the tagging scale factor for c jets. We assume a common scale factor for jets from b and c quarks and we increase the uncertainty for a c quark scale factor by 100% to take into account additional uncertainties due to this assumption.

These results have been checked using an alternative method which does not require knowledge of the heavy flavor fraction, F_{HF}, as an input. Two independent measurements are used to solve directly for the scale factor, and the results are in good agreement with our double tag method. This method is described in detail in Appendix A.

5.2 Measurement of the Mistag Rate

An important ingredient of any analysis which uses heavy flavor tagging is the background from light quark or gluon jets incorrectly tagged as heavy flavor. The probability of (positively) tagging a light jet (the "mistag rate") is closely related to the negative tag rate. We remind the reader that a positive (negative) P_J is calculated using positively (negatively) signed impact parameter tracks, and a jet which has positive (negative) P_J smaller than a certain cut is said to be positively (negatively) tagged. It is assumed that the negative tags are due to detector resolution effects only, while the positive tag rate has an additional contribution from real heavy flavor in the jets. Under this assumption, the mistag rate is equal to the negative tag rate, although in reality there is also a small contribution from heavy flavor jets to the negative tag rate and there are contributions from K's, Λ's and nuclear interactions with the detector material to the positive tag rate. These effects are considered later in Section 5.2.1.

Since the tag rate has a considerable dependence on jet kinematics, it is parameterized as a 6 dimensional tag rate matrix, or look-up table, of the transverse energy E_T of the jet, the number of jet probability tracks in the jet N_{trk}, the sum of the transverse energy of all jets in the event $\sum E_T^{jet}$, the η of the jet computed with respect to the center of the detector, the z vertex position z_{vtx} and the ϕ of the jet. The tag rates are obtained from four inclusive jet samples selected by requiring the E_T of the most energetic jet in the event to be greater than 20, 50, 70 or 100 GeV respectively. For a 1% (5%) P_J cut, the overall negative tag rate is $(1.22 \pm 0.08)\%$ $((5.30 \pm 0.25)\%)$, while the overall positive tag rate is $(3.54 \pm 0.18)\%$

($(9.20 \pm 0.26)\%$). Overall tag rates depend on the sample, which is why the tag rates are parameterized as a function of different variables. Figure 5.7 shows the negative tag rates for $P_J < 1\%$ and $P_J < 5\%$ as a function of the jet E_T and pseudo-rapidity. The bands represent the total uncertainty.

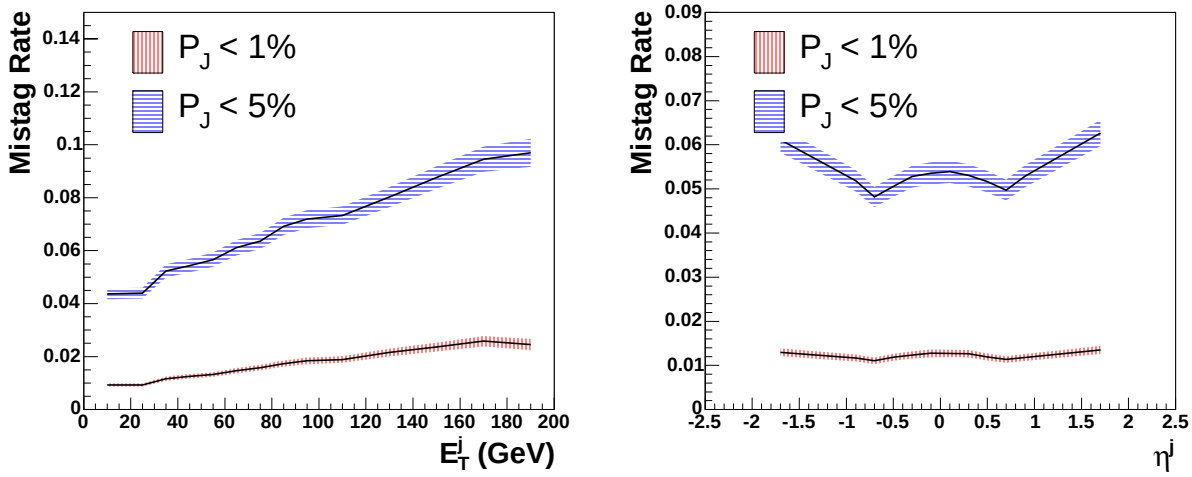

Figure 5.7: Mistag rate for jet probability cuts of 1% and 5% as a function of jet E_T (left) and jet pseudo-rapidity (right) in inclusive jet data sample. The bands represent the statistical and systematic uncertainties added in quadrature.

We estimate the systematic uncertainties by comparing the observed and predicted tag rates in different data samples. We apply tag rate matrices, constructed using different inclusive jet subsamples, to different datasets. Results are shown in Table 5.4 for a P_J cut of 1%. The largest deviation between observed and predicted tag rates across the different jet samples is taken as the systematic uncertainty due to the sample dependence of the matrix. In order to account for any possible bias due to the trigger selection, we apply the matrix separately to trigger and non-trigger jets. A trigger jet is defined as the jet closest in η-ϕ space to the level 2 cluster that fired the trigger. We also apply a matrix built with a high statistics sample of Jet20 events, to the Jet50 sample which has several jets below the trigger threshold of 50 GeV. Also considered is a sample selected by requiring at least four jets with $E_T > 15$ GeV and $\sum E_T^{jet} > 125$ GeV. These events are expected to give a reasonable estimate of the systematic uncertainty because of the higher jet and track multiplicities. Furthermore, this sample is not used to build the matrix, making it sensitive to any additional sources of systematic uncertainty. Figure 5.8 compares the observed and predicted tag rates in the $\sum E_T^{jet}$ sample as a function of jet E_T. The total systematic uncertainty on the overall tag rates is conservatively taken as the sum in quadrature of the $\sum E_T^{jet}$, Jet20 to Jet50, and the largest of the trigger and sample contributions. Table 5.5 summarizes the relative uncertainties on the overall tag rates for P_J cuts of 1% and 5%. The total relative uncertainty is 5.0% (2.8%) for positive tag rate and 6.7% (4.7%) for negative tag rate for a P_J cut of 1% (5%).

Table 5.4: Ratios of observed to predicted rates of positive and negative tags when a P_J cut of 1% is applied. The first column specifies the sample used to build the matrix, while the second column reports the sample used to compute the rates. All(even)[odd] means that all(only even event number)[only odd event number] events are used. The errors shown are statistical only.

Matrix	Sample	Obs./Pred. Pos. Tag Rate Ratio	Obs./Pred. Neg. Tag Rate Ratio
Inc. Jet Even	Inc. Jet Odd	0.997±0.002	0.999±0.003
Inc. Jet Even	Jet20 Odd	0.987±0.003	0.970±0.006
Inc. Jet Even	Jet50 Odd	0.991±0.003	0.998±0.006
Inc. Jet Even	Jet70 Odd	0.997±0.004	0.996±0.006
Inc. Jet Even	Jet100 Odd	0.989±0.003	1.029±0.005
Jet20 All	Jet50 All	1.020±0.003	1.044±0.008
Inc. Jet Even	Trig. Jet Odd	0.976±0.002	0.978±0.004
Inc. Jet Even	Non trig. Jet Odd	1.028±0.003	1.028±0.005
Inc. Jet All	$\sum E_T^{jet}$ All	1.037±0.002	0.966±0.003

Table 5.5: Total relative uncertainties on the overall positive and negative tag rates. Different tag rate matrices are applied to orthogonal samples of jets as shown in Table 5.4, and the total uncertainty is taken as the sum in quadrature of the most relevant contributions. Sample refers to the largest uncertainty from lines 2 to 5 in Table 5.4.

P_J cut	Statistical	Trigger	$\sum_j$	Jet20→Jet50	Sample	TOTAL
Pos. $P_J < 1\%$	0.11%	2.4%	3.7%	2.0%	1.3%	5.0%
Neg. $P_J < 1\%$	0.25%	2.2%	3.4%	4.4%	3.0%	6.7%
Pos. $P_J < 5\%$	0.07%	1.5%	1.2%	1.6%	1.2%	2.8%
Neg. $P_J < 5\%$	0.09%	1.3%	2.4%	3.1%	2.2%	4.7%

5.2.1 Mistag Asymmetry

The rate of negatively tagged jets does not reflect the rate of positive mistags of light jets because of residual lifetime effects from Λ's and K's or interactions with the detector material. Corrections for these effects are determined by studying the flavor composition of tagged jets in data.

The set of jet probability tracks inside a tagged jet is used to build a variable sensitive to the flavor content of the jet itself. The relative contributions from heavy and light partons to data are determined by fitting the distribution of this variable for tagged jets in data to Monte Carlo simulation templates for b, c and light jets. For data, a sample selected by requiring a jet with $E_T > 50$ GeV at the trigger level is used. For Monte Carlo simulation distributions, `HERWIG` is used to generate $2 \to 2$ processes with an outgoing parton $p_T > 40$ GeV/c. We perform the fit using six different variables, the maximum impact parameter d_0 of the tracks in the jet, the maximum impact parameter significance S_{d_0} of the tracks in the jet, the mass

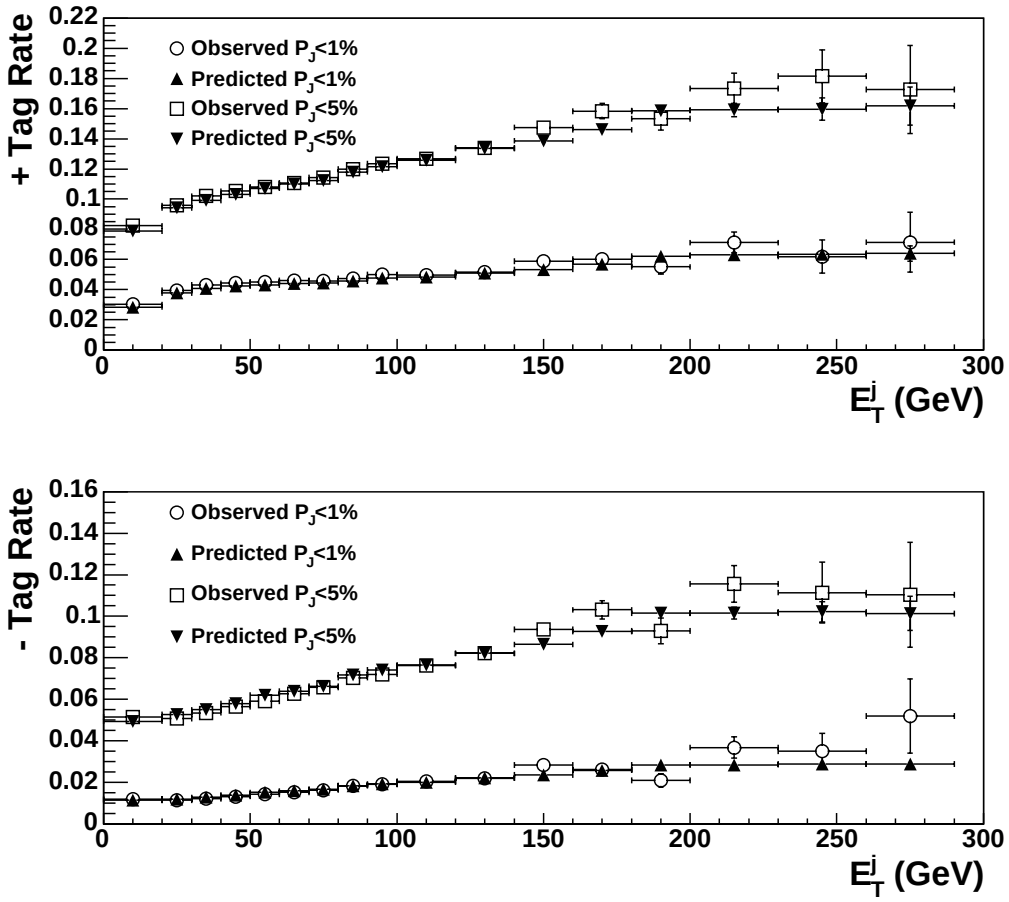

Figure 5.8: Observed positive (top) and negative (bottom) tag rates as a function of E_T for events in $\sum E_T$ data *vs.* prediction from the matrix built with events in inclusive jet data. The two curves correspond to P_J cuts of 1% and 5%.

of the system of tracks with $|d_0| > 0.01$ cm and $S_{d_0} > 2$, and the transverse momentum (P_T^{rel}) with respect to the jet direction of the system of tracks with $|d_0| > 0.01$ cm and $S_{d_0} > 2$.

The fit is made more robust by fitting the positive excess only, for which the distributions for negative tags are subtracted from the positive side. This removes contribution to the mistags due to detector resolution, which could be simulated poorly. The number of negative tags obtained for b, c and light jets in Monte Carlo simulation is normalized to the total number of negative tags found in data. From the fit, the fractions of b, c and light jets in data are obtained; thus the ratio of positive to negative tags from light jets, β.

Figure 5.9 shows the result of the fit of the positive tag excess in data to Monte Carlo templates of the maximum impact parameter of the tracks contained within b, c and light tagged jets. A P_J cut of 1% is used. It should be noted that the c/b ratio gets a contribution

from the c/b tagging efficiency ratio of about 0.2. The observed rise of light jets is the result of the fact that tags for light jets are usually due to one large impact parameter track. Table 5.6 summarizes the results of the mistag asymmetry measurement with the six variables chosen for $P_J < 1\%$ and 5%. As a final estimate of the mistag asymmetry, we take the average of the six measurements and assign the maximum difference between the average and each single determination as the uncertainty. The results are 1.56 ± 0.14 and 1.27 ± 0.17 for P_J cuts of 1% and 5%, respectively. The asymmetry is caused by secondary interactions with the detector material and residual lifetime effects from K's and Λ's, giving an excess of positive mistags. We study the expected contribution of K's and Λ's decays to the mistag asymmetry in Monte Carlo simulated events. We find the ratio of positively to negatively tagged light jets to be 1.55 ± 0.11 (1.21 ± 0.04) for a P_J cut of 1% (5%). Uncertainties are statistical only. These results are in good agreement with our measurements on data and suggest K's and Λ's to be the main source of mistag asymmetry. The negative tag rates measured have therefore to be scaled up by the asymmetry factor in order to obtain an accurate estimate of the positive mistag rate. We repeat the measurement in bins of jet transverse energy to study the dependence of the mistag asymmetry on the jet E_T. Results are shown in Fig. 5.10. The asymmetry exhibits a small dependence with jet E_T which is taken into account to estimate the mistag background.

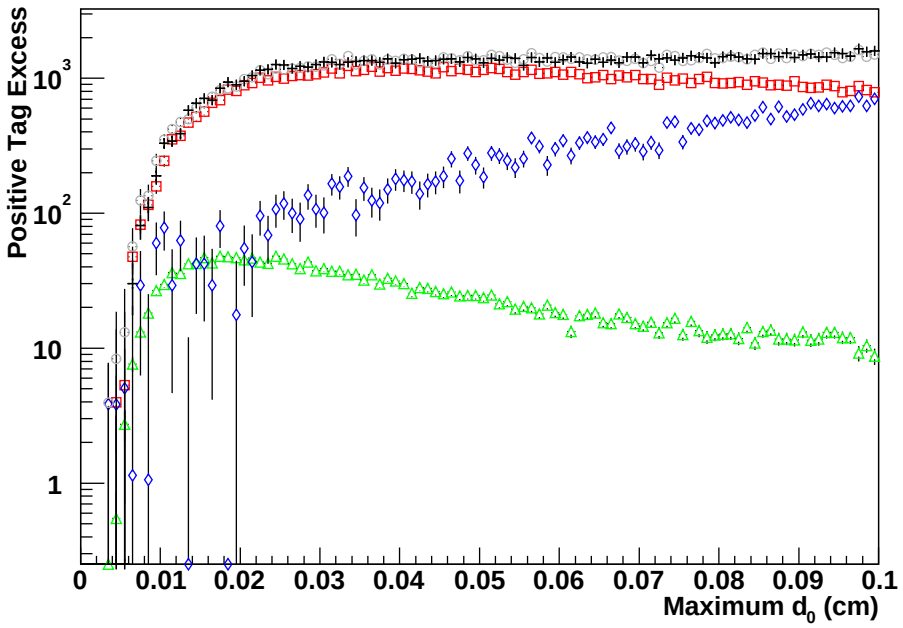

Figure 5.9: Result of the fit of the positive tag excess in JET50 data as a function of the maximum impact parameter d_0 of jet probability tracks inside the tagged jets. A P_J cut of 1% is used. Observed data are the crosses, while the fitted component from b, c and light jets are the squares, triangles and diamonds, respectively. The circles are the sum of the three fitted components.

Table 5.6: Mistag asymmetry measured in Jet50 data for P_J cuts at 1% and 5%. The quoted uncertainties are derived from the uncertainty in the fits. The uncertainty used for the average is the maximum difference between the average and each measurement.

Fitted variable	β ($P_J < 1\%$)	β ($P_J < 5\%$)
Maximum d_0	1.64 ± 0.02	1.37 ± 0.02
Maximum S_{d_0}	1.56 ± 0.03	1.10 ± 0.02
Mass of the system of tracks with $\|d_0\| > 0.01\ cm$	1.51 ± 0.04	1.30 ± 0.02
Mass of the system of tracks with $S_{d_0} > 2$	1.43 ± 0.03	1.20 ± 0.02
$P_T^{rel.}$ of the system of tracks with $\|d_0\| > 0.01\ cm$	1.67 ± 0.03	1.32 ± 0.02
$P_T^{rel.}$ of the system of tracks with $S_{d_0} > 2$	1.57 ± 0.02	1.30 ± 0.02
Average	1.56 ± 0.14	1.27 ± 0.17

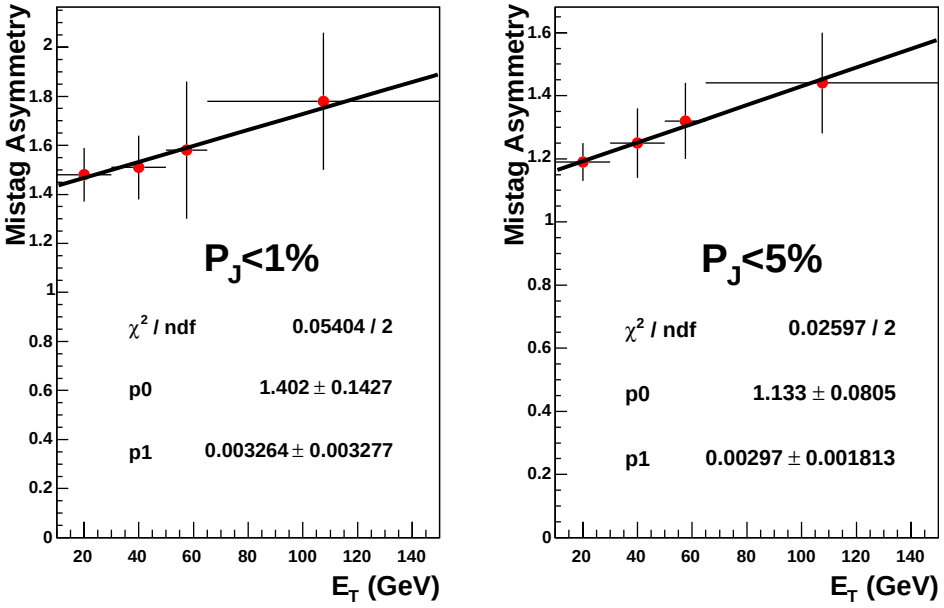

Figure 5.10: Mistag asymmetry as a function of the jet transverse energy for $P_J < 1\%$ (left plot) and $P_J < 5\%$ (right plot).

5.3 Jet Probability Performance on $t\bar{t}$ Events

We study the performance of the jet probability algorithm by computing the efficiency to tag a b jet in PYTHIA Monte Carlo $t\bar{t}$ events generated with a top mass = 178 GeV/c^2. Results are shown in Fig. 5.11 as a function of the transverse energy E_T and of the pseudo-rapidity η of the jets for P_J cuts of 1% and 5%. Jets are matched to b quarks (by requiring

$\Delta R < 0.4$ between the reconstructed jet and the b quark) and the tagging SF is applied to the resulting efficiency. We also measure the average efficiency to tag a b or a c jet in $t\bar{t}$ events passing the kinematic event selection described in Chapter 6. Results are shown in Table 5.7 before and after applying the tagging SF. The scaled per-jet efficiencies, together with the mistag matrix, are used to determine the efficiency to tag at least n jets per $t\bar{t}$ event, as described in Chapter 8. Although the tagging requirement results in some loss of efficiency for the $t\bar{t}$ signal, it significantly increases the signal-to-background ratio by heavily suppressing the dominant W+jets background.

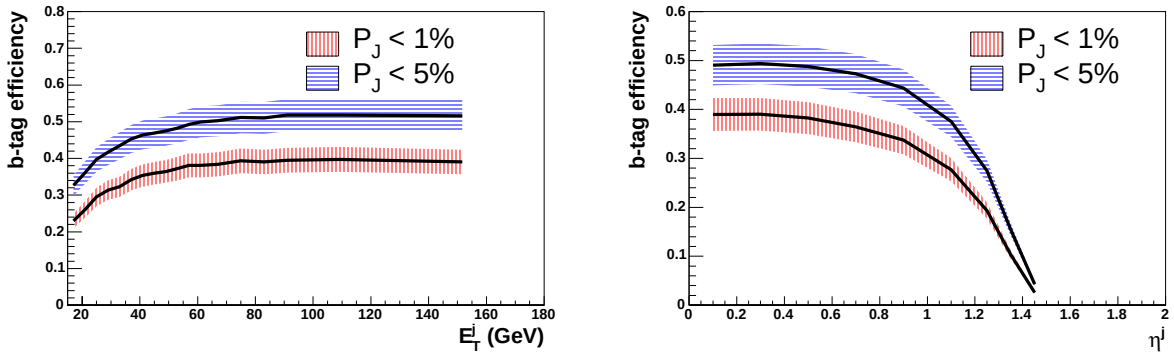

Figure 5.11: Efficiency to tag b jets in $t\bar{t}$ Monte Carlo simulated events as a function of jet E_T (left) and jet η (right) for two different P_J cuts. The efficiency is obtained by multiplying the tag rate for jets matched to b quarks in the Monte Carlo simulation by the appropriate tagging scale factor. The bands represent the systematic uncertainty on the scale factors.

Table 5.7: Tagging efficiencies for b and c jets in $t\bar{t}$ events ($m_t = 178$ GeV/c^2) before (raw efficiency) and after (scaled efficiency) applying the tagging scale factor.

	b jets		c jets	
	Raw Eff. (%)	Scaled Eff. (%)	Raw Eff. (%)	Scaled Eff. (%)
$P_J < 1\%$	43.2 ± 0.1	35.3 ± 3.0	9.6 ± 0.2	7.8 ± 0.7
$P_J < 5\%$	54.6 ± 0.1	46.5 ± 3.9	20.3 ± 0.2	17.3 ± 1.5

Chapter 6

Event Selection

Top quark events in the lepton+jets channel are characterized by the presence of an electron or muon with high transverse energy, large missing transverse energy and four high energy jets, two of which are b jets. The basic pretag selection requires one tight electron or muon, $\not\!\!E_T > 20$ GeV and jets with corrected $E_T > 15$ GeV and $|\eta| < 2$.

In order to select a lepton+jets sample completely disjoint from the top dilepton sample ($t\bar{t} \to l^+l^-\nu\bar{\nu}q\bar{q}$), we reject events with an extra lepton that passes the loose requirements. Events consistent with $Z \to l^+l^-$ are removed if a tight lepton and a second object form an invariant mass within the range [76, 106] GeV/c^2. If the tight lepton is an electron, the second object may be an isolated electromagnetic object, a jet with electromagnetic fraction greater than 0.95 or an oppositely-signed isolated track. If the tight lepton is a muon, the second object may be an isolated muon or an opposite-signed isolated track.

The event vertex z position is used to cluster jets and to ensure leptons and jets come from the same interaction. If more than one primary vertex is reconstructed in the event, the vertex closest to the lepton track is selected as event vertex. Events are rejected if the z of the lepton track is farther than 5 cm from the z of the event vertex. The vertex z position is required to be within 60 cm of the center of the detector in order to ensure good event reconstruction in the projective tower geometry of the CDF detector. The efficiency of this requirement is measured using minimum bias data and found to be (95.1 $\pm$ 0.3)%. For consistency with the b-tagging algorithm, events are also rejected if the z of the vertex with highest $\sum p_T$ of all tracks is farther than 5 cm from the event vertex z. The efficiency of this requirement is (98 $\pm$ 2)%, where the 2% error accounts for the uncertainty in the simulation of multiple interactions. We also reject events consistent with photon conversions (electrons) or cosmic rays (muons).

The events selected by the above criteria are dominated by QCD production of W bosons in association with jets. Figure 6.1 shows the P_J distribution for taggable jets in this sample. In order to improve the signal to background ratio for $t\bar{t}$ events, we require at least one jet in the event to be tagged as a b jet. A $t\bar{t}$ event is expected to have four jets in the final state, but due to gluon radiation, jet merging, and inefficiencies in jet reconstruction, this number can eventually be different. We therefore use the tagged events with three or more jets to define our signal sample, while the events with one and two jets are used as a control

sample.

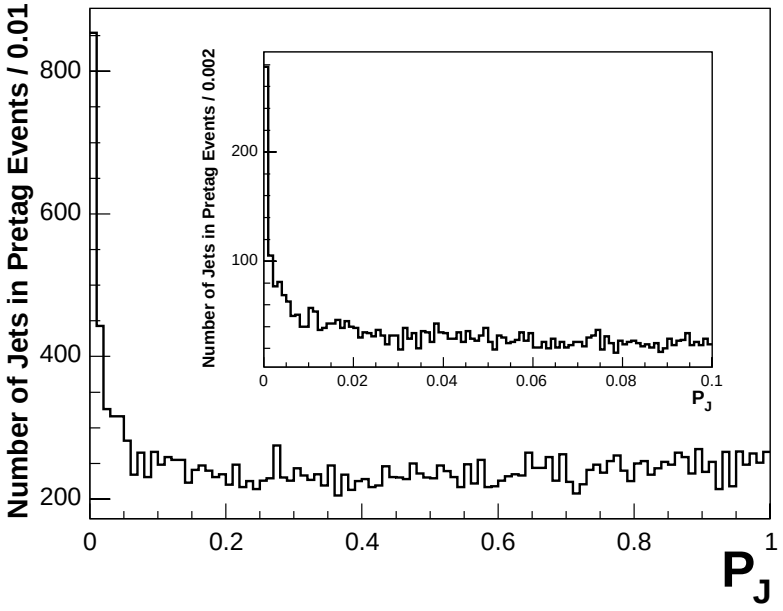

Figure 6.1: The P_J distribution for taggable jets in the pretag sample (note that the vertical axis does not start at 0). The inset shows a zoom of the P_J distribution from 0.0 to 0.1.

6.1 Optimized Selection

The variable H_T, defined as the scalar sum of all the transverse energy in the event, i.e., the sum of the $\not\!\!E_T$, the electron E_T or muon p_T, and the E_T of the jets, is a measure of the energy in the hard scatter, and is a powerful discriminant between the $t\bar{t}$ pair production signal events (S) and background events (B). In order to find the optimal H_T cut, we maximize the statistical significance ($S/\sqrt{S+B}$) in the signal region. Figure 6.2 (left) shows the H_T distribution of the $t\bar{t}$ Monte Carlo simulation, together with the various background contributions, properly normalized. Figure 6.2 (right) shows the statistical significance as a function of the H_T cut. Details about the background estimates and datasets used can be found in Chapter 7. Optimal statistical significance is reached with a cut of $H_T > 200$ GeV.

In addition, we enhance the W component of the sample by requiring the transverse mass of the lepton and the missing energy, $M_T^W = \sqrt{(E_T(l) + E_T(\nu))^2 - (\vec{P}_T(l) + \vec{P}_T(\nu))^2}$, be consistent with W boson production. Figure 6.3 (left) shows the M_T^W distribution for the $t\bar{t}$ Monte Carlo simulation together with the various normalized background contributions. Figure 6.3 (right) shows the statistical significance as a function of the M_T^W cut. Note that

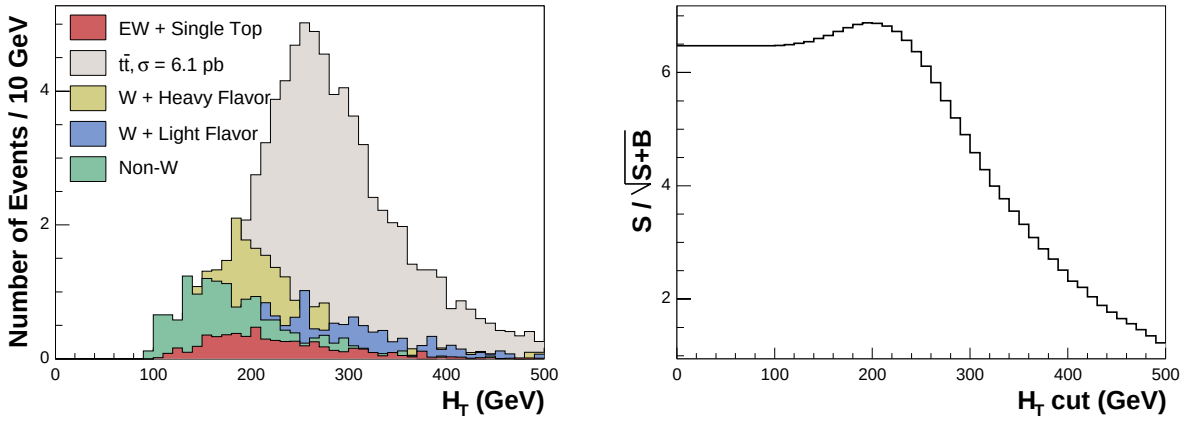

Figure 6.2: Left: H_T distribution for tagged events with 3 or more tight jets in $t\bar{t}$ Monte Carlo simulation (6.1 pb) and main backgrounds, for an integrated luminosity of 318 pb^{-1}. Right: statistical significance as a function of the cut applied.

the non-W background lies at lower values of M_T^W. In the optimization of the M_T^W cut, we take S to be the number of events from real W bosons and B to be the number of events from non-W background. A cut of $M_T^W > 20$ GeV/c^2 gives optimal statistical significance.

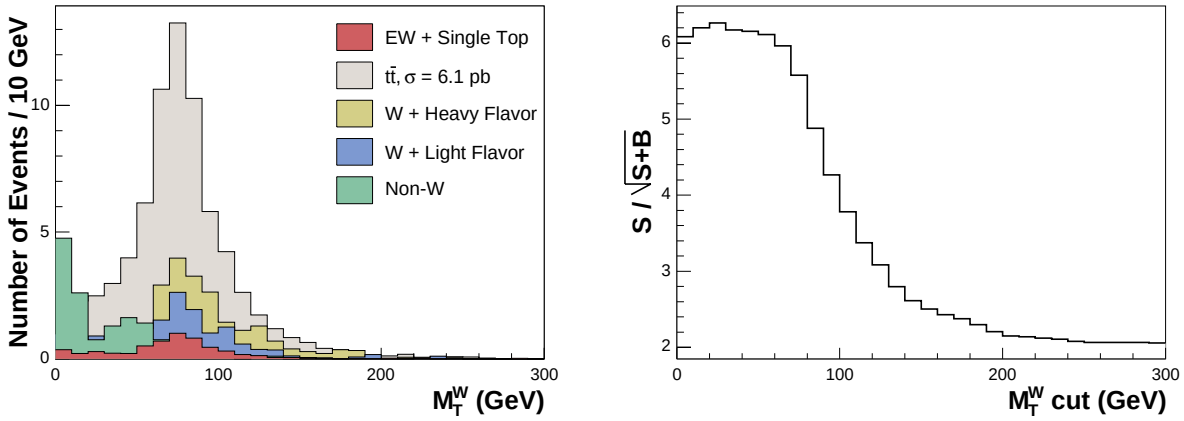

Figure 6.3: Left: W_T^M distribution for tagged events with 3 or more tight jets in $t\bar{t}$ Monte Carlo simulation (6.1 pb) and main backgrounds, for an integrated luminosity of 318 pb^{-1}. Right: statistical significance as a function of the cut applied.

6.2 Yields of Events

Events which pass the selection criteria described so far, before applying b-tagging, form the pretag sample. The number of observed events in both the pretag and tagged samples

for $P_J < 1\%$ and $P_J < 5\%$ are summarized in Table 6.1 as a function of the number of tight jets in the event.

Table 6.1: Yield of events in 318 pb^{-1} of data for $P_J < 1\%$ and $P_J < 5\%$.

Jet Multiplicity	1 jet	2 jets	3 jets	≥ 4 jets
Pretag Events				
CEM	16897	2657	182	105
CMUP	8169	1175	83	44
CMX	4273	610	35	17
Total	29339	4442	300	166
Single Tagged Events, $P_J < 1\%$ (5%)				
CEM	207 (571)	106 (230)	33 (53)	36 (53)
CMUP	92 (256)	58 (105)	13 (24)	24 (29)
CMX	51 (148)	27 (50)	6 (10)	8 (11)
Total	350 (975)	191 (385)	52 (87)	68 (93)
Double Tagged Events, $P_J < 1\%$ (5%)				
CEM	—	8 (16)	7 (15)	9 (18)
CMUP	—	3 (9)	4 (4)	8 (17)
CMX	—	2 (3)	1 (3)	1 (4)
Total	—	13 (28)	12 (22)	18 (39)

Chapter 7

Backgrounds

Other processes besides $t\bar{t}$ are expected to contribute to the tagged lepton+jets sample. The backgrounds that mimic the $l\not{E}_T jjbX$ signature are:

- ***W* + heavy flavor jets**. This background consists of a real W boson in association with either quarks (from heavy flavor excitation) or gluons. The gluon can split into a pair of heavy flavor quarks producing W + heavy flavor events ($Wb\bar{b}$, $Wc\bar{c}$, Wc). Figure 7.1(a) shows the Feynman diagram for W + jets production with heavy flavor tags.

- ***W* + light jets**. Alternatively, the gluon or initial quark can hadronize into a jet which is mistagged producing W + light flavor mistag events. Figure 7.1(b) shows the Feynman diagram for W + jets production with light flavor tags.

- **Non-*W* QCD production**. This background arises when the event does not contain a real W boson. This can occur in two ways. The first is when a heavy flavor hadron decays semileptonically, and the resulting lepton and $\not{E}_T$ pass the event selection. The second is when ordinary multijet QCD production produces a faked lepton plus $\not{E}_T$ due to mis-measured jets. These two processes are shown in Figs. 7.1(c) and 7.1(d), respectively.

- **Electroweak processes**. These backgrounds occur when vector bosons are created in pairs WW, WZ or ZZ. The WW background has two real W bosons. One can decay leptonically, and the other hadronically. The hadronic W daughters can the produce a b-tag. Similarly, the WZ background can have the W decay leptonically, while the Z can decay into heavy flavor quarks. The ZZ background can mimic the experimental signatyure if one Z decays leptonically and one leg is mis-reconstructed (faking a W boson) and the other decays into heavy flavor quarks. Also it is possible for the process $Z \to \tau^+\tau^-$ to fake this signature because one τ can fake the W signature while the other τ is tagged. Fig. 7.1(e) shows the diboson production for WW (WZ and ZZ are very similar). The single top production, although contains real top quarks, is also a background to top pair production. If the W from the top decays leptonically, this

process mimis the experimental signature of pair production. Fig. 7.1(f) shows the t-channels production of single top. There is an analogous s-channel diagram as well.

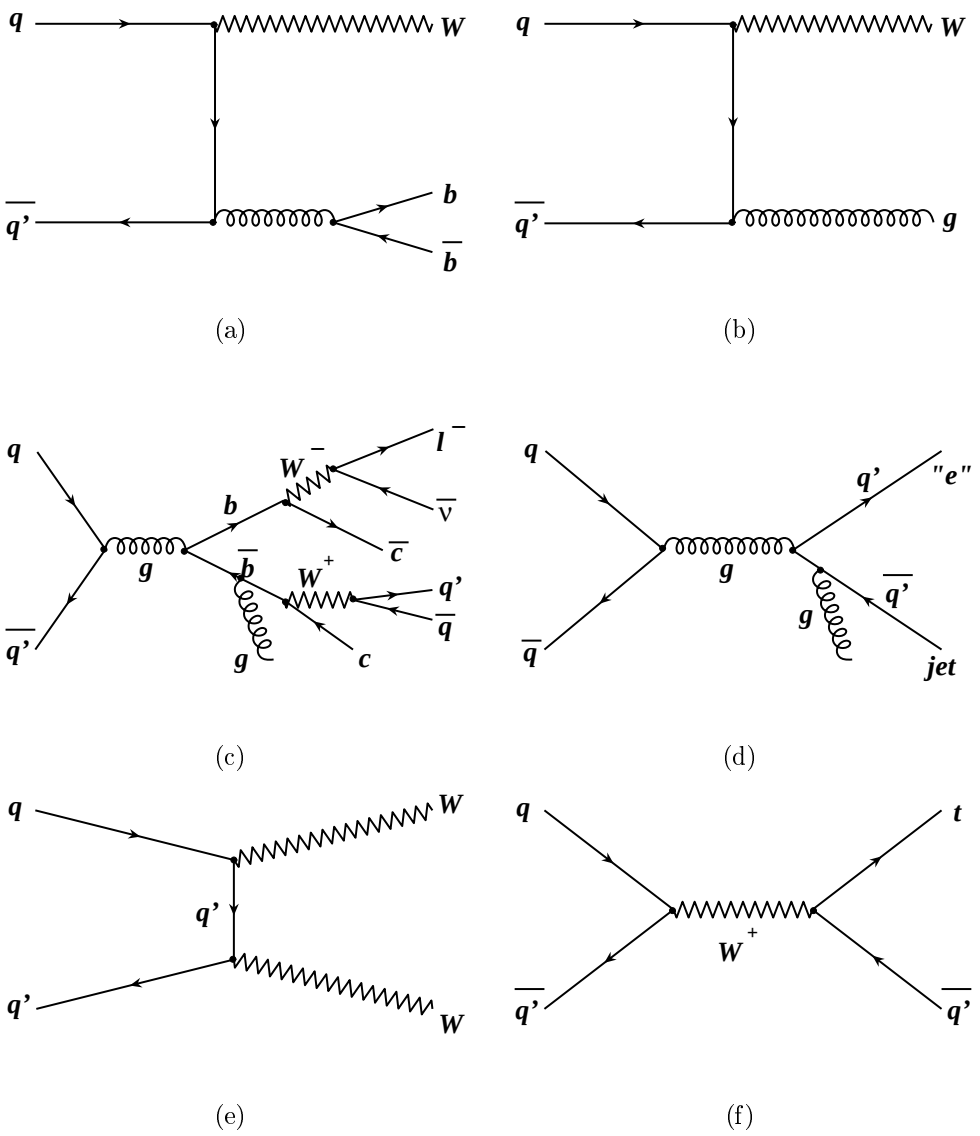

Figure 7.1: Feynman diagrams for backgrounds to $t\bar{t}$ lepton plus jets production: a) W + heavy flavor jets, b) W + light jets, c) Non-W QCD production from heavy flavor decays, d) Non-W QCD production from fake leptons, e) diboson production and f) single top production, t-channel.

7.1 Electroweak Processes

Electroweak processes are studied using Monte Carlo simulated samples. Diboson events (WW, WZ and ZZ) can contribute to the tagged lepton+jets sample when one boson decays

leptonically and the other decays into heavy quarks. The process $Z \to \tau^+\tau^-$ can also give a contribution due to the leptonic decays of the tau. Finally, there is a contribution from single top quarks produced in association with a b quark through $q\bar{q}$ annihilation in W^* (s-channel) or W-gluon fusion (t-channel), in which an initial gluon splits into a $b\bar{b}$ pair and a b quark interacts with a virtual W.

The number of events from these processes are predicted based on their theoretical cross sections [137–139] (listed in Table 7.1), the measured integrated luminosity, and the acceptances and tagging efficiencies derived from Monte Carlo simulations. The expectations for these backgrounds are corrected for differences between Monte Carlo simulations and data, which include the lepton identification scale factor, trigger efficiencies, the z vertex cut efficiency and the tagging scale factor.

The total diboson, $Z \to \tau^+\tau^-$ and single top predictions for $P_J < 1\%$ (5%) are shown in Table 7.9 (Table 7.10) and account for 2.5% (3.0%) of the number of events in the signal region of 3 and $\geq$4 jets. Following the same procedure, we also compute the electroweak background contributions to the pretag sample. The results are shown in Table 7.8.

Table 7.1: Cross sections used to estimate electroweak backgrounds. For diboson and single top production, the theoretical values are used. For $Z \to \tau^+\tau^-$, we use the cross section measured by CDF.

Process	Cross Section (pb)
WW	13.25 ± 0.25
WZ	3.96 ± 0.06
ZZ	1.58 ± 0.02
Single Top $W - g$ (t-channel)	1.98 ± 0.08
Single Top W^* (s-channel)	0.88 ± 0.05
$Z \to \tau^+\tau^-$	254.3 ± 5.4

7.2 Non-W Background

The non-W background consists of events for which the lepton+$\not\!\!E_T$ signature is not due to the decay of a W boson. The main contribution to this source of background comes from QCD jet production where a jet provides the signature of a lepton and the missing transverse energy is due to a bad measurement of the jet energies. Semileptonic decays of b mesons and misidentified photon conversions can also contribute. Due to its inherent instrumental nature, this background is difficult to estimate. In the event selection, its contribution to the lepton+jets sample is minimized by the requirement on the W boson transverse mass M_T^W. In particular, note that the optimization of this cut has been performed by requiring the lepton to be non-isolated in order to have an independent data sample to construct the kinematical variables (we use region C of Fig. 7.2).

The method used to estimate the non-W background assumes that the isolation of the high-p_T lepton and the event $\not\!\!E_T$ are uncorrelated for QCD processes, so that the ratio of non-W events with low lepton isolation to those with high lepton isolation in the region at low $\not\!\!E_T$ is the same as in the high $\not\!\!E_T$ region. Four regions in the lepton isolation *versus* missing transverse energy plane are defined (see Fig. 7.2):

- Region A: Isolation > 0.2 and $\not\!\!E_T < 15$ GeV
- Region B: Isolation < 0.1 and $\not\!\!E_T < 15$ GeV
- Region C: Isolation > 0.2 and $\not\!\!E_T > 20$ GeV
- Region D: Isolation < 0.1 and $\not\!\!E_T > 20$ GeV.

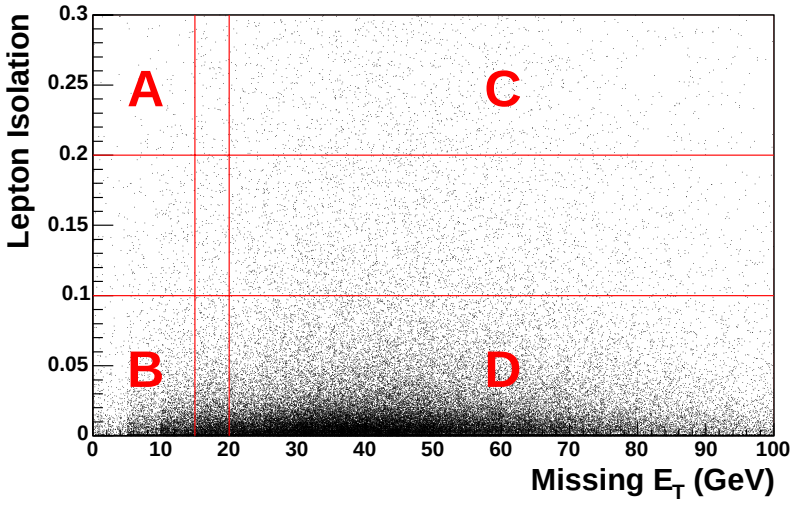

Figure 7.2: Definition of the sideband regions used to estimate the non-W background. Lepton isolation *versus* missing transverse energy distribution for $t\bar{t}$ simulated events is also shown.

The $t\bar{t}$ signal is expected to populate region D (signal region), while the non-W events dominate regions A, B and C (sideband regions). We can therefore estimate the fraction of events in the signal region which originate from non-W backgrounds as follows:

$$F_{non-W} = \frac{N_B \times N_C}{N_A \times N_D}, \tag{7.1}$$

where N_A, N_B, N_C and N_D are the total numbers of observed events in the four regions. We describe next the estimate of the non-W events in both the pretag and tagged samples.

7.2.1 Fraction of non-W Events in the Pretag Sample

An estimate of the contribution of the non-W events to the pretag sample is mandatory to correctly normalize most of the backgrounds in the tagged sample. Table 7.2 summarizes the results for the non-W fractions in the pretag sample as a function of the jet multiplicity for electrons and muons. Note that we do not apply the H_T and M_T^W cuts in regions A and B to preserve statistics. We correct the yields in regions A, B and C by subtracting the expected contribution from $t\bar{t}$ events assuming $\sigma_{t\bar{t}} = 6.1$ pb (this assumption is found to have a negligible impact on the final non-W estimate). Uncertainties in Table 7.2 are statistical only. The main source of systematic uncertainty comes from the lepton isolation and missing transverse energy not being fully uncorrelated for QCD events. We study the effect of this assumption by varying the values of the $\not\!\!E_T$ and lepton isolation cuts in the definition of the sideband regions. We observe a maximum variation of 50% in the resulting non-W fraction, which we assign as a systematic uncertainty on our estimates.

Table 7.2: Number of events in the sideband regions and fraction of non-W events in the signal region before and after correcting for $t\bar{t}$ contribution. Quoted errors are statistical only.

Jet Multiplicity	1 jet	2 jets	3 jets	$\geq$ 4 jets
		Pretag Electrons		
Region A	100600	12756	1745	216
Region B	61818	5228	593	98
Region C	1651	428	27	15
Region D	16897	2657	182	105
$F_{non-W}^{uncorr.}$	0.060 $\pm$ 0.002	0.066 $\pm$ 0.004	0.05 $\pm$ 0.01	0.06 $\pm$ 0.02
F_{non-W}	0.060 $\pm$ 0.002	0.066 $\pm$ 0.004	0.05 $\pm$ 0.01	0.05 $\pm$ 0.02
		Pretag Muons		
Region A	36599	5248	657	97
Region B	11718	968	114	21
Region C	737	181	12	11
Region D	12442	1785	118	61
$F_{non-W}^{uncorr.}$	0.0190 $\pm$ 0.0007	0.019 $\pm$ 0.002	0.018 $\pm$ 0.006	0.04 $\pm$ 0.02
F_{non-W}	0.0190 $\pm$ 0.0007	0.019 $\pm$ 0.002	0.014 $\pm$ 0.005	0.03 $\pm$ 0.01

To further cross check the accuracy of the predictions, we define new intermediate isolation regions B′ and D′:

- Region B: $\not\!\!E_T < 15$, Isol$< 0.1 \rightarrow$ Region B′: $\not\!\!E_T < 15$, 0.1$<$Isol< 0.2,
- Region D: $\not\!\!E_T > 20$, Isol$< 0.1 \rightarrow$ Region D′: $\not\!\!E_T > 20$, 0.1$<$Isol< 0.2.

From the intermediate region B′, we estimate the number of non-W events in region D′. The predicted non-W fractions are shown in Table 7.3. The uncertainties quoted are statistical

only. In the same table, these fractions are compared with the expected non-W fractions computed from the difference between the observed events and the contributions from $t\bar{t}$ and W+jets events. The expected number of $t\bar{t}$ events is derived by normalizing the Monte Carlo prediction to a cross section of 6.1 pb. In order to estimate the W+jets contribution in region D$'$, we compute the ratio of W+jets events in the regions D$'$ and D using simulations and normalize the expectations for W+jets production in D$'$ to the number of events in the signal region after removing $t\bar{t}$, electroweak contributions. We compute the relative differences as the ratio of the difference between expected and predicted non-W fractions to the predicted fraction. For each jet multiplicity bin, the differences between predicted and expected non-W fractions in region D$'$ are consistent with the 50% uncertainty we derived varying the $\not\!\!E_T$ and lepton isolation cuts in the definition of the sideband regions.

Table 7.3: Predicted and expected fractions of non-W events in the intermediate region D$'$ for the electron and muon samples. Errors are statistical only.

Jet Multiplicity	1 jet	2 jets	3 jets	$\geq$ 4 jets
Electron+Jets Sample				
Predicted Non-W Fraction	0.82 $\pm$ 0.03	0.60 $\pm$ 0.05	0.53 $\pm$ 0.16	0.49 $\pm$ 0.21
Expected Non-W Fraction	0.78 $\pm$ 0.01	0.82 $\pm$ 0.02	0.76 $\pm$ 0.10	0.59 $\pm$ 0.16
Fractional Relative Difference	-0.05	0.37	0.42	0.20
Muon+Jets Sample				
Predicted Non-W Fraction	0.41 $\pm$ 0.03	0.41 $\pm$ 0.06	0.40 $\pm$ 0.23	0.40 $\pm$ 0.33
Expected Non-W Fraction	0.70 $\pm$ 0.02	0.62 $\pm$ 0.05	0.44 $\pm$ 0.22	0.26 $\pm$ 0.25
Fractional Relative Difference	0.70	0.50	0.11	-0.35

7.2.2 Non-W Events in the Tagged Sample

The non-W background contributes to the tagged sample through both real heavy flavor production ($b\bar{b}$ and $c\bar{c}$ events) and mistags. We compute the number of non-W events with tagged jets in the signal region using equation 7.1 with the numbers of tagged events in the sideband regions. Yields in regions A, B and C are corrected for $t\bar{t}$ contributions. The results are summarized in Table 7.4: $(N_B/N_A)^{tagged}$ is the ratio of tagged events in regions B and A and it is used to normalize the number N_C^{tagged} of tagged events in the region C to get the expected number $N_{non-W}^{tagged,l}$of non-W events on the signal region. The precision of these estimates is limited by the number of tagged events in the sideband regions.

We cross check these results by estimating the non-W contribution to the tagged lepton+jets sample following two alternative methods. In the first one (*check* 1), we assume the tag rate in region D to be the same as in region B:

$$N_{non-W}^{tagged} = F_{non-W} \times N_D \times \epsilon_B, \tag{7.2}$$

Table 7.4: The number of non-W events in the signal region D estimated from the corrected numbers of tagged events in the sideband regions with equation 7.1. Uncertainties are statistical only.

Jet Multiplicity	1 jet	2 jets	3 jets	≥ 4 jets
Electron+Jets Sample ($P_J < 1\%$)				
$(N_B/N_A)^{tagged}$	0.36 ± 0.01	0.26± 0.02	0.26 ± 0.05	0.4 ± 0.2
N_C^{tagged}	74.8	25.1	1.8	1.0
$N_{non-W}^{tagged,e}$	26.7 ± 3.3	6.6 ± 1.4	0.5 ± 0.4	0.4 ± 0.4
Muon+Jets Sample ($P_J < 1\%$)				
$(N_B/N_A)^{tagged}$	0.102 ± 0.008	0.10 ± 0.02	0.11 ± 0.04	0.2 ± 0.1
N_C^{tagged}	36.9	20.3	4.0	0.81
$N_{non-W}^{tagged,\mu}$	3.8 ± 0.7	2.0 ± 0.6	0.5 ± 0.3	0.2 ± 0.1
Electron+Jets Sample ($P_J < 5\%$)				
$(N_B/N_A)^{tagged}$	0.42 ± 0.01	0.33 ± 0.02	0.29 ± 0.04	0.5 ± 0.1
N_C^{tagged}	142.8	52.9	3.5	1.5
$N_{non-W}^{tagged,e}$	59.6 ± 5.2	17.6 ± 2.6	1.0 ± 0.5	0.7 ± 0.6
Muon+Jets Sample ($P_J < 5\%$)				
$(N_B/N_A)^{tagged}$	0.141 ± 0.007	0.12 ± 0.01	0.09 ± 0.03	0.17 ± 0.07
N_C^{tagged}	65.8	32.1	3.7	0.6
$N_{non-W}^{tagged,\mu}$	9.3 ± 1.2	3.8 ± 0.8	0.3 ± 0.2	0.1 ± 0.1

where ϵ_B is the event tag rate in region B and N_D is the number of events in region D. This method has a large systematic uncertainty since the tag rate could depend on the missing transverse energy due to the contribution of $b\bar{b}$ events with a b quark decaying into leptons. Events with large $\not\!\!E_T$ would have a larger heavy flavor contribution due to real neutrino production from semileptonic b decay. In the second alternative method (*check* 2), we compute the tagging rates per jet in the sideband regions, and then we predict the tag rate per jet in the signal region D as

$$Pred\ Tag\ Rate\ D = \frac{Tag\ Rate\ B \times Tag\ Rate\ C}{Tag\ Rate\ A}. \tag{7.3}$$

We compute the jet tagging rate by assuming it to be the same in all the jet multiplicity bins and use this estimate to predict the non-W background in the signal region taking into account the jet multiplicity and the number of non-W events expected in the pretag lepton+jets sample. Table 7.5 compares the non-W contributions predicted by the three methods.

Finally, we use the results of the two alternative estimates to assign a systematic uncertainty of 50% which takes into account the differences with the base method. The total non-W background accounts for 1.2% of the observed events with tagged jets in the signal region, both for $P_J < 1\%$ and $P_J < 5\%$.

Table 7.5: Number of non-W events expected in the tagged lepton+jets sample as a function of the jet multiplicity for the three methods described. Uncertainties are statistical only.

Jet Multiplicity	1 jet	2 jets	3 jets	$\geq$ 4 jets
		$P_J < 1\%$		
N_{non-W}^{tagged}	30.5 $\pm$ 3.3	8.6 $\pm$ 1.5	0.9 $\pm$ 0.5	0.5 $\pm$ 0.4
$N_{non-W}^{tagged,\ check\ 1}$	19.0 $\pm$ 0.7	6.7 $\pm$ 0.6	0.6 $\pm$ 0.1	0.6 $\pm$ 0.3
$N_{non-W}^{tagged,\ check\ 2}$	27.7 $\pm$ 2.6	9.3 $\pm$ 0.9	0.7 $\pm$ 0.1	0.6 $\pm$ 0.2
		$P_J < 5\%$		
N_{non-W}^{tagged}	68.8 $\pm$ 5.4	21.4 $\pm$ 2.8	1.3 $\pm$ 0.6	0.8 $\pm$ 0.6
$N_{non-W}^{tagged,\ check\ 1}$	43.5 $\pm$ 1.3	16.2 $\pm$ 1.0	1.1 $\pm$ 0.2	1.6 $\pm$ 0.5
$N_{non-W}^{tagged,\ check\ 2}$	65.4 $\pm$ 4.4	21.9 $\pm$ 1.8	1.6 $\pm$ 0.3	1.5 $\pm$ 0.4

7.3 W + Heavy Flavor Processes

W+heavy flavor production is the main source of background in the tagged lepton+jets sample. It is estimated using the heavy flavor fractions in W boson production in association with partons and the tagging efficiency for these processes. These quantities are derived from Monte Carlo simulations. The overall normalization is obtained from the number of observed events in the pretag sample.

The estimate of the heavy flavor fraction in W+jets events is described elsewhere [7]. We use the `ALPGEN` event generator, which is able to compute exact matrix element calculations at leading order for parton level QCD and electroweak processes. We can therefore compute the ratio between the W+heavy flavor production cross section and the inclusive W+jets cross section since it is expected to be stable in the transition from leading-order to next-to-leading-order matrix elements. We generate events where inclusive W, $Wb\bar{b}$, $Wc\bar{c}$ and Wc are produced in association with n light partons. Parton level events from `ALPGEN` are fed to the `HERWIG` parton shower program which generates additional jets from gluon radiation, and a full CDF detector simulation is applied. Events containing a different number n of light partons are combined following a rigorous prescription in order to avoid double counting due to parton shower radiation, which causes $W + n$ parton events to populate part of the phase space described by the $W+(n+1)$ parton sample. The $Wb\bar{b}$ and $Wc\bar{c}$ samples are further divided into two classes according to the number of reconstructed heavy flavor jets in the event. We refer to these classes as 1B and 2B (1C and 2C) for $Wb\bar{b}$ ($Wc\bar{c}$). By means of these combined Monte Carlo simulated samples, the heavy flavor fractions for W+jets events are measured as the ratio between the computed W+heavy flavor and W+jets cross sections. Jet data samples are used to correct for residual discrepancies between data and Monte Carlo simulations: a factor 1.5 $\pm$ 0.4 is applied to the $Wb\bar{b}$ and $Wc\bar{c}$ fractions [7], where the uncertainty is dominated by the systematic uncertainties associated with the `ALPGEN` heavy flavor calculations. The final heavy flavor fractions are shown in Table 7.6.

The contribution of W+heavy flavor production to the pretag lepton+jets sample is

Table 7.6: Summary of $Wb\bar{b}$, $Wc\bar{c}$ and Wc fractions. 1B and 2B (1C and 2C) indicate the $Wb\bar{b}$ ($Wc\bar{c}$) events with one and two b-jets (c-jets) reconstructed, respectively. Uncertainties are statistical only.

Jet Multiplicity	1 jet	2 jets	3 jets	$\geq$ 4 jets
1B	0.010 ± 0.003	0.014 ± 0.004	0.024 ± 0.006	0.022 ± 0.006
2B	—	0.014 ± 0.004	0.023 ± 0.006	0.026 ± 0.007
1C	0.016 ± 0.004	0.024 ± 0.006	0.038 ± 0.010	0.035 ± 0.010
2C	—	0.018 ± 0.005	0.029 ± 0.008	0.037 ± 0.010
Wc	0.043 ± 0.009	0.060 ± 0.013	0.060 ± 0.013	0.059 ± 0.013

estimated by multiplying heavy flavor fractions by the observed number of events in the pretag sample, corrected for the non-W, and electroweak background expectations. The results are shown in Table 7.8.

The above Monte Carlo simulated samples after pretag selection are used to compute the tagging efficiencies. In order to avoid double counting of the mistag background, the jet probability algorithm is applied only to jets known to be due to a b or c quark. Each tagged jet is weighted according to the scale factor. Results are summarized in Table 7.7. The systematic uncertainties are dominated by the uncertainties on the scale factor for b and c jets.

Table 7.7: Jet probability tagging efficiencies for $Wb\bar{b}$, $Wc\bar{c}$ and Wc events. The first uncertainty is statistical, while the second is systematic.

Jet Multiplicity	1 jet	2 jet	3 jet	$\geq$ 4 jets
Event Tagging Efficiencies (%), $P_J < 1\%$				
1B ($\geq$1 tag)	29.5 ± 0.3 ± 2.5	30.7 ± 0.6 ± 2.6	37.0 ± 1.5 ± 3.2	33.5 ± 3.2 ± 2.9
2B ($\geq$1 tag)	—	50.5 ± 0.7 ± 4.3	56.0 ± 1.6 ± 4.8	54.6 ± 2.2 ± 4.7
1C ($\geq$1 tag)	6.8 ± 0.2 ± 0.9	7.8 ± 0.4 ± 1.0	9.1 ± 1.0 ± 1.2	8.0 ± 1.9 ± 1.0
2C ($\geq$1 tag)	—	13.5 ± 0.6 ± 1.7	16.8 ± 1.5 ± 2.2	14.3 ± 1.7 ± 1.8
Wc ($\geq$1 tag)	7.2 ± 0.2 ± 0.9	7.9 ± 0.3 ± 1.0	8.3 ± 0.9 ± 1.1	6.9 ± 1.1 ± 0.9
Event Tagging Efficiencies (%), $P_J < 5\%$				
1B ($\geq$1 tag)	39.6 ± 0.3 ± 3.4	40.8 ± 0.6 ± 3.4	47.1 ± 1.6 ± 4.0	41.4 ± 3.4 ± 3.5
2B ($\geq$1 tag)	—	63.5 ± 0.7 ± 5.4	68.4 ± 1.5 ± 5.8	66.7 ± 2.1 ± 5.6
1C ($\geq$1 tag)	14.8 ± 0.3 ± 1.9	17.2 ± 0.5 ± 2.2	18.7 ± 1.4 ± 2.4	16.3 ± 2.6 ± 2.1
2C ($\geq$1 tag)	—	27.1 ± 0.8 ± 3.4	33.2 ± 1.9 ± 4.2	32.3 ± 2.3 ± 4.1
Wc ($\geq$1 tag)	15.3 ± 0.3 ± 1.9	16.4 ± 0.5 ± 2.1	19.4 ± 1.3 ± 2.5	18.6 ± 1.7 ± 2.4

The pretag expectations are multiplied by the tagging efficiencies to estimate the contributions of these processes to the tagged sample. The numbers of $Wb\bar{b}$, $Wc\bar{c}$ and Wc events

expected in the tagged lepton+jets sample for $P_J < 1\%$ (5%) are shown, along with the rest of the backgrounds, in Table 7.9 (Table 7.10) and account for 12.3% (13.2%) of the observed number of events in the signal region.

7.4 Mistag Background

Events in which jets from light partons are tagged as heavy flavor jets can contribute to the tagged sample. The number of events with negative tags in the pretag sample would be a simple estimate of this background, but this method has the problem of a large statistical uncertainty. Instead, we count the events in the pretag sample weighted by their probability to have at least one mistagged jet. This probability is computed by applying the negative tag rate matrix to all the taggable jets in the event.

This estimate is corrected for the mistag asymmetry derived in Section 5.2.1. In order to take into account the dependence of the mistag asymmetry on the jet E_T, we convolute it with the jet E_T spectra in events with W+three or more jets for data and $t\bar{t}$ Monte Carlo simulation, as shown in Fig. 7.3. The observed difference between the means of the distributions and the mistag asymmetry values measured in Section 5.2.1 are negligible within the uncertainties. We therefore decide to use the former in our analysis. The RMS of the distributions gives an estimate of how much the asymmetry changes over the jets in our samples, and it is taken as an additional uncertainty on the mistag asymmetry. The final mistag asymmetry scale factors are 1.56 ± 0.17 for $P_J < 1\%$ and 1.27 ± 0.20 for $P_J < 5\%$.

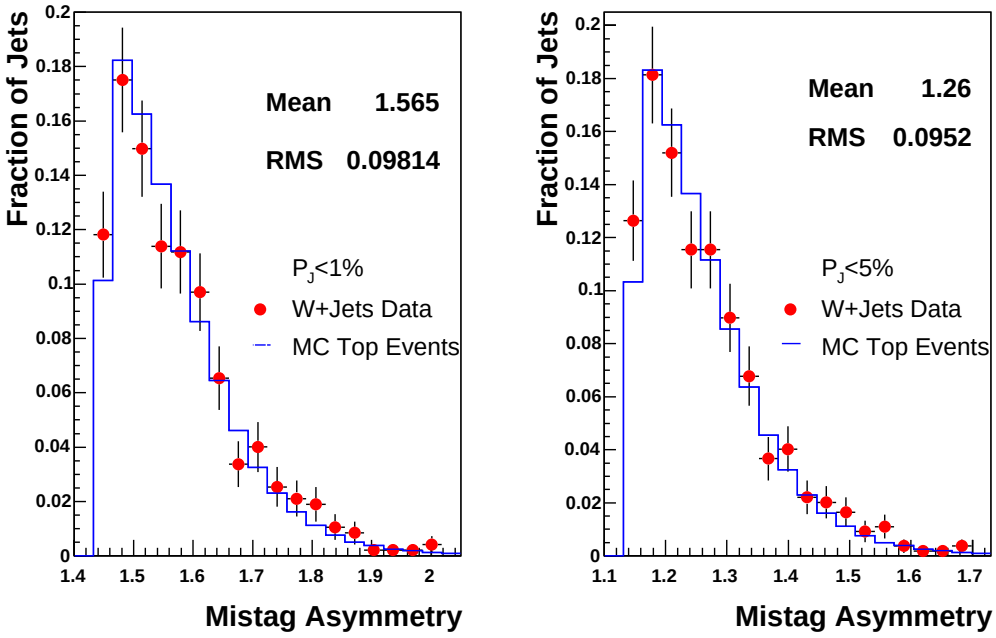

Figure 7.3: Mistag asymmetry distribution for jets in data (dots) and $t\bar{t}$ Monte Carlo simulated events (histogram) in the signal region for $P_J < 1\%$ (5%) in the left (right) side.

The estimate of the mistag background is also scaled down by one minus the fraction of pretag events which are due to non-W, and electroweak backgrounds. The contribution of the mistag background to the lepton+jets sample when a jet with $P_J < 1\%$ (5%) is required is shown in Table 7.9 (Table 7.10) and accounts for 12.8% (27.9%) of the observed number of events in the signal region.

7.4.1 Mistag Cross Check

The negative tag rate matrix has been extensively tested on inclusive jet samples. Results are discussed in Section 5.2. The mistag matrix is found to correctly predict the number of events with negatively tagged jets observed in independent samples to within a few percent. To further test the mistag matrix reliability on lepton+jets data, we select a subsample of events by requiring $\not\!\!E_T < 20$ GeV. This sample is expected to be dominated by QCD jet production with the high-p_T lepton signature provided by a jet. Figure 7.4 compares the observed number of events with negative tags and the matrix prediction as a function of the jet multiplicity. Good agreement is observed confirming the reliability of the mistag matrix to predict the negative tag rate in events dominated by prompt jets. We repeat the test on

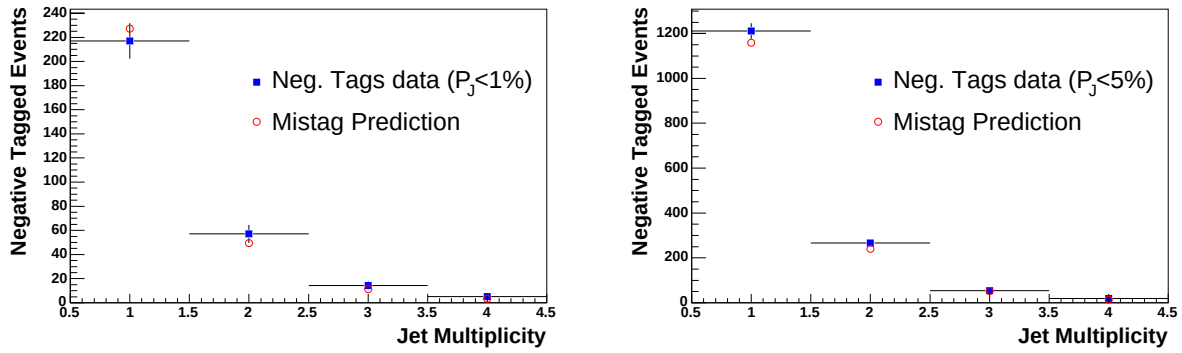

Figure 7.4: Events with negative tagged jets compared to the prediction using the mistag matrix. We select events in the high-p_T lepton sample with $\not\!\!E_T < 20$ GeV. P_J cuts of 1% and 5% are used on the top and bottom plots respectively.

the pretag lepton+jets sample, where a $\not\!\!E_T > 20$ GeV requirement is applied. Results are shown in Fig. 7.5. We observe a discrepancy between observed and predicted negative tags which we attribute to the higher fraction of heavy flavor in lepton+jets events with high value of $\not\!\!E_T$ with respect to the inclusive jet samples where the matrix has been computed. To corroborate this hypothesis, we make a first-order correction to the mistag prediction by using the heavy flavor fractions (f_T) in W+jets events (see Table 7.6). We compute the negative tag rates for light (M_l) and heavy (M_h) flavor jets in $t\bar{t}$ Monte Carlo simulation. For each jet multiplicity bin, a scale factor R is then determined as:

$$R = (1 - \sum f_T) + \sum f_T C_T, \tag{7.4}$$

$$T = 1B,\ 2B,\ 1C,\ 2C,\ Wc, \tag{7.5}$$

where

$$C_T = \frac{1-(1-M_l)^{j-k}(1-M_h)^k}{1-(1-M_l)^j}. \tag{7.6}$$

The numbers j and k in the formula are the jet multiplicity and the number of heavy flavor jets ($k = 1$ for $T = 1B$, $1C$ or Wc and $k = 2$ for $T = 2B$ or $2C$), respectively. The corrected distributions, also shown in Fig. 7.5, show a much better agreement with the observed rates of negative tagged events. We therefore use the mistag matrix prediction corrected by the mistag asymmetry as an estimate of the number of events with a tagged light jet.

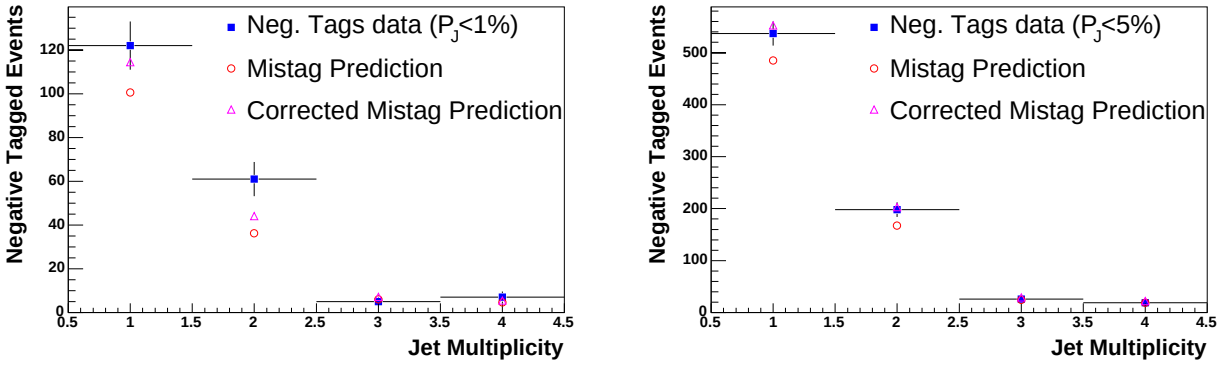

Figure 7.5: Events with negative tagged jets (squares) in the pretag lepton+jets sample compared to the prediction using the mistag matrix before (empty circles) and after (empty triangles) heavy flavor corrections for $P_J < 1\%$ (5%) in the top (bottom) plot.

7.5 Background Summary

Table 7.8 summarizes the contributions of the different background estimates in the pretag sample. The difference between the observed number of events and the total background estimate is due to W+light flavor and $t\bar{t}$ contributions.

Table 7.9 and Table 7.10 summarize the contributions of the different background sources in the tagged lepton+jets sample for $P_J < 1\%$ and $P_J < 5\%$ respectively.

We observe good agreement between data and background predictions in events with one and two jets, which supports the validity of our background estimates. In events with three or more jets, we observe an excess of tagged events in data which we attribute to $t\bar{t}$ events. The estimates of the W+heavy flavor and mistag background contributions have been normalized to the data in the pretag sample assuming no signal. Having actually observed a significant number of $t\bar{t}$ events in the tagged sample, we need to correct those estimates by the number of signal events in the pretag sample. We make this correction through an iterative procedure which is described in Chapter 9.

Table 7.8: Summary of the background estimate in the pretag sample. The difference between the total background estimate and the observed number of events is due to W+light flavor and $t\bar{t}$ contributions.

Jet Multiplicity	1 jet	2 jets	3 jets	≥ 4 jets
		Electroweak		
WW	127 ± 9	123 ± 9	10.0 ± 0.8	3.6 ± 0.3
WZ	16.8 ± 1.2	18.8 ± 1.4	1.7 ± 0.1	0.61 ± 0.06
ZZ	0.67 ± 0.05	0.68 ± 0.05	0.14 ± 0.02	0.052 ± 0.008
Single Top $W-g$	13.4 ± 1.1	13.6 ± 1.1	1.44 ± 0.12	0.38 ± 0.04
Single Top W^*	4.0 ± 0.4	7.9 ± 0.7	1.02 ± 0.10	0.24 ± 0.02
$Z \to \tau^+\tau^-$	87 ± 7	16.5 ± 1.7	1.0 ± 0.3	0 ± 0
Total	249 ± 18	180 ± 13	15.3 ± 1.2	4.9 ± 0.4
		W + Heavy Flavor		
Wbb	281 ± 75	116 ± 31	12.9 ± 3.3	7.4 ± 2.0
$Wc\bar{c}$	459 ± 123	170 ± 46	18.4 ± 5.0	11.1 ± 3.1
Wc	1197 ± 252	243 ± 53	16.9 ± 3.6	9.1 ± 2.0
Total	1938 ± 322	530 ± 94	47.8 ± 9.0	27.5 ± 5.5
		Others		
Non-W	1250 ± 626	208 ± 104	10.0 ± 5.3	7.3 ± 4.1
Total Background	3436 ± 741	917 ± 150	73 ± 11	39.7 ± 7.2
Data	29339	4442	300	166

Table 7.9: Summary of the background estimate in the lepton+jets sample when a jet with $P_J < 1\%$ is required.

Jet Multiplicity	1 jet	2 jets	3 jets	≥ 4 jets
		Electroweak		
WW	2.2 ± 0.3	5.0 ± 0.6	0.7 ± 0.1	0.28 ± 0.06
WZ	1.0 ± 0.1	2.0 ± 0.2	0.23 ± 0.03	0.09 ± 0.02
ZZ	0.027 ± 0.006	0.09 ± 0.01	0.012 ± 0.004	0.007 ± 0.002
Single Top $W-g$	4.1 ± 0.5	4.9 ± 0.6	0.73± 0.08	0.20 ± 0.02
Single Top W^*	1.3 ± 0.2	4.2 ± 0.5	0.60 ± 0.07	0.14 ± 0.02
$Z \to \tau^+\tau^-$	0.7 ± 0.3	0.4 ± 0.2	0.04 ± 0.04	0 ± 0
Total	9.3 ± 1.1	16.6 ± 1.8	2.3 ± 0.3	0.71 ± 0.09
		W + Heavy Flavor		
Wbb	83 ± 23	47 ± 13	6.0 ± 1.6	3.3 ± 0.9
$Wc\bar{c}$	31 ± 9	17.5 ± 5.2	2.3 ± 0.7	1.2 ± 0.4
Wc	86 ± 21	19.2 ± 5.0	1.4 ± 0.4	0.6 ± 0.2
Total	200 ± 42	84 ± 20	9.6 ± 2.4	5.2 ± 1.4
		Others		
Mistag	149 ± 17	51.8 ± 5.9	8.5 ± 1.0	6.7 ± 0.8
Non-W	31 ± 16	8.6 ± 4.6	0.9 ± 0.6	0.5 ± 0.5
Total Background	389 ± 49	161 ± 22	21.4 ± 2.7	13.1 ± 1.7
Data	350	191	52	68

Table 7.10: Summary of the background estimate in the lepton+jets sample when a jet with $P_J < 5\%$ is required.

Jet Multiplicity	1 jet	2 jets	3 jets	≥ 4 jets
		Electroweak		
WW	5.5 ± 0.6	12.5 ± 1.4	1.81 ± 0.21	0.74 ± 0.10
WZ	1.6 ± 0.2	3.3 ± 0.3	0.40 ± 0.05	0.16 ± 0.02
ZZ	0.049 ± 0.009	0.14 ± 0.02	0.027 ± 0.006	0.014 ± 0.004
Single Top $W-g$	5.4 ± 0.6	6.5 ± 0.7	0.92 ± 0.10	0.26 ± 0.03
Single Top W^*	1.7 ± 0.2	5.2 ± 0.6	0.74 ± 0.08	0.17 ± 0.02
$Z \to \tau^+\tau^-$	2.1 ± 0.5	1.1 ± 0.3	0.13 ± 0.10	0 ± 0
Total	16.3 ± 1.8	28.8 ± 3.0	4.0 ± 0.4	1.4 ± 0.1
		W + Heavy Flavor		
Wbb	111 ± 31	61 ± 17	7.4 ± 2.0	4.1 ± 1.2
$Wc\bar{c}$	68 ± 20	36 ± 11	4.6 ± 1.4	2.7 ± 0.8
Wc	184 ± 45	40 ± 10	3.2 ± 0.8	1.7 ± 0.5
Total	363 ± 75	137 ± 31	15.2 ± 3.6	8.5 ± 2.1
		Others		
Mistag	585 ± 92	194 ± 30	28.2 ± 4.4	22.1 ± 3.5
Non-W	69 ± 35	21 ± 11	1.3 ± 0.9	0.79 ± 0.74
Total Background	1033 ± 125	381 ± 46	48.8 ± 5.9	32.7 ± 4.2
Data	975	385	87	93

Chapter 8

Signal Acceptance

The signal acceptance, or $t\bar{t}$ event detection efficiency, is defined as the fraction of $t\bar{t}$ events that satisfy all selection requirements, and includes trigger and reconstruction efficiencies as well as the efficiencies of the kinematic selection and of the b-tagging algorithm. We measure it using a PYTHIA $t\bar{t}$ Monte Carlo sample generated with a top quark mass $m_t = 178$ GeV/c^2 and simulated as discussed in Chapter 4. Wherever possible, effects which are not sufficiently well modeled in the simulation are measured using data. The acceptance is defined as

$$\begin{aligned} \epsilon_{t\bar{t}} &= (A_{t\bar{t}} \times K_{lep} \times \epsilon_{trig} \times \epsilon_{z_0} \times \epsilon_{zvtx}) \times \epsilon_{b-tag} \\ &= \epsilon_{t\bar{t}}^{\text{pretag}} \times \epsilon_{b-tag} \end{aligned} \tag{8.1}$$

where $A_{t\bar{t}}$ is the fraction of Monte Carlo simulated $t\bar{t}$ events which pass the kinematic requirements (except b-tagging) and includes the branching fraction for $t\bar{t} \to e/\mu + jets$, the lepton identification efficiency (including isolation and cosmic/conversion veto efficiency, as described in Chapter 4), the dilepton and $Z^0 \to l^+l^-$ veto efficiencies, and the kinematic and geometric acceptances. $A_{t\bar{t}}$ is measured separately for electron and muon events. K_{lep} is a scale factor which takes into account the difference in lepton identification efficiency between data and Monte Carlo simulations estimated using $Z \to l^+l^-$ events; ϵ_{trig} is the trigger efficiency for identifying high p_T leptons and is measured using data from independent triggers. Both K_{lep} and ϵ_{trig} are discussed in Chapter 4. ϵ_{z_0} and ϵ_{zvtx} are the efficiencies for the z vertex cuts described in Chapter 6 and ϵ_{b-tag} is the efficiency to tag at least one tight jet in a $t\bar{t}$ event and includes a tagging scale factor to account for differences between Monte Carlo simulations and data.

The event tagging efficiency ϵ_{b-tag} is obtained from the same $t\bar{t}$ Monte Carlo simulated sample. We compute, for each $t\bar{t}$ event, the probability of having n tagged jets in the event by assigning to each jet a probability to be tagged. The sum of these probabilities over all the events returns the number of expected events with at least n tags, from which we calculate the tagging efficiency. For light flavor jets, this probability is computed using the mistag matrix, while for heavy flavor jets the probability is the value of the tagging scale factor (see Chapter 5) if the jet is tagged and zero otherwise. We estimate the systematic uncertainty on the event tagging efficiency by varying the tagging scale factor and mistag prediction by $\pm 1\sigma$.

Table 8.1 summarizes the acceptance for $t\bar{t}$ events. For P_J cuts of 1% and 5%, the combined acceptance times integrated luminosity are, respectively, $11.00 \pm 0.05(\text{stat}) \pm 1.17(\text{syst})$ pb^{-1} and $13.89 \pm 0.06(\text{stat}) \pm 1.38(\text{syst})$ pb^{-1}, where the statistical uncertainty is uncorrelated between the lepton types, and the systematic uncertainty is assumed to be 100% correlated since it is dominated by the luminosity and tagging scale factor uncertainties.

Table 8.1: Summary of acceptances for $t\bar{t}$ events. Efficiencies are expressed as percentages. The average ϵ_{b-tag} is the luminosity-weighted CEM/CMUP/CMX tagging efficiency. First uncertainty is statistical and the second one corresponds to systematics.

Quantity	CEM	CMUP	CMX
$\epsilon_{t\bar{t}}^{\text{pretag}}$	$3.67 \pm 0.02 \pm 0.22$	$1.92 \pm 0.01 \pm 0.12$	$0.751 \pm 0.008 \pm 0.046$
$\int Ldt$ (pb^{-1})	318 ± 19	318 ± 19	305 ± 18
Single Tag, $P_J < 1\%$, $SF = 0.817 \pm 0.070$			
ϵ_{b-tag}	$54.7 \pm 0.2 \pm 3.6$	$54.1 \pm 0.3 \pm 3.5$	$55.2 \pm 0.5 \pm 3.6$
Average ϵ_{b-tag}		$54.5 \pm 0.2 \pm 3.6$	
$\epsilon_{t\bar{t}}$	$2.00 \pm 0.01 \pm 0.18$	$1.04 \pm 0.01 \pm 0.09$	$0.41 \pm 0.01 \pm 0.04$
$\epsilon_{t\bar{t}} \int Ldt$ (pb^{-1})	$6.38 \pm 0.04 \pm 0.68$	$3.30 \pm 0.03 \pm 0.36$	$1.32 \pm 0.02 \pm 0.14$
Total $\epsilon_{t\bar{t}} \int Ldt$		$11.00 \pm 0.05(\text{stat}) \pm 1.17(\text{syst})$ pb^{-1}	
Single Tag, $P_J < 5\%$, $SF = 0.852 \pm 0.072$			
ϵ_{b-tag}	$68.8 \pm 0.2 \pm 3.7$	$68.6 \pm 0.3 \pm 3.7$	$69.6 \pm 0.5 \pm 3.7$
Average ϵ_{b-tag}		$68.8 \pm 0.2 \pm 3.7$	
$\epsilon_{t\bar{t}}$	$2.52 \pm 0.01 \pm 0.20$	$1.315 \pm 0.009 \pm 0.108$	$0.523 \pm 0.006 \pm 0.042$
$\epsilon_{t\bar{t}} \int Ldt$ (pb^{-1})	$8.03 \pm 0.05 \pm 0.80$	$4.19 \pm 0.03 \pm 0.42$	$1.67 \pm 0.02 \pm 0.17$
Total $\epsilon_{t\bar{t}} \int Ldt$		$13.89 \pm 0.06(\text{stat}) \pm 1.38(\text{syst})$ pb^{-1}	

Table 8.2 summarizes the contributions to the systematic uncertainty on the signal acceptance. Trigger, lepton identification and z vertex cuts have already been discussed in Chapters 4 and 6. The observed difference in the conversion veto efficiency between $t\bar{t}$ events and the $Z \to e^+e^-$ sample used to measure the electron identification scale factor is added as an uncertainty on the tight electron identification efficiency. The efficiency of the cosmic ray veto is measured from data and accounts for a 1% uncertainty on the tight muon identification efficiency. Additional uncertainties in the electron (muon) acceptance are due to E_T (p_T) scale, E_T (p_T) resolution and material (geometrical) effects, and are found to be 0.3% (1.2%) in inclusive W events. The lepton isolation uncertainty accounts for differences in the modeling of the lepton identification in events with different jet multiplicity. It has been evaluated by comparing data to Monte Carlo simulations for W+jets and $t\bar{t}$ events. The uncertainty due to the jet energy scale is estimated by the shift in signal acceptance observed by changing the jet energy corrections within their uncertainties. The uncertainty due to parton distribution functions (`PDF`) is estimated by re-weighting the $t\bar{t}$ events generated with `CTEQ5L` for different sets of `PDF`s [129]. In particular, we consider the difference in

signal acceptance between NLO CTEQ6M and CTEQ5L, between MRST for two different values of α_S, and between NLO CTEQ6M and the 20 CTEQ eigenvectors, and we add in quadrature all the contributions. Differences in the modeling of $t\bar{t}$ production and decay are evaluated as the difference in acceptance between samples of signal events generated with HERWIG and PYTHIA. Samples of $t\bar{t}$ events with different levels of initial and final state radiation (ISR/FSR) are used to evaluate the effect of this source of uncertainty on the signal acceptance. The systematic uncertainty on the event tagging efficiency is estimated by varying the tagging scale factor and the mistag prediction by $\pm$ 1σ. The total systematic uncertainty on the signal acceptance is 8.9% (8.0%) for $P_J < 1\%$ (5%), and is dominated by the tagging scale factor and the jet energy scale uncertainties.

Table 8.2: Summary of the systematic uncertainties on the signal acceptance. The second column quotes the relative uncertainty on the indicated quantities, while the third column shows the effect on the overall $t\bar{t}$ acceptance.

Source	Relative Uncertainty (%)	Uncertainty on the Acceptance (%)
Central Electron Trigger	0.6	0.3
Central Electron ID *SF*	0.5	0.3
Conversion Veto Eff.	1.4	0.8
E_T Scale of Electron	0.3	0.2
Central Muon Trigger	0.5	0.2
Central Muon ID *SF*	1.0	0.3
CMX Muon Trigger	0.4	0.05
CMX Muon ID *SF*	0.6	0.07
Cosmic Veto Eff.	1.0	0.4
p_T Scale of Muon	1.2	0.5
Lepton Isolation	2.0	2.0
$\|Z_{vtx}\|$ Cut Eff.	0.3	0.3
$Z_{vtx}^{JetProb}$ Cut Eff.	2.0	2.0
Jet Energy Scale	—	4.2
PDF	—	2.0
MC Modeling	—	1.6
ISR/FSR	—	1.3
Tagging *SF* $P_J < 1\%$ (b's/c's)	8.6/12.9	6.5
Mistag Asymmetry $P_J < 1\%$	11.0	0.2
Tagging *SF* $P_J < 5\%$ (b's/c's)	8.5/12.7	5.4
Mistag Asymmetry $P_J < 5\%$	15.5	0.4
Total Uncertainty ($P_J < 1\%$)	—	8.9
Total Uncertainty ($P_J < 5\%$)	—	8.0

Chapter 9

Cross Section for Single Tagged Events

We measure the cross section as

$$\sigma_{t\bar{t}} = \frac{N_{obs} - N_{bck}}{\epsilon_{t\bar{t}} \times \int L\ dt}, \tag{9.1}$$

where N_{obs} is the observed number of events with at least one jet tagged, N_{bck} is the background estimate in the signal region, $\epsilon_{t\bar{t}}$ is the signal acceptance including the tagging efficiency and $\int L\ dt$ is the integrated luminosity. The estimated number of background events must be corrected for the $t\bar{t}$ contribution, since we normalize mistag and W+heavy flavor backgrounds assuming no $t\bar{t}$ signal events in the pretag sample. We apply an iterative procedure in which we first estimate the number of tagged top candidates in the sample as the number of tagged signal events minus the total background in the ≥ 3 jet bins. Successively, the obtained signal cross section is used to estimate the number of $t\bar{t}$ events before the b-tagging requirement, and this contribution is subtracted from the total number of events to which we normalize the mistag, $Wb\bar{b}$, $Wc\bar{c}$ and Wc backgrounds. The expectations for single top, diboson and Z$\rightarrow\tau^+\tau^-$ do not change with the number of $t\bar{t}$ events in the signal region. The change for non-W background is found to be negligible compared to its uncertainty. Therefore, this background is also kept fixed. Having obtained a new estimate for the tagged background, we re-evaluate the number of $t\bar{t}$ candidates. The procedure is repeated until the cross section $\sigma_{t\bar{t}}$ changes by less than 0.1%.

Starting with the backgrounds shown in Tables 7.9 and 7.10, we apply the iterative procedure and measure

$$\sigma_{t\bar{t}} = 8.9^{+1.0}_{-1.0}(\text{stat.})^{+1.1}_{-1.0}(\text{syst.})\ \text{pb}$$

for $P_J < 1\%$. As a cross check, we apply the iterative procedure for $P_J < 5\%$ and measure

$$\sigma_{t\bar{t}} = 9.6^{+1.0}_{-0.9}(\text{stat.})^{+1.2}_{-1.1}(\text{syst.})\ \text{pb}.$$

The final signal and background estimates are shown in Table 9.1, together with the observed number of events.

Table 9.1: Summary of the final signal and background estimates and observed data in the single tag sample.

Jet Multiplicity	1 jet	2 jets	3 jets	≥ 4 jets
Pretag Data	29339	4442	300	166
		$P_J < 1\%$		
Electroweak	9.3 ± 1.1	16.6 ± 1.8	2.3 ± 0.3	0.71 ± 0.09
$Wb\bar{b}$	83 ± 23	47 ± 13	4.3 ± 1.2	1.1 ± 0.3
$Wc\bar{c}$	31 ± 9	17.3 ± 5.2	1.6 ± 0.5	0.4 ± 0.1
Wc	86 ± 21	19.0 ± 4.9	1.0 ± 0.3	0.21 ± 0.06
Mistag	149 ± 17	51 ± 6	6.1 ± 0.7	2.2 ± 0.3
Non-W	31 ± 16	8.6 ± 4.6	0.9 ± 0.6	0.5 ± 0.5
Total Background	389 ± 49	159 ± 22	16.3 ± 2.0	5.1 ± 0.7
$t\bar{t}$ (8.9 pb)	2.5 ± 0.5	20.6 ± 2.4	40.4 ± 4.5	58.1 ± 6.2
Data	350	191	52	68
		$P_J < 5\%$		
Electroweak	16.3 ± 1.8	28.8 ± 3.0	4.0 ± 0.4	1.4 ± 0.1
$Wb\bar{b}$	111 ± 31	60 ± 17	5.2 ± 1.4	1.1 ± 0.3
$Wc\bar{c}$	68 ± 20	36 ± 11	3.2 ± 1.0	0.76 ± 0.24
Wc	184 ± 45	40 ± 10	2.2 ± 0.6	0.5 ± 0.13
Mistag	585 ± 92	191 ± 30	19.6 ± 3.1	6.1 ± 1.0
Non-W	69 ± 35	21 ± 11	1.3 ± 0.9	0.8 ± 0.7
Total Background	1033 ± 125	377 ± 46	35.5 ± 4.2	10.6 ± 1.4
$t\bar{t}$ (9.6 pb)	3.6 ± 0.6	28.4 ± 3.1	55.1 ± 5.7	78.6 ± 7.8
Data	975	385	87	93

Figure 9.1 compares the numbers of observed data to background and signal expectations, for $P_J < 1\%$ and 5%, for the measured $t\bar{t}$ production cross sections.

The statistical uncertainty on the measured cross section is dominated by the data sample size. Table 9.2 summarizes the systematic contributions to the cross section uncertainty. The correlations in acceptances, tagging scale factor and luminosity uncertainty are taken into account. $Wb\bar{b}$ and $Wc\bar{c}$ systematics are considered correlated across all the bins. All the other uncertainties are treated as uncorrelated.

9.1 $t\bar{t}$ Cross Section Dependence on the Top Quark Mass

The signal acceptance used in this analysis has been computed using a sample of $t\bar{t}$ events generated with `PYTHIA` for $m_t = 178$ GeV/c^2, which corresponds to the combined Run I top mass measurement at the Tevatron Collider [3]. We study the dependence of the $t\bar{t}$ cross

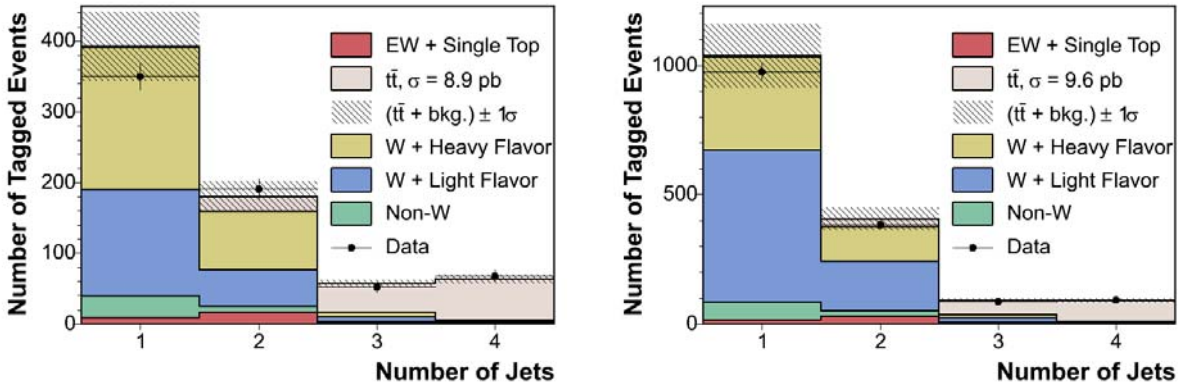

Figure 9.1: Single tag data and background contributions (for an integrated luminosity of 318 pb^{-1}) as a function of the event jet multiplicity for $P_J < 1\%$ (left) and $P_J < 5\%$ (right). A top mass of $m_t = 178$ GeV/c^2 is assumed.

Table 9.2: Summary of the systematic uncertainties in the single tag analysis.

Source	Fractional Syst. Uncert. (%)	Contribution to $\sigma_{t\bar{t}}$ (%)	
		$P_J < 1\%$	$P_J < 5\%$
Central Electron ID	1.6	+0.99/-0.97	+1.00/-0.98
Central Muon ID	1.9	+0.61/-0.61	+0.62/-0.61
CMX Muon ID	1.8	+0.22/-0.22	+0.22/-0.22
PDF	2.0	+2.1/-2.0	+2.1/-2.0
Jet Energy Scale	4.2	+4.5/-4.2	+4.6/-4.2
Lepton Isolation	2.0	+2.1/-2.0	+2.1/-2.0
ISR/FSR	1.3	+1.4/-1.3	+1.4/-1.3
MC Modeling	1.6	+1.7/-1.6	+1.7/-1.6
Z Vertex	2.0	+2.1/-2.1	+2.2/-2.1
Tagging SF $P_J < 1\%$ (b's/c's)	8.6/12.9	+8.2/-7.2	—
Tagging SF $P_J < 5\%$ (b's/c's)	8.5/12.7	—	+7.0/-6.3
Mistag Asymmetry $P_J < 1\%$	11.0	+0.93/-0.93	—
Mistag Asymmetry $P_J < 5\%$	15.5	—	+3.0/-3.0
Non-W Fraction	50	0.33	0.56
Non-W Prediction	50	0.71	0.79
W+HF Prediction	30	2.6	2.9
Cross Sections Bck.	1.8	0.056	0.072
Luminosity	5.9	+6.5-5.7	+6.5-5.8
Total Systematic Uncertainty		+12.5/-11.3	+12.3/-11.3

section on the top quark mass by reevaluating the signal acceptance through a set of Monte Carlo simulated samples generated by HERWIG for different values of the top mass. Results are shown in Fig. 9.2. A linear fit to the measured cross sections as a function of the top mass returns a slope of -0.052 ± 0.008 pb/(GeV/c^2) and -0.066 ± 0.008 pb/(GeV/c^2) for P_J <1% and 5% respectively, where the uncertainties are due to Monte Carlo simulation statistics. Note that the fit results for $m_t = 178$ GeV/c^2 agree with the measured cross section within the 1.6% uncertainty estimated in Section 8 due to different modeling in PYTHIA and HERWIG.

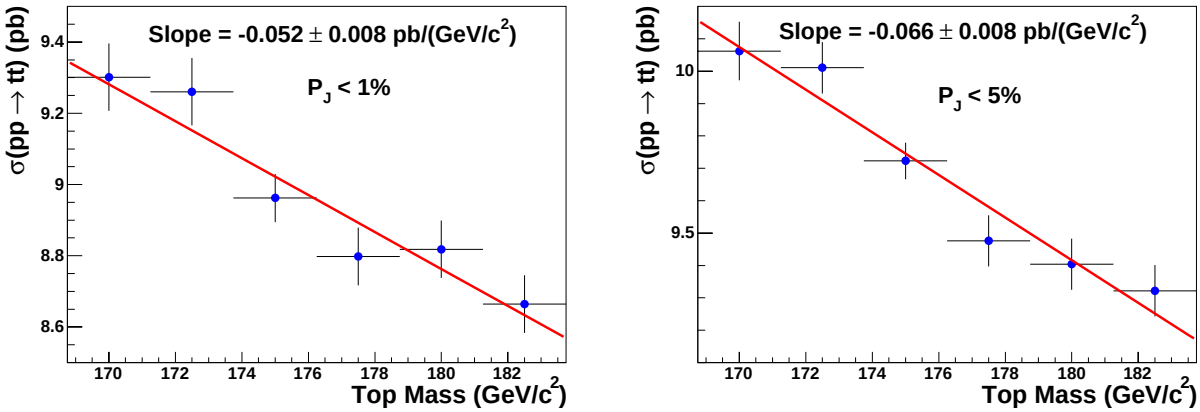

Figure 9.2: Top pair production cross sections as a function of the top quark mass for $P_J <$ 1% (left) and $P_J < 5\%$ (right). The uncertainties shown are the statistical uncertainties on the acceptances for each mass.

9.2 Electron versus Muon $t\bar{t}$ Cross Section Measurements

As an additional cross check, we measure the cross section separately for events with tight electrons and muons. Table 9.3 summarizes the cross sections for the two analyses with $P_J <$ 1% and $P_J < 5\%$. The cross section measurements in the electron and muon+jets samples agree within their statistical uncertainty.

Table 9.3: Summary of the cross sections for $P_J < 1\%$ and $P_J < 5\%$ and for each lepton type. Results are expressed in pb.

	Total	Electrons	Muons
$P_J < 1\%$	$8.9^{+1.0}_{-1.0}(\text{stat.})^{+1.1}_{-1.0}(\text{syst.})$	$8.6^{+1.4}_{-1.2}(\text{stat.})^{+1.1}_{-1.0}(\text{syst.})$	$9.4^{+1.7}_{-1.4}(\text{stat.})^{+1.2}_{-1.0}(\text{syst.})$
$P_J < 5\%$	$9.6^{+1.0}_{-0.9}(\text{stat.})^{+1.2}_{-1.1}(\text{syst.})$	$9.4^{+1.3}_{-1.2}(\text{stat.})^{+1.2}_{-1.1}(\text{syst.})$	$9.9^{+1.6}_{-1.4}(\text{stat.})^{+1.2}_{-1.1}(\text{syst.})$

Chapter 10

Cross Section for Double Tagged Events

The measurement of the $t\bar{t}$ cross section in a sample with at least two b tags follows the same procedure as the single tag analysis, with a much purer sample of $t\bar{t}$ events. As shown in Table 6.1, after requiring the event selection described in Chapter 6, we observe 30 (61) events with two b-tagged jets out of the 120 (180) events with at least one b-tagged jet for $P_J < 1\%$ ($P_J < 5\%$). Table 10.1 shows the signal acceptances and the efficiencies to tag two jets in signal events passing the pretag selection. The total acceptance times luminosity for $P_J < 1\%$ and $P_J < 5\%$ is $2.57 \pm 0.02(\text{stat}) \pm 0.49(\text{syst})$ pb^{-1} and $4.92 \pm 0.04(\text{stat}) \pm 0.87(\text{syst})$ pb^{-1} respectively.

10.1 Backgrounds in the Double *b*-Tag Sample

A few differences with respect to the single tag analysis must be taken into account in order to estimate the backgrounds. We define the mistag background as the events with at least two mistagged jets. The negative tag rate matrix is applied to negatively taggable jets in the event and the probability to have at least two mistagged jets is summed over all events. The mistag prediction is scaled by the fraction of non-W, electroweak backgrounds and by the mistag asymmetry as is done for the single tag analysis.

Events with one real heavy flavor tag plus a mistag are included in the other background sources. The contribution of mistags to the W+heavy flavor background is taken into account by applying the mistag rate matrix to light flavor jets in events with an extra real tag when computing the tagging efficiency. Results are summarized in Table 10.2.

The strategy to estimate the non-W background is changed, compared to that used for the single tag sample, due to low statistics in the double tagged event sample in the sideband regions (see Section 7.2). We compute a common tag rate for all the jet multiplicity bins by using data in region B (isolation < 0.1 and $\not\!\!E_T < 15$ GeV). We divide the total number of double tagged events by the sum of the number of pretag events scaled by the jet pair multiplicity. Finally, we apply this tag rate to the pretag expectation in the signal region derived in Section 7.2.1.

Table 10.1: Summary of acceptances for $t\bar{t}$ events. Efficiencies are expressed as percentages. The first uncertainty quoted is statistical and the second is systematic. The average ϵ_{b-tag} is the luminosity-weighted CEM/CMUP/CMX tagging efficiency.

Quantity	CEM	CMUP	CMX
$\epsilon_{t\bar{t}}^{\mathrm{pretag}}$	$3.67 \pm 0.02 \pm 0.22$	$1.92 \pm 0.01 \pm 0.12$	$0.751 \pm 0.008 \pm 0.046$
$\int Ldt\ (pb^{-1})$	318 ± 19	318 ± 19	305 ± 18
Double Tag, $P_J < 1\%$, $SF = 0.817 \pm 0.070$			
ϵ_{b-tag}	$12.7 \pm 0.2 \pm 2.1$	$12.6 \pm 0.2 \pm 2.0$	$13.4 \pm 0.4 \pm 2.2$
Average ϵ_{b-tag}		$12.7 \pm 0.1 \pm 2.1$	
$\epsilon_{t\bar{t}}$	$0.465 \pm 0.006 \pm 0.081$	$0.241 \pm 0.004 \pm 0.042$	$0.101 \pm 0.003 \pm 0.018$
$\epsilon_{t\bar{t}} \int Ldt$ (pb^{-1})	$1.48 \pm 0.02 \pm 0.27$	$0.77 \pm 0.01 \pm 0.14$	$0.32 \pm 0.01 \pm 0.06$
Total $\epsilon_{t\bar{t}} \int Ldt$		2.57 ± 0.02(stat) ± 0.49(syst) pb^{-1}	
Double Tag, $P_J < 5\%$, $SF = 0.852 \pm 0.072$			
ϵ_{b-tag}	$24.4 \pm 0.2 \pm 3.6$	$24.1 \pm 0.3 \pm 3.6$	$25.2 \pm 0.5 \pm 3.7$
Average ϵ_{b-tag}		$24.4 \pm 0.2 \pm 3.6$	
$\epsilon_{t\bar{t}}$	$0.895 \pm 0.009 \pm 0.142$	$0.462 \pm 0.006 \pm 0.074$	$0.189 \pm 0.004 \pm 0.030$
$\epsilon_{t\bar{t}} \int Ldt$ (pb^{-1})	$2.85 \pm 0.03 \pm 0.48$	$1.47 \pm 0.02 \pm 0.25$	$0.60 \pm 0.01 \pm 0.10$
Total $\epsilon_{t\bar{t}} \int Ldt$		4.92 ± 0.04(stat) ± 0.87(syst) pb^{-1}	

Table 10.2: Jet probability tagging efficiencies for $Wb\bar{b}$, $Wc\bar{c}$ and Wc events for double tagged events. Values are expressed as percentages. The first uncertainty quoted is statistical and the second is systematic. 1B and 2B (1C and 2C) refer to $Wb\bar{b}$ ($Wc\bar{c}$) events with one and two reconstructed heavy flavor jets respectively.

jet multiplicity	2 jets	3 jets	≥ 4 jets
Double Tag Tagging Efficiencies, $P_J < 1\%$			
1B ($\geq$2 tags)	$0.27 \pm 0.06 \pm 0.05$	$0.90 \pm 0.30 \pm 0.15$	$1.3 \pm 0.8 \pm 0.2$
2B ($\geq$2 tags)	$10.3 \pm 0.4 \pm 1.8$	$13.\ 1\pm 1.1 \pm 2.2$	$14.1 \pm 1.5 \pm 2.4$
1C ($\geq$2 tags)	$0.067 \pm 0.037 \pm 0.017$	$0.23 \pm 0.17 \pm 0.06$	$0.29 \pm 0.38 \pm 0.08$
2C ($\geq$2 tags)	$0.43 \pm 0.12 \pm 0.11$	$1.3 \pm 0.5 \pm 0.3$	$1.1 \pm 0.5 \pm 0.3$
Wc ($\geq$2 tags)	$0.05 \pm 0.03\pm 0.01$	$0.20 \pm 0.14 \pm 0.05$	$0.22 \pm 0.21 \pm 0.06$
Double Tag Tagging Efficiencies, $P_J < 5\%$			
1B ($\geq$2 tags)	$1.3 \pm 0.1 \pm 0.2$	$3.7 \pm 0.6 \pm 0.6$	$5.0 \pm 1.5 \pm 0.8$
2B ($\geq$2 tags)	$18.6 \pm 0.6 \pm 3.1$	$23.9 \pm 1.4 \pm 4.0$	$26.0 \pm 1.9 \pm 4.4$
1C ($\geq$2 tags)	$0.54 \pm 0.11 \pm 0.14$	$1.6 \pm 0.4 \pm 0.4$	$1.8 \pm 0.9 \pm 0.5$
2C ($\geq$2 tags)	$2.5 \pm 0.3 \pm 0.6$	$5.6 \pm 0.9 \pm 1.4$	$6.3 \pm 1.2 \pm 1.6$
Wc ($\geq$2 tags)	$0.40 \pm 0.08 \pm 0.10$	$1.5 \pm 0.4 \pm 0.4$	$2.1 \pm 0.6 \pm 0.5$

Background predictions for $P_J < 1\%$ and $P_J < 5\%$ are compared to the data in Tables 10.3 and 10.4, respectively.

Table 10.3: Summary of the background estimate in the double tag sample for $P_J < 1\%$.

Jet Multiplicity	2 jets	3 jets	≥ 4 jets
	Electroweak		
WW	0.05 ± 0.02	0.03 ± 0.02	0.006 ± 0.006
WZ	0.25 ± 0.05	0.03 ± 0.01	0.013 ± 0.006
ZZ	0.014 ± 0.005	0.001 ± 0.001	0.001 ± 0.001
Single Top $W-g$	0.17 ± 0.03	0.12 ± 0.03	0.05 ± 0.01
Single Top W^*	0.88 ± 0.17	0.14 ± 0.03	0.035 ± 0.007
$Z \to \tau^+\tau^-$	0.06 ± 0.06	0 ± 0	0 ± 0
Total	1.4 ± 0.3	0.33 ± 0.06	0.10 ± 0.02
	W + Heavy Flavour		
Wbb	6.2 ± 2.0	0.89 ± 0.29	0.61 ± 0.21
$Wc\bar{c}$	0.38 ± 0.17	0.13 ± 0.06	0.077 ± 0.046
Wc	0.13 ± 0.08	0.03 ± 0.03	0.02 ± 0.02
Total	6.7 ± 2.1	1.1 ± 0.3	0.71 ± 0.24
	Others		
Mistag	0.21 ± 0.05	0.10 ± 0.02	0.12 ± 0.03
Non-W	0.19 ± 0.12	0.03 ± 0.02	0.05 ± 0.03
Total Background	8.5 ± 2.3	1.5 ± 0.4	0.97 ± 0.25
Data	13	12	18

The iterative procedure described in Chapter 9 is applied, and we obtain a cross section of

$$\sigma_{t\bar{t}} = 11.1^{+2.3}_{-1.9}(\text{stat.})^{+2.5}_{-1.9}(\text{syst.}) \text{ pb}$$

for $P_J < 1\%$ and

$$\sigma_{t\bar{t}} = 11.6^{+1.7}_{-1.5}(\text{stat.})^{+2.4}_{-1.8}(\text{syst.}) \text{ pb}$$

for $P_J < 5\%$. Signal and background estimates after the iterative procedure are shown in Table 10.5, together with the observed number of events. Figure 10.1 compares the numbers of observed data to background and signal expectations for $P_J < 1\%$ and 5% for the measured $t\bar{t}$ production cross sections.

The statistical uncertainty on the measured cross section is dominated by the data sample size. Table 10.6 summarizes the systematic contributions to the cross section uncertainty.

Table 10.4: Summary of the background estimate in the double tag sample for $P_J < 5\%$.

Jet Multiplicity	2 jets	3 jets	≥ 4 jets
	Electroweak		
WW	0.29 ± 0.06	0.13 ± 0.04	0.07 ± 0.03
WZ	0.51 ± 0.10	0.06 ± 0.02	0.03 ± 0.01
ZZ	0.026 ± 0.007	0.004 ± 0.002	0.002 ± 0.001
Single Top $W-g$	0.39 ± 0.07	0.23 ± 0.04	0.09 ± 0.02
Single Top W^*	1.5 ± 0.3	0.26 ± 0.05	0.06 ± 0.01
$Z \to \tau^+\tau^-$	0.07 ± 0.07	0 ± 0	0 ± 0
Total	2.83 ± 0.51	0.70 ± 0.12	0.25 ± 0.05
	W + Heavy Flavour		
Wbb	11.5 ± 3.7	1.8 ± 0.6	1.2 ± 0.4
$Wc\bar{c}$	2.4 ± 0.9	0.61 ± 0.24	0.45 ± 0.19
Wc	0.98 ± 0.38	0.25 ± 0.11	0.19 ± 0.09
Total	14.9 ± 4.7	2.6 ± 0.8	1.9 ± 0.6
	Others		
Mistag	2.7 ± 0.9	1.0 ± 0.3	1.3 ± 0.4
Non-W	0.63 ± 0.34	0.09 ± 0.05	0.14 ± 0.09
Total Background	21.1 ± 5.1	4.4 ± 0.9	3.5 ± 0.7
Data	28	22	39

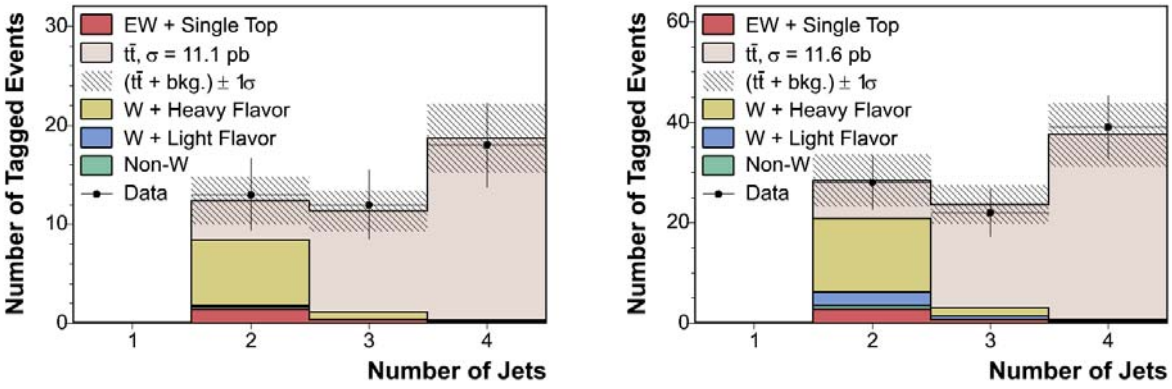

Figure 10.1: Double tag data and background contributions (for an integrated luminosity of 318 pb^{-1}) as a function of the event jet multiplicity for $P_J < 1\%$ (left) and $P_J < 5\%$ (right). A top mass of $m_t = 178$ GeV/c^2 is assumed.

10.2 Cross Section Dependence on the Top Quark Mass

We study the dependence of the $t\bar{t}$ cross section using the double tag sample on the top quark mass in an analogous way to Section 9.1. Results are shown in Fig. 10.2. A linear

Table 10.5: Summary of the final signal and background estimates and observed data in the double tag sample. MC derived refers to electroweak processes.

Jet Multiplicity	2 jets	3 jets	$\geq$ 4 jets
Pretag Data	4442	300	166
	$P_J < 1\%$		
MC Derived	1.4 ± 0.3	0.33 ± 0.06	0.10 ± 0.02
$Wb\bar{b}$	6.1 ± 1.9	0.57 ± 0.19	0.10 ± 0.03
$Wc\bar{c}$	0.38 ± 0.17	0.09 ± 0.04	0.013 ± 0.008
Wc	0.12 ± 0.08	0.02 ± 0.02	0.003 ± 0.003
Mistag	0.21 ± 0.05	0.06 ± 0.01	0.019 ± 0.004
Non-W	0.19 ± 0.12	0.03 ± 0.02	0.05 ± 0.03
Total Background	8.4 ± 2.2	1.1 ± 0.3	0.28 ± 0.06
$t\bar{t}$ (11.1 pb)	3.9 ± 0.9	10.2 ± 2.0	18.4 ± 3.4
Data	13	12	18
	$P_J < 5\%$		
MC Derived	2.83 ± 0.51	0.70 ± 0.12	0.25 ± 0.05
$Wb\bar{b}$	11.4 ± 3.6	1.1 ± 0.3	0.16 ± 0.05
$Wc\bar{c}$	2.3 ± 0.9	0.38 ± 0.15	0.06 ± 0.03
Wc	0.97 ± 0.37	0.16 ± 0.07	0.03 ± 0.01
Mistag	2.7 ± 0.8	0.65 ± 0.20	0.15 ± 0.05
Non-W	0.63 ± 0.34	0.09 ± 0.05	0.14 ± 0.09
Total Background	20.9 ± 5.0	3.1 ± 0.6	0.80 ± 0.15
$t\bar{t}$ (11.6 pb)	7.5 ± 1.5	20.5 ± 3.7	36.6 ± 6.1
Data	28	22	39

fit to the measured cross sections as a function of the top mass returns a slope of -0.096 ± 0.022 pb/(GeV/c^2) and -0.082 ± 0.019 pb/(GeV/c^2) for P_J <1% and P_J <5%, respectively, where the uncertainties are due to Monte Carlo simulation statistics. As before, note that the fit results for m_t = 178 GeV/c^2 agree with the measured cross section within the 1.6% uncertainty estimated in Chapter 8 due to different modeling in `PYTHIA` and `HERWIG`.

10.3 Comparison Between Single and Double Tag Cross Sections

Although the measurements of the single and double tag cross sections are statistically compatible, we observe a ratio of about 1.2 between the measured cross sections in the double and single tag samples. We use pseudo-experiments to estimate the probability to obtain a cross section greater than the measured double tag cross section when we assume that the measured single tag cross section is correct. For each pseudo-experiment, we vary

Table 10.6: Summary of the systematical uncertainties in the double tag analysis.

Source	Fractional Syst. Uncert. (%)	Contribution to $\sigma_{t\bar{t}}$ (%)	
		$P_J < 1\%$	$P_J < 5\%$
Central Electron ID	1.6	+0.98/-0.96	+0.98/-0.96
Central Muon ID	1.9	+0.60/-0.60	+0.61/-0.60
CMX Muon ID	1.8	+0.21/-0.21	+0.21/-0.21
PDF	2.0	+2.1/-2.0	+2.1/-2.0
Jet Energy Scale	4.2	+4.5/-4.1	+4.5/-4.1
Lepton Isolation	2.0	+2.1/-2.0	+2.1/-2.0
ISR/FSR	1.3	+1.3/-1.3	+1.3/-1.3
MC Modeling	1.6	+1.7/-1.6	+1.7/-1.6
Z Vertex	2.0	+2.1/-2.0	+2.1/-2.0
Tagging SF $P_J < 1\%$ (b's/c's)	8.6/12.9	+20.3/-14.7	—
Tagging SF $P_J < 5\%$ (b's/c's)	8.5/12.7	—	+18.3/-13.6
Mistag Asymmetry $P_J < 1\%$	11.0	+0.063/-0.063	—
Mistag Asymmetry $P_J < 5\%$	15.5	—	+0.44/-0.44
Non-W Fraction	50	0.060	0.092
Non-W Prediction	50	0.13	0.21
W+HF Prediction	30	0.84	1.0
Cross Sections Bkg.	1.8	0.027	0.030
Luminosity	5.9	+6.4/-5.7	+6.4/-5.7
Total Systematic Uncertainty		+22.2/-16.8	+20.4/-15.9

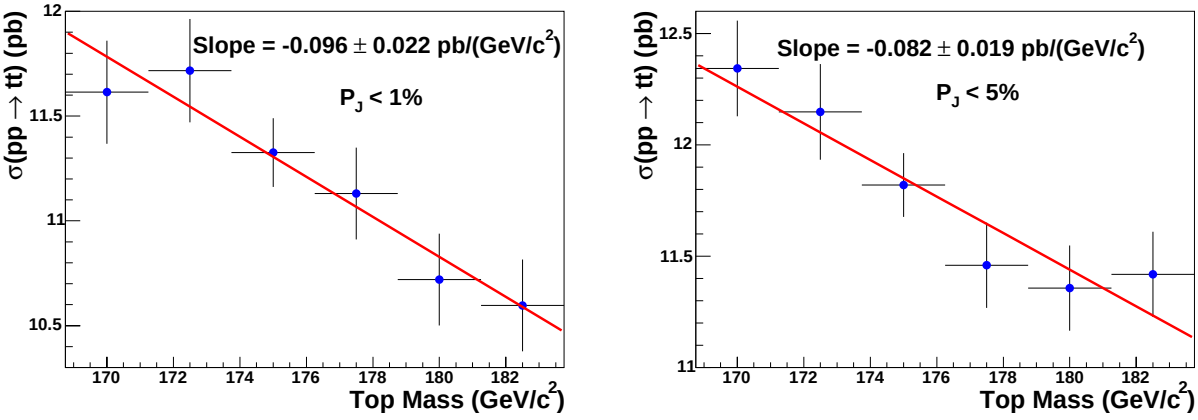

Figure 10.2: Top pair production cross sections as a function of the top quark mass for P_J <1% (left) and P_J <5% (right) in the double tag analysis. The uncertainties shown are the statistical uncertainties on the acceptances for each mass.

the total double tag background estimate according to a Gaussian distribution with a width equal to its uncertainty. Successively, we add the background to the expected signal by assuming the single tag $t\bar{t}$ cross section and we vary the total number of events according to a Poisson distribution. We repeat this procedure 10,000 times and count the number of pseudo-experiments in which we have a result greater than the one observed in data. We find a probability of 13.2% for $P_J < 1\%$ and 15.6% for $P_J < 5\%$.

The systematic uncertainty in the double tag measurement is dominated by the uncertainties on the acceptance, luminosity and tagging scale factor. The systematic uncertainties on the background prediction are negligible. A bias on the values of acceptance and luminosity would affect the cross section measurement in the single and double tag samples in the same way. However, a bias on the tagging scale factor would have a greater effect in the double tag analysis than in the single tag one. To study this, we vary the tagging scale factor by $\pm 1\sigma$ and we repeat the cross section measurements and the pseudo-experiments. Results are summarized in Tables 10.7 and 10.8. As expected, the cross sections measured in the double tag sample are more sensitive to a change in the scale factor, resulting in a better agreement between the single and double tag cross sections when a larger value for the scale factor is used.

Table 10.7: Cross section for $t\bar{t}$ event production in single and double tag analysis for $P_J < 1\%$ and $< 5\%$ and different values of the tagging scale factors (SF). Results are expressed in pb.

	SF - 1 σ	SF	SF + 1 σ
$P_J < 1\%$, $\geq$1 tag	$9.8^{+1.1}_{-1.0}(\text{stat.})^{+1.3}_{-1.1}(\text{syst.})$	$8.9^{+1.0}_{-1.0}(\text{stat.})^{+1.1}_{-1.0}(\text{syst.})$	$8.3^{+1.0}_{-0.9}(\text{stat.})^{+1.0}_{-0.9}(\text{syst.})$
$P_J < 1\%$, $\geq$2 tags	$13.3^{+2.8}_{-2.3}(\text{stat.})^{+3.3}_{-2.4}(\text{syst.})$	$11.1^{+2.3}_{-1.9}(\text{stat.})^{+2.5}_{-1.9}(\text{syst.})$	$9.4^{+2.0}_{-1.7}(\text{stat.})^{+2.0}_{-1.4}(\text{syst.})$
$P_J < 5\%$, $\geq$1 tag	$10.5^{+1.1}_{-1.0}(\text{stat.})^{+1.3}_{-1.2}(\text{syst.})$	$9.6^{+1.0}_{-0.9}(\text{stat.})^{+1.2}_{-1.1}(\text{syst.})$	$9.0^{+1.0}_{-0.9}(\text{stat.})^{+1.1}_{-1.0}(\text{syst.})$
$P_J < 5\%$, $\geq$2 tags	$13.7^{+2.0}_{-1.7}(\text{stat.})^{+3.3}_{-2.4}(\text{syst.})$	$11.6^{+1.7}_{-1.5}(\text{stat.})^{+2.4}_{-1.8}(\text{syst.})$	$9.9^{+1.5}_{-1.3}(\text{stat.})^{+2.0}_{-1.5}(\text{syst.})$

Table 10.8: Probability to measure a cross section greater than the one obtained in the double tag analysis when the $t\bar{t}$ cross section measured in the single tag analysis is assumed.

	SF - 1 σ	SF	SF + 1 σ
$P_J < 1\%$	4.5%	13.2%	30%
$P_J < 5\%$	2.8%	15.6%	35%

Chapter 11

Conclusions

The top quark is the most massive fundamental particle observed so far, and the study of its properties is interesting for several reasons ranging from its possible special role in electroweak symmetry breaking to its sensitivity to physics beyond the standard model (SM). In this thesis, we present a measurement of the $t\bar{t}$ production cross section in $p\bar{p}$ collisions at $\sqrt{s} = 1.96$ TeV with an integrated luminosity of 318 ± 18 pb^{-1}.

These data were recorded during Run II of the Tevatron, right now the source of the highest energy proton-antiproton collisions and the only apparatus capable of producing top quarks, by the CDF II detector, a general purpose detector which combines charged particle trackers, sampling calorimeters, and muon detectors.

The data sample has been collected by triggers based on the selection of a high transverse momentum lepton (electron or muon). CDF has a three-level trigger system to filter events from a 2.5 MHz beam crossing rate down to 60 Hz for permanent storage. The first two levels of triggers are special purpose hardware and the third consists of a farm of computers. The lepton identification is done, mostly, applying different tracking requirements. Jets are reconstructed from calorimieter towers information using a cone algorithm with radius $R = 0.4$.

The jet probability b-tagging algorithm is used to determine wheter a jet has been produced from the hadronization of a heavy or a light quark and, therefore, allows us to enhance the purity of the signal sample. This is an algorithm based on track impact parameter information which provides a continous variable in order to discrimate heavy flavor jets. Any b-tagging algorithm is characterized by the fraction of light jets that are identify as heavy flavor ones (mistag rate) and by the fraction of heavy flavor jets that are actually tagged (efficiency). The jet probability b-tagging algorithm has an efficiency for $t\bar{t}$ events around 55% while the mistag rate is $\sim 1\%$ (for $P_J < 1\%$).

We select events compatible with the $t\bar{t} \to l\nu q\bar{q}b\bar{b}$ decay mode by requiring one isolated electron (muon) with transverse energy E_T (p_T) > 20 GeV and missing transverse energy $\not\!\!E_T > 20$ GeV and at least three jets with transverse energy $E_T > 15$ GeV. We further require at least one jet tagged by the jet probability algorithm. This selection accepts an estimated $(3.5 \pm 0.3)\%$ of all $t\bar{t}$ events when a $P_J < 1\%$ cut is applied, and an estimated $(4.4 \pm 0.4)\%$ with a looser P_J cut at 5% (these efficiencies include the branching ratio for

$t\bar{t} \rightarrow e/\mu + jets$).

There are four different types of backgrounds to our signal events: $W+$ heavy flavor jets (a real W is produced in association with quarks or gluons), mistags (a light jet is misstagged as a heavy flavor one), non-W (events that have no real W bosons) and electroweak processes (dibosons, single top and $Z \rightarrow \tau^+\tau^-$). These backgrounds are estimated using data and Monte Carlo simulations.

The signal acceptance, fraction of $t\bar{t}$ events that satisfy all selection requirements, includes trigger and reconstruction efficiencies as well as the efficiencies of the kinematic selection and of the b-tagging algorithm. We measure it using a `PYTHIA` $t\bar{t}$ Monte Carlo sample generated with a top quark mass $m_t = 178$ GeV/c^2. For P_J cuts of 1% and 5%, the combined acceptance times integrated luminosity are, respectively, $11.00 \pm 0.05(\text{stat}) \pm 1.17(\text{syst})$ pb^{-1} and $13.89 \pm 0.06(\text{stat}) \pm 1.38(\text{syst})$ pb^{-1}.

Once we estimate the number of background events, we find good agreement with the observed data in a control region defined by events with W+one or two jets. Using the excess of events with three or more jets and at least one b tag with $P_J < 1\%$, we measure a top pair production cross section of

$$\sigma_{t\bar{t}} = 8.9^{+1.0}_{-1.0}(\text{stat.})^{+1.1}_{-1.0}(\text{syst.}) \text{ pb.}$$

As cross checks, we measure the cross section using samples with different b-tagging requirements. Using events with at least one b tag with $P_J < 5\%$ we obtain

$$\sigma_{t\bar{t}} = 9.6^{+1.0}_{-0.9}(\text{stat.})^{+1.2}_{-1.1}(\text{syst.}) \text{ pb.}$$

We also measure the $t\bar{t}$ production cross section in events with at least two tagged jets. In this case, the acceptance for signal events is estimated to be $(0.8 \pm 0.1)\%$ for $P_J < 1\%$ and $(1.5 \pm 0.3)\%$ for $P_J < 5\%$. We measure a cross section of

$$\sigma_{t\bar{t}} = 11.1^{+2.3}_{-1.9}(\text{stat.})^{+2.5}_{-1.9}(\text{syst.}) \text{ pb}$$

for $P_J < 1\%$ and

$$\sigma_{t\bar{t}} = 11.6^{+1.7}_{-1.5}(\text{stat.})^{+2.4}_{-1.8}(\text{syst.}) \text{ pb}$$

for $P_J < 5\%$.

Figure 11.1 shows our main result together with other CDF $t\bar{t}$ cross section measurements and theoretical predictions. Our result is above the central theoretical value by $\sim$1.9 σ. It should be noted that our result is highly correlated with the lepton+jets measurement using secondary vertex b-tagging, described in [140], where a comparison between the jet probability and secondary vertex b-taggers is given.

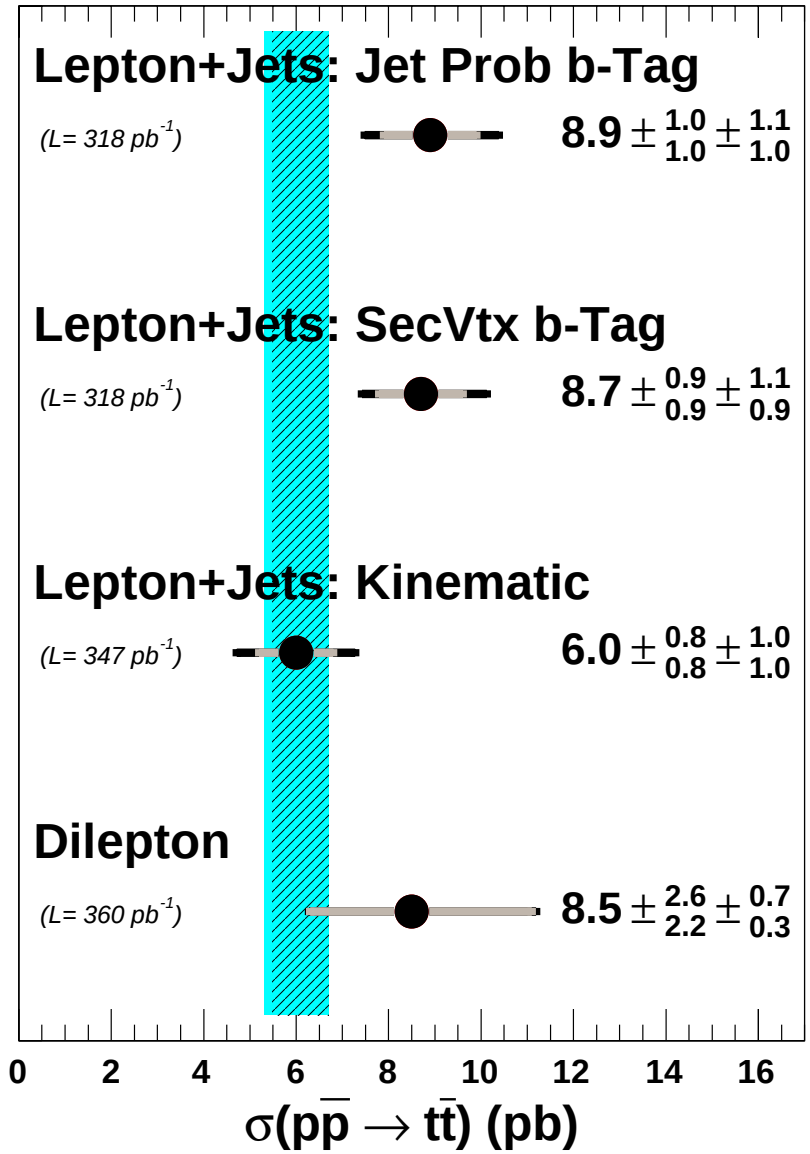

Figure 11.1: Comparison of the $t\bar{t}$ production cross section measurement presented in this paper with theoretical predictions (solid band [1], dashed band [4]). Also shown are the CDF results obtained in the lepton+jets channel when using the secondary vertex tagger [140] and when no b-tagging is applied (only kinematic information) [141], and the result obtained in the dilepton channel [142]. All the measured cross sections are evaluated at $m_t = 178$ GeV/c^2. The grey (black) lines represent the statistical (total) uncertainties. For the dilepton analysis, the grey (black) lines represent the uncertainties coming from the fit (shape).

Resumen

Introducción

El quark top es la partícula fundamental con más masa observada hasta ahora, y el estudio de sus propiedades es muy interesante por varias razones, desde el posible papel especial que juega en la ruptura de simetría de la teoría electrodébil hasta su sensibilidad a procesos físicos mas allá del modelo estándar. En particular, la medida de la sección eficaz de producción de pares top $\sigma_{t\bar{t}}$ es de gran interés como test de predicciones QCD. Cálculos recientes de QCD hechos con teorías perturbativas "next-to leading order" predicen $\sigma_{t\bar{t}}$ con una incertidumbre menor del 15% [1, 2], lo que sirve de motivación para medidas de una precisión comparable.

Según el modelo estándard, los pares de quarks top-antitop se producen en colisionadores hadrónicos bien via aniquilación quark-antiquark o bien por fusión gluón-gluón. En el colisionador del Tevatron en Fermilab, con una energía de centro de masas de 1.96 TeV en colisiones $p\bar{p}$, sobre el 85% de la producción total de pares top-antitop se debe a aniquilación quark-antiquark. A esta energía de centro de masas, la sección eficaz calculada, para la masa del top medida por el Tevatron en el Run I de 178 GeV/c^2 [3], es $6.1^{+0.6}_{-0.8}$ pb [1] y decrece aproximadamente unos 0.2 pb por cada incremento de 1 GeV/c^2 en el valor de la masa del top en el rango 170 GeV/c^2 $< m_t <$ 190 GeV/c^2.

El quark top del modelo estándard se desintegra, casi en un 100% de las veces, dando lugar a dos bosones W y dos jets b debidos a la fragmentación de quarks b. Cuando uno de los bosones W se desintegra leptónicamente y el otro se desintegra dando lugar a quarks, el suceso $t\bar{t}$ típicamente contiene un leptón cargado de alto momento, un neutrino que no se detecta y cuatro jets con alto momento transverso, dos de los cuales provienen de jets b. El neutrino no detectado da lugar a un desajuste en la energía transversa del suceso, que se conoce como "energía transversa perdida" ($\not\!\!E_T$). Este modo de desintegración se conoce como "leptón+jets".

En esta tesis, se describe la medida de la sección eficaz de producción de pares top-antitop en el canal leptón+jets con 318 pb^{-1} de datos de colisiones $p\bar{p}$ con $\sqrt{s} = 1.96$ TeV. Los datos han sido recogidos desde marzo del 2002 hasta septiembre del 2004, durante el Run II del Tevatron, por el detector CDF II, un detector de partículas de carácter general que combina sistemas de detección de trazas de partículas cargadas, calorímetros y detectores de muones.

Procesos en los que se produce un bosón W junto con varios jets con de alto momento transverso pueden ser confundidos como sucesos $t\bar{t}$ ya que presentan el mismo estado final.

Con el fin de separar los sucesos $t\bar{t}$ de estos sucesos de fondo, hemos desarrollado un método de etiquetado de jets b basado en información del sistema de trazas del detector de silicio. En la selección principal del suceso, pedimos que haya, al menos, un jet b.

Las contribuciones de fondo debidas a producción de sucesos con sabor fuerte, tales como $Wb\bar{b}$, $Wc\bar{c}$ or Wc, falsas identificaciones de bosones W, procesos electrodébiles y falsos etiquetados de jets b se calculan utilizando una combinación de cálculos con Monte Carlo y medidas independientes de muestras de control con datos. Se asume como señal de $t\bar{t}$ el exceso sobre el fondo en el número de sucesos con un leptón, energía perdida y tres o más jets con, al menos, un jet identificado como jet b. Este exceso se utiliza para medir la sección eficaz de producción $t\bar{t}$.

Teoría

En la actualidad, los quark top solo se producen en el Tevatron. El quark top es, de lejos, el más pesado de los seis quarks fundamentales en el modelo estándard de física de partículas. Como se muestra en la Fig. 2.1, el quark top es unas 40 veces más pesado que el segundo quark más pesado, el quark "bottom". Su gran masa hizo que su búsqueda fuera un largo proceso ya que eran necesarios aceleradores de muy alta energía. El descubrimiento del quark "bottom" en 1977 puso en evidencia la existencia de una tercera generación de quarks y dió lugar a una carrera por el descubrimiento del quark top, el cual tuvo lugar en 1995 en el colisionador $p\bar{p}$ del Tevatron en Fermilab. Después, se ha medido con gran precisión su masa dando como resultado $M_{\rm top} = (178.0 \pm 4.3)\,{\rm GeV}/c^2$ [10] [†]. La precisión relativa de esta medida (2.4%) es mejor que cualquiera de las del resto de quarks.

Su gran masa hace del top un campo ideal como prueba de física mas allá del modelo estándard. Aún es una pregunta abierta para los físicos de partículas si la masa observada es un producto de dinámica de partículas fundamentales todavía desconocida. Se ha sugerido que el quark top podría ser la llave para comprender cómo se genera la masa de las partículas mediante el mecanismo de ruptura de simetría electrodébil, ya que su masa es cercana a la escala de energía para la cual se produce la ruptura. El marco mas utilizado para describir la ruptura de simetría electrodébil es el mecanismo de Higgs. Las masas del bosón de Higgs, el bosón W y del quark top están relacionadas a través de correciones de alto nivel en varios procesos físicos. Por tanto, un conocimiento muy preciso de la masa del quark top, junto con otras medidas electrodébiles de precisión, puede ser utilizado para predecir la masa del bosón de Higgs.

Modelo Estándard

El Modelo Estándar (ME) de la física de partículas es una teoría de partículas fundamentales que describe las interacciones entre los componentes fundamentales de la materia,

[†] Recientemente, se ha medido la masa del quark top con aún más precisión obteniéndose $M_{\rm top} = (172.5 \pm 2.3)\,{\rm GeV}/c^2$ [11] (precisión relativa del 1.3%). En el trabajo presentado aqui, se asume un top quark del modelo estándard con una masa de $178\,{\rm GeV}/c^2$ ya que esta era la media mundial de la masa del top cuando se comenzó el análisis.

fermiones de spin 1/2, mediante el intercambio de bosones de spin 1.

El ME postula que la materia está formada por unos pocos constituyentes, básicos, puntuales y sin estructura llamados partículas fundamentales. Se puede distinguir dos grupos de partículas: quarks y leptones. Ambos son fermiones y tienen spin 1/2. Los quarks se pueden presentar en seis sabores diferentes: up, down, charm, strange, top y bottom; y están ligados por la interacción fuerte, formando hadrones de tres quarks de valencia (bariones), o de quark-antiquark (mesones). Por su parte, hay seis tipos distintos de leptones: el electrón (e^-) y el neutrino electrónico (ν_e), el muon (μ^-) y el neutrino muónico (ν_μ), el tau (τ^-) y el neutrino tauónico (ν_τ). Los quarks y leptones se pueden agrupar en tres generaciones como se muestra en la Tabla 2.1. En esta tabla se muestra también la carga y masa de estas partículas. Cada quark y leptón lleva asociado una antipartícula con la misma masa pero carga opuesta. Los antiquarks se denotan por $\bar{u}$, $\bar{d}$, etc. La antipartícula del electrón es el positrón (e^+).

Estas tres generaciones presentan una jerarquía de masas muy llamativa, siendo el top, con mucho, el quark más pesado. Comprender la razón detrás de esta jerarquía y la estructura de las generaciones es una de las preguntas abiertas de la física de partículas.

Las fuerzas de la naturaleza que actúan entre los quarks y los leptones se describen a través de campos cuantizados. Las interacciones entre partículas elementales se deben al intercambio de cuantos que son los mediadores de las fuerzas. El ME incorpora la fuerza electromagnética, responsable de la emisión de luz por parte de los átomos excitados, la fuerza débil, la causante, por ejemplo, de la desintegración nuclear beta, y la fuerza fuerte que mantiene a los núcleos estables. La gravitación no está incluida en el marco del ME sino por la teoría general de la relatividad. Todas las partículas con masa o energía sienten la fuerza gravitacional. Sin embargo, debido a la debilidad de la gravitación con respecto a las otras fuerzas que actúan en reacciones de partículas elementales, no se considera en esta tesis.

Las fuerzas electromagnética, débil, y fuerte se describen mediante las llamadas teorías cuánticas de campos gauge. Los cuantos de estos campos tienen spin 1 y se llaman bosones. La Tabla 2.2 muestra la carga y la masa de estos bosones. El mediador de la fuerza electromagnética es el fotón (γ) que es una partícula sin masa, los masivos $W^\pm$, $M_W = (80.425 \pm 0.038)$ GeV/c^2 [13], y el Z^0, $M_Z = (91.1876 \pm 0.0021)$ GeV/c^2 [13] son los mediadores de la fuerza débil y los ocho gluones (g), sin masa, de la fuerza fuerte.

Los quarks pueden experimentar interacción electromagnética, débil, y fuerte. Todos los leptones experimentan la interacción débil y los cargados también la electromagnética. Los leptones no toman parte en interacciones fuertes.

Topología de sucesos $t\bar{t}$

Como ya hemos dicho, el modo de desintegración dominante en el ME es $t \to W + b$, con una razón de desintegración cercana al 100%. En este caso, una vez que el quark top se ha desintegrado, un suceso $t\bar{t}$ presenta dos bosones W y dos quarks b. La Fig. 2.5 muestra el diagrama de Feynman para la producción de pares $t\bar{t}$ via aniquilación $q\bar{q}$ y la subsecuente desintegración del quark top. Experimentalmente, los sucesos $t\bar{t}$ se clasifican según el modo

de desintegración de los bosones W. Existen tres modos leptónicos ($e\nu_e$, $\mu\nu_\mu$, $\tau\nu_\tau$) y seis modos de desintegración dando lugar a quarks de diferente sabor ($u\bar{d}$, $u\bar{s}$, $u\bar{b}$, $c\bar{d}$, $c\bar{s}$, $c\bar{b}$). Se distinguen 4 categorías de suceso $t\bar{t}$:

1. Ambos bosones W se desintegran dando lugar a leptones (bien $e\nu_e$ o $\mu\nu_\mu$) que pueden ser detectados directamente. Esta categoría se llama canal dileptónico.

2. Un bosón W se desintegra leptónicamente a $e\nu_e$ o $\mu\nu_\mu$ y el otro a quarks. Este canal se llama leptón+jets y es el utilizado en esta tesis.

3. Ambos bosones W se desintegran dando lugar a quarks. Nos referiremos a este modo como canal hadrónico.

4. Al menos un bosón W se desintegra dando lugar a un leptón tau ($\tau\nu_\tau$) el cual puede desintegrarse bien leptónicamente ($e\nu_e$ or $\mu\nu_\mu$) o bien hadrónicamente.

Cada canal leptónico tiene una razón de desintegración de 1/9 mientras que la desintegración hadrónica tiene una razón de 6/9. Por tanto, para las cuatro categorías de sucesos $t\bar{t}$ descritas anteriormente se tiene las probabilidades listadas en la Tabla 2.3. (i) Modo dileptónico: 4/81, (ii) leptón+jets: 24/81, (iii) canal hadrónico: 36/81, (iv) modos con taus: 17/81.

Los cuatro tipos de sucesos $t\bar{t}$ presentan también cuatro topologias de suceso distinta. Así, el canal que nos ocupa en esta tesis, leptón+jets, se caracteriza por tener (1) exactamente un electrón o muón de alto momento, (2) energía transversa perdida, (3) dos jets b de las desintegraciones de los dos quark top y (4) dos jets adicionales de la desintegración de uno de los dos bosones W. La Fig. 2.6 muestra un suceso candidato del canal leptón+jets recogido por el detector CDF II. La gran ventaja de este canal es, además de su alta razón de desintegración de alrededor 30%, que la presencia de un leptón aislado reduce los fondos de QCD. Y, si además se pide que uno de los jets sea etiquetado como jet b, entonces se incrementa considerablemente el cociente señal sobre fondo.

Motivación

En el ME, la sección eficaz de producción $\sigma_{t\bar{t}}$ se calcula con una precisión de alrededor del 15% [27,28]. Además, el ME predice que el quark top se desintegra dando lugar a un bosón W y un quark b casi el 100% de las veces. Por tanto, medir la sección eficaz en todos los canales posibles es un test tanto del mecanismo de producción como de desintegración del quark top. Una desviación significativa de la predicción del ME indicaría bien la presencia de un nuevo mecanismo de producción o bien un nuevo mecanismo de desintegración.

La sección eficaz de producción de pares $t\bar{t}$ depende de la masa del quark top. En el intervalo de masas de $170 \leq M_{\rm top} \leq 190\,{\rm GeV}/c^2$, la sección eficaz se reduce aproximadamente 0.2 pb por cada incremento 1 GeV/c^2 en $M_{\rm top}$. Esta dependencia teórica se puede utilizar para convertir la medida de la sección eficaz en una determinación indirecta de la masa del quark top. Una medida con una incertidumbre aproximada del 15% en la sección eficaz es aproximadamente equivalente a medir la masa del quark top con una incertidumbre del 3%.

Se puede dar la vuelta a este argumento y utilizar las medidas de la sección eficaz y la masa del quark top para comprobar su compatibilidad con la sección eficaz predicha teóricamente y su dependecnia con la masa.

Por último, las medidas de la sección eficaz $t\bar{t}$ son fundamentales para el programa de física del top en el Tevatron puesto que estos análisis proporcionan muestras de datos enriquecidas en sucesos $t\bar{t}$ y son, por tanto, el cimiento de otras investigaciones de las propiedades del quark top.

Método

El análisis descrito en esta tesis mide la sección eficaz de producción de pares $t\bar{t}$ en el canal leptón+jets asumiendo un quark top del ME con una masa de 178 GeV/c^2 [10]. Como esta medida es sensible a la masa del quark top, se dará el resultado como una función de la misma.

El estado final de un suceso $t\bar{t}$ en el canal de leptón+jets presenta un electrón o muón de alto momento, energía transversa perdida y cuatro jets. La razón de desintegración de este canal es de alrededor el 30%, lo que es una de las ventajas sobre otros canales. Sin embargo, los fondos de W+jets son grandes y requieren distintas estrategias con el fin de incrementar el cociente señal sobre fondo.

El Tevatron y el detector CDF II

El análisis presentado en esta tesis utiliza los datos recogidos entre marzo del 2002 y septiembre del 2004 de colisiones protón-antiprotón producidas por el Tevatron y observadas por el detector CDF II.

El Tevatron es un complejo acelerador-colisionador de protones y antiprotones situado en Fermilab (Fermi National Accelerator Laboratory) en Batavia, Illinois (EEUU). Con una energía de centro de masas de $\sqrt{s} = 1.96$ TeV es, en la actualidad, la fuente de colisiones protón-antiprotón ($p\bar{p}$) a más alta energía y la única máquina capaz de producir pares top-antitop ($t\bar{t}$). Las colisiones tienen lugar en dos puntos del anillo, de cerca de 1 km de radio, bajo tierra: en CDF II y DØ. Este anillo es el útimo eslabón de una compleja cadena de aceleradores que produce y acelera haces de protones y antiprotones. Esta cadena de aceleradores se muestra en la Fig. 3.1.

El detector CDF II [100, 101] es una mejora sustancial respecto del detector original CDF [102]. Es un detector de partículas de carácter general. Está diseñado con el fin de detectar y medir las propiedades de las partículas producto de colisiones $p\bar{p}$. Un diagrama del detector CDF II se muestra en la Fig. 3.3. Como se ve, el detector está formado por tres subsistemas primarios: el sistema de trazas, el de calorimetría y el de muones.

La parte más interna es el sistema de trazas. Se trata de varios subsistemas (Layer00, Silicon Vertex Detector, Intermediate Silicon Layers y COT) con simetría cilíndrica y forma de barril. Está diseñado para detectar partículas cargadas, medir su momento y desplazamientos respecto del vértice de la colisión. El sistema de trazas está rodeado por el detector

de tiempo de vuelo, diseñado para proporcionar una buena identificación de partículas a bajo momento transverso. Estos dos sistemas se encuentran inmersos dentro de un solenoide superconductor capaz de generar un campo magnético de 1.4 T. Este imán está rodeado por el sistema de calorimetría, formado por calorímetros electromagnéticos y hadrónicos, que miden la energía de las partículas que interaccionan con la materia que lo forma. Y en la parte más externa del detector, rodeando al resto de subsistemas, se encuentran las cámaras de muones.

Muestra de datos y reconstrucción del suceso

Los datos utilizados en este análisis son de colisiones $p\bar{p}$ con una energía de centro de masas de $\sqrt{s}$ = 1.96 TeV recogidos por el detector CDF II desde marzo del 2002 hasta septiembre del 2004. Esta muestra de datos contiene electrones o muones de alto momento y corresponde con una luminosidad integrada de 318 pb^{-1}.

Para la selección del electrón pedimos, básicamente, una deposición de energía aislada en el calorímetro central con $E_{\rm T} > 20\,{\rm GeV}$ y asociada a una traza con $p_{\rm T} > 10\,{\rm GeV}/c$. Por su parte, los muones candidatos han de tener una traza en las cámaras de deriva con $p_{\rm T} > 20\,{\rm GeV}/c$ y que esté asociada a una traza en las cámaras de muones. Para mejorar la pureza de la selección de leptones se aplican otros cortes que se muestran en las Tablas 4.1 y 4.2.

Los jets utilizados son reconstruidos en el calorímetro utilizando un algoritmo de cono [125] con un radio $R \leq 0.4$. La energía de los jets es corregida [126] por la dependencia con la pseudo-rapidez de la respuesta del calorímetro, por la dependencia temporal del calorímetro y por extra E_T debida a interacciones múltiples. Los jets que utilizamos tienen energía corregida $E_T \geq 15$ GeV y detector $|\eta| < 2.0$. Detector η es la pseudo-rapidez del jet calculada con respecto al centro del detector.

La presencia de neutrinos en un suceso se deduce a partir de un desajuste en la energía transversa en el detector. La energía transversa perdida, $\not\!\!E_T$, se define como $-\sum_i [E_{T,i} cos(\phi_i), E_{T,i} sin(\phi_i)]$, donde $E_{T,i}$ es la energía transversa de la torre i del calorímetro calculada con respecto a la coordenada z del suceso, ϕ_i es su ángulo azimutal y la suma es sobre todas las torres del calorímetro. La $\not\!\!E_T$ está corregida restando el momento transverso de la traza del muón y añadiendo en las torres del calorímetro atravesadas por el muón.

El conocimiento de la aceptancia, eficiencias y fondos se basa en simulaciones detalladas de procesos físicos y de respuesta del detector. La aceptancia del detector para sucesos $t\bar{t}$ se modela utilizando `PYTHIA v6.2` [127] y `HERWIG v6.4` [128]. En este análisis, utilizamos el primero para el cálculo final de la sección eficaz y el segundo para el cálculo de errores sistemáticos debido a las diferencias en el modelado de la producción y desintegración de pares $t\bar{t}$. La simulación del detector CDF II reproduce la respuesta del detector y utiliza la misma geometría que en la reconstrucción del suceso. Las interacciones de las partículas al atravesar la materia se simulan con `GEANT3` [131]. El modelo de deriva en la COT utiliza una parametrización de `GARFIELD` [132]. Y la simulación del calorímetro utiliza la parametrización de `GFLASH` [133] junto con `GEANT3`.

El algoritmo Jet Probability

Mientras que cada suceso $t\bar{t}$ presenta dos quarks b, solo cerca del 2% del fondo de W+jets contiene un quark b. Por tanto, la señal de $t\bar{t}$ puede verse mejorada notablemente sin más que identificar jets b, jets provenientes de quarks b. En el análisis presentado en esta tesis, se ha utilizado el algoritmo Jet Probability como herramienta de etiquetado de jets b.

El algoritmo de etiquetado de jets b Jet Probability [135] se utiliza para determinar si un jet se ha producido debido al proceso de hadronización de un partón ligero o de un partón con sabor fuerte. En el segundo caso, se tiene como resultado hadrones con vida media grande cuya desintegración da lugar a trazas desplazadas del vértice primario de la interacción. Este algoritmo utiliza trazas asociadas con los jets para determinar la probabilidad de estos de provenir del vértice primario. El cálculo de la probabilidad está basado en el parámetro de impacto (d_0) de las trazas y su incertidumbre. El parámetro de impacto se define positivo o negativo dependiendo de la posición del punto de máxima aproximación entre la traza y el vértice primario con respecto a la dirección del jet, como se muestra en la Fig. 5.1. Por construcción, la probabilidad para trazas originadas en el vértice primario es una distribución uniforme entre 0 y 1. Para un jet proveniente de la hadronización de un quark con sabor pesado la distribución presenta un pico en 0 debido a trazas de partículas con gran vida media que tienen un gran parámetro de impacto con respecto al vértice primario.

Las partículas de un jet proveniente de un partón ligero se originan en el vértice primario, pero estas trazas se reconstruyen con un parámetro de impacto no nulo debido a la finita resolución del sistema de trazas. Estas trazas presentan una probabilidaed igual de tener signo positivo o negativo. Jets provenientes de un partón con sabor fuerte contienen hadrones con gran vida media que dan lugar a trazas desplazadas del vértice primario en la dirección del jet y que preferentemente ocupan el lado positivo de la distribución del parámetro de impacto. La anchura de la distribución de parámetro de impacto negativo es, por tanto, solamente debida a efectos de resolución del sistema de trazas.

Una característica de este algortimo es que utiliza una variable continua en vez de un objeto discreto como en los algoritmos con reconstrucción de vértice secundario. Esta variable es la probabilidad P_J de que un jet sea consistente con una hipótesis de vida media nula y viene dada por la ecuación 5.4.

Cualquier algoritmo de etiquetado de jets b queda caracterizado por la fracción de jets ligeros que son identificados como jets de sabor fuerte (mistag) y por la fracción de jets de sabor fuerte que son identificados como tales (eficiencia). El algoritmo de etiquetado Jet Probability, para $P_J < 1\%$, tiene una eficiencia de en torno al 55% para sucesos de $t\bar{t}$ mientras que el mistag es del $\sim 1\%$.

Selección del suceso

Como ya hemos dicho, los sucesos $t\bar{t}$ se caracterizan por la presencia de un electrón o muón de alto momento transverso, gran energía transversa perdida y cuatro jets energéticos. La selección básica de sucesos requiere la presencia de un electrón o muón, $\not\!\!E_T > 20$ GeV y jets con energía transversa corregida $E_T > 15$ GeV y $|\eta| < 2$.

Además, con el fin de seleccionar una muestra disjunta de la del canal dileptónico, rechazamos sucesos con más de un leptón identificado. Sucesos consistentes con $Z \to l^+l^-$ son también rechazados si un leptón y un segundo objeto forman una masa invariante en el rango [76, 106] GeV/c^2. Los sucesos cuyo vértice está en una posición z mas allá de 5 cm de la z de la traza del leptón son también rechazados. Además, para asegurarnos una buena reconstrucción del suceso, requerimos que la posición z del vértice del suceso esté a menos de 60 cm del centro del detector.

Los sucesos seleccionados con este criterio están dominados por producción QCD de bosones W asociados a jets. Para mejorar el cociente de señal sobre fondo para sucesos $t\bar{t}$ pedimos que haya, al menos, un jet en el suceso que sea identificado como jet b. Se espera que un suceso $t\bar{t}$ presente cuatro jets en el estado final pero, debido a la radiación de gluones, solapamiento de jets en el calorímetro e ineficiencias en la reconstrucción de jets, este número puede ser diferente. Por tanto, utilizamos los sucesos con tres o más jets, de los cuales uno es un jet b, para definir nuestra región de señal mientras que los sucesos con uno o dos jets son utilizados como muestra de control.

Con el fin de mejorar aún más la pureza de la muestra, realizamos dos cortes adicionales. Por un lado, pedimos que la suma escalar de todas las energías transversas del suceso (H_T) sea mayor de 200 GeV. Y, por otro, que la masa transversa reconstruida del bosón W, M_T^W, sea mayor de 20 GeV. Con este último corte, conseguimos mejorar la componente de W de la muestra y, por tanto, reducir el fondo de sucesos no W.

Los sucesos que pasan el criterio de selección descrito hasta ahora, a excepción del etiquetado de jet b, forman lo que se llama muestra "pretag". El número de sucesos observados en esta muestra junto con los sucesos candidatos después de pedir la presencia de, al menos, un jet con $P_J < 1\%$ y $P_J < 5\%$ se muestran en la Tabla 6.1 en función del número de jets del suceso.

Fondos

Además de los sucesos $t\bar{t}$, existen otro tipo de procesos que contribuyen en la muestra de sucesos candidatos de leptón+jets. Estos fondos son (i) sucesos con W+ jets de sabor fuerte, (ii) sucesos con W+ jets de quarks ligeros donde un jet es falsamente etiquetado como jet b, (iii) producción directa de QCD de quarks con sabor fuerte sin un bosón W asociado (non-W QCD), (iv) procesos electrodébiles (producción de dibosones, producción de quark top y $Z \to \tau^+\tau^-$). En la Fig. 7.1 se muestran diagramas de Feynman para cada uno de estos procesos.

La estimación de estos fondos se realiza utilizando tanto datos recogidos por el detector CDF II como simulaciones Monte Carlo.

Procesos electrodébiles

Estos procesos se estudian utilizando muestras de Monte Carlo. Los sucesos de dibosones (WW, WZ y ZZ) pueden contribuir a la muestra de señal si uno de los bosones se desintegra

leptónicamente y el otro lo hace dando lugar a quarks pesados. El proceso $Z \to \tau^+\tau^-$ también puede contribuir debido a desintegraciones leptónicas del tau. Finalmente, está la contribución de single top quarks producidos en asociación a un quark b, en los cuales un gluón inicial se desdobla a un par $b\bar{b}$ y el quark b interacciona con un W virtual.

Los números de sucesos estimados para estos procesos se calculan en base a su sección eficaz teórica (dadas en la Tabla 7.1), la luminosidad total integrada y las aceptancias y efficiencias de etiquetado calculadas a partir de la simulación Monte Carlo. Las predicciones finales para $P_J < 1\%$ (5%) se muestran en la Tabla 7.9 (Tabla 7.10) y equivalen al 2.5% (3.0%) del número total de sucesos en la región de señal.

Non-W

El fondo de non-W consiste en sucesos para los cuales la signatura de leptón+energía perdida ($\not\!\!E_T$) no es debida a la desintegración de un bosón W. La principal contribución en este tipo de fondo se debe a producción QCD de jets donde un jet es mal identificado como electrón y la energía perdida es debida a malas medidas de la energía de los jets.

Para estimar este fondo se definen cuatro zonas en el plano aislamiento-$\not\!\!E_T$ (ver Fig. 7.2) y se asume que el aislamiento del leptón y la $\not\!\!E_T$ del sucesos no están correlacionados de modo que el cociente entre el número de sucesos de non-W con bajo y alto aislamiento en la zona de pequeña $\not\!\!E_T$ es el mismo que en la zona de alta $\not\!\!E_T$.

Se espera que los sucesos de señal $t\bar{t}$ ocupen la región D mientras que los de non-W dominarán las regiones A, B y C. Por tanto, se puede estimar la fracción de sucesos en la región de señal que se deben a fondo de non-W siguiendo la ecuación 7.1.

El número de sucesos de non-W con jets identificados como jets b en la región de señal se puede calcular utilizando la ecuación 7.1 y el número de sucesos con jets identificados como jets b en las regiones dominadas por el fondo de non-W. Los resultados se muestran en la Tabla 7.4.

W+ jets de sabor fuerte

Este fondo consiste en sucesos que presentan un bosón W real asociado a quarks con sabor fuerte. Estos se pueden originar bien en sucesos $q_1\bar{q}_2 \to W + g$ donde el gluon da lugar a pares $b\bar{b}$ o $c\bar{c}$ o bien en sucesos $gq \to Wc$.

Esta es la principal fuente de sucesos de fondo. La contribución de sucesos de W+ jets de sabor fuerte se calcula utilizando la fracción de sabor fuerte en la producción de bosones W asociados con partones y las eficiencias de etiquetado para estos procesos, y normalizando por el número de sucesos observados en la muestra pretag. El número de sucesos estimados debido a esta contribución se muestra en la Tabla 7.8.

W+ jets de sabor ligero

Sucesos en los que un jet de sabor ligero es identificado como jet de sabor fuerte también contribuyen a la muestra de señal. El número de sucesos en la muestra pretag con etiquetados

negativos podría ser una estimación de este fondo pero presenta el problema de tener una gran incertidumbre estadística. En vez de esto, se cuentan los sucesos en la muestra pretag y se pesan por la probabilidad de estos de tener, al menos, un jet mal identificado. Esta probabilidad se calcula aplicando la matriz de etiquetado negativo a todos los jets "taggable" de la muestra.

Una vez hecha esta estimación, se escala por uno menos la fracción de sucesos pretag que son debidos a fondos electrodébiles y de non-W. La contribución de este fondo a la muestar de leptón+jets cuando se requiere la presencia de un jet con $P_J < 1\%$ (5%) se muestra en la Tabla 7.9 (Tabla 7.10).

Aceptancia

La aceptancia de señal, o eficiencia de detección de sucesos $t\bar{t}$, se define como la fracción de sucesos $t\bar{t}$ que satisfacen todos los requisitos de la selección incluyendo tanto eficiencias de reconstrucción y de trigger como eficiencias de la selección cinemática y del algortimo de etiquetado. Se mide utilizando una muestra de Monte Carlo de $t\bar{t}$ generada asumiendo una masa del quark top de 178 GeV/c^2. Matemáticamente se expresa como

$$\epsilon_{t\bar{t}} = (A_{t\bar{t}} \times K_{lep} \times \epsilon_{trig} \times \epsilon_{z_0} \times \epsilon_{zvtx}) \times \epsilon_{b-tag} = \epsilon_{t\bar{t}}^{\mathrm{pretag}} \times \epsilon_{b-tag} \tag{1}$$

donde $A_{t\bar{t}}$ es la fracción de sucesos $t\bar{t}$ generados en Monte Carlo que pasan los requisitos cinemáticos (excepto etiquetado de jets b) e incluye la fracción de desintegración del proceso $t\bar{t} \to e/\mu + jets$, K_{lep} es el factor de escala que tiene en cuenta la diferencia en la eficiencia de identificación de leptones entre datos y Monte Carlo, ϵ_{trig} es la eficiencia de trigger de identificar leptones de alto momento, ϵ_{z_0} y ϵ_{zvtx} son las eficiencias de los cortes en la z del vértice del suceso y ϵ_{b-tag} es la eficiencia de etiquetar al menos un jet en un suceso $t\bar{t}$.

La Tabla 8.1 muestra los distintos factores de la aceptancia de sucesos $t\bar{t}$. Para los cortes de P_J de 1% y 5%, la aceptancia final (multiplicada por la luminosidad integrada) es de, respectivamente, $11.00 \pm 0.05(\mathrm{stat}) \pm 1.17(\mathrm{syst})$ pb^{-1} y $13.89 \pm 0.06(\mathrm{stat}) \pm 1.38(\mathrm{syst})$ pb^{-1}.

Resultados

Para medir la sección eficaz hacemos uso de la expresión

$$\sigma_{t\bar{t}} = \frac{N_{obs} - N_{bck}}{\epsilon_{t\bar{t}} \times \int L\ dt}, \tag{2}$$

donde N_{obs} es el número de sucesos observados con al menos un jet etiquetado como b, N_{bck} es el número de sucesos estimados como fondo en la región de señal, $\epsilon_{t\bar{t}}$ es la aceptancia de señal (incluyendo la eficiencia de etiquetado) y $\int L\ dt$ es la luminosidad total integrada. Por

tanto, teniendo en cuenta la estimación de sucesos de fondo dada en la Tabla 7.9 se tiene que, para $P_J < 1\%$, la sección eficaz de producción de pares $t\bar{t}$ es de

$$\sigma_{t\bar{t}} = 8.9^{+1.0}_{-1.0}(\text{stat.})^{+1.1}_{-1.0}(\text{syst.})\ \text{pb}.$$

Del mismo modo, teniendo en cuenta la estimación de sucesos de fondo dada en la Tabla 7.9 se tiene que, para $P_J < 5\%$, la sección eficaz de producción de pares $t\bar{t}$ es de

$$\sigma_{t\bar{t}} = 9.6^{+1.0}_{-0.9}(\text{stat.})^{+1.2}_{-1.1}(\text{syst.})\ \text{pb}.$$

La estimación final de sucesos de señal y fondo así como el número observado de sucesos candidatos se muestra en la Tabla 9.1.

Como se ha dicho en el apartado anterior, la aceptancia utilizada en este análisis se ha calculado utilizando una muestra de sucesos $t\bar{t}$ generada asumiendo una masa del quark top de 178 GeV/c^2, que se corresponde con la medida combinada del Run I del Tevatron. Por tanto, es necesario estudiar la dependencia de la sección eficaz de producción en función de la masa del quark top. Esta dependencia se muestra en la Fig. 9.2. Un ajuste lineal de la sección eficaz medida en función de la masa del top da como resultado una pendiente de -0.052 $\pm$ 0.008 pb/(GeV/c^2) y -0.066 $\pm$ 0.008 pb/(GeV/c^2) para P_J <1% y 5% respectivamente.

Por último, con el fin de aumentar la pureza de la muestra de señal, se puede requerir la presencia de al menos dos jets b en el suceso. Así, se puede repetir el análisis requiriendo la presencia de 2 jets b en vez de 1 obteniéndose un valor para la sección eficaz de

$$\sigma_{t\bar{t}} = 11.1^{+2.3}_{-1.9}(\text{stat.})^{+2.5}_{-1.9}(\text{syst.})\ \text{pb}$$

para $P_J < 1\%$ y

$$\sigma_{t\bar{t}} = 11.6^{+1.7}_{-1.5}(\text{stat.})^{+2.4}_{-1.8}(\text{syst.})\ \text{pb}$$

para $P_J < 5\%$. Las estimaciones de señal y fondo en este caso se muestran en la Tabla 10.5, junto con el número observado de sucesos candidatos.

Conclusiones

El quark top es la partícula fundamental con más masa observada hasta ahora, y el estudio de sus propiedades es muy interesante por varias razones, desde el posible papel especial que juega en la ruptura de simetría de la teoría electrodébil hasta su sensibilidad a procesos físicos mas allá del modelo estándar.

En esta tesis, se describe la medida de la sección eficaz de producción de pares top-antitop en el canal leptón+jets con 318 pb^{-1} de datos de colisiones $p\bar{p}$ con $\sqrt{s} = 1.96$ TeV. Los datos han sido recogidos desde marzo del 2002 hasta septiembre del 2004, durante el Run II del Tevatron, por el detector CDF II, un detector de partículas de carácter general que combina sistemas de detección de trazas de partículas cargadas, calorímetros y detectores de muones.

Con el fin de mejorar la pureza de la muestra, se utiliza el algoritmo Jet Probability como herramienta de etiquetado de jets b. Este algoritmo determina, en base a información

del parámetro de impacto de las trazas y utilizando una variable continua, si un jet se ha producido debido al proceso de hadronización de un partón ligero o de un partón con sabor fuerte.

La selección básica de sucesos requiere la presencia de un electrón o muón de alto momento transverso, $\not\!\!E_T > 20$ GeV y jets con energía transversa corregida $E_T > 15$ GeV y $|\eta| < 2$.

Pero, además de los sucesos $t\bar{t}$, existen otro tipo de procesos que contribuyen en la muestra de sucesos candidatos de leptón+jets y que es necesario estimar. Para ello, se utilizan datos y simualaciones Monte Carlo.

Finalmente, se tiene que, para $P_J < 1\%$, la sección eficaz de producción de pares $t\bar{t}$ es de

$$\sigma_{t\bar{t}} = 8.9^{+1.0}_{-1.0}(\text{stat.})^{+1.1}_{-1.0}(\text{syst.})\ \text{pb},$$

valor consistente con otras medidas realizadas aplicando un criterio distinto en la identificación de jets b. Este resultado, como muestra la Fig. 11.1, también es consistente con otras medidas llevadas a cabo en CDF y también con la predicción teórica.

Appendix A

Alternative Determination of the Scale Factor

The b-tagging scale factor and its uncertainty are crucial elements in the single and specially the double tag analysis. Because of this, we use another method to check the results obtained in Section 5.1. We select events containing an electron jet and an away jet as defined in Section 5.1. Since heavy flavor particles are often produced in pairs, the contamination of light quark jets can be reduced by requiring the away jet to be tagged. The efficiency to tag a b jet can be measured using the electron jets for events where the away jet is tagged (a "double tag" method) and for events where no tag is required for the away jet (a "single tag" method). In both methods one needs to measure the fraction of electron jets which contain heavy flavor, leading to a significant systematic uncertainty. The advantage of the double tag methods is that the systematic uncertainty due to the heavy flavor fraction determination is smaller.

The method described in this appendix differs from both single and double tag methods in that it does not require the knowledge of the heavy flavor fraction in the data sample as an input. Instead, by assuming that the tagging efficiencies for heavy flavor jets are uncorrelated with the characteristics of the recoiling jet, or, in other words, that the scale factor obtained from a single tag method and a double tag method are equivalent, one can solve for the scale factor directly. This assumption is made as well in the determination of the $t\bar{t}$ cross section, where the SF calculated from a double tag method is applied to the single tag analysis. We also assume that the b and c jets are sufficiently similar in data and Monte Carlo that we can determine a single scale factor for both.

A.1 Notation

- N refers to the number of data events in a certain (tag) category; the category is indicated by superscripts and subscripts.
- F refers to the fraction of data events of a certain (flavor) type; this type is indicated by superscripts and subscripts.

- N_{mc} and F_{mc} are correspondingly defined for Monte Carlo events.
- N_{conv} and F_{conv} are correspondingly defined for events where the electron has an opposite sign conversion partner.

and superscripts refer to the tag or flavor of the electron jet and subscripts refer to the tag or flavor of the away jet. An omitted superscript or subscript implies no requirement on that jet; or equivalently, a sum over all possible superscripts and subscripts on that quantity. Hence $F^H \equiv F^H_L + F^H_H$ and $N_+ \equiv N^+_+ + N^-_+ + N^0_+$.

- $(\epsilon^{+H}, \epsilon^{-H})$ are positive and negative tagging efficiencies for heavy flavor electron jets in data.
- $(\epsilon^+_H, \epsilon^-_H)$ are positive and negative tagging efficiencies for heavy flavor away jets in data.
- $(\epsilon^{+L}, \epsilon^{-L})$ are positive and negative tagging efficiencies for light flavor electron jets in data.
- $(\epsilon^+_L, \epsilon^-_L)$ are positive and negative tagging efficiencies for light flavor away jets in data.
- $\beta \equiv (\epsilon^{+L}/\epsilon^{-L})$ is a factor designed to account for the asymmetry in light flavor L_{xy} distributions.
- $\alpha \equiv (\epsilon^+_L/\epsilon^-_L)$ is the corresponding factor for electron jets.
- (e^H, e^L) are the probabilities that an opposite sign conversion is found in a (heavy,light) flavor e-jet.

A.2 Calculation

From the basic equations for any event with an A tag on the e-jet and a B tag on the a-jet, we have

$$N^A_B = N \sum_{i,j=(H,L)} (\epsilon^A)^i (\epsilon^B)_j F^i_j \tag{A.1}$$

$$1 = \sum_{i,j=(H,L)} F^i_j. \tag{A.2}$$

Therefore, for any event with a tag, we can write for the away jet (a-jet):

$$N_+ = N(\epsilon^+_H F_H + \epsilon^+_L F_L) \tag{A.3}$$

$$N_- = N(\epsilon^-_H F_H + (\epsilon^+_L/\alpha) F_L) \tag{A.4}$$

hence

$$N_+ - \alpha N_- = N(\epsilon^+_H - \alpha\epsilon^-_H) F_H. \tag{A.5}$$

And the same for the electron jet (e-jet):

$$N^+ = N(\epsilon^{+H}F^H + \epsilon^{+L}F^L) \quad (A.6)$$
$$N^- = N(\epsilon^{-H}F^H + (\epsilon^{+L}/\beta)F^L) \quad (A.7)$$

hence

$$N^+ - \beta N^- = N(\epsilon^{+H} - \beta\epsilon^{-H})F^H. \quad (A.8)$$

Here, α is the ratio of $\epsilon_L^+/\epsilon_L^-$ for the a-jet, believed to be independent of the e-jet characteristics, and $\beta = \epsilon^{+L}/\epsilon^{-L}$is the same ratio for the e-jets. These ratios are different from one due to material interactions and long-lived particles.

Similarly for double tag events one can write:

$$N_+^+ = N(\epsilon_H^+(\epsilon^{+H}F_H^H + \epsilon^{+L}F_H^L) + \epsilon_L^+(\epsilon^{+H}F_L^H + \epsilon^{+L}F_L^L)) \quad (A.9)$$
$$N_-^+ = N(\epsilon_H^-(\epsilon^{+H}F_H^H + \epsilon^{+L}F_H^L) + (\epsilon_L^+/\alpha)(\epsilon^{+H}F_L^H + \epsilon^{+L}F_L^L)) \quad (A.10)$$

hence,

$$N_+^+ - \alpha N_-^+ = N((\epsilon_H^+ - \alpha\epsilon_H^-)(\epsilon^{+H}F_H^H + \epsilon^{+L}F_H^L)) \quad (A.11)$$
$$N_+^- = N(\epsilon_H^+(\epsilon^{-H}F_H^H + (\epsilon^{+L}/\beta)F_H^L) + \epsilon_L^+(\epsilon^{-H}F_L^H + (\epsilon^{+L}/\beta)F_L^L)) \quad (A.12)$$
$$N_-^- = N(\epsilon_H^-(\epsilon^{-H}F_H^H + (\epsilon^{+L}/\beta)F_H^L) + (\epsilon_L^+/\alpha)(\epsilon^{-H}F_L^H + (\epsilon^{+L}/\beta)F_L^L)) \quad (A.13)$$

hence,

$$N_+^- - \alpha N_-^- = N((\epsilon_H^+ - \alpha\epsilon_H^-)(\epsilon^{-H}F_H^H + (\epsilon^{+L}/\beta)F_H^L)) \quad (A.14)$$

and,

$$N_+^+ - \alpha N_-^+ - \beta(N_+^- - \alpha N_-^-) = N(\epsilon_H^+ - \alpha\epsilon_H^-)(\epsilon^{+H} - \beta\epsilon^{-H})F_H^H \quad (A.15)$$

so, dividing this by Equation A.5, we have

$$\frac{(N_+^+ - \alpha N_-^+) - \beta(N_+^- - \alpha N_-^-)}{(N_+ - \alpha N_-)} = (\epsilon^{+H} - \beta\epsilon^{-H})\frac{F_H^H}{F_H}. \quad (A.16)$$

The fraction $\frac{F_H^H}{F_H}$ can be rewritten as $(1 - \frac{F_H^L}{F_H})$ using Equation A.2 , so

$$\frac{(N_+^+ - \alpha N_-^+) - \beta(N_+^- - \alpha N_-^-)}{(N_+ - \alpha N_-)(1 - \frac{F_H^L}{F_H})} = (\epsilon^{+H} - \beta\epsilon^{-H}). \quad (A.17)$$

Now, using the rate of identified conversions to distinguish between light and heavy flavor e-jets one can determine $(N_+ - \alpha N_-)(F_H^L/F_H)$. If the conversion finder is uncorrelated with

the tagger algorithm, then the probability to find that the electron is a conversion in a given event only depends on the flavor of the electron jet.

$$\begin{aligned} N_{conv} &= N(e^H F^H + e^L F^L) && \text{(A.18)} \\ N^+_{conv} &= N(e^H \epsilon^{+H} F^H + e^L (\epsilon^{+L}) F^L) \\ N^-_{conv} &= N(e^H \epsilon^{-H} F^H + e^L (\epsilon^{+L}/\beta) F^L), \quad \text{so} \\ N^+_{conv} - \beta N^-_{conv} &= N(e^H (\epsilon^{+H} - \beta \epsilon^{-H}) F^H). && \text{(A.19)} \end{aligned}$$

Similarly

$$\begin{aligned} N_{conv+} &= N(e^H(\epsilon^+_H F^H_H + \epsilon^+_L F^H_L) + e^L(\epsilon^+_H F^L_H + \epsilon^+_L F^L_L) && \text{(A.20)} \\ N_{conv-} &= N(e^H(\epsilon^-_H F^H_H + (\epsilon^+_L/\alpha) F^H_L) + e^L(\epsilon^-_H F^L_H + (\epsilon^+_L \alpha) F^L_L) \quad \text{so} \\ N_{conv+} - \alpha N_{conv-} &= n(e^H(\epsilon^+_H - \alpha\epsilon^-_H) F^H_H + e^L(\epsilon^+_H - \alpha\epsilon^-_H) F^L_H). && \text{(A.21)} \end{aligned}$$

Now, by Equation A.5,

$$e^H(N_+ - \alpha N_-) = N(e^H(\epsilon^+_H - \alpha\epsilon^-_H) F^H_H + e^H(\epsilon^+_H - \alpha\epsilon^-_H) F^L_H). \quad \text{(A.22)}$$

and, subtracting Equations A.21 and A.22,

$$N_{conv+} - \alpha N_{conv-} - e^H(N_+ - \alpha N_-) = N(e^L - e^H)(\epsilon^+_H - \alpha\epsilon^-_H) F^L_H. \quad \text{(A.23)}$$

Since quite obviously $e^H N = N\ (e^H F^H + e^H F^L)$, using Equation A.18 we have

$$N_{conv} - e^H N = N(e^L - e^H) F^L \quad \text{(A.24)}$$

and, using this to divide Equation A.23,

$$\frac{N_{conv+} - \alpha N_{conv-} - e^H(N_+ - \alpha N_-)}{N_{conv} - e^H N} = (\epsilon^+_H - \alpha\epsilon^-_H)\frac{F^L_H}{F^L} \quad \text{(A.25)}$$

e^H is easily found from Equation A.19, since the left-hand side is $e^H(N^+ - \beta N^-)$. Hence

$$\frac{N_{conv+} - \alpha N_{conv-} - \left(\frac{N^+_{conv} - \beta N^-_{conv}}{N^+ - \beta N^-}\right)(N_+ - \alpha N_-)}{N_{conv} - \left(\frac{N^+_{conv} - \beta N^-_{conv}}{N^+ - \beta N^-}\right) N} = (\epsilon^+_H - \alpha\epsilon^-_H)\frac{F^L_H}{F^L} \quad \text{(A.26)}$$

or

$$\frac{(N_{conv+} - \alpha N_{conv-})(N^+ - \beta N^-) - (N^+_{conv} - \beta N^-_{conv})(N_+ - \alpha N_-)}{N_{conv}(N^+ - \beta N^-) - N(N^+_{conv} - \beta N^-_{conv})} = (\epsilon^+_H - \alpha\epsilon^-_H)\frac{F^L_H}{F^L}. \quad \text{(A.27)}$$

Then, we write, for simplicity,

$$\frac{(N_{conv+} - \alpha N_{conv-})(N^+ - \beta N^-) - (N^+_{conv} - \beta N^-_{conv})(N_+ - \alpha N_-)}{N_{conv}(N^+ - \beta N^-) - N(N^+_{conv} - \beta N^-_{conv})} \equiv \chi. \quad \text{(A.28)}$$

And after some algebra we have

$$NF^L\chi = (N_+ - \alpha N_-)\frac{F_H^L}{F_H},$$

but from Equation A.2, $F^L = (1 - F^H)$, so

$$N(1 - F^H)\chi = (N_+ - \alpha N_-)\frac{F_H^L}{F_H}. \tag{A.29}$$

Using this and applying the definition of the scale factor, one can write

$$\frac{(N_+^+ - \alpha N_-^+) - \beta(N_+^- - \alpha N_-^-)}{(N_+ - \alpha N_-) - N(1 - F^H)\chi} = (SF)(\epsilon_{mc}^{+H} - \beta\epsilon_{mc}^{-H}) \tag{A.30}$$

From definitions (see Equation A.8), we can write the scale factor as follows:

$$SF = \frac{N^+ - \beta N^-}{NF^H} \div \frac{N_{mc}^+ - \beta N_{mc}^-}{N_{mc}F_{mc}^H} \tag{A.31}$$

or

$$F^H = \frac{N^+ - \beta N^-}{N(SF)}\frac{N_{mc}F_{mc}^H}{N_{mc}^+ - \beta N_{mc}^-}. \tag{A.32}$$

Substituting F^H into equation A.30 and rearranging the expression to solve for the scale factor, we finally obtain:

$$SF = \frac{\frac{(N_+^+ - \alpha N_-^+) - \beta(N_+^- - \alpha N_-^-)}{\frac{(N_{mc+}^+ - \alpha N_{mc-}^+) - \beta(N_{mc+}^- - \alpha N_{mc-}^-)}{(N_{mc+} - \alpha N_{mc-})(1 - F_{mcH}^L/F_{mcH})}} - \chi\frac{N^+ - N^-}{N_{mc}^+ - \beta N_{mc}^-}(N_{mc}F_{mc}^H)}{(N_+ - \alpha N_-) - N\chi} \tag{A.33}$$

with

$$\chi \equiv \frac{(N^+ - \beta N^-)(N_{conv+} - \alpha N_{conv-}) - (N_+ - \alpha N_-)(N_{conv}^+ - \beta N_{conv}^-)}{N_{conv}(N^+ - \beta N^-) - N(N_{conv}^+ - \beta N_{conv}^-)}. \tag{A.34}$$

A.3 Results

Since all the magnitudes in the right hand side of Equation A.33 are measurable, we can calculate the value of the sacle factor. For $P_J < 1\%$, we have a value of

$$SF = 0.826 \pm 0.023\ (stat.) \pm 0.018\ (stat.MC) \pm 0.050\ (syst.)$$

and of

$$SF = 0.857 \pm 0.027\ (stat.) \pm 0.016\ (stat.MC) \pm 0.050\ (syst.)$$

for $P_J < 5\%$. These numbers are in good agreement within the uncertainties with the values obtained in sections 5.1.

Once we calculate the scale factor, we can obtain the heavy flavor fraction and the double tag efficiency. Table A.1 summarizes the scale factor, heavy flavor fraction and efficiencies for $P_J < 1$ and 5%.

Table A.1: Scale factors, heavy flavor fraction and efficiencies for data and Monte Carlo for $P_J < 1$ and 5%.

P_J cut	Scale Factor	Heavy Flavor Fraction	Efficiency (Data)	Efficiency (MC)
$P_J < 1\%$	0.83 ± 0.03	0.218 ± 0.002	0.264 ± 0.006	0.319 ± 0.005
$P_J < 5\%$	0.86 ± 0.03	0.230 ± 0.003	0.340 ± 0.006	0.397 ± 0.005

Appendix B

Kinematic Distributions

We compare the distributions for different kinematic variables observed in data to the expectations for signal and backgrounds derived from a combination of simulation and $t\bar{t}$ cross section measurements. Figures B.1 to B.4 show the results for the four samples of events passing the selection criteria with at least three jets and one or two tags for $P_J < 1\%$ or $P_J < 5\%$. The considered kinematic variables are the sum of the transverse energies of each object in the final state (H_T), the reconstructed transverse mass of the W boson, the missing transverse energy ($\not\!\!E_T$) of the event, the E_T of the lepton, the transverse energy of the tagged jets, and the pseudo-rapidity of the tagged jets with respect to the center of the detector. Kolmogorov-Smirnov (KS) probabilities are computed to test the agreement between observed and expected distributions. The distributions observed in the data are statistically consistent with the expected signal-plus-background distributions.

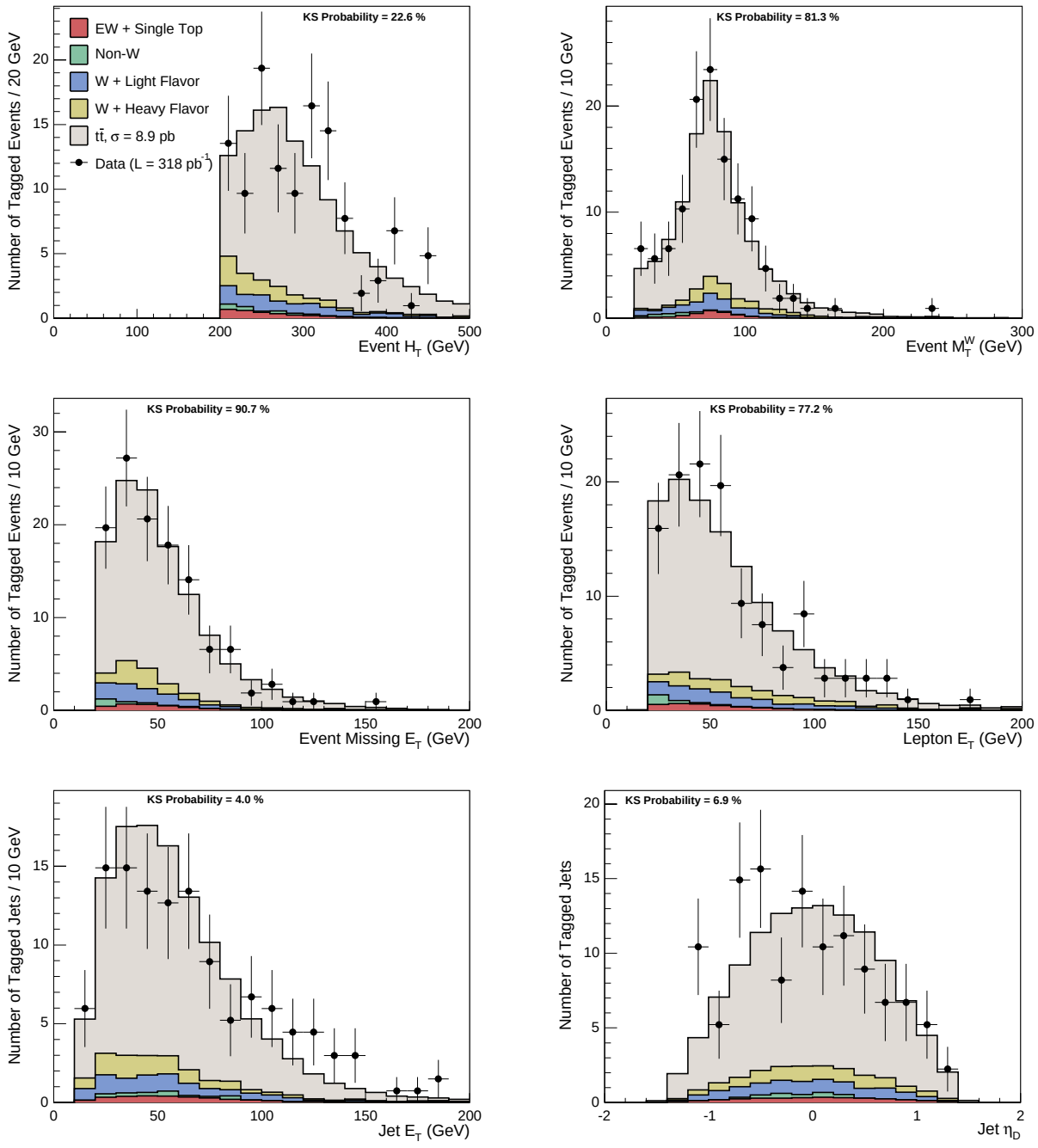

Figure B.1: Comparison of kinematic distributions in data to signal and background expectations for events passing the selection criteria with at least three jets and at least one tag for $P_J < 1\%$. From the top-left corner: sum of the transverse energies of each object in the final state (H_T), reconstructed transverse mass of the W boson, missing transverse energy ($\not\!\!E_T$), lepton E_T, transverse energy of the tagged jets, and the pseudo-rapidity of the tagged jets with respect to the center of the detector.

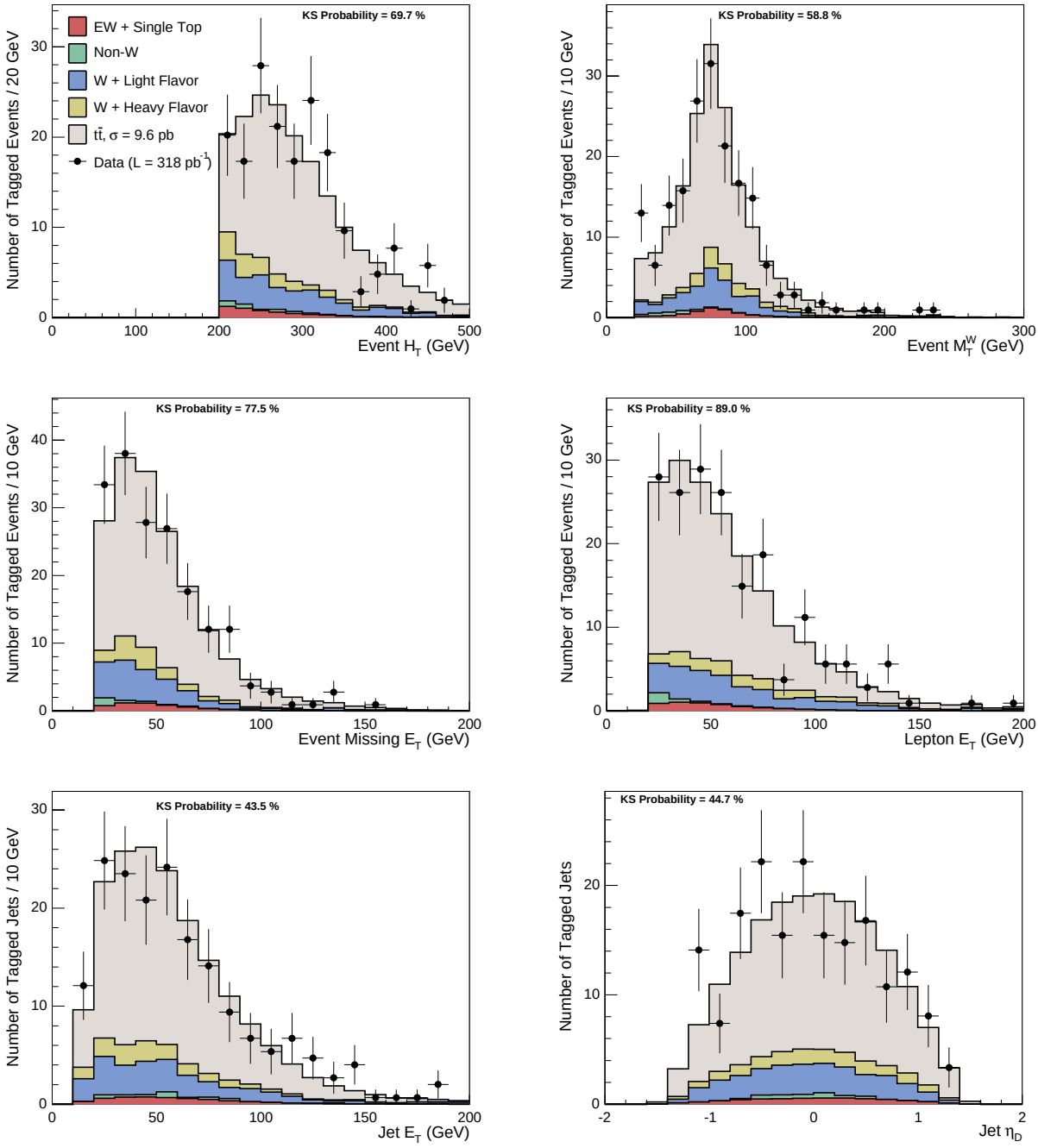

Figure B.2: Comparison of kinematic distributions in data to signal and background expectations for events in the single tag sample ($P_J < 5\%$).

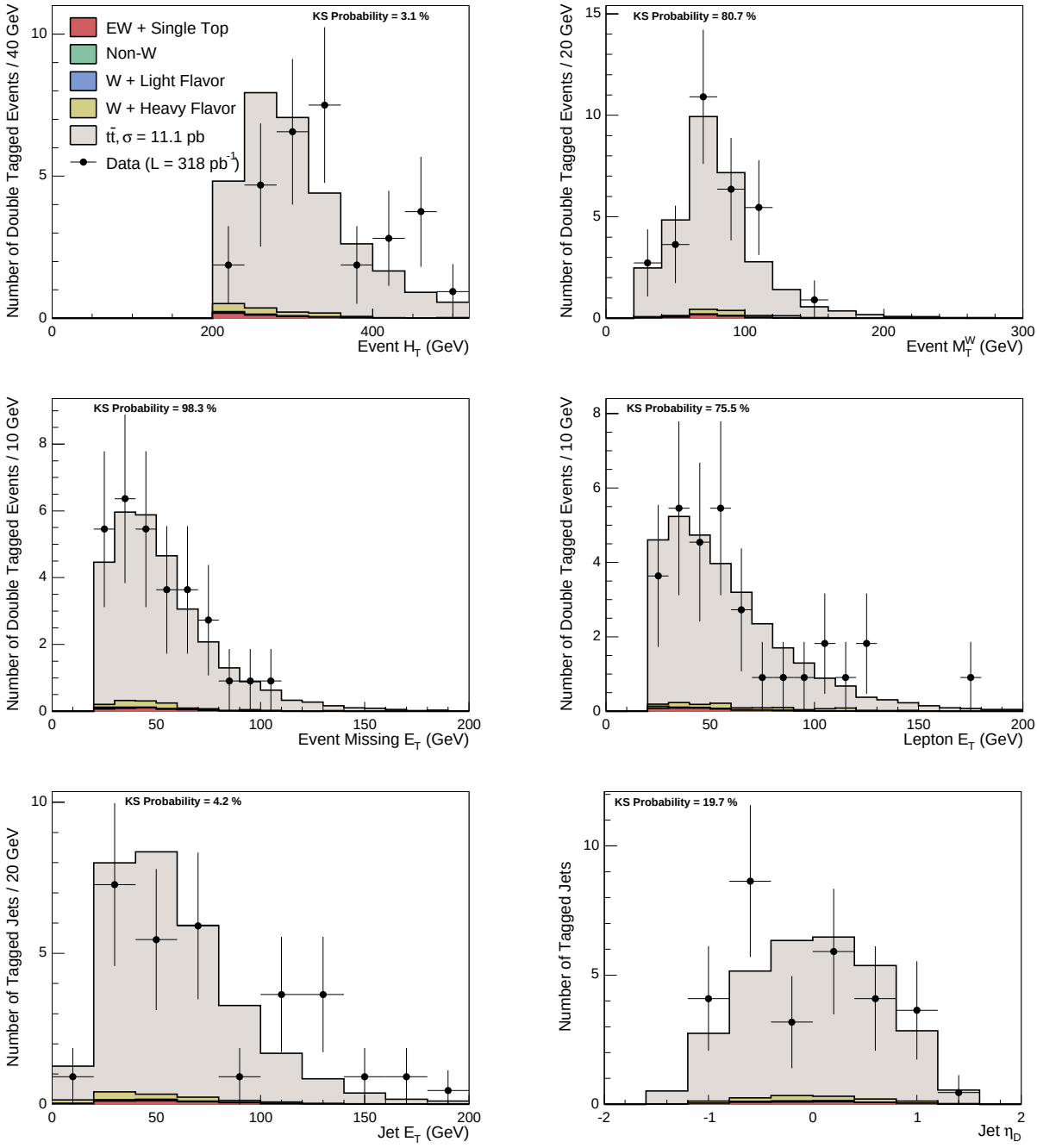

Figure B.3: Comparison of kinematic distributions in data to signal and background expectations for events in the double tag sample ($P_J < 1\%$).

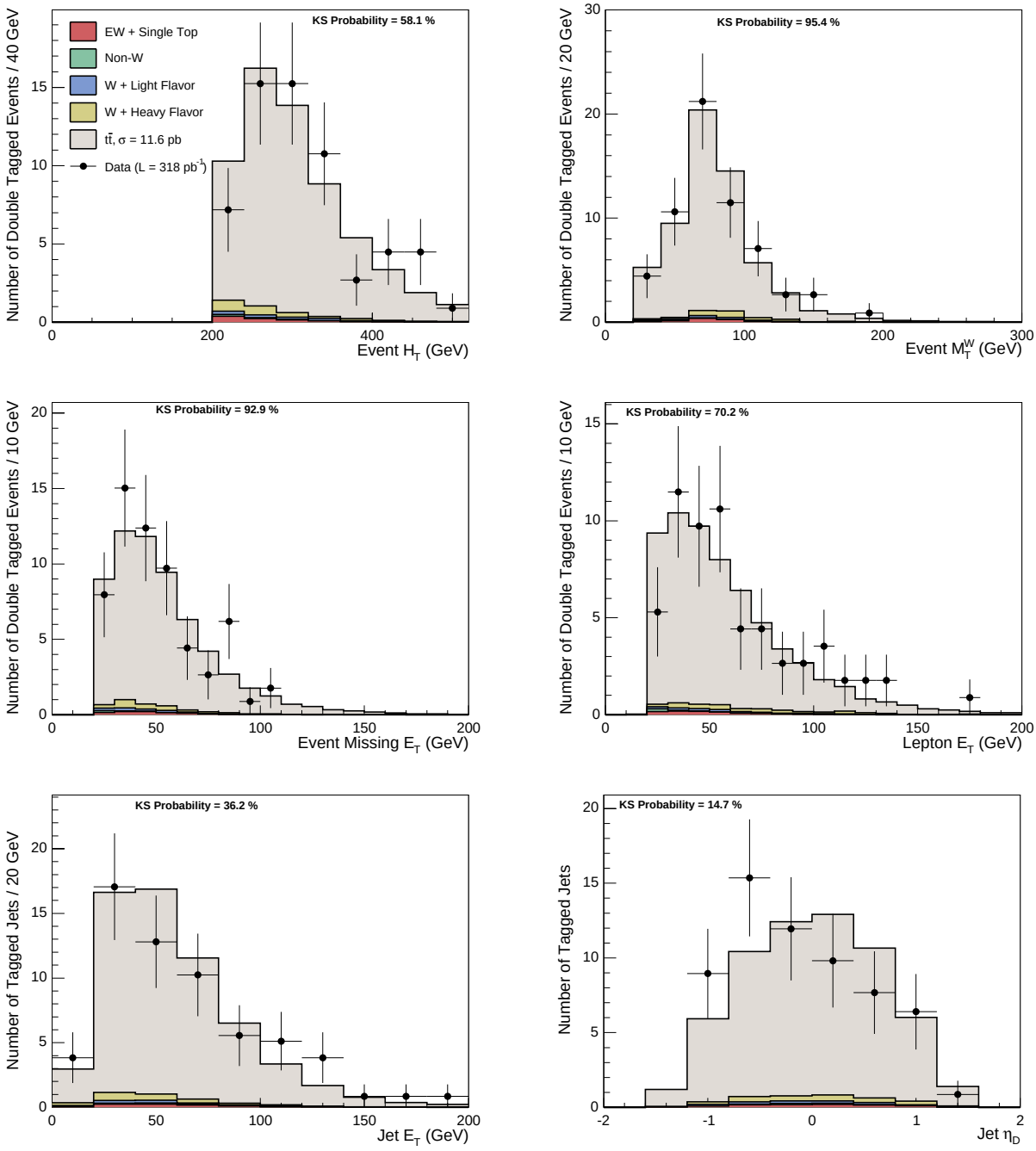

Figure B.4: Comparison of kinematic distributions in data to signal and background expectations for events in the double tag sample ($P_J < 5\%$).

Bibliography

[1] M. Cacciari, S. Frixione, G. Ridolfi, M. Mangano, and P. Nason, J. High Energy Phys. **0404**, 068 (2004).

[2] N. Kidonakis and R. Vogt, Phys. Rev. D **68**, 114014 (2003).

[3] P. Azzi *et al.* (CDF/DØ Collaborations), hep-ex/0404010.

[4] A. Affolder *et al.* (CDF Collaboration), Phys. Rev. D **64**, 032002 (2001), Erratum-ibid: Phys. Rev. D **67**, 119901 (2003);
V.M. Abazov *et al.* (DØ Collaboration), Phys. Rev. D **67**, 012004 (2003).

[5] D. Acosta *et al.* (CDF Collaboration), Phys. Rev. Lett. **93**, 142001 (2004).

[6] D. Acosta *et al.* (CDF Collaboration), Phys. Rev. D **71**, 072005 (2005).

[7] D. Acosta *et al.* (CDF Collaboration), Phys. Rev. D **71**, 052003 (2005).

[8] D. Acosta *et al.* (CDF Collaboration), Phys. Rev. D **72**, 032002 (2005).

[9] D. Acosta *et al.* (CDF Collaboration), Phys. Rev. D **72**, 052003 (2005).

[10] P. Azzi *et al.*, *Preprint* hep-ex / 0404010 (2004).

[11] A. Abulencia *et al.*, *Preprint* hep-ex / 0603039 (2006).

[12] R. D. Peccei, S. Peris and X. Zhang, Nucl. Phys. B **349**, 305–322 (1991).

[13] S. Eidelman *et al.*, Phys. Lett. B **592**, 1 (2004).

[14] V. D. Barger and R. J. N. Phillips, *Collider Physics* Frontiers in physics. Addison-Wesley Reading 1987

[15] F. Halzen and A. D. Martin, *Quarks & leptons* John Wiley & Sons New York 1984

[16] D. J. Griffiths, *Introduction to elementary particles* John Wiley & Sons New York 1987

[17] D. H. Perkins, *Introduction to high energy physics* Addison-Wesley Reading 1987

[18] S. Fukuda *et al.*, Phys. Lett. B **539**, 179–187 (2002)

[19] Q. R. Ahmad *et al.*, Phys. Rev. Lett. **87**, 071301 (2001)

[20] Q. R. Ahmad *et al.*, Phys. Rev. Lett. **89**, 011301 (2002)

[21] S. L. Glashow, Nucl. Phys. **22**, 579–588 (1961)

[22] S. Weinberg, Phys. Rev. Lett. **19**, 1264–1266 (1967)

[23] A. Salam, Elementary particle theory: relativistic groups and analyticity. In Svartholm N, editor, *Nobel symposium No. 8* page 367 Stockholm 1968. Almquist and Wiksell

[24] J. Goldstone, Nuovo Cim. **19**, 154–164 (1961)

[25] J. Goldstone, A. Salam and S. Weinberg, Phys. Rev. **127**, 965–970 (1962)

[26] M. Kobayashi and K. Maskawa, Prog. Theor. Phys. **49**, 652–657 (1973)

[27] M. Cacciari *et al.*, JHEP **404**, 68 (2004)

[28] N. Kidonakis and R. Vogt, Phys. Rev. D **68**, 114014 (2003)

[29] A. P. Heinson, A. S. Belyaev and E. E. Boos, Phys. Rev. D **56**, 3114–3128 (1997)

[30] F. Anselmo, van B. Eijk and G. Bordes, Phys. Rev. D **45**, 2312–2322 (1992)

[31] J. H. Kühn, *Preprint* hep-ph / 9707321 (1997)

[32] M. Jezabek and J. H. Kühn, Nucl. Phys. B **314**, 1–6 (1989)

[33] M. Jezabek and J. H. Kühn, Phys. Lett. B **207**, 91–96 (1988)

[34] A. Czarnecki and K. Melnikow, Nucl. Phys. B **544**, 520–531 (1999)

[35] K. G. Chetyrkin, R. Harlander, T. Seidensticker and M. Steinhauser, Phys. Rev. D **60**, 114015 (1999)

[36] V. S. Fadin, V. A. Khoze and A. D. Martin, Phys. Rev. D **49**, 2247–2256 (1994)

[37] S. Mrenna and C. P. Yuan, Phys. Rev. D **46**, 1007–1021 (1992)

[38] A. Denner and T. Sack, Nucl. Phys. B **358**, 46 (1991)

[39] R. Migneron, G. Eilam, R. R. Mendel and A. Soni, Phys. Rev. Lett. **66**, 3105 (1991)

[40] M. Jezabek and J. H. Kühn, Phys. Rev. D **48**, R1910 (1993). Erratum: Phys. Rev. D **49**, 4970 (1994)

[41] J. H. Kühn, Act. Phys. Pol. B **12**, 347 (1981)

[42] J. H. Kühn, Act. Phys. Austr. Suppl. **XXIV**, 203 (1982)

[43] I. I. Bigi, Y. Dokshitzer, V. Khoze, J. H. Kühn and P. Zerwas, Phys. Lett. B **181**, 157–163 (1986)

[44] L.H. Orr, Phys. Rev. D **44**, 88–98 (1991)

[45] M. Jezabek and J. H. Kühn, Phys. Lett. B **329**, 317–324 (1994)

[46] G. Mahlon, *Preprint* hep-ph / 981121 (1998)

[47] Hill C. T. and Parke S. J., Phys. Rev. D **49**, 4454 (1994)

[48] W. A. Bardeen, C. T. Hill and M. Lindner, Phys. Rev. D **41**, 1647 (1990)

[49] S. L. Glashow, J. Iliopoulos and L. Maiani, Phys. Rev. D **2**, 1285–1292 (1970)

[50] G. Eilam, J. L. Hewett and A.Soni , Phys. Rev. D **44**, 1473 (1991)

[51] H. Fritzsch, Phys. Lett. B **224**, 423–425 (1989)

[52] T. Han, K. Whisnant, B. L. Young and X. Zhang, Phys. Lett. B **385**, 311 (1996)

[53] T. Han, R. D. Peccei and X. Zhang, Nucl. Phys. B **454**, 527 (1995)

[54] W. S. Hou, Phys. Lett. B **296**, 179 (1992)

[55] G. Eilam, A. Gemintern, T. Han, J. Yang and X. Zhang, Phys. Lett. B **510**, 227 (2001)

[56] C. Yue, G. Lu, Q. Xu, G. Liu and G. Gao, Phys. Lett. B **508**, 290 (2001)

[57] S. Pakvasa and H. Sugawara, Phys. Lett. B **82**, 105 (1979)

[58] G. Preparata, Phys. Lett. B **82**, 398 (1979)

[59] K. T. Mahanthappa and M. A. Sher, Phys. Lett. B **86**, 294 (1979)

[60] F. Abe *et al.*, Phys. Rev. Lett. **64**, 142 (1990)

[61] F. Abe *et al.*, Phys. Rev. D **43**, 664 (1991)

[62] S. Abachi *et al.*, Phys. Rev. Lett. **72**, 2138 (1994)

[63] F. Abe *et al.*, Phys. Rev. Lett. **73**, 225 (1994)

[64] F. Abe *et al.*, Phys. Rev. D **50**, 2966 (1994)

[65] F. Abe *et al.*, Phys. Rev. Lett. **74**, 2626 (1995)

[66] S. Abachi *et al.*, Phys. Rev. Lett. **74**, 2422 (1995)

[67] S. Abachi *et al.*, Phys. Rev. D **52**, 4877 (1995)

[68] S. Abachi *et al.*, Phys. Rev. Lett. **74**, 2632 (1995)

[69] F. Abe *et al.*, Phys. Rev. D **51**, 4623 (1995)

[70] F. Abe *et al.*, Phys. Rev. D **52**, 2605 (1995)

[71] C. Berger *et al.*, Phys. Lett. B **86**, 413 (1979)

[72] R. Brandelik *et al.*, Phys. Lett. B **113**, 499 (1982)

[73] B. Adeva *et al.*, Phys. Rev. Lett. **50**, 799 (1983)

[74] B. Adeva *et al.*, Phys. Lett. B **152**, 439 (1985)

[75] H. Yoshia *et al.*, Phys. Lett. B **198**, 570 (1987)

[76] C. Albajar *et al.*, Z. Phys. C **37**, 505 (1988)

[77] F. Abe *et al.*, Phys. Rev. Lett. **68**, 447 (1992)

[78] S. L. Glashow, Phys. Rev. Lett. **45**, 1914 (1980)

[79] G. M. Pinna, Phys. Lett. B **146**, 78 (1984)

[80] J. Kubo, K. Sibold and W. Zimmermann, Nucl. Phys. B **259**, 331 (1985)

[81] K. Just and L. S. The, Z. Naturforsch. **42a**, 241 (1986)

[82] H. Alhendi, M. Özer and M. O. Taha, Phys. Lett. B **213**, 337 (1988)

[83] W. J. Marciano, Phys. Rev. Lett. **62**, 2793 (1989)

[84] J. Ellis and G. L. Fogli, Phys. Lett. B **249**, 543 (1990)

[85] J. Bernabeu, A. Pich and A. Santamaria, Nucl. Phys. B **363**, 326 (1991)

[86] L. Arnaudon *et al.*, Phys. Lett. B **307**, 187 (1993)

[87] D. Schaile, Fortsch. Phys. **42**, 429–484 (1994)

[88] D. Abbaneo *et al.*, CERN-PPE **96-183**, (1996)

[89] D. Abbaneo *et al.*, CERN-EP **2001-021**, (2001)

[90] F. Abe *et al.*, Phys. Rev. Lett. **80**, 2767–2772 (1998)

[91] T. Affolder *et al.*, Phys. Rev. D **63**, 32003 (2001)

[92] S. Abachi *et al.*, Phys. Rev. Lett. **79**, 1197–1202 (1997)

[93] B. Abbott *et al.*, Phys. Rev. D **60**, 052001 (1999)

[94] V. M. Abazov *et al.*, Nature **429**, 638 (2004)

[95] M. Mangano *et al.*, J. High Energy Phys. **0307**, 001 (2003).

[96] G. Aubrecht *et al.*, *A Teachers Guide to the Nuclear Science Wall Chart*, Contemporary Physics Education Project, 2003, `http://www.lbl.gov/abc/wallchart/teachersguide/pdf/Chap11.pdf`.

[97] C. W. Schmidt, *The Fermilab 400-MeV Linac upgrade*, FERMILAB-CONF-93-111 (1993).

[98] J. Marriner, *Stochastic Cooling Overview*, FERMILAB-CONF-03-158 (2003).

[99] Fermilab Beams Division, *Run II Handbook*, `http://www-bd.fnal.gov/runII/index.html`.

[100] R. Blair *et al.*, *The CDF-II detector: Technical Design Report*, FERMILAB-PUB-96/390-E (1996).

[101] D. Acosta *et al.*, Phys. Rev. D **71**, 032001 (2005).

[102] F. Abe *et al.*, *The CDF Detector: an Overview*, Nucl. Instrum. Methods A **271**, 387-403 (1988).

[103] C.S. Sill, *Operational Experience and Performance of the CDF II Silicon Detector*, Nucl. Instrum. Methods A **530**, 1-6 (2004).

[104] A. Sill *et al.*, *CDF Run II Silicon Tracking Projects*, Nucl. Instrum. Methods A **447**, 1-8 (2000).

[105] A. Affolder *et al.*, *Intermediate Silicon Layers Detector for the CDF Experiment*, Nucl. Instrum. Methods A **453**, 84-88 (2000).

[106] A. Affolder *et al.* (CDF Collaboration), Nucl. Instrum. Methods A **526**, 249 (2004).

[107] `http://penn01.fnal.gov/~cot/`.

[108] D. Acosta *et al.*, *A Time-of-Flight Detector in CDF-II*, Nucl. Instrum. Methods A **518**, 605-608 (2004).

[109] Enrique Palencia, *Calibraciones del Detector de Tiempo de Vuelo del Experimento CDF en el Tevatron*, Tesis de Licenciatura (2005).

[110] L. Balka *et al.*, *CDF Central Electromagnetic Calorimeter*, Nucl. Instrum. Methods A **267**, 272-279 (1988).

[111] S. Bertolucci *et al.*, *The CDF Central and Endwall Hadron Calorimeter*, Nucl. Instrum. Methods A **267**, 301-314 (1988).

[112] M. Albrow *et al.*, *The CDF Plug Upgrade Electromagnetic Calorimeter: Test Beam Results*, Nucl. Instrum. Methods A **480**, 524-546 (2002).

[113] G. Ascoli *et al.*, *CDF Central Muon Detector*, Nucl. Instrum. Methods A **268**, 33 (1988).

[114] T. Dorigo *et al.*, *The Muon System Upgrade for the CDF II Experiment*, Nucl. Instrum. Methods A **461**, 560-562 (2001).

[115] D. Acosta *et al.*, *The CDF Cherenkov Luminosity Monitor*, Nucl. Instrum. Methods A **461**, 540-544 (2001).

[116] D. Acosta *et al.*, *The Performance of the CDF Run II Luminosity Monitor*, Nucl. Instrum. Methods A **494**, 57-62 (2002).

[117] S. Klimenko, J. Konigsberg and T.M. Liss, FERMILAB-FN-0741 (2003).

[118] E. J. Thomson *et al.*, *Online Track Processor for the CDF Upgrade*, IEEE Trans. Nucl. Sci. **49**, 1063 (2002).

[119] `http://web.hep.uiuc.edu/Engin/CDF/XTRP/`.

[120] W. Ashmanskas *et al.*, *The CDF Silicon Vertex Trigger*, Nucl. Instrum. Methods A **518**, 532-536 (2004).

[121] W. Wagner *et al.*, FERMILB-CONF-02269-E, International Europhysics conference on High-Energy Physics (HEP 2001), Budapest, Hungary, 12-18 Jul 2001.

[122] B. Angelos *et al.*, International conference on Computing in High-Energy Physics and Nuclear Physics (CHEP 2000), Padova Italy, 7-11 Feb 2000.

[123] E. J. Thomson *et al.*, IEEE Trans. Nucl. Sci. **49**, 1063 (2002).

[124] A. Abulencia *et al.* (CDF Collaboration), hep-ex/0508029.

[125] F. Abe *et al.* (CDF Collaboration), Phys. Rev. D **45**, 1448 (1992).

[126] A. Bhatti *et al.*, hep-ex/0510047, Fermilab-Pub-05-470.

[127] T. Sjostrand *et al.*, Comput. Phys. Commun. **135**, 238 (2001).

[128] G. Corcella *et al.*, J. High Energy Phys. **0101**, 010 (2001).

[129] H.L. Lai *et al.* (CTEQ Collaboration), Eur. Phys. J **C12**, 375 (2000).

[130] P. Avery, K. Read, and G. Trahern, CLEO Report CSN-212, 1985 (Unpublished).

[131] R. Brun and F. Carminati, CERN Programming Library Long Writeup **W5013** 1993.

[132] R. Veenhof, Nucl. Instrum. Methods A **419**, 726 (1998).

[133] G. Grindhammer, M. Rudowitz, and S. Peters, Nucl. Instrum. Methods A **290**, 469 (1990).

[134] E. Gerchtein and M. Paulini, ECONF **C0303241**, TUMT005 (2003), physics/0306031.

[135] D. Buskulic *et al.* (ALEPH Collaboration), Phys. Lett. B **313**, 535 (1993);
F. Abe *et al.* (CDF Collaboration), Phys. Rev. D **53**, 1051 (1996);
A. Affolder *et al.* (CDF Collaboration), Phys. Rev. D **64**, 032002 (2001), Erratum-ibid: Phys. Rev. D **67**, 119901 (2003)

[136] S. Eidelman *et al.* (Particle Data Group), Phys. Lett. B **592**, 1 (2004).

[137] J.M. Campbell *et al.*, Phys. Rev. D **60**, 113006 (1999).

[138] B.W. Harris *et al.*, Phys. Rev. D **66**, 054024 (2002).

[139] D. Acosta *et al.* (CDF Collaboration), Phys. Rev. Lett. **94**, 091803 (2005).

[140] A. Abulencia *et al.* (CDF Collaboration), hep-ex/0606017.

[141] J. Guimaraes da Costa (CDF Collaboration), FERMILAB-PUB-05-593-E (2005).

[142] A. Abulencia *et al.* (CDF Collaboration), to be submitted to Phys. Rev. Lett.